

Jordan Journal of Mechanical and Industrial Engineering (JJMIE)

JJMIE is a high-quality scientific journal devoted to fields of Mechanical and Industrial Engineering. It is published by Hashemite University in cooperation with the Jordanian Scientific Research and Innovation Support Fund, Ministry of Higher Education and Scientific Research.

EDITORIAL BOARD

Editor-in-Chief

Prof. Moh'd Sami Ashhab

Assistant Editors

Dr. Ahmad AlMigdady

Dr. Mohammad Jreissat

Editorial Board

Prof. Tariq A. ALAzab

Al Balqa Applied University

Prof. Jamal Jaber

Al- Balqa Applied University

Prof. Mohamad Al-Widyan

Jordan University of Science and Technology

Prof. Mohammed Taiseer Hayajneh

Jordan University of Science and Technology

Prof. Mohammad Al-Tahat

The University of Jordan

Prof. Ali M. Jawarneh

The Hashemite University

THE INTERNATIONAL ADVISORY BOARD

Abu-Qudais, Mohammad

Jordan University of Science & Technology, Jordan

Tzou, Gow-Yi

Yung-Ta Institute of Technology and Commerce, Taiwan

Abu-Mulaweh, Hosni

Purdue University at Fort Wayne, USA

Jubran, Bassam

Ryerson University, Canada

Afaneh Abdul-Hafiz

Robert Bosch Corporation, USA

Kakac, Sadik

University of Miami, USA

Afonso, Maria Dina

Institute Superior Tecnico, Portugal

Khalil, Essam-Eddin

Cairo University, Egypt

Badiru, Adedji B.

The University of Tennessee, USA

Mutoh, Yoshiharu

Nagaoka University of Technology, Japan

Bejan, Adrian

Duke University, USA

Pant, Durbin

Iowa State University, USA

Chalhoub, Nabil G.

Wayne State University, USA

Riffat, Saffa

The University of Nottingham, U. K

Cho, Kyu-Kab

Pusan National University, South Korea

Saghir, Ziad

Ryerson University, Canada

Dincer, Ibrahim

University of Ontario Institute of Technology,
Canada

Sarkar, MD. Abdur Rashid

Bangladesh University of Engineering &
Technology, Bangladesh

Douglas, Roy

Queen's University, U. K

Siginer, Dennis

Wichita State University, USA

El Bassam, Nasir

International Research Center for Renewable
Energy, Germany

Sopian, Kamaruzzaman

University Kebangsaan Malaysia, Malaysia

Haik, Yousef

United Arab Emirates University, UAE

EDITORIAL BOARD SUPPORT TEAM

Language Editor

Dr. Baker M. Bani-khair

Publishing Layout

Eng. Ali Abu Salimeh

SUBMISSION ADDRESS:

Prof. Moh'd Sami Ashhab, Editor-in-Chief
Jordan Journal of Mechanical & Industrial Engineering,
Hashemite University,
PO Box 330127, Zarqa, 13133, Jordan
E-mail: jjmie@hu.edu.jo



Hashemite Kingdom of Jordan



Hashemite University

Jordan Journal of
Mechanical and Industrial Engineering

JJMIE

An International Peer-Reviewed Scientific Journal

Financed by Scientific Research Support Fund

Volume 15, Number 4, August 2021

<http://jjmie.hu.edu.jo/>

ISSN 1995-6665

Jordan Journal of Mechanical and Industrial Engineering (JJMIE)

JJMIE is a high-quality scientific journal devoted to fields of Mechanical and Industrial Engineering. It is published by Hashemite University in cooperation with the Jordanian Scientific Research and Innovation Support Fund, Ministry of Higher Education and Scientific Research.

Introduction: The Editorial Board is very committed to build the Journal as one of the leading international journals in mechanical and industrial engineering sciences in the next few years. With the support of the Ministry of Higher Education and Scientific Research and Jordanian Universities, it is expected that a heavy resource to be channeled into the Journal to establish its international reputation. The Journal's reputation will be enhanced from arrangements with several organizers of international conferences in publishing selected best papers of the conference proceedings.

Aims and Scope: *Jordan Journal of Mechanical and Industrial Engineering* (JJMIE) is a refereed international journal to be of interest and use to all those concerned with research in various fields of, or closely related to, mechanical and industrial engineering disciplines. *Jordan Journal of Mechanical and Industrial Engineering* aims to provide a highly readable and valuable addition to the literature which will serve as an indispensable reference tool for years to come. The coverage of the journal includes all new theoretical and experimental findings in the fields of mechanical and industrial engineering or any closely related fields (Materials, Manufacturing, Management, Design, Thermal, Fluid, Energy, Control, Mechatronics, and Biomedical). The journal also encourages the submission of critical review articles covering advances in recent research of such fields as well as technical notes.

Guide for Authors

Manuscript Submission:

High-quality submissions to this new journal are welcome now and manuscripts may be either submitted online or email.

Online: For online and email submission upload one copy of the full paper including graphics and all figures at the online, submission site, accessed via <http://jjmie.hu.edu.jo>. The manuscript must be written in MS Word Format. All correspondence including notification of the Editor's decision and requests for revision, takes place by e-mail and via the Author's homepage, removing the need for a hard-copy paper trail

Submission address and contact :

Prof. Moh'd Sami Ashhab
Editor-in-Chief
Jordan Journal of Mechanical & Industrial Engineering, Hashemite University
PO Box 330127, Zarqa, 13115, Jordan
E-mail: jjmie@hu.edu.jo

Types of contributions: Original research papers and Technical reports

Corresponding author: Clearly indicate who is responsible for correspondence at all stages of refereeing and publication, including post-publication. Ensure that telephone and fax numbers (with country and area code) are provided in addition to the e-mail address and the complete postal address. Full postal addresses must be given for all co-authors.

Original material: Submission of an article implies that the work described has not been published previously (except in the form of itstan abstract or as part of a published lecture or academic thesis), that it is not under consideration for publication elsewhere, the publication is approved by all authors and that, if accepted, it will not be published elsewhere in the same form, in English or in any other language, without the written consent of the Publisher. Authors found to be deliberately contravening the submission guidelines on originality and exclusivity shall not be considered for future publication in this journal.

Withdrawing: If the author chooses to withdraw his article after it has been assessed, he shall reimburse JJMIE with the cost of reviewing the paper.

Manuscript Preparation:

General: Editors reserve the right to adjust style to certain standards of uniformity. Original manuscripts are discarded after publication unless the Publisher is asked to return original material after use. Please use MS Word for the text of your manuscript

Structure: Follow this order when typing manuscripts: Title, Authors, Authors title, Affiliations, Abstract, Keywords, Introduction, Main text, Conclusions, Acknowledgements, Appendix, References, Figure Captions, Figures and then Tables. Please supply figures imported into the text AND also separately as original graphics files. Collate acknowledgements in a separate section at the end of the article and do not include them on the title page, as a footnote to the title or otherwise.

Text Layout: Use 1.5 line spacing and wide (3 cm) margins. Ensure that each new paragraph is clearly indicated. Present tables and figure legends on separate pages at the end of the manuscript. If possible, consult a recent issue of the journal to become familiar with layout and conventions. All footnotes (except for table and corresponding author footnotes) should be identified with superscript Arabic numbers. To conserve space, authors are requested to mark the less important parts of the paper (such as records of experimental results) for printing in smaller type. For long papers (more than 4000 words) sections which could be deleted without destroying either the sense or the continuity of the paper should be indicated as a guide for the editor. Nomenclature should conform to that most frequently used in the scientific field concerned. Number all pages consecutively; use 12 or 10 pt font size and standard fonts.

Corresponding author: Clearly indicate who is responsible for correspondence at all stages of refereeing and publication, including post-publication. The corresponding author should be identified with an asterisk and footnote. Ensure that telephone and fax numbers (with country and area code) are provided in addition to the e-mail address and the complete postal address. Full postal addresses must be given for all co-authors. Please consult a recent journal paper for style if possible.

Abstract: A self-contained abstract outlining in a single paragraph the aims, scope and conclusions of the paper must be supplied.

Keywords: Immediately after the abstract, provide a maximum of six keywords (avoid, for example, 'and', 'of'). Be sparing with abbreviations: only abbreviations firmly established in the field may be eligible.

Symbols: All Greek letters and unusual symbols should be identified by name in the margin, the first time they are used.

Units: Follow internationally accepted rules and conventions: use the international system of units (SI). If other quantities are mentioned, give their equivalent quantities in SI

Maths: Number consecutively any equations that have to be displayed separately from the text (if referred to explicitly in the text).

References: All publications cited in the text should be presented in a list of references following the text of the manuscript.

Text: Indicate references by number(s) in square brackets in line with the text. The actual authors can be referred to, but the reference number(s) must always be given.

List: Number the references (numbers in square brackets) in the list in the order in which they appear in the text.

Examples:

Reference to a journal publication:

[1] M.S. Mohsen, B.A. Akash, "Evaluation of domestic solar water heating system in Jordan using analytic hierarchy process". Energy Conversion & Management, Vol. 38 (1997) No. 9, 1815-1822.

Reference to a book:

[2] Strunk Jr W, White EB. The elements of style. 3rd ed. New York: Macmillan; 1979.

Reference to a conference proceeding:

[3] B. Akash, S. Odeh, S. Nijmeh, "Modeling of solar-assisted double-tube evaporator heat pump system under local climate conditions". 5th Jordanian International Mechanical Engineering Conference, Amman, Jordan, 2004.

Reference to a chapter in an edited book:

[4] Mettam GR, Adams LB. How to prepare an electronic version of your article. In: Jones BS, Smith RZ, editors. Introduction to the electronic age, New York: E-Publishing Inc; 1999, p. 281-304

Free Online Color : If, together with your accepted article, you submit usable color and black/white figures then the journal will ensure that these figures will appear in color on the journal website electronic version.

Tables: Tables should be numbered consecutively and given suitable captions and each table should begin on a new page. No vertical rules should be used. Tables should not unnecessarily duplicate results presented elsewhere in the manuscript (for example, in graphs). Footnotes to tables should be typed below the table and should be referred to by superscript lowercase letters.

Notification: Authors will be notified of the acceptance of their paper by the editor. The Publisher will also send a notification of receipt of the paper in production.

Copyright: All authors must sign the Transfer of Copyright agreement before the article can be published. This transfer agreement enables Jordan Journal of Mechanical and Industrial Engineering to protect the copyrighted material for the authors, but does not relinquish the authors' proprietary rights. The copyright transfer covers the exclusive rights to reproduce and distribute the article, including reprints, photographic reproductions, microfilm or any other reproductions of similar nature and translations.

Proof Reading: One set of page proofs in MS Word format will be sent by e-mail to the corresponding author, to be checked for typesetting/editing. The corrections should be returned within 48 hours. No changes in, or additions to, the accepted (and subsequently edited) manuscript will be allowed at this stage. Proofreading is solely the author's responsibility. Any queries should be answered in full. Please correct factual errors only, or errors introduced by typesetting. Please note that once your paper has been proofed we publish the identical paper online as in print.

PAGES**PAPERS**

-
- | | |
|-----------|---|
| 319 - 328 | Establishing Process Capability Indices in a Sugar Manufacturing Industry – an Industrial Engineering Perspective
<i>G.V.S.S.Sharma, P. Srinivasa Rao, B. Surendra Babu</i> |
| 329 - 335 | Aluminium Alloys Nanostructures Produced by Accumulative Roll Bonding (ARB)
<i>Yazan M. Almaetah, khaleel N. Abushgair, Mohammad A. Hamdan</i> |
| 337 - 345 | Simulation of Trajectory Tracking and Motion Coordination for Heterogeneous Multi-Robots System
<i>Samer Mutawe, Mohammad Hayajneh, Suleiman BaniHani, Mohammad Al Qaderi</i> |
| 347 - 355 | Control of Wake Behind an Unconfined Wedge Structure by Magnetohydrodynamics
<i>Shailendra Rana, Hari B. Dura, Rajendra Shrestha</i> |
| 357 - 376 | Numerical Study of Fluid Dynamics and Heat Transfer Characteristics for the Flow Past a Heated Square Cylinder
<i>Rashid Ali , Anshumaan Singh</i> |
| 377 - 385 | Investigation on the Performance of Order Release Methods in a Flow Shop with Bottlenecks
<i>Aruna Prabhu, Raghunandana K, Yogesh Pai P</i> |
| 387 - 393 | The Effects of Sulfur Content on the Mechanical Properties of Nitrile Butadiene Rubber with Different Aging Conditions
<i>Nabeel Alshabatat, Ahmad Abouel-Kasem</i> |
| 395 - 409 | A Hybrid Batch-Fabrication Decision for a Vendor–Buyer Integrated System with Multiple Deliveries, Rework, and Machine Failures
<i>Yuan-Shyi Peter Chiu, Chia-Ming Lai, Tiffany Chiu, Chung-Li Chou</i> |

Establishing Process Capability Indices in a Sugar Manufacturing Industry – an Industrial Engineering Perspective

G.V.S.S.Sharma^{a*}, P. Srinivasa Rao^b, B. Surendra Babu^c

^aAssociate Professor, Mechanical Engineering Department, GMR Institute of Technology, Rajam-532127, India

^bProfessor, Dept. of Mechanical Engineering, Centurion University, Parlakhemundi, Odisha State, India

^cProfessor, Mechanical Engineering Department, GITAM Institute of Technology, Visakhapatnam-530045, India

Received February 12 2021

Accepted September 2 2021

Abstract

Quality of the product is a very important factor to any organization on which the future of the company depends. There are many tools available to check and control the quality of the product, and among them is the process capability study which is highly important. This work is an attempt towards applying the concepts of process capability principles pertaining to discrete manufacturing into the scenario of continuous process oriented industries. In this work, the process capability study is carried out in a sugar processing industry. Data pertaining to Critical-To-Quality parameters of sugar have been collected for several sugar samples. The reasons for the variability are identified and the necessary and corrective actions are suggested to overcome the variations in the sugar manufacturing process. A significant improvement is registered in the process capability indexes of CP and CPK for the identified Critical-To-Quality (CTQ) characteristics of sugar turbidity and minimum aperture. An increase of 7 folds is observed for the CPM value for the CTQ characteristic of minimum aperture. Thus, the process capability indexes are calculated and the capability of the process is determined based on their values.

© 2021 Jordan Journal of Mechanical and Industrial Engineering. All rights reserved

Keywords: Quality Assurance; Process capability; Sugar processing; Statistical Process Control; ANOVA analysis; Critical-To-Quality (CTQ) characteristic;

1. Introduction

Industrial engineering principles are extensively applied in a wide domain of manufacturing as well as service sectors. Process capability study is one of such industrial engineering method which is extensively applied in discrete manufacturing industries. The preliminary process capability study is a logical and methodical procedure that examines the interactions of the potential causal factors for identification of the process deviations. Process run charts are employed to identify the outliers and detect the unnatural reasons (special causes) for variations until a condition of statistical control is reached. Natural variations because of common causes like wear of tool insert tip, can be identified and controlled, as they indicate a certain trend in run charts (increasing trend, or decreasing trend, or cyclic trend and so on). All in all, the process capability study anticipates the degree to which the process adheres to the client's prerequisites. In this work, study is carried out in a process based sugar manufacturing industry.

To measure the capability of the process quantitatively, certain indexes are used. They are of three types; one is the process potential capability index, another one is process performance capability index and the third one is the process capability index accounting for Taguchi's Loss Function. The formulae required for calculating the process

capability indexes and their descriptions are given in the Table 1. The CTQ characteristics identified are the "sugar turbidity" and "minimum aperture" as they depict the process performance as well as the end product quality of the outcome of the sugar manufacturing process.

The parameter "turbidity" is a "smaller-the-better" type of characteristic, i.e., the lower the turbidity value, the better is the process capability. The lower bound (LSL) is taken to be an ideal value of "0" and the upper bound (USL) is taken to be a relative value of "100". Turbidity is a one-sided parameter with the process capability being higher when the values for turbidity obtained are more nearer to the ideal value of "0". Thus, the process performance capability index with respect to upper specification limit (C_{PKU}) is employed for measurement of the process capability of the Critical-To-Quality characteristic of turbidity. The higher the value of C_{PKU} , the better is the process with the turbidity values nearer to the ideal value of "0".

Whereas, the CTQ characteristic, the minimum aperture is a double sided value with optimal sieve size ranging between 0.3 (LSL) and 0.6 (USL) sieve size. Process capability index accounting for Taguchi's Loss Function, C_{PM} , is introduced and added for this double sided characteristic of minimum aperture, with a target value of $T=0.7$ sieve size.

The structure of the paper is as follows. Firstly, introduction to process capability indexes with respect to

* Corresponding author e-mail: sharma.gvss@gmrit.edu.in.

process manufacturing is discussed in the introduction section. This is followed by a comprehensive literature review. Data is collected for the CTQ characteristics of sugar turbidity and minimum aperture. This data collected is analyzed for the process capability in the data analysis section. Corrective actions have been applied for the process deviations and discussed in the results and discussions section. The conclusions have been derived in the conclusions sections followed by the list of references.

2. Literature Review

Quality Assurance tools and techniques like quality circles, TPM (Total Productive Maintenance), kaizen, JIT (Just-In-Time) are extensively used in the manufacturing sector [1]. Statistical analysis finds its application in a wide domain of areas[2]. Statistical process control (SPC) is not only limited to manufacturing domain, but is also successfully applied in commercial bank's operation performance [3]. The concepts of process capability are successfully deployed into service sector of banking. Eric shao[4]proposed technique for identification, isolation and correction of assignable causes of a disturbance in manufacturing process, thus paving way for integration of SPC and EPC (Engineering process control). Balamurali and Usha[5]proposed a quick switching variables sampling system for deciding whether the component under inspection has to be accepted or rejected. This sampling system is limited to a quality characteristic with double specification limits and is based on the process performance capability index (CP_K). Kumaravadivel et al.[6]analyzed the casting process by Taguchi method and employed ANOVA analysis for determining the optimal process parameters and their contribution to process variations. Lee et al. [7]proposed a method to design control charts for detecting state changes as well as to rebuild manufacturing process model.

Adeoye et al.[8] conducted process capability study in a drug manufacturing company where they studied about the process deviations by employing control charts. Shinde et

al. [9]investigated the significance of process capability indexes with respect to machines. It is inferred that the process capability examination can also be extended to machines or machine instruments, in addition to the manufacturing process analysis. S. Bangphan et al.[10] conducted process capability analysis by using SPC of rice polishing cylinder turning practice. John et al. [11]studied the process capability analysis by using curve fitting methods.

J.Subramani et al. [12]studied the process performance using control charts for variables with known process capability indexes. Stefan et al.[13] gave the complete explanation of understanding process capability indexes, their classification and method of calculation. Details of both process capability indexes and process performance indexes were given. They concluded that process performance indexes are most efficient indexes to measure variability since process performance indexes are calculated by considering the standard deviation of entire data. Sharma and Rao have improved the production process capability of connecting rod [14] and crankshaft [15]production. Sharma et al.[16] have registered an improvement in the process capability indexes of CTQ characteristics of aluminium alloy wheel production. Sharma et al.[17] have established a relation between the process capability and the dimensional tolerances for the manufacture of the connecting rod component. Vannan and Vizhian[18]adopted the ANOVA analysis for analysing the coating parameters in the process of electroless coating. Mandahawi et al.[19] registered a significant process improvement in a paper manufacturing industry by following the DMAIC (Define-Measure-Analyze-Improve-Control) approach. Hypothesis formulation and testing the hypothesis forms a scientific method to judge, prove and register a process improvement. Mujbil Al-Marsumi[20] formulated and tested the hypothesis for obtaining significant process improvements in the Dairy Industry in Jordan. PederLundkvist[21] in his PhD dissertation established procedures for capability analysis in process industry.

Table 1. Formulae of process capability indexes

Index	Formula	Description
C_p	$\frac{\text{Upper Specification Limit} - \text{Lower Specification Limit}}{6\sigma}$	Process potential capability index
C_{PKU}	$\frac{\text{Upper Specification Limit} - \text{Mean of process Limits}}{3\sigma}$	Process performance capability with respect to upper specification limit. This measures the smaller-the-better type of characteristic. The larger the value of C_{PKU} the better is the characteristic.
C_{PKL}	$\frac{\text{Mean of process Limits} - \text{Lower Specification Limit}}{3\sigma}$	Process performance capability with respect to lower specification limit. This measures the larger-the-better type of characteristic. The larger the value of C_{PKL} the better is the characteristic.
C_{PK}	Minimum of C_{PKU} and C_{PKL}	Process performance capability index responsible for process centering.
C_{PM}	$\frac{\text{Upper Specification Limit} - \text{Lower Specification Limit}}{6\sigma_{CPM}}$ where, $\sigma_{CPM} = \sqrt{\frac{\sum_{i=1}^n (x_i - T)^2}{(n-1)}}$ where, $T = T \text{ arg et value}$	Process capability index accounting for Taguchi's Loss Function

Jairo Munoz [22] studied the process capability of TIG welding process and applied the fuzzy logic theory for the uncertain data obtained during the TIG welding process. The quality inspection personnel have different individual opinions regarding the same weld quality. Such induced individual uncertainty can be addressed through fuzzy logic method which is a combination of possibilistic and probabilistic approached towards process capability. Baghbani et al. [23] implemented a fuzzy Process Failure Modes and Effects Analysis (PFMEA) in a sugar manufacturing set-up at Kurdistan. They identified as many as 49 potential failure modes and proposed solutions for starting with the highest Risk-Priority-Number (RPN). Kustiyo and Arkeman[24] adopted the statistical methodology of reducing the process variation through a separate framework for identification of common causes and special causes for process deviations. They believed in the philosophy of Statistical Process Control approach for optimizing the sugar manufacturing process as a whole. Pearn and Chen [25] and Pearn et al.[26] have focused on the different process capability indexes including the CPM index accounting for the Taguchi's Loss Function. Mohan and Yadav [27] suggested process improvements in the sugar manufacturing process in the limelight of carbonation and phosphatation process. Aljebory and Alshebeb[28] registered an improvement in quality of a process oriented chemical industry through Statistical and Engineering process control.

This paper examines the process capability in a sugar manufacturing scenario. The structure of the paper is as follows. The first section of the paper starts with a brief introduction to process capability and formulae related to process capability indexes. This is followed by an exhaustive literature survey which comprehends the various works related to process capability and statistical process control. Data pertaining to multiple Critical-To-Quality parameters namely sugar turbidity and minimum aperture have been collected from sugar manufacturing process. The collected data is analyzed and validated through ANOVA analysis for suitability towards further process capability analysis. The results and discussion session summarizes the process capability indexes' values and generalizes that, the

upper limit process performance index (C_{PKU}) is taken as the measure for smaller-the-better type of Critical-to-Quality characteristics respectively. Finally the paper ends with conclusion followed by the list of references cited in this paper.

3. Data Collection

In this study, data has been collected in a sugar processing industry. There are two important Critical-To-Quality (CTQ) characteristics in sugar manufacturing, namely, turbidity and minimum aperture that are used for determining process capability indexes. Out of total no. of samples collected, 75 samples of the parameter which describe the process in as-it-is state are given below. Some precautions must be taken before going to proceed for process capability analysis. They are that the collected data must be normally distributed. The collected data must be statistically stable.

3.1. Sugar Turbidity

Sugar turbidity is regularly assessed in sugar manufacturing plants. It represents the presence of suspended particles in sugar solution which is detected based on change in characteristics like wavelength and refractive index when light is diffused through the sugar solution with suspended particles[29]. Table 2 shows the continuous observations of turbidity.

3.2. Minimum aperture

Minimum aperture measures average grain size of the sugar crystal. The size of sugar crystals is determined when the crystals are passed through different sizes of multiple sieves. Coefficient of variation (CV) of sugar crystals size determines the consistency in homogeneity of crystal size. A Lower CV portrays a superior consistency while a high CV means a higher variation in sugar crystal sizes. A variation within 35% is generally desirable. Table 3 shows the continuous observations of this characteristic.

Table 2. Observations for Turbidity

S.No.	Level-1	Level-2	Level-3	S.No.	Level-1	Level-2	Level-3
1	120	136	95	14	84.9	83.4	85.2
2	98.2	98.4	96.2	15	83.4	126	68.5
3	86.6	86.6	84	16	70.3	89	88
4	79.5	72.4	86	17	84	68.5	65
5	114	94	81	18	86	85.2	89
6	81	87.3	86	19	88	80.6	78
7	80	80	88	20	86.5	84	80
8	65	80.6	80.6	21	71	79	79
9	89	88	86.5	22	81	80	70.3
10	78	73	71	23	78	78	88
11	80	84	81.7	24	83	89	81
12	85.5	82	83	25	80	65	81.7
13	79	78	82.6				

4. Data Analysis

4.1. Hypothesis formulation for ANOVA analysis

For analyzing the observations of the Critical-To-Quality characteristics, the observations must be analyzed whether they are significantly different or not. This is done through ANOVA analysis. Firstly the Hypothesis must be formulated and tested subsequently[30]. The following hypothesis are to be tested:

- Null Hypothesis - $H_0: \mu_i = \mu$ for all $i = 1, 2, 3$
 - Alternate Hypothesis - $H_1: \mu_i \neq \mu$ for some $i = 1, 2, 3$
- where μ_i is the population mean for level i and μ is the overall grand mean of all levels

Each level consists of 25 measurement readings with a total of three such levels (Table 2 and Table 3).

4.2. Turbidity

4.2.1. ANOVA Analysis for turbidity

The data pertaining to turbidity is tabulated in Table 2. The statistical calculations for turbidity are summarized in Table 4 and the ANOVA table is depicted in Table 5.

For 95% confidence levels, the probability level “ p ” is of a significance of 0.05. For this value of “ p ” the critical value for the rejection region is $F_{CRITICAL(p, K-1, N-K)}$ i.e., $F_{CRITICAL(0.05, 2, 72)}$ and is obtained to be 3.1239. Thus,

$$F_{STATISTIC} < F_{CRITICAL}$$

Hence, the null hypothesis is accepted. If the judgment from ANOVA is in favor of the null hypothesis, then it suggests that the result is not significantly different, and, $\mu_i \approx \mu$ for all $i = 1, 2, 3$. Therefore, a *post hoc* test is not a requisite. Hence the data is statistically stable and ready for performing process capability study.

Table 3. Observations for Minimum Aperture

S.No.	Level-1	Level-2	Level-3	S.No.	Level-1	Level-2	Level-3
1	0.98	1.07	1.07	14	1.09	0.94	1.19
2	1	1	1.3	15	1.19	1.14	1.13
3	1	1.1	1	16	0.9	0.9	0.94
4	1	1.2	1.1	17	0.99	0.8	0.98
5	1.09	1.09	1.04	18	1.01	1.18	1.07
6	1.07	1.07	1.18	19	1.09	1.22	1.3
7	0.82	0.8	0.8	20	0.94	1.18	1.08
8	0.8	0.94	0.94	21	1.01	0.8	0.82
9	1.04	0.94	1.01	22	1.15	1.19	1.01
10	1.01	1.08	1.15	23	1.16	1.09	1.16
11	1.08	1.16	1.16	24	1.13	1.07	1.14
12	1.06	1.16	1.3	25	0.94	1.22	1.3
13	1.3	1.22	1.2				

Table 4. Statistical calculations for turbidity

S.No.	Statistical calculation	Level-1	Level-2	Level-3
1	n (Number of observations)	25	25	25
2	$\sum X$ (sum of observations)	2111.9	2148	2055.3
3	μ_i (Mean of observations)	84.476	85.92	82.212
4	$\sum X^2$ (sum of squares)	181760.21	190337.74	170326.97
5	σ (Standard Deviation)	11.824	15.5209	7.5184
6	μ (Grand mean)	[($\mu_1 + \mu_2 + \mu_3$) / 3] = 84.203		

Table 5. ANOVA table for turbidity

Source	SS	df	MS	
Between-treatments	174.6675	2	87.3337	F = 0.59923
Within treatments	10493.572	72	145.7441	
Total	10668.2395	74		

4.2.2. Process capability and control study for turbidity

Figure 1 shows that the control chart of both \bar{X} and R chart for turbidity is lying in between the UCL and LCL. There are no outliers seen in this chart.

Now it is seen that the process capability curve is skewed towards right i.e., towards Upper Specification Limit (USL). This is depicted in Figure 2 below.

Thus, the process is found to be incapable for achieving the sugar of expected turbidity levels, as the turbidity is a smaller-the-better type of characteristic.

The following are the corrective actions suggested to overcome this problem. If the suspended particles are present in the sugar juice, then, this impacts the productivity

of steps in the refining cycle. Clarification is the process where these suspended particles are eliminated. Here, a blend of lime, activated carbon, and a clarifying agent, are imparted to the sugar juice. Firstly, the activated carbon eliminates flavonoids and natural acids which when normally present in the sugar results in a bad flavour. Next, the kind of clarifying agent used depends on whether the raw material is a sugar stick or sugar beet. Turbidity investigation on the sugar juice is the measure for the effectiveness of the clarification process. A lower turbidity shows adequate clarification done. pH meters have capacity to show readings to indicate juice turbidity for optimal usage of the clarifying agents. More care has been taken than the usual during these processes so that turbidity levels can be reduced.

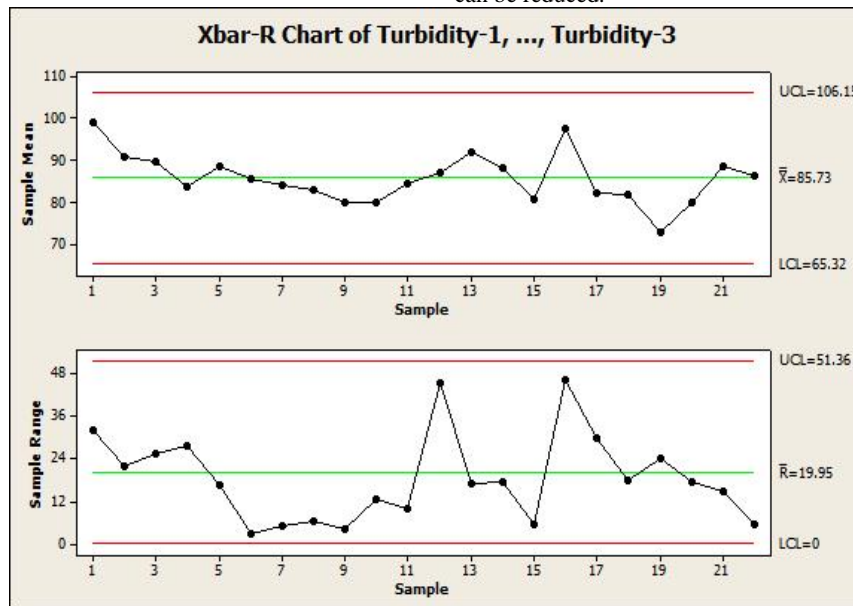


Figure 1: \bar{X} and R chart for Turbidity.

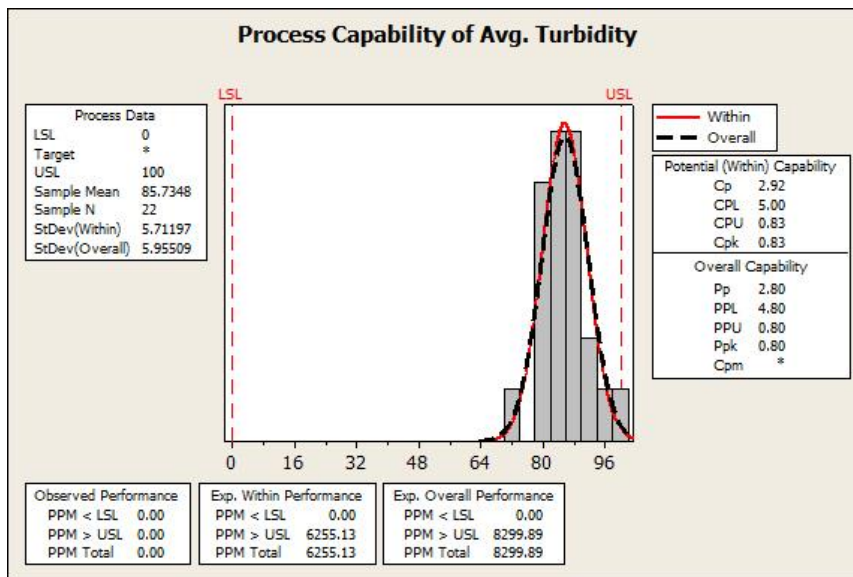


Figure 2: Process capability analysis of turbidity

The process run charts are employed after taking corrective actions, so that the process shall not deteriorate. Figure 3 shows the run chart of turbidity after taking corrective action.

The C_{PKU} index is applicable to turbidity, as it is a smaller-the-better type of characteristic. Hence, From Table 1 it is clear that C_{PKU} is given by the formula:

$$C_{PKU} = \frac{USL - \bar{X}}{3\sigma} = \frac{100 - 26.45758}{3 \times 7.181799} = \frac{73.54242}{21.5454} = 3.41337 \quad (1)$$

Thus, after taking the corrective action, there is an increase in C_{PKU} from 0.43856 to 3.4133.

4.3. Minimum aperture

Minimum aperture is the optimum size of the sugar crystal that is generally suggested for industrial use. For

analyzing the observations of minimum aperture, firstly the observations must be analyzed whether they are significantly different or not. This is done through ANOVA analysis.

4.3.1. ANOVA analysis for minimum aperture

The data pertaining to minimum aperture is tabulated in Table 3. The statistical calculations for minimum aperture are summarized in Table 6 and the ANOVA table is depicted in Table 7.

For 95% confidence levels, the probability level “ p ” is of a significance of 0.05. For this value of “ p ” the critical value for the rejection region is $F_{CRITICAL(p,K-I,N-K)}$ i.e., $F_{CRITICAL(0.05,2,72)}$ and is obtained to be 3.1239. Thus,

$$F_{STATISTIC} < F_{CRITICAL}$$

Hence, the null hypothesis is accepted. If the judgment from ANOVA is in favor of the null hypothesis, then it suggests that the result is not significantly different, and, $\mu_i \approx \mu$ for all $i = 1,2,3$. Therefore, a *post hoc* test is not a requisite. Hence the data is statistically stable and ready for performing process capability study.

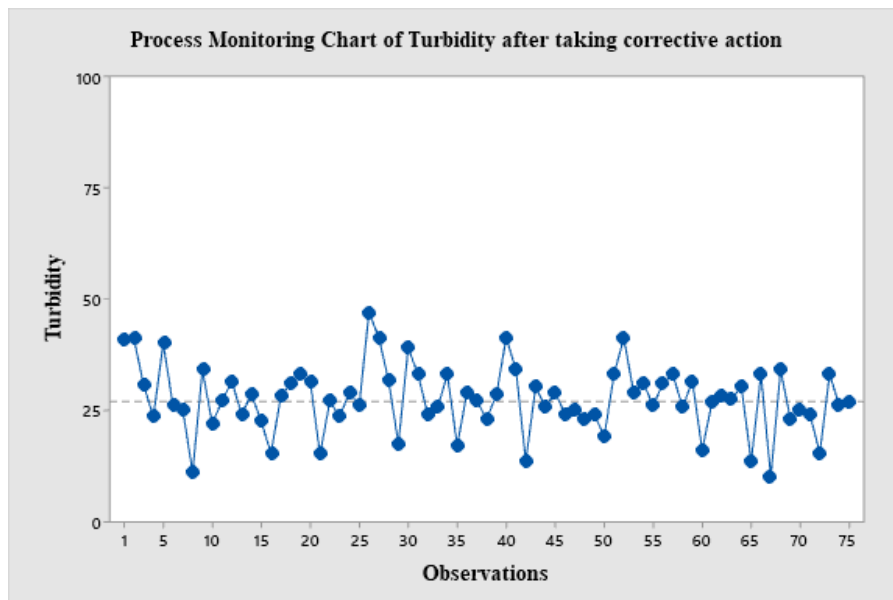


Figure 3. Process run chart for turbidity post corrective action

Table 6. Statistical calculations for minimum aperture

S.No.	Statistical calculation	Level-1	Level-2	Level-3
1	n (Number of observations)	25	25	25
2	$\sum X$ (sum of observations)	25.85	26.56	26.79
3	μ_i (Mean of observations)	1.034	1.0624	1.0716
4	$\sum X^2$ (sum of squares)	27.0223	28.665	29.2335
5	σ (Standard Deviation)	0.1106	0.1366	0.1479
6	μ (Grand mean)	[($\mu_1 + \mu_2 + \mu_3$) / 3] = 1.056		

Table 7. ANOVA table for minimum aperture

Source	SS	df	MS	
Between-treatments	0.0192	2	0.0096	F = 0.54603
Within treatments	1.2664	72	0.0176	
Total	1.2856	74		

4.3.2. Process capability and control study for minimum aperture

Figure 4 shows that the control chart of both \bar{X} and R chart for minimum aperture is lying in between the UCL and LCL. There are no outliers seen in this chart.

$$C_P = \frac{USL - LSL}{6\sigma} = \frac{0.9 - 0.6}{6 \times 0.129935} = \frac{0.3}{0.779612} = 0.384807 \quad (2)$$

$$C_{PKU} = \frac{USL - \bar{X}}{3\sigma} = \frac{0.9 - 1.063733}{3 \times 0.129935} = \frac{-0.16373}{0.389806} = -0.42004 \quad (3)$$

$$C_{PKL} = \frac{\bar{X} - LSL}{3\sigma} = \frac{1.063733 - 0.6}{3 \times 0.129935} = \frac{0.463733}{0.389806} = 1.189652 \quad (4)$$

$$C_{PK} = \text{Minimum of } C_{PKU} \text{ and } C_{PKL} = -0.42004. \quad (5)$$

Consider a process Target Value of aperture size of $T = 0.70$ which is on the lower side of aperture size. Then, we have the CPM value calculations as follows:

$$C_{PM} = \frac{USL - LSL}{6\sigma_{CPM}} \quad \text{where, } \sigma_{CPM} = \sqrt{\frac{\sum_{i=1}^n (x_i - T)^2}{(n-1)}} \quad \text{where, } T = \text{Target value} \quad (6)$$

Thus,

$$C_{PM} = \frac{0.9 - 0.6}{6 \times 0.682276} = 0.073$$

Thus the C_P value is 0.4, C_{PK} value is -0.42004 and C_{PM} value is 0.073

Now it is seen that the process capability curve is completely skewed towards right with the process mean extending outside the Upper Specification Limit (USL). This shows an incapable manufacturing process which requires a corrective action. This is depicted in Figure 5 below.

Thus the process is found to be incapable for achieving the sugar of expected minimum aperture levels. The following are the corrective actions suggested to overcome this problem. Coefficient of variation (CV) is a method of portraying the accuracy of the measurements. Lower Coefficient of Variation describes a superior consistency

while a high coefficient of variation means an inconsistent size of sugar crystal with more variation. A Coefficient of variation of below 35% is preferred for crystals of sugar. Commonly, sugar crystals of coarser size are easier to separate through the centrifuging screen and constitute a superior yield. Fine sugar crystals on the other hand, pass through the sieve and again mix-up with the mother liquor which must be solidified once more, thus minimising the recovery rate. The dissolvability of finer crystals of sugar is more when compared to larger crystals of sugar, thus, making the finer crystals more preferred and costlier. Therefore, in order to strike a balance in the size of sugar crystal, the sugar factories manufacture medium sized crystals (neither large nor small) of the sieve size of 350 to 400 micro-meters aperture size.

The process run charts are employed after taking corrective actions, so that the process shall not deteriorate. Figure 6 shows the run chart of minimum aperture after taking corrective action. The USL of minimum aperture is 0.9 and the LSL is 0.6. Hence, From Table 1 it is clear that C_P and C_{PK} is given by the formula:

$$C_P = \frac{USL - LSL}{6\sigma} = \frac{0.9 - 0.6}{6 \times 0.043817} = \frac{0.3}{0.262902} = 1.14111 \quad (7)$$

$$C_{PKU} = \frac{USL - \bar{X}}{3\sigma} = \frac{0.9 - 0.731733}{3 \times 0.043817} = \frac{0.168267}{0.131451} = 1.280072 \quad (8)$$

$$C_{PKL} = \frac{\bar{X} - LSL}{3\sigma} = \frac{0.731733 - 0.6}{3 \times 0.043817} = \frac{0.131733}{0.131451} = 1.002148 \quad (9)$$

$$C_{PK} = \text{Minimum of } C_{PKU} \text{ and } C_{PKL} = 1.002148 \quad (10)$$

$$C_{PM} = \frac{USL - LSL}{6\sigma_{CPM}} \quad \text{where, } \sigma_{CPM} = \sqrt{\frac{\sum_{i=1}^n (x_i - T)^2}{(n-1)}} \quad \text{where, } T = \text{Target value} \quad (11)$$

Thus,

$$C_{PM} = \frac{0.9 - 0.6}{6 \times 0.095219} = 0.525$$

Thus, after taking the corrective action for minimum aperture, there is an increase in C_P from 0.3848 to 1.1411 and increase in C_{PK} from -0.4200 to 1.00214 and C_{PM} has increased from an initial value of 0.073 to 0.525, which records an increase of 7 folds.

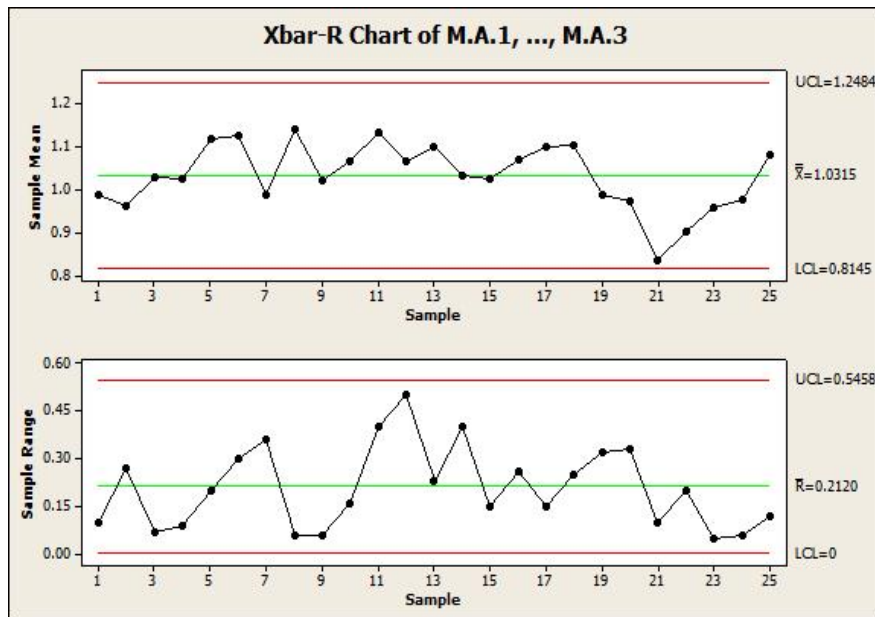


Figure 4. \bar{X} and R chart for Minimum aperture

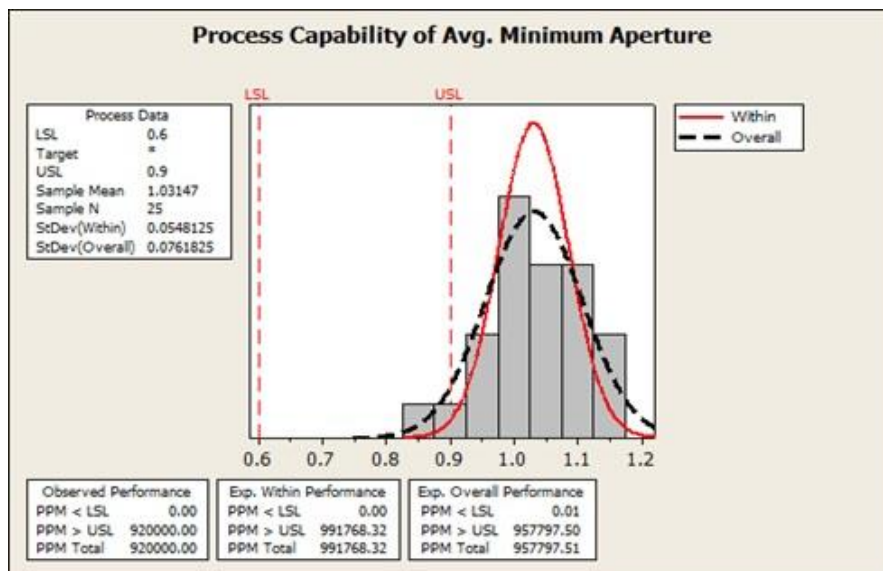


Figure 5. Process capability analysis of minimum aperture

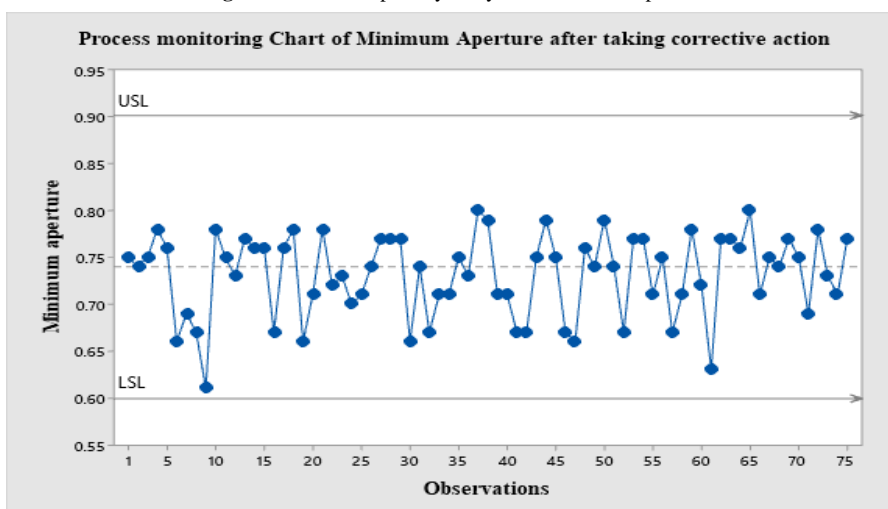


Figure 6. Process run chart for minimum aperture post corrective action

5. Results and Discussions

5.1. The process capability indexes' values

Based on the formulae of capability indexes depicted in Table 1, the final process performance capability indexes for the critical-to-quality characteristics are consolidated in the tabular format in Table 8.

Table 8. Final Process Capability indexes

S.No.	CTQ characteristic	Type of CTQ	C_P	C_{PKU}	C_{PKL}
1	Turbidity	Smaller-the-better	2.32	3.41	1.22
2	Minimum Aperture	Double sided characteristic	1.14	1.28	1.002

6. Discussion

It is observed from initial studies that for Turbidity (which is smaller-the-better type characteristic) and Minimum aperture (which is double sided type characteristic), the capability indexes are smaller than 1.0. For achieving a target value of the capability index to be more than 1.0 following are the corrective actions taken:

- Clarification process is intensified for raising the CP_{KU} levels of turbidity
- The coefficient of variation is preferably kept to a value of less than 35% for raising the C_P and CP_K levels of Minimum Aperture

Thus, this work horizontally deploys the concept of process capability pertaining to discrete manufacturing industries into a continuous process production scenario. The characteristics pertaining to continuous process industries are one-sided and are either a larger-the-better characteristic or smaller-the-better characteristic. In such a situation, the process performance capability index upper limit (CP_{KU}) is dedicated for smaller-the-better and process performance capability index lower limit (CP_{KL}) is dedicated for larger-the-better characteristics. The greater the index value, the better is the Critical-To-Quality characteristic.

It is observed from Table 8 that for the CTQ characteristic of Turbidity, the process performance capability index upper limit (CP_{KU}) is to be considered as Turbidity is a smaller-the-better type of characteristic. It is evident that for turbidity the final $CP_{KU} = 3.41$ after implementing the corrective action of intensifying the clarification process. On the other hand, the Minimum Aperture is a double sided CTQ Characteristic. Hence for Minimum Aperture the smaller value among the CP_{KU} and CP_{KL} is to be considered. Thus, for Minimum Aperture, the final process performance capability index $CP_K = 1.002$. Considering for a target value $T = 0.7$ for minimum aperture, this study has witnessed around a 7 folds increase of the value of C_{PM} from an initial value of 0.07 to a final value of 0.525 post corrective action. Therefore, after implementing the corrective actions, the process performance indexes for the CTQ characteristics of "Turbidity" and "Minimum Aperture" are both obtained as greater than the value of 1.0.

In this way, the process capability concepts are successfully applied to a process oriented industry.

Future scope of this work can be extended to other quality assurance parameters like Sucrose content, Moisture Content, Dextran content, Conductivity Ash and SO_2 content for performing process capability studies.

7. Conclusions

Nowadays all organizations are craving to maintain good quality in their products and services to survive in this high competitive world. Though there are many tools to improve and scrutinize the quality of the product, SPC (Statistical Process Control) and process capability analysis have carved a niche importance.

In this study, sugar industry was chosen for the process capability study. Quality parameters of sugar were collected for required number of samples. To get the trust worthy results in process capability analysis, control charts for all quality parameters were drawn and checked whether the collected data is stable or not. Process performance capability indexes CP_{KU} and CP_{KL} were considered as a measure for smaller-the-better and larger-the-better critical-to-quality characteristics. Process capability indexes for CTQ parameters were calculated and process capability histograms were drawn. As the process for producing with the turbidity and minimum aperture within specification limits is incapable, corrective actions were suggested to make process capable. Process capability index accounting for Taguchi's Loss Function, C_{PM} , is introduced and added for this double sided characteristic of minimum aperture, with a target value of $T=0.7$ sieve size. A significant increase in C_{PM} from an initial value of 0.073 to a final value of 0.525 is observed, which records an increase of 7 folds.

Thus, the concept of process capability pertaining to discrete manufacturing processes is extended to continuous process oriented industry like sugar manufacturing. Hence, the procedures adopted in this work can be horizontally deployed onto other process dominant industries like pharmaceuticals, cement and refinery, where the process characteristics are predominantly one-sided of either smaller-the-better or of larger-the-better nature.

References

- [1] J. A. Farooque and A. B. Mohapatra, "Japanese manufacturing techniques and practices: an Indian perspective," Jordan Journal of Mechanical and Industrial Engineering, Vol. 3, No. 3, 2009.
- [2] R. H. Fouad and A. Mukattash, "Statistical process control tools: a practical guide for Jordanian industrial organizations," Jordan Journal of Mechanical and Industrial Engineering, Vol. 4, No. 6, 2010, 693-700.
- [3] M.-C. Tsai and C. Ou-Yang, "Improving a commercial bank's operation performance through statistical process control," Journal of the Chinese Institute of Industrial Engineers, Vol. 27, No. 3, 2010, 226-236.
- [4] Y. E. Shao, "The identification techniques that result from using an integrated SPC-EPC control system," Journal of the Chinese Institute of Industrial Engineers, Vol. 15, No. 2, 1998, 179-184.
- [5] S. Balamurali and M. Usha, "Optimal designing of variables quick switching system based on the process capability index C_{pk} ," Journal of Industrial and Production Engineering, Vol. 31, No. 2, 2014, 85-94.
- [6] A. Kumaravadeivel, U. Natarajan, and C. Ilamparithi, "Determining the optimum green sand casting process

- parameters using Taguchi's method," *Journal of the Chinese Institute of Industrial Engineers*, Vol. 29, No. 2, 2012, 148-162.
- [7] S.-P. Lee, D. S.-H. Wong, C.-I. Sun, W.-H. Chen, and S.-S. Jang, "Integrated statistical process control and engineering process control for a manufacturing process with multiple tools and multiple products," *Journal of Industrial and Production Engineering*, Vol. 32, No. 3, 2015, 174-185.
- [8] A. Adeoye Akeem, "Process Capability Analysis as a Means of Decision Making in manufacturing company," *International Journal of Advanced Research in Computer Science & Technology (IJARCST)*, Vol. 1, No. 1, 2013, 15-18.
- [9] J. Shinde and R. Katikar, "Importance of process capability and process performance indices in machine tool," *International Journal of Research in Engineering & Applied Sciences*, Vol. 2, No. 2, 2012, 1211-1217.
- [10] S. Bangphan, P. Bangphan, and T. Boonkang, "Process Capability Analysis by Using Statistical Process Control of Rice Polished Cylinder Turning Practice," *International J. of Mechanical, Aerospace, Industrial, Mechatronic and Manufacturing Engineering*, Vol. 8, No. 12, 2014, 2037-2043.
- [11] J. J. Flaig and F. Khorasani, "Process capability analysis using curve fitting methods," *Global Journal of Research In Engineering*, 2013,
- [12] J. Subramani and S. Balamurali, "Control charts for variables with specified process capability indices," *International journal of probability and statistics*, Vol. 1, No. 4, 2012, 101-110.
- [13] S. Steiner, B. Abraham, and J. MacKay, "Understanding process capability indices," Waterloo, Ontario, 1997,
- [14] G. Sharma and P. S. Rao, "Process capability improvement of an engine connecting rod machining process," *Journal of industrial engineering international*, Vol. 9, No. 1, 2013, 1-9.
- [15] G. Sharma and P. S. Rao, "A DMAIC approach for process capability improvement an engine crankshaft manufacturing process," *Journal of Industrial Engineering International*, Vol. 10, No. 2, 2014, 1-11.
- [16] G. Sharma, P. S. Rao, and B. S. Babu, "Process capability improvement through DMAIC for aluminum alloy wheel machining," *Journal of Industrial Engineering International*, Vol. 14, No. 2, 2018, 213-226.
- [17] G. Sharma, P. S. Rao, and B. S. Babu, "Process-based tolerance assessment of connecting rod machining process," *Journal of Industrial Engineering International*, Vol. 12, No. 2, 2016, 211-220.
- [18] S. E. Vannan and S. P. Vizhian, "Statistical Investigation on Effect of Electroless Coating Parameters on Coating Morphology of Short Basalt Fiber," *Jordan Journal of Mechanical and Industrial Engineering*, Vol. 8, No. 3, 2014,
- [19] N. Mandahawi, R. H. Fouad, and S. Obeidat, "An application of customized lean six sigma to enhance productivity at a paper manufacturing company," *Jordan Journal of Mechanical and Industrial Engineering*, Vol. 6, No. 1, 2012, 103-109.
- [20] M. Al-Marsumi, "Total quality management in the top rank of the dairy industry in Jordan," *Jordan Journal of Mechanical and Industrial Engineering*, Vol. 3, No. 1, 2009, 47-58.
- [21] P. Lundkvist, "Experiments and Capability Analysis in Process Industry," Luleå tekniska universitet, 2012.
- [22] J. Munoz, "Process capability analysis using fuzzy sets theory," in *Applications of Fuzzy Logic Technology*, 1993, pp. 212-223.
- [23] S. Iranzadeh, "Investigating the relationship between RPN parameters in fuzzy PFMEA and OEE in a sugar factory," *Journal of Loss Prevention in the Process Industries*, Vol. 60, 2019, 221-232.
- [24] A. Kustiyo and Y. Arkeman, "Design for improvement of sugar factory performance based on statistical thinking," in *IOP Conference Series: Earth and Environmental Science*, 2019, p. 012033.
- [25] W. Pearn and K. Chen, "Making decisions in assessing process capability index Cpk," *Quality and reliability engineering international*, Vol. 15, No. 4, 1999, 321-326.
- [26] W. Pearn, M. Shu, and B. Hsu, "Testing process capability based on Cpm in the presence of random measurement errors," *Journal of Applied Statistics*, Vol. 32, No. 10, 2005, 1003-1024.
- [27] N. Mohan and M. Yadav, "Carbonation and Phosphatation Process for Refined Sugar Production: A Comparative Evaluation," in *Sugar and Sugar Derivatives: Changing Consumer Preferences*, ed: Springer, 2020, pp. 225-240.
- [28] K. M. Aljebory and M. Alshebeb, "Integration of Statistical and Engineering Process Control for Quality Improvement (A Case Study: Chemical Industry-National Chlorine Industries)," *Ind. Eng.*, Vol. 8, No. 4, 2014, 243-256.
- [29] F. Carpenter and V. Deitz, "Status of Sugar Colour and Turbidity Measurements," *Journal of the American Society of Sugar Beet Technologists*, Vol. 12, 1963, 326-347.
- [30] A. Khalili and K. Subari, "Understanding the linkage between soft and hard total quality management: evidence from Malaysian manufacturing industries," 2013,

Aluminium Alloys Nanostructures Produced by Accumulative Roll Bonding (ARB)

Yazan M. Almaetah^a, Khaleel N. Abushgair^b, Mohammad A. Hamdan^{*c}

^aDepartment of Mechanical Engineering, The University of Jordan. Amman- Jordan, 11942

^bDepartment of Mechanical Engineering, Al Balqa Applied University. Amman- Jordan, 11134

^cDepartment of Mechanical Engineering, The University of Jordan. Amman- Jordan, 11942

Received February 10 2021

Accepted September 10 2021

Abstract

The accumulative roll-bonding process (ARB) is one of the severe plastic deformation methods. It aims at producing nano/ultra-fine-grained materials along with enhancements in the mechanical properties. In this work, ARB was performed on commercially cheap and available aluminium alloys in Jordan's local market; AL-2024-O and AL-1100-O alloys. Four bonding cycles were applied to promote grain refinement at room temperature with no pre/post heat treatment. In ARB processes, the thickness is reduced by 50% in each pass. A new stacking technique has been performed at the alternate layers depending on the friction of its scratched edges. After the production of samples and the investigation of mechanical properties through micro hardness test, tensile test was accomplished at room temperature after each cycle with the aim of determining whether ARB increases the mechanical properties of both aluminium alloys besides identifying the instance where material experiences high ultimate tensile strength. Information about the texture, microstructure and average crystalline size of the samples was obtained using SEM and XRD. The hardness test shows improvements for AL-2024-O/1100-O for each cycle and reported 125 HV and 80 HV respectively after four rolling cycles. The highest UTS was recorded for AL-2024-O and 1100-O on the 4th pass and reported 370 MPa and 170MPa respectively. It was also found out that the percentage elongation decreased due to a decrease in ductility after undergoing the ARB process. Moreover, after four rolling cycles, the average grain size for AL-2024/1100 decreased to 39.6 nm and 59.9 nm respectively.

© 2021 Jordan Journal of Mechanical and Industrial Engineering. All rights reserved

Keywords: Severe plastic deformations, Accumulative roll bonding, Nanostructures, Aluminium alloys;

1. Introduction

In this era, the world is eager to find new metals with superior features and properties, especially in the metallurgical industry. In fact, the experts are endeavouring for new hard, strong and refractory materials, but it's really difficult to find materials that possess all these specific properties. Very recently, the experts and engineers have been able to find a new way to fabricate and develop the existing materials by using a severe plastic deformation (SPD). Over the past few decades, numerous studies have been conducted with a primary emphasis is on the development and production of alternative materials, with high strength-weight ratio, unique and distinguished mechanical properties. Aluminium is extensively utilised in products and markets. In fact, it is the most common material used in numerous applications. Aluminium alloys can offer high strength alongside simple fabrication, manufacturing and formability at a relatively low cost as compared to other metals[1].The studies have focused primarily on the production of UFG materials and improving the mechanical properties. Many SPD processes have been performed in order to produce nano/ultra-fine

grain materials such as accumulative roll bonding (ARB) where two metal sheets are scratched, chemically polished, stacked and then subjected to high strain using a roller mill for several cycles to achieve thickness reduction. Since the thickness of the sheets remain unchanged, ARB has been performed at the metal sheets for many cycles to obtain ultra-fine grain size and enhanced mechanical properties [2], [3].Using ARB is effective to enhance mechanical properties, DEGHAN and QODS cold rolled AA1050 sheets. They enhanced the U.T.S and Y.S from 69.25 MPa and 40 MPa to 201.7 MPa and 185.05 MPa respectively after 10th rolling cycle with 191% and 167% rise in tensile strength [4]. Yang wang and his colleagues investigated the microstructure and mechanical properties. of ultra-lightweight Mg-Li-Al/Al-Li composite produced by ARB at room temperature. They documented an increase in tensile strength (UTS) of 308 MPa after 4-cycles of ARB process [5]. Another investigation of the microstructure and mechanical properties of Ni/Ti/Al/Cu composite produced by (ARB) at ambient temperature showed enhancement in tensile strength after eight passes, reaching 298.2 MPa [6].Mechanical properties of nano-structured Cu/Ni multilayer fabricated by ARB revealed high ultimate tensile strength of 950 MPa which is five time higher than pure Cu

* Corresponding author e-mail: mashamdan@yahoo.com

metal [7]. It was found that applying low strain at room temperature is slightly effective to produce nano-grained metals less than 100 nm[8].

Others used SPD methods include groove pressing (CGP)[9, 10], equal channel angular pressing (ECAP) [11], friction stir processing and high pressing torsion (HPT)[12],[13],[14]. These methods have two major drawbacks. To begin with, the forming machines have large load capacities and are outfitted with expensive dies. Furthermore, productivity is extremely low, therefore the quantity of the created material is extremely constrained as compared to ARB[15],[16]. Accumulative roll bonding is a new SPD method created and developed by satio, in which a very large plastic strain is imposed in bulk process to produce ultra-fine grain metallic materials[17]. During this method, two metal sheets of comparable thickness are treated, stacked and roll bonded by a 50% thickness reduction or more during a single cycle. The process is often administered using a standard steel mill. Within the next cycles of ARB processing, the deformed bonded sheet is halved into two equal pieces, cleaned again, grinded and stacked together for the second ARB cycle and so forth. At low temperatures, ultra-fine-grained metals and alloys exhibit outstanding mechanical properties such as high strength, high toughness, and super plasticity.[18].

In this work, the accumulative roll bonding process was used in the production of bulk nanostructure alloy with a high strength-to-weight ratio of commercial aluminium for different applications in the automobile and aerospace industries. This bulk nanostructure has very high strength with a noticed decline in ductility and exhibits high values of fatigue resistance and fracture toughness [19]. Two types of aluminium alloys were used: (AA2024-O, AA1100-O). These aluminium alloys were rolled at room temperature (cold roll bonding) using a rolling mill machine. Surface polishing and cleaning process were applied on aluminium alloys before ARB. It can be noted from previous experiences that copper wires and riveting tools were used to stack aluminium sheets together, allowing a slight slipping and deviation leading to mismatch and cracking of the stacked sheets while applying a huge strain. The reason is that the copper wires or the riveting material have different mechanical properties. In this work, we were able to use a new method to stack the aluminium sheets utilising the roughness of the surface edges in order to enhance the cohesion of the sheets together, preventing the slipping during the rolling process. This new technique provided

proportional cohesion strength to the applied strain. In addition, the pre-conditioned roughened surface is an additional advantage in enhancing the bonding between the aluminium sheets. The homogeneity and the particle size for the new aluminium alloys were tested by using X-ray diffraction (XRD) and scanning electron microscope (SEM), while the strength was tested by the tensile test machine.

2. Materials and Experimental procedure

Two types of aluminium alloys were used, AA2024-O and AA 1100-O, with a geometry of $15 \times 10 \text{ cm} \pm 0.05 \text{ mm}$ and a thickness of $1 \text{ mm} \pm 0.03 \text{ mm}$ and $1.5 \text{ mm} \pm 0.05 \text{ mm}$ respectively. The chemical compositions areas shown in table 1 and table 2 were analysed by using XRF spectrometer. The main reason behind selecting AA2024-O and AA1100-O is their availability and low cost. These aluminium alloys were rolled at room temperature (cold roll bonding) up to four rolling cycles using a roller mill with 40 cm diameter and a speed of 13 rev/min fig (1/a). These specimens were abraded using a (CORYN) $115 \times 22 \text{ mm}$ in order to roughen its surface, for improving friction and bonding between the sheets as well as to remove the oxidized layer. In addition to abrading, the surface was polished and cleaned as an important part of the surface preparation using acetone due to its natural propensity to melt most oils and greases [20]. In addition, this volatile chemical solvent removes contaminants and dust and prevents the emergence of oxidation layer on the materials surface alloys before accumulative roll bonding. The roughened edges provided the ability of stacking the sheets instead of using a riveting tool and a copper wire. These roughened edges provided excellent cohesion stacking strength once huge strain is applied. Afterwards, the sheets are introduced to ARB for many cycles. Fig (1/b) shows the sheets after cut into two similar pieces. Figure (1/c) shows AL-2024 sheet thickness after four rolling cycles.

Table 1. chemical composition of Al 2024-O

material	Cu	Mg	Si	Mn	Fe	Ti	Al
Wt.%	4.4	1.5	0.5	0.6	0.5	0.20	balance

Table 2: chemical composition of Al 1100-O

Material	Fe	Si	Cu	Zn	Mn	K	Ca	Ni	AL
Wt.%	0.43	0.21	0.041	0.036	0.033	0.03	0.015	0.008	99.2

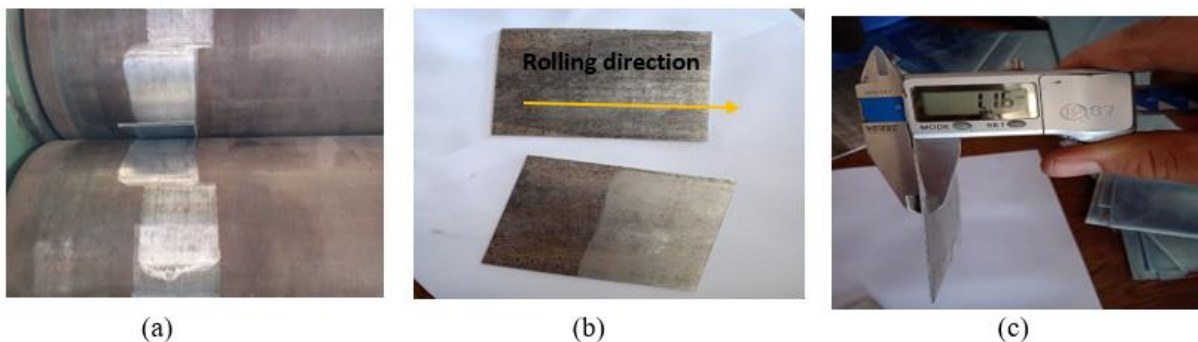


Figure 1. (a) ARB process, (b) two similar sheets after cut and (c) AL-sheet alloy after four rolling cycles.

3. Results and Discussion

Hardness test: The AA2024-O and AA 1100-O sheets have been tested for hardness by VICKERS hardness test. A load of 100 kgf (AA2024-O) and 30 kgf (AA1100-O) were used. To ensure an accurate test result, three measurements were conducted for each sample and the average hardness values are as shown in fig (4). Figure (4/a) shows the improvement in hardness for AA2024-O. After four cycles, we noticed that there is obviously increase in hardness. After one rolling cycle, the hardness improved by (70 %) and after the next cycles, the hardness improved by 8 % and 4 % respectively. The original hardness for unhardened aluminium alloy AA2024 was 60 HV which means that the hardness was doubled after four rolling cycles.

The hardness test for AA 1100-O was set on 30 kgf. The results show a slight increase in hardness through each cycle to reach 80 HV. The unhardened Al-AA1100-O was measured 48 HV as shown in figure (2). The improvement in hardness after one rolling cycle was 20 %. After the next cycles, the hardness improved by 11 %, 12.3 % and 13 % respectively.

Tensile test: Tensile test has been performed using the Shimadzu 1000 Kn Digital tensile testing machine. The original aluminium alloy AA2024 is of ultimate tensile strength (U.T.S) and yield strengths (Y.S) are 175 MPa and 70 MPa respectively. As shown in fig (3), the strength (U.T.S) changes after one cycle of cold rolling to 183 ±2 MPa. After two rolling cycles, the U.T.S is improved by 13 %. After performing the 3rd pass, the U.T.S is dramatically increased by 9 % to record 230 MPa ±2 MPa. After four cycles of cold rolling, the U.T.S improved incredibly by 38

% to reach 370 ±2 MPa. As seen, the cold-rolling leads to a notable change in mechanical properties of the AA2024alloy as shown in figure (3/a). The impact of the strength of the composed layer on the bond strength of sheets has not been fully understood yet and still being investigated. [21], because the weak bonding provides an ideal environment for germination and cracks growth, fractures frequently arise in the distorted layers [22].By increasing cold-rolling reduction, the U.T.S increases gradually, while the elongation reduces. Since the metal lost its ductility, the mechanical behaviour depends primarily on the number and distribution of dislocations introduced due to cold deformation.

ARB has proved to be an outstanding method to enhance material strength. However, low ductility is usually noticed in this method [23]often because the appearance of premature necking minimizes the required general energy to failure [1]. Figure (3) shows the improvements of tensile strength for AA1100-O. The U.T.S and Y.S before hardening were 85MPa±2 MPa and 35MPa ±2MPa respectively. After one rolling cycle, the U.T.S was improved to 120MPa ± 2MPa, showing an improvement of 29.2 %. For second, third and four cycles, the U.T.S improved tremendously to 150 MPa, 163MPa and 173 MPa respectively, showing an improvement of 20 %, 8 % and 6.3 % respectively. The improvement in the mechanical behaviour of the aluminium alloy can be attributed to the following reasons. First, as the rolling cycles increase, thickness decreases and grains were extremely elongated along the rolling direction, which raises the tensile strength. This can result in a higher density of dislocations and the formation of new substructures, resulting in increased in tensile strength and lower elongation.

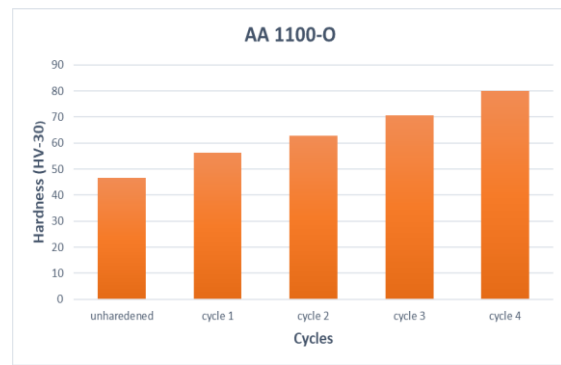
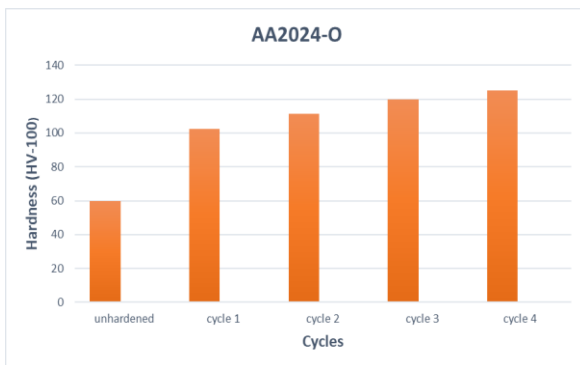


Figure 2. hardness value for AL- alloy for each cycle. (a) Hardness value forAA2024-O, (b) hardness value for AA1100-O.

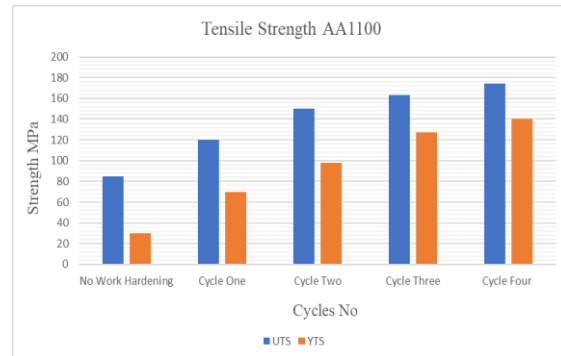


Figure 3: Tensile test for AL-alloys for each cycle. (a) tensile strength for AA2024-O, (b) tensile strength for AA1100-O

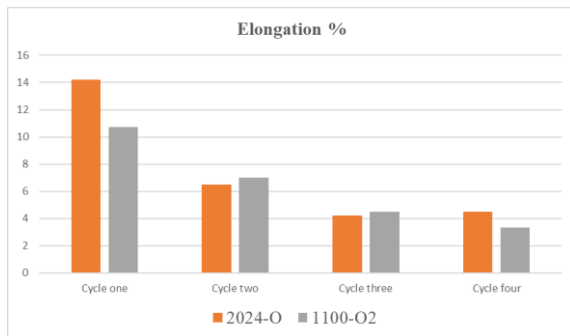


Figure 4. Elongation

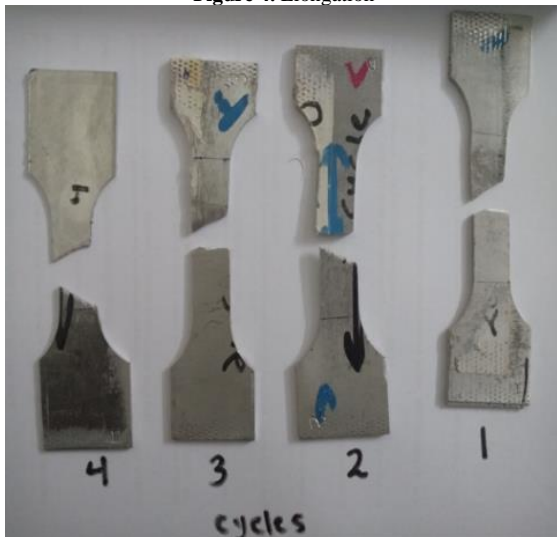


Figure 5. Dog-bone shape

Figure (4) shows a significant decrease in the elongation of both metals due to the decrease in ductility. Some results showed different values due to the possibility of the presence of cracking or slipping of the sample during testing which effect dislocations introduced due to cold deformation. The shapes of tested samples after fracture are shown in figure (5) with failure angle.

3.1. XRD & SEM

The XRD patterns of AA 2024-O and AA1100-O aluminium alloys in different cycles are shown in Fig (6) and Fig (7). Each peak represents a diffraction event from two successive crystallographic planes with a certain orientation. Peaks could be analysed with respect to the value of 2θ (X-axis) in order to calculate the value of d-spacing (the distance between two successive crystallographic planes) from which the diffraction took place. The width of the peak is an indication parameter that reflects the crystallite size, represented by a factor known as a full width at half maxim (FWHM), which is a function of any size. It is expressed by Scherrer's equation $(0.9 \times \lambda) / (d \cos\theta)$ [24]. Density of the plane means that the plane is crowded with atoms, leaving no significant spaces. The width of peaks is an indication of crystalline size. The effect of crystallite size on the diffraction pattern appears in the width of the peak. Table 3 shows the average crystalline size for AA2024/1100 for each cycle. The XRD patterns of AA 2024-O and AA1100-O samples in annealed and ARB processed conditions at different cycles are shown in Figure 6. They include typical corresponding alloy diffraction peaks. The increase in XRD peaks is an indicator of a large deformation of polycrystalline materials in plastic reign due to an increase in lattice strain. In turn, this process helps create UFG and NG structures strength. Peak broadening becomes more pronounced as the number of ARB cycles increases. In addition, the ARB rolling process produces texture in the microstructure, resulting in variation in ARB samples of the relative intensities of different planes.

The (111) plane, therefore, becomes the sharpest peak in the samples on 4 passes for AA 2024-O and 3 passes for AA1100-O samples, while the (200) plane has the highest intensity after the first ARB pass for each material.

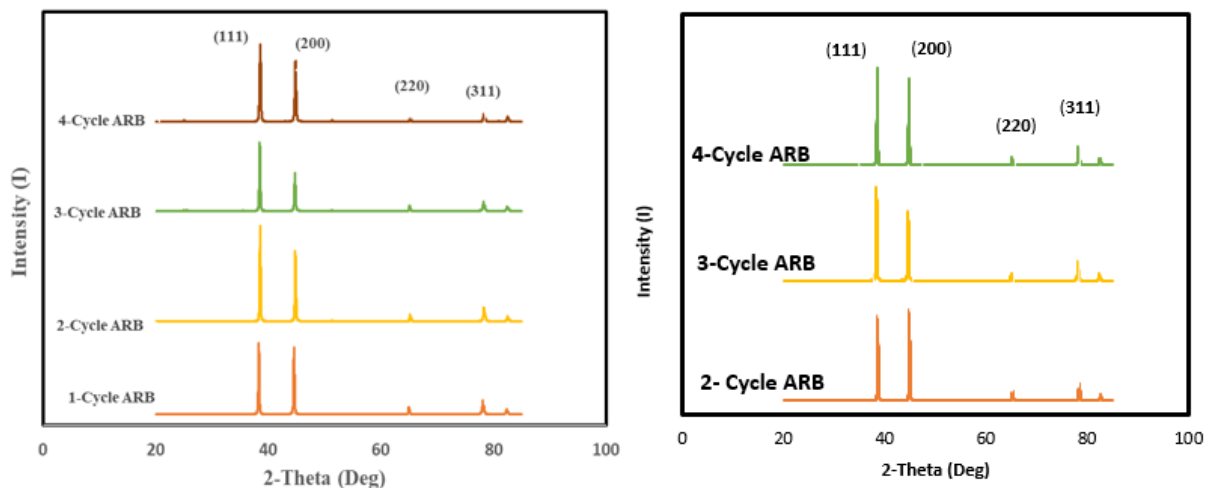


Figure 6. XRD patterns of rolled AA 2024-O alloy and AA 1100-O with 50% reduction.

Table 3. average crystalline size for AA2024 for each cycle.

#NO of rolling.	Peak position 2θ (°)	FWHM Size (°)	Dp (nm)	Dp Average (nm)
1 st pass	38.2999	0.1631	53.89	58.28
	44.5478	0.1633	54.95	
	64.9358	0.1613	61.02	
	78.0702	0.1885	56.71	
	82.2825	0.1701	64.82	
2 nd pass	38.5354	0.1533	57.38	57.34
	44.7845	0.1591	56.45	
	78.2741	0.1984	53.96	
	65.156	0.1604	61.44	
	82.4846	0.1922	57.46	
3 rd pass	38.4652	0.1797	48.94	47.73
	44.7087	0.186	48.27	
	78.1988	0.2384	44.88	
	65.0867	0.191	51.57	
	82.4097	0.2454	44.98	
4 th pass	38.5439	0.2309	38.10	39.60
	44.7918	0.2354	38.15	
	78.2703	0.2713	39.46	
	82.4667	0.2671	41.34	
	65.1659	0.2407	40.94	

Table 4. average crystalline size for AA1100 for each cycle.

#NO of rolling.	Peak position 2θ (°)	FWHM B_{size} (°)	Dp (nm)	Dp Average (nm)
1 st pass	44.8337	0.1521	59.06	60.57
	38.5873	0.1522	57.80	
	78.3141	0.1733	61.79	
	65.1965	0.1609	61.26	
	82.517	0.1755	62.94	
2 nd pass	38.3079	0.1873	46.93	53.55
	44.5615	0.1796	49.97	
	78.0878	0.1882	56.81	
	64.9463	0.1752	56.18	
	82.2971	0.1905	57.89	
3 rd pass	38.4599	0.1824	48.21	51.69
	44.7098	0.1838	48.85	
	65.0884	0.1852	53.19	
	78.2114	0.1985	53.91	
	82.4185	0.2034	54.27	

Electron Scanning Microscope (SEM): The deformed aluminium alloys AA2024-O and AA1100-O for all cycles have been tested and scanned to different scale ranges in order to study the surface and the textured topography. The figures below show SEM images for both aluminium (AA2024-O, AA1100-O) for each cycle. Figure (7) shows 10 μ m and 5 μ m of the aluminium surface. The scratch lines appear clearly and the small grain are seen blurry. After

many rolling cycles, these grains are still blurry but the X-ray diffraction equation (Scherrer's equation) $(0.9 \times \lambda) / (d \cos\theta)$ proves that the new deformed metal contains a nano-grain size.

For AA1100-O, figure (8) below shows 20 μ m and 10 μ m, where the small grain size parts can be seen in nanoscale, providing us a proof of nano grains of the material.

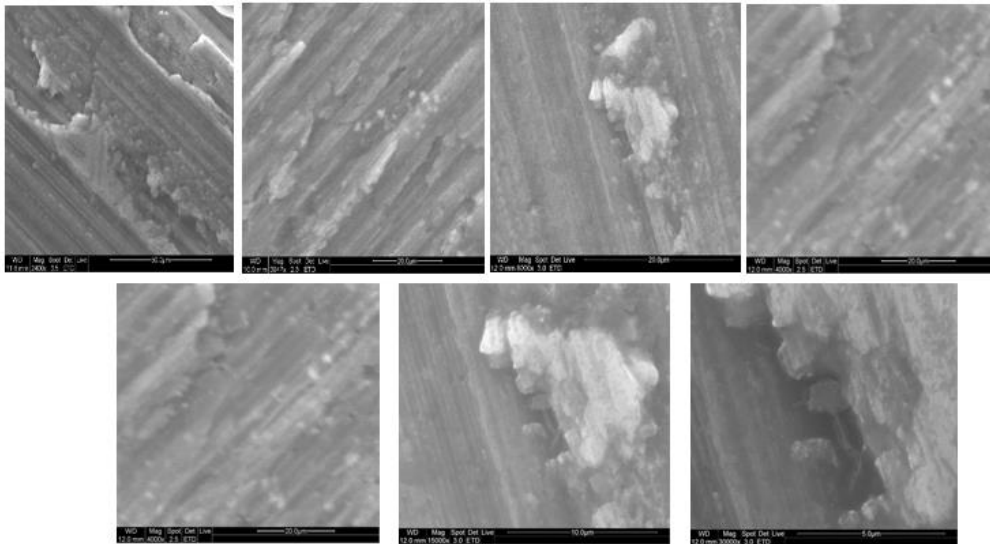


Figure 7. SEM image for Al-2024 surface.

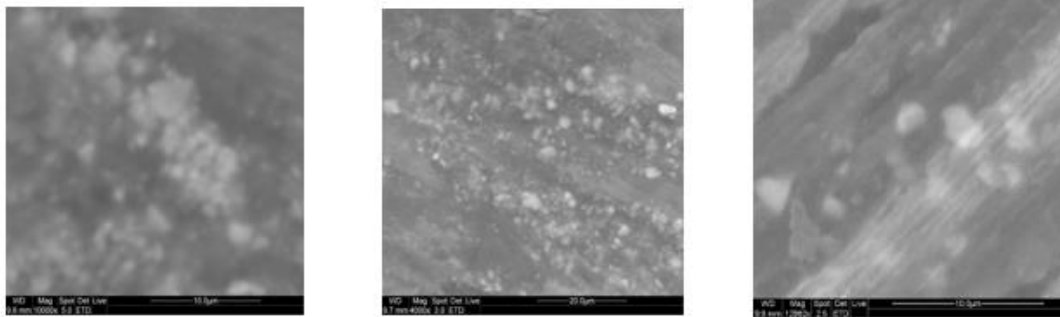


Figure 8. SEM image for AA1100-O after three and four rolling cycles.

4. Conclusion

The presented outcomes expound the high potency of the process that induces high plastic strain like ARB for AA2024-O and AA1100-O at ambient temperature in order to produce bulk nanostructure with high strength-weight ratio, durability, toughness and low ductility as compared to the conventional coarse-grained techniques. The results are visible after only one rolling cycle, making the technique appealing for practical applications. The novel stacking approach has been shown to be salutary in reducing slippage and increasing bonding time. Furthermore, the mechanical characteristics of this novel bulk nanostructure make it superior to other valuable metals such as 7070-O and 6063-O. This new distinguished material could be used widely in many applications that include, ballistic protection, the aviation and automobile industry.

By increasing the number of ARB cycles, the ultimate tensile strength for both aluminium alloys is increased. The highest ultimate tensile strength for AA2024 and AA100 is 370 MPa and 173 MPa respectively.

It is obvious that the hardness and tensile tests show extreme improvement in mechanical properties. It is also noticed that the elongation for both new nanostructure metals is decreased due to the reduction in ductility.

According to X-ray diffraction equation and (SEM) images, the average crystallite size is decreased for each single rolling cycle. For AA2024-O, the average crystallite size after four rolling cycle is 39.9 nm, while the average

crystalline size for AA2024-O after four rolling cycle is 51.69nm. The grain size has a significant influence on the mechanical properties of alloys.

Acknowledgments

This project would have been impossible without the support of Jordan Design & Development Bureau (JODDB) presented by Eng. Radi Alwardat.

References

- [1] Najafzadeh, N., Microstructural Analysis of accumulative Roll-Bonded Aluminium. 2016, The university of New southwales.
- [2] Jafarian, H., et al., Microstructure analysis and observation of peculiar mechanical properties of Al/Cu/Zn/Ni multi-layered composite produced by Accumulative-Roll-Bonding (ARB). *Materials Science and Engineering: A*, 2020; p. 140556.
- [3] Rahmatabadi, D., et al., Production of Al/Mg-Li composite by the accumulative roll bonding process. *Journal of Materials Research and Technology*, 2020. 9(4): p. 7880-7886.
- [4] DEGHAN, M., et al., Effect of inter-cycle heat treatment in accumulative roll-bonding (ARB) process on planar isotropy of mechanical properties of AA1050 sheets. *Transactions of Nonferrous Metals Society of China*, 2020. 30(9): p. 2381-2393.
- [5] Wang, Y., et al., Microstructure and mechanical properties of ultra-lightweight Mg-Li-Al/Al-Li composite produced by accumulative roll bonding at ambient temperature. *Materials Science and Engineering: A*, 2020. 787: p. 139494.

- [6] Ye, N., X. Ren, and J. Liang, Microstructure and mechanical properties of Ni/Ti/Al/Cu composite produced by accumulative roll bonding (ARB) at room temperature. *Journal of Materials Research and Technology*, 2020. 9(3): p. 5524-5532.
- [7] Sun, Y., et al., Microstructural evolution and mechanical properties of nanostructured Cu/Ni multilayer fabricated by accumulative roll bonding. *Journal of Alloys and Compounds*, 2020. 819: p. 152956.
- [8] Gholami, M.D., R. Hashemi, and M. Sedighi, The effect of temperature on the mechanical properties and forming limit diagram of aluminum strips fabricated by accumulative roll bonding process. *Journal of Materials Research and Technology*, 2020. 9(2): p. 1831-1846.
- [9] Yadav, P.C., et al., Microstructural inhomogeneity in constrained groove pressed Cu-Zn alloy sheet. *Journal of Materials Engineering and Performance*, 2016. 25(7): p. 2604-2614.
- [10] Shin, D.H., et al., Constrained groove pressing and its application to grain refinement of aluminum. *materials Science and Engineering: A*, 2002. 328(1-2): p. 98-103.
- [11] Liu, M., et al., Microstructure, mechanical properties and wear resistance of an Al-Mg-Si alloy produced by equal channel angular pressing. *Progress in Natural Science: Materials International*, 2020. 30(4): p. 485-493.
- [12] Mishra, R.S., Z. Ma, and I. Charit, Friction stir processing: a novel technique for fabrication of surface composite. *Materials Science and Engineering: A*, 2003. 341(1-2): p. 307-310.
- [13] Mishra, R.S., et al., High strain rate superplasticity in a friction stir processed 7075 Al alloy. 1999.
- [14] Su, J.-Q., et al., Development of nanocrystalline structure in Cu during friction stir processing (FSP). *Materials Science and Engineering: A*, 2011. 528(16-17): p. 5458-5464.
- [15] Saito, Y., Ultra-fine grained bulk aluminum produced by accumulative roll-bonding (ARB) process. *Scripta Mater.*, 1998. 39(9): p. 1221-1227.
- [16] Tsuji, N., Production of bulk nanostructured metals by accumulative roll bonding (ARB) process. *Severe Plastic Deformation: Toward Bulk Production of Nanostructured Materials*, 2006: p. 545-565.
- [17] Azushima, A., et al., Severe plastic deformation (SPD) processes for metals. *CIRP annals*, 2008. 57(2): p. 716-735.
- [18] Segal, V., Equal channel angular extrusion: from macromechanics to structure formation. *Materials Science and Engineering: A*, 1999. 271(1-2): p. 322-333.
- [19] Zehetbauer, M. and Y.T. Zhu, *Bulk nanostructured materials*. 2009: Wiley Online Library.
- [20] Govindaraj, N.V., Light-weight materials produced by accumulative rollbonding, in *Materials Science and Engineering*. 2013, Norwegian University of Science and Technology Faculty of Natural Sciences and Technology.
- [21] Miyajima, Y., et al., Effects of rolling reduction and strength of composed layers on bond strength of pure copper and aluminium alloy clad sheets fabricated by cold roll bonding. *Advances in Materials Science and Engineering*, 2014. 2014.
- [22] Al-Shamma, F.A., The Effect of Fatigue on Crack Propagation in Flat Plates under Buckling Bending and Shear. *Jordan Journal of Mechanical and Industrial Engineering*, 2009. 3(3).
- [23] Valiev, R.Z. and T.G. Langdon, Principles of equal-channel angular pressing as a processing tool for grain refinement. *Progress in materials science*, 2006. 51(7): p. 881-981.
- [24] Monshi, A. and A.S. SOLTAN, A new method to measure nano size crystals by scherrer equation using XRD. 2008.

Simulation of Trajectory Tracking and Motion Coordination for Heterogeneous Multi-Robots System

Samer Mutawe, Mohammad Hayajneh, Suleiman BaniHani, Mohammad Al Qaderi

Department of Mechatronics Engineering, Hashemite University, Zarqa 13115 Jordan

Received May 4 2021

Accepted September 15 2021

Abstract

The paper addresses developing a team of aerial and ground robots to accomplish multi-robot system navigation task in an accessible way. The motions of two different robotic structures, namely quadcopter, and differential drive mobile robots are simulated and controlled. Two-level controller has been adopted for the multi-robot system. A low-level controller is utilized for each robotic platform to insure its motion stability and robustness. Then, a formulation of high-level tracking controller is presented to allow each robot to avoid obstacles in a dynamic environment and to organize its motion with other flying/ground robots. The performance of the proposed system is demonstrated in a simulation environment. A modeling platform is adopted to construct the simulation environment, which allows the user to easily adjust the models and controller parameters as well as to implement different control algorithms. In addition, the simulation environment helps in analyzing the obtained results and performing several tasks in different conditions. The real-time motion of multi-robot system is monitored in the created environment that provides three-dimensional graphical displays of the robotic platforms. Simulation results show that the aerial and ground robots produced trajectories individually to reach different targets. Meanwhile, each robot in the system was able to navigate among obstacles without colliding with other agents in the network.

© 2021 Jordan Journal of Mechanical and Industrial Engineering. All rights reserved

Keywords: Ground robot, Multi-robots, Path planning, Quadcopter, Trajectory tracking;

1. Introduction

Due to rapid revolution in micro-electronics and communication technologies, robots have been employed for autonomous tasks such as security [1], inspection [2], and monitoring [3, 4]. Therefore, authors in many interesting research have developed ground and aerial robots to work in uncertain environments [2], [5-9]. In such scenarios, the ability to reach the goal point without a collision with any obstacle is the task of the navigation system [6], [10-12]. However, it is difficult or impossible for an individual robot to fulfill its tasks in a mission. Thus, a team of small and inexpensive robots with various capabilities can cooperate with each other in one network to accomplish a common goal easier and faster.

In multi-agent or multi-robot systems, the cooperation takes place among the agents using the information available from the network. Therefore, accurately measuring the vehicle's position with respect to other vehicles and the local environment helps in two ways; avoiding collisions between robots and obstacles and locating targets effectively [13]. Many researchers work on developing allocation and path planning strategies of multiple robots (i.e. flying and ground) system for obstacle avoidance [14-16]. More specifically, a group of people developed a framework of multiple robots cooperating with

each other for building indoor geometric maps [17]. Other research studies have been conducted on locating accurately or tracking a ground-moving target by aerial robot [18-20].

Several authors have looked at differences of the multi-robot motion planning. Most of these algorithms are classified into coupled or decoupled approaches to find collision-free trajectories for many automatic ground vehicles (AGVs) moving toward separate targets within a common environment [21-23]. Other approaches of robotic manipulator optimal motion planning have been proposed in [24, 25]. In contrast with coupled approach, the decoupled methods cannot achieve completeness and optimality. However, by planning the motion of robots successively, the decoupled planner has lower complexity and greater scalability than a coupled planner.

In multi-robot systems, coordination is defined as the mechanism used for achieving cooperation. Coordination and cooperation can be viewed as "joint operation or action amongst a group of robots" [26]. Coordination approaches for multi-robot systems are classified based on various parameters, where each parameter is considered as one dimension for classification. One of the comprehensive classifications of coordination approaches for multi-robot system has been presented in [27]. The paper considered three key parameters, namely decision-making strategy, communication mode, and adaptivity as basis for the classification. Coordination can be static or dynamic

* Corresponding author e-mail: samerk@hu.edu.jo

* This work is supported by the Royal Academy of Engineering grant Transforming Systems through Partnership TSP1040

according to the environment and the associated task. In dynamic coordination approaches, implicit and explicit communication modes have been used to fulfill the task [28, 29]. The coordination approaches can be categorized into three groups, namely centralized, decentralized, and hybrid, based on decision-making strategy parameter. Task planning and motion planning are key problems that need to be addressed first for multi-robot system to accomplish any task efficiently [30]. Therefore, a mechanism is needed to coordinate robots in order to generate efficient path for each robot while taking into account static and dynamic obstacles in the environment as well as the movement of other robots [31]. Motion planning coordination approaches adopt mostly decoupling method which can be centralized or decentralized coordination [32, 33].

The complexity of mathematical description for most robotic systems such as in [34-37] needs more effort to analyze their dynamic character. Therefore, those people take the advantage of appropriate modeling and simulation methods to analyze diverse movements of the mechanical system, and to provide a convenient way for practical engineering application in order to reduce time and cost as well as to find error early [34, 35].

Visual based autonomy was mainly used for cooperative multi robot systems. A vision-guided quadrotor was presented in [38]. The quadrotor was equipped with a monocular camera. It was able to achieve smooth take-off, stable tracking and safe landing with respect to a moving ground robot where a marker-based and optical-flow-based pose/motion estimation methods were used. In [39] a vision based localization and target detection algorithm was proposed for a cooperative team of one UAV and a number of UGVs to be used in crowd detection and GIS localization. The UAVs localization algorithm converts the crowds' image locations into their real-world positions, using perspective transformation. The authors in [40] present an implementation of a hybrid system consisting of a low-cost quadrotor and a small pushcart, a RGB computer vision algorithm was used for tracking and landing a quadrotor on a moving carrier using a classical PID controller. In [41] a Wii remote infrared (IR) camera fixed under a miniature unmanned aerial vehicle (UAV) was used to allow for robust tracking and landing over a small carrier vehicle without communication between them and works with an onboard 8-bit microcontroller.

Another approach is to use intelligent control algorithms, in [46] a fuzzy logic controller and a neural network were used for positioning and maneuvering of aerial robots. A fuzzy logic controller with nine rules was implemented by [47] for autonomous tracking of a multi robot team. In [48] a robotic team is presented in hostile environment. Algorithms for human detection and deep learning architecture for terrorist is presented. In [49] a surveillance system for early detection of escapers from a restricted area is presented based on a new swarming mobility model called Chaotic Rössler Mobility Model for multi Swarms. A Genetic Algorithm was used to optimize the vehicles' parameters and escapers' evasion ability using a predator-prey approach. In [50] a path tracking control system was designed using an adaptive preview model. A camera is used to collect images that are fed to the monitoring module, then operation instructions are sent to the bottom control module to create a line to judge the UAV

path, then the adaptive preview time model is constructed to complete the trajectory tracking of UAV.

The ambition of this work is not only to develop a high-level framework where aerial and ground robots interact with each other, but also to evaluate different control and navigation algorithms for building geometric paths cooperatively. The current work illustrates a high-level approach that utilized Simulink to perform modeling, simulation, and control for the robotic system. A quadcopter and a mobile robot were designed in ProEngineer CAD environment with all the mass and inertial properties defined there, and then these models were exported as XML files to be read by SimMechanics in MATLAB. At this stage, joints, actuators, sensors, and inertial bodies were defined properly. This work also introduces a design of a decoupled method for multi-robot motion planning by generating small variations of robot motions on a predefined trajectory and scheduled velocity. In other words, this method first finds obstacle-free paths, and then, regulates velocities of individual robots to avoid collisions.

This paper is organized as follows: Section 2 describes the overall architecture of the robotic platforms. Mathematical models of ground robot and quadcopter are provided in Section 3. Then control systems are designed for robots stability in Section 4. In addition, Section 5 describes the design of an algorithm for robot's path planning and motion coordination. The simulation tests used to demonstrate the robots performances exist in Section 6. Finally, some conclusive remarks on the work are given in Section 7.

2. Multi-robot System Structure

The purpose of the proposed dynamic simulator for the robotic system is to develop collaborative active simulation package that supports user's interactive operation in the loop. Furthermore, it supports the applied operations by the simulation environment.

This section describes the overall construction of a robotic system, which was created by means of Simulink modeling and SimMechanic tool in MATLAB. The system combines several aerial and ground robots as shown in Figure 1. In this system, the robotic platforms were created in CAD modeling environment (e.g. ProEngineer) and were interfaced with MATLAB tools for motion control developments. The proposed robotic system allows one to insert as many aerial and ground robots as needed to demonstrate a mission performed by a multi-agent system.

The geometric models of a quadcopter and ground robot were built for simulation. The parameter values for each robot adopted in the simulations are presented in Table 1.

Table 1. CAD-model robots

Robot platform	Dimensions (m)	Weight (Kg)	Inertia ($kg.m^2 \times 10^{-3}$)
Ground robot	0.45 x 0.65 x 0.9	8.4	$I_{robot} = 175$
Quadcopter	0.2 x 0.4 x 0.4	1.2	$I_{rotor} = 0.0105 [4.836 \ 0 \ 0; 0 \ 4.836 \ 0; 0 \ 0 \ 8.325]$

It is noteworthy here that during the simulation process, users can apply and change the parameters of forces and torques on the created components of each robot as well as

change the constraint relationship between the robots in the system.

3. Robots

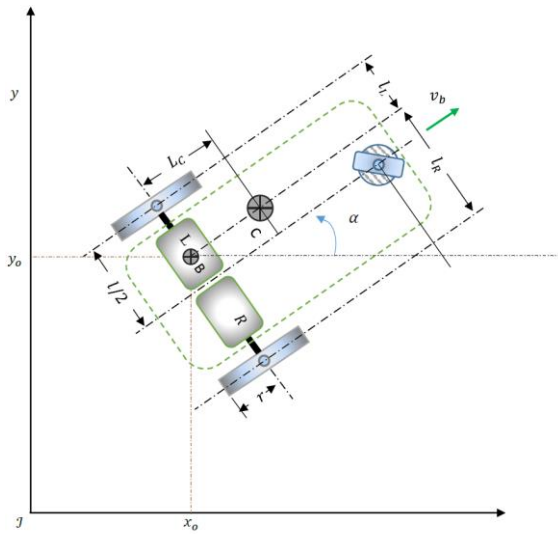


Figure 1. The schematic of differentially steered robot

Modeling

This section shows the dynamics and kinematics of a ground mobile robot and a quadcopter to derive their mathematical models. The objective of deriving mathematical models is to assist in developing controllers for physical robots.

3.1. Ground robot model

The dynamics of a differential steering robot can be defined with vector of translation speed v_b and its rotation with angular velocity ω_b which are produced by the changes of speeds of the right and the left wheels as shown in Figure 1. The robot is driven by two independent wheels while the third wheel is a castor wheel needed for static stability of mobile robot. Particularly when the two wheels rotate at the same speed, the robot will move forward. While turning left/right is achieved by driving the right/left wheel at a higher rate than the other wheel.

To develop the equation of motion of a differential steering system, an arbitrary point B is chosen and treated as a frame of reference as shown in Figure 1. By linear motion, the force vector causing the movement acts in point B and goes through center of gravity. Considering F_L and F_R as forces caused by the left and the right actuators in addition to F_O as a resistance force, the balance of forces influencing linear motion is given as follows:

$$F_L + F_R + F_O = m\dot{v}_b$$

$$\frac{M_L}{r} + \frac{M_R}{r} - k_v v_b = m\dot{v}_b \tag{1}$$

Where m is robot mass. k_v is resistance coefficient against linear motion, M_L, M_R are drive torques. v_b is linear motion speed, and r is radius of the wheels.

By rotational motion, a moment M_E caused by Euler's force and a resistance moment M_O are

considered. The total moments generated on the point B can be summed up in the following relation:

$$M_{BL} + M_{BR} + M_O + M_E = J_C \dot{\omega}_b$$

$$-\frac{M_L}{r} l_L + \frac{M_R}{r} l_R - k_\omega \omega_b - m \dot{\omega}_b l_C^2 = J_C \dot{\omega}_b \tag{2}$$

Where M_{BL}, M_{BR} are moments by drive forces. k_ω is resistance coefficient and J_C is moment of inertia with respect to rotation axis in center of gravity. ω_b is angular speed in point B.

l_L, l_R, l_C are distances from point B to left drive, right drive, and center of gravity respectively.

Using the parallel axis theorem, the moment of inertia J_B with respect to rotation around point B is given by:

$$J_B = J_C + ml_C^2 \tag{3}$$

Where J_C is moment of inertia at point C.

It is important to study the mechanical performance of the mobile robot in order to build suitable control structure for a desired task. The coordinate system of the robot is governed by combined action of both the linear velocity v and the angular velocity ω . Therefore, the vehicle kinematic model is given by:

$$\begin{cases} \dot{x} = v_b \cos\alpha \\ \dot{y} = v_b \sin\alpha \\ \dot{\alpha} = \omega_b \end{cases} \tag{4}$$

Where (x, y) are the positions of point B in inertial frame coordinate. α is the heading angle of the robot with respect to x axis.

To minimize the error distance $\rho > 0$ between the desired location and the current one, the robot position can be represented in polar coordinates as follows:

$$\begin{cases} \dot{\rho} = -v_b \cos\alpha \\ \dot{\theta} = -\omega_b + \frac{v_b \sin\theta}{\rho} \\ \dot{\beta} = \frac{v_b \sin\theta}{\rho} \end{cases} \tag{5}$$

Where $\rho = \sqrt{(x_d - x_c)^2 + (y_d - y_c)^2}$ is the measured distance between the current position and the desired position. $\theta = (\beta - \alpha)$ is the angle measured between the robot axes frame and the vector ρ . The system in (5) is valid when $\rho > 0$ and it will be engaged in creating feedback control law for robot maneuvering as discussed in section 4.

The linear speed v_b of point B and the angular velocity of rotation ω_b are directly produced by the change of the speeds of the right and left drives, v_R , and v_L respectively. Both drive wheels are linked to motors over ideal gearbox with gear ratio p_G that reduces the output velocities (ω_R, ω_L) and simultaneously increases the output torques.

$$\begin{cases} v_b = \frac{v_L l_R + v_R l_L}{l_L + l_R} = \frac{r}{p_G(l_L + l_R)} (l_R \omega_L + l_L \omega_R) \\ \omega_b = \frac{v_R - v_L}{l_L + l_R} = \frac{r}{p_G(l_L + l_R)} (\omega_R - \omega_L) \end{cases} \tag{6}$$

Where ω_L and ω_R are the angular speeds of the left and the right motors respectively.

3.2. Quadrotor model

The quadrotor is considered as a rigid body in the space SO(3) under external forces applied to the center of mass and expressed on earth fixed frame.

$$\begin{cases} \sum_P F = M\dot{v}_p \\ -\Omega \times J_Q \Omega + \sum_P \tau = J_Q \dot{\Omega} \end{cases} \quad (7)$$

Where M is the rigid body mass, J_C is 3x3 inertia matrix around the center of mass expressed in the body-fixed frame, v is the linear velocity of the body expressed in the inertial frame J , Ω is the angular velocity of the body expressed in the body-fixed frame Q , f is the total forces on the body and, τ is the total torques on the body.

The kinematics of the quadrotor motion is given by the following relations

$$\begin{cases} \dot{\xi} = v_b \\ \dot{R} = R\hat{\Omega} \end{cases} \quad (8)$$

Where ξ is the body position with respect to inertial frame, $\hat{\Omega}$ is the skew-symmetric matrix of the body angular speed vector Ω , R is 3 x 3 rotation matrix that move the body vector into inertial frame.

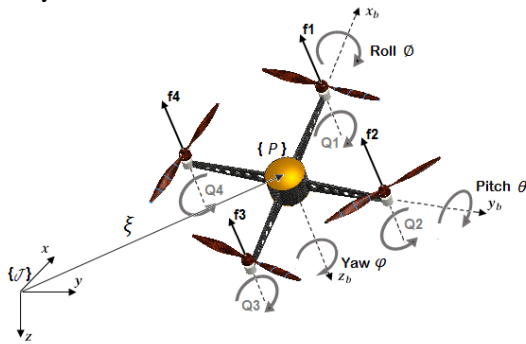


Figure 2. The quadrotor control inputs

Each rotor in the quadcopter generates a translational force f_i and torque Q_i as a function of the motor speed as shown in Figure 2. The gravitational force and the translational force (thrust) T_f are the only forces acting on the body and can be represented in inertial frame as follow:

$$\sum_P F = -R \begin{bmatrix} 0 \\ 0 \\ T_f \end{bmatrix} + \begin{bmatrix} 0 \\ 0 \\ Mg \end{bmatrix} \quad (9)$$

Where g is the gravitational acceleration and the trust T_f is given as:

$$T_f = \sum_{i=1}^4 f_i = k \sum_{i=1}^4 \omega_i^2 \quad (10)$$

where ω_i is the angular speed of i^{th} motor. As shown in Figure 2, the torque produced by each i^{th} motor is denoted by Q_i . Considering motor's torque is related to an aerodynamic drag $\tau_d = k_Q \omega_i^2$, then the total torques generated at motor shaft are:

$$Q_i - \tau_d = J_M \dot{\omega}_i \quad (11)$$

Where J_M is the moment of inertia of the i^{th} motor, $k_Q > 0$ is a constant for quasi stationary maneuvers in free flight. The control torques applied at the quadrotor center of mass are thus

$$\tau_P = \begin{bmatrix} \tau_\theta \\ \tau_\phi \\ \tau_\psi \end{bmatrix} = \begin{bmatrix} (f_1 - f_3)l \\ (f_4 - f_2)l \\ \sum_{i=1}^4 Q_i \end{bmatrix} \quad (12)$$

Where l is the distance between the motor shaft and the center of gravity. τ_θ is the pitching moment around x_b . τ_ϕ is the rolling moment around y_b . τ_ψ is the yawing moment around z_b .

The rotation of each rotor with respect to a rotating body leads to a gyroscopic torque τ_G to the air frame and is given by the following relationship

$$\tau_G = \sum_{i=1}^4 J_M (\Omega \times z_b) \omega_i = (\Omega \times z_b) \sum_{i=1}^4 J_M \omega_i \quad (13)$$

Where $(\Omega \times z_b)$ denotes the cross product between the body angular speeds vector and the axis z_b . This yield to the final quadcopter model:

$$\begin{cases} \dot{\xi} = v_b \\ \dot{R} = R\hat{\Omega} \\ -R \begin{bmatrix} 0 \\ 0 \\ T_f \end{bmatrix} + \begin{bmatrix} 0 \\ 0 \\ Mg \end{bmatrix} = M\dot{v}_b \\ -\Omega \times J_Q \Omega + \tau_P + \tau_G = J_Q \dot{\Omega} \end{cases} \quad (14)$$

4. Robots controllers

Several control approaches in the literature have been proposed for controlling the mobile robot and the quadcopter. Recently, many modern control methodologies such as nonlinear control [20, 51], optimal control [52], adaptive control [53], and fuzzy control [54, 55] have been widely intended for robots control. However, these approaches are difficult to implement in embedded systems. Therefore, the choice of a PID control approach in many world control problems refers to its simple structure and efficiency with its three-term functionality covering both transient and steady states. However, the difficulty in this type of controller is to obtain the optimal solution through tuning its gains.

Ground robot control

The control algorithm is designed to drive the robot from its current configuration (x_c, y_c, α_c) to the desired one (x_d, y_d, α_d) with respect to the inertial frame. Using kinematics motion models, the control inputs are the linear and angular velocities of the robot (i.e. $u = (v \ \omega)$) which are acting on its center of gravity. PI controllers are adopted here to control the robot as follows:

$$\begin{cases} v = \left(k_\rho \rho + k_i \int_0^{\delta T} \rho dt \right) \cos(e_\alpha) \\ \omega = k_\alpha(e_\alpha) + k_{i\alpha} \int_0^{\delta T} e_\alpha dt \end{cases} \quad (15)$$

Where $\rho = \sqrt{(x_d - x)^2 + (y_d - y)^2}$ is the error distance, and $e_\alpha = \alpha_d - \alpha_c$ is the difference between the desired heading angle and the current angle from the x axis in the inertial frame. The control vectors stated in (15) makes the robot motion behavior to be smooth and stable.

The linear and angular velocities of the robot are transformed to right and left wheel speeds. Considering that the rotating point occurs at the middle between the right and left drive (i.e. $l_L = l_R = l$), then the motors speeds can be given as follows:

$$\begin{cases} \omega_R = \frac{v}{r} + \frac{l\omega}{2r} \\ \omega_L = \frac{v}{r} - \frac{l\omega}{2r} \end{cases} \quad (16)$$

Quadcopter control

The controlled inputs of the quadcopter are three torques and thrust. The attitude is controlled by the quadcopter torques which are related to angular velocities by $\tau = J_Q \dot{\Omega}$, when Coriolis and gyroscopic terms are neglected. The attitude stability depends mainly on the accuracy in altitude, which keeps the quadcopter aloft. Therefore, a PID controller is adopted for the attitude stability and another PID is used to stabilize the vehicle altitude. The controller outputs are given in the following relationships:

$$\begin{cases} \tau = \begin{bmatrix} \tau_x \\ \tau_y \\ \tau_z \end{bmatrix} = J_Q \left(K_p e_\Omega(t) + K_i \int_0^{\delta T} e_\Omega(t) dt + K_d \frac{de_\Omega(t)}{dt} \right) \\ T = \frac{M}{\cos\phi \cos\theta} \left(g - \left(K_p e_z(t) + K_i \int_0^{\delta T} e_z(t) dt + K_d \frac{de_z(t)}{dt} \right) \right) \end{cases} \quad (17)$$

where $K_p, K_i,$ and K_d are the proportional, integral, and derivative gains respectively. The difference between the desired state (i.e. ϕ_d, θ_d, ψ_d in attitude and z_d in altitude) and the current state is represented by the error signals e , which are computed in a sample period.

The quadcopter horizontal positions are coupled with thrust vector and are controlled by orienting the vector towards the desired direction. Referring to (14), the desired linear horizontal accelerations are calculated from PD feedback of the position and velocity errors by the following relationships:

$$\begin{cases} \ddot{x}_d = K_p e_x + K_d \frac{de_x(t)}{dt} + \ddot{x}_f \\ \ddot{y}_d = K_p e_y + K_d \frac{de_y(t)}{dt} + \ddot{y}_f \end{cases} \quad (18)$$

where $K_p, K_i,$ and K_d are the proportional, integral, and derivative gains respectively. $e_x = x_d - x$ and $e_y = y_d - y$ are the position error vectors. The terms \ddot{x}_f and \ddot{y}_f represent feedforward accelerations. The horizontal positions are relative to the rolling and pitching angles ϕ and θ . By assuming small rolling and pitching angles and a thrust magnitude equal to Mg , the desired angles ϕ_d and θ_d can be given by the following relationships:

$$\begin{cases} \phi_d = \frac{1}{g} (\ddot{x}_d \sin\psi_d - \ddot{y}_d \cos\psi_d) \\ \theta_d = \frac{1}{g} (\ddot{x}_d \cos\psi_d + \ddot{y}_d \sin\psi_d) \end{cases} \quad (19)$$

Finally, the resultant thrust and torques that are generated by the controllers in (17) can be computed as four thrusts generated from quadrotor's propellers. For this task, proper allocation matrix is computed accordingly to mechanical parameters such as "plus" mounted quadrotor and is given as follows:

$$\begin{bmatrix} T \\ \tau \end{bmatrix} = \begin{bmatrix} -1 & -1 & -1 & -1 \\ 0 & -l & 0 & l \\ l & 0 & -l & 0 \\ -K_Q & K_Q & -K_Q & K_Q \end{bmatrix} \begin{bmatrix} f_1 \\ f_2 \\ f_3 \\ f_4 \end{bmatrix} \quad (20)$$

where l is the distance between the rotor and the center of gravity. For each $i = 1, \dots, 4, f_i$ is the generated thrust

from each rotor and it is a function of the angular speed of the motor (i.e. $f = k\omega^2$).

5. Path Planning and Motion Coordination

In this work a centralized decoupled planner is adopted for path planning and motion coordination of multi-robot system. In this approach an individual path is generated independently for each robot in order to reach its desired target where all of the state information is available to a single processor. Then another plan is involved to generate velocity profile for each robot to avoid collisions with other moving agent in the network.

Each robot in the proposed system is required to track a desired trajectory to reach a target. Specifically, the control structure proposed in section 4 for each robot is sufficient to control the tracking error to converge to zero, where the tracking error of the i_{th} -robot is defined as:

$$e_{ti} = q_{di} - q_i \quad (21)$$

Where ($i = 1, 2, 3, \dots, n$) denotes the i_{th} robot in the network and n is the total number of the individual robots. In addition, q_i is a vector of robot's positions in the inertial coordinate system and q_{di} is a vector of robot's desired trajectory.

Each robot in the proposed robotic system shares its position information with other robots. Moreover, the positions of unknown non-moving obstacles are assumed to be learned by robots using their own sensors. The robot is required to navigate to its target avoiding fixed and moving obstacles.

Based on the equation given in (21), the robot will move to the desired target by following the given trajectory, unless an obstacle is presented in the path of the robot or another robot is coming towards it. In this case, it is essential to look for alternative solution paths by feeding small variations of robot motions by affecting both its predefined path and its scheduled velocity. Hence, we define a new control law for the ground robot to provide feed forward signals on the robot motion as follows:

$$\begin{cases} \omega_{fi} = \sum_{j \neq i}^n k_f \frac{\cos(\theta_{ij})}{e^{(|q_{ij}|-1)^2}} \\ v_{fi} = \frac{1}{k_v} \omega_{fi} \end{cases} \quad (22)$$

Where ($1 \leq i \leq n$) denotes the i_{th} robot in the network and n is the total number of the individual robots. In addition q_{ij} denotes the vector of displacements of the i_{th} robot coordinates from the j_{th} robot coordinates in inertial frame. θ is the angle between the q_{ij} vector and the vector of displacement of i_{th} robot from the target coordinates in inertial frame as shown in 3. ω_{fi} and v_{fi} are the feed-forward angular and linear speed control inputs which are tuned by the gain constants k_f and k_v respectively. It is obvious from (22) that the value of ω_{fi} increases when θ_{ij} and q_{ij} decrease. For example, the effect on the value ω_f from robot 4 is greater than the effects coming from robot 2 and robot 3 because of the shortest distance between robot 1 and robot 4 as well as the smallest angle value (θ_{14}) as shown in Figure 3.

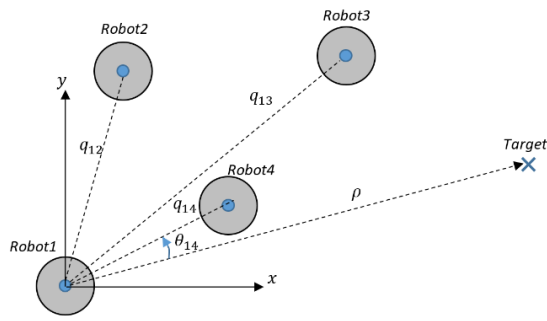


Figure 3. Robot coordinates with other robots in the network

In the case of the aerial robot, it is possible to avoid collision with other aerial vehicles by finding a path in three dimensions, but we assume that a number of quadcopters are required to stay at the same height. Therefore, the quadcopter should find a path in the horizontal plane to avoid collision with other quadcopters by the following control inputs:

$$\begin{cases} v_{fxi} = \sum_{j \neq i}^n k_r \frac{\cos(\theta_{ij})}{e^{(|q_{ij}|-1)^2}} \\ v_{fyi} = \sum_{j \neq i}^n k_r \frac{\sin(\theta_{ij})}{e^{(|q_{ij}|-1)^2}} \end{cases} \quad (23)$$

Where v_{fxi} and v_{fyi} are the feed-forward linear velocities to the i_{th} quadcopter in x and y directions respectively. We assume that the feed-forward velocities are equal to zero when there is enough height distance between the i_{th} quadcopter and other quadcopters. As we discussed in the ground robot case, the velocity values in (23) are approaching to zero when the horizontal distances between i_{th} quadcopter and the others are very long. The velocities in (23) are represented in inertial frame. Therefore, the values required in body frame are calculated by considering the heading angle.

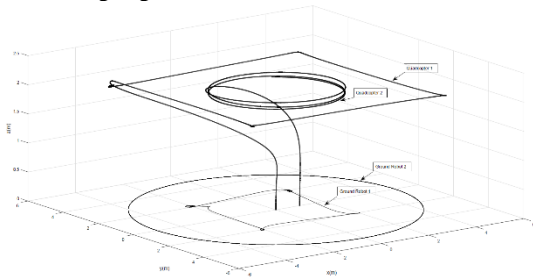


Figure 4. Motion of aerial and ground robots on assigned trajectories

6. Simulation Results

This section serves to illustrate the effectiveness of the proposed control algorithms for robot’s trajectory tracking and path coordination. The simulation results are executed first to show the performance of each robot independently, and to study its stability and ability to track a pre-defined trajectory. Then the second part of the simulation shows the performance of each aerial and ground robot in generating new paths to avoid collision with other robots.

6.1. Trajectory tracking

Position and orientation stability of each robot were achieved by using PID controllers. The gains of the

controllers were tuned properly to guarantee best performance. More precisely, attitude and position controller gains were chosen in order to minimize oscillations and settling time. The adjusted gains of the PIDs in the quadcopter and ground robot are given in Table. To ensure the validity of the used PID controllers in the proposed robots, external disturbances as random form signals were carried out on each robot. These signals are applied on all axes in body frame of each robot with a value range of $(-0.4 \text{ to } 0.4)N$.

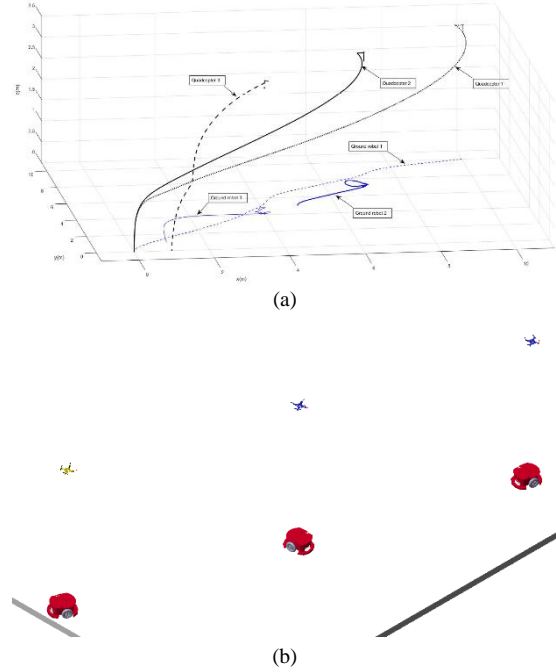


Figure 5. Mission Scenario 2: (a) Robots trajectories, (b) The final positions of the system robots

Table 2: PIDs gains in the quadcopter and ground robot

Quadcopter PIDs	Ground robot PIDs						
	P	I	D				
Alt	30	20	15	Position x	15	5	0
Positions x,y	5	0	3	Position y	15	5	0
Roll/Pitch	3	0	2	Rotation	5	3	0
Yaw	0.5	0.1	0.1				

Figure 4 shows how the robots (i.e. two quadcopters and two ground robots) track the assigned paths correctly. In this scenario the robotic platforms were initialized on the ground from different positions. One of the ground robots and one of the quadcopters were demanded to follow rectangular-shape paths. Meanwhile, the other quadcopter and ground robot were needed to track a circular-shape trajectory. The vehicles maintain the performance of the motion in terms of stability and proves quite perfect characteristics in terms of ability to track the predefined trajectories.

6.2. Path planning for collision avoidance

The following two figures illustrate the performance of the robotic platforms which are demonstrated by two different scenarios in order to validate the ability of each

robot for collision avoidance with other aerial or ground robots in a multi-robots network.

Figure 5 shows the performance of the proposed system in a mission scenario where each robot moves towards a specific target point and then it waits there for a while. More specifically, ground robot 1, 2, and 3 are requested to move toward points (4,4), (7,7), and (10,10) respectively which are aligned on a straight line. Also, quadcopter 1, 2, and 3 are needed to move from their initial positions on the ground to the points (4,4,3), (7,7,3), and (10,10,3) respectively which are also falling on a straight line. It is clear from the figure that robot 3 (ground or aerial) is creating a curved-line instead of straight line during motion to its target, in order to avoid collision with robot 1, and 2. The same methodology is applied also on robot 2 to move away from robot 1.

When a robot reaches its desired fixed-point location, it stops over that point for a period of time. The stopped robot can react quickly to other robots approaching it, accordingly it moves enough distance from the coming robot to avoid an accident and at the same time to allow the robot to return to its desired position as soon as possible. This situation is characterized through the figure by the irregular path, which is formed at the end of the robot track around the fixed point.

Finally, Figure 6 shows the performance of the robotic platforms in a different scenario where two of the ground robots were required to follow a circular path. The ground robot 1 was moving in an opposite direction of robot 2. The third ground robot was required to travel to a home location at (0, 0). This scenario also included three quadcopters; one of the quadcopters (quadcopter 1) was trying to track a circular path, and two of them were targeting the points (2, 0, 2) and (0, 2, 2) which were located on the same path of quadcopter 1. The figure shows also how the ground robot and the quadcopter on the circular paths were reconstructing the desired trajectory when it was needed to avoid collisions between robots.

7. Conclusions

This work presented the modeling, simulation, and control of a multi-robot system, which contains models of aerial and mobile robots. Each of the robotic platforms was built by means of Simulink modeling and SimMechanics and was controlled by applicable control methods for motion stability and maneuverability. This work also proposed a new strategy for path planning of robot motion in a network of several aerial and ground robots. Providing this method, the robot can change its predefined path to avoid collisions with other robots on the path by manipulating feed-forward speeds via PID controller. The results demonstrated the validation of this strategy on a multi-robot system, and illustrated how the track path of a robot can be reshaped smoothly. The robotic system was built in a simulation environment that provides many advantages for multi-agent robotic systems; one can insert and remove several robots easily as well as modifying the parameters of the robot model in CAD platform, which can be reconsidered in the simulation, needs less time and effort. The performance of the robotic system was demonstrated and validated in different motion scenarios. The results showed high stability in robots' motions and good performance in trajectory tracking, even when disturbances

exist. The performance of the proposed system when evaluated on different scenarios suggests that the robotics system has very good maneuverability for collision avoidance when multi-agent robots are engaged in common tasks. The present work will be extended to include real implementation of the proposed system in real application such as security in university campus.

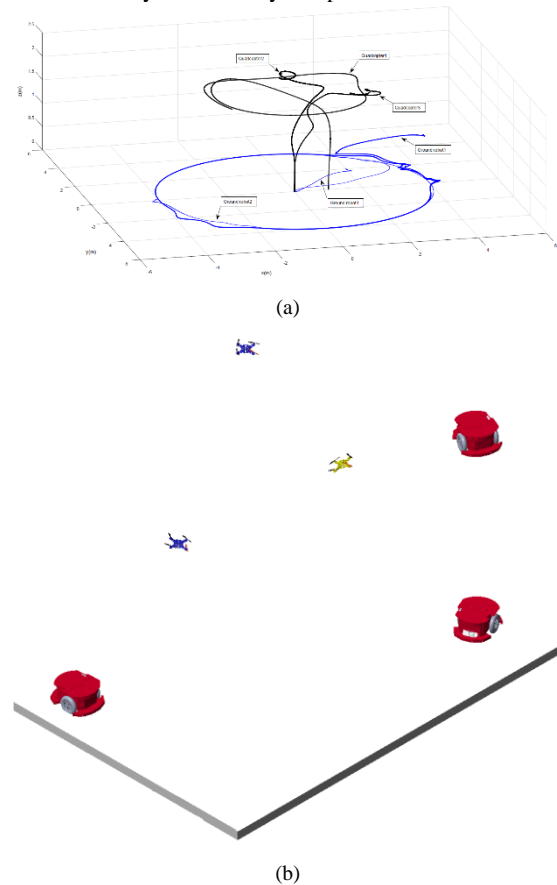


Figure 6. Mission Scenario 2: (a) Robots trajectories, (b) The final positions of the system robots

References

- [1] G. Marek, Š. Peter, "Design the robot as security system in the home". *Procedia Engineering*, vol. 96, pp. 126–130, 2014.
- [2] P. Rea, E. Ottaviano, "Design and development of an inspection robotic system for indoor applications". *Robotics and Computer-Integrated Manufacturing*, vol. 49, pp. 143–151, 2018.
- [3] A. Kurkin, D. Y. Tyugin, V. Kuzin, A. Chernov, V. Makarov, P. Beresnev, V. Filatov, D. Zeziulin, "Autonomous mobile robotic system for environment monitoring in a coastal zone". *Procedia Computer Science*, vol. 103, pp. 459–465, 2017.
- [4] J. Peterson, W. Li, B. Cesar-Tondreau, J. Bird, K. Kochersberger, W. Czaja, M. McLean, "Experiments in unmanned aerial vehicle/unmanned ground vehicle radiation search," *Journal of Field Robotics*, vol. 36, no. 4, pp. 818–845, 2019.
- [5] A. K. Nasir, A. Hsino, H. Roth, K. Hartmann, "Aerial robot localization using ground robot tracking—towards cooperative slam". *IFAC Proceedings Volumes*, vol. 46, no. 19, pp. 313–318, 2013.

- [6] R. Abiyev, D. Ibrahim, B. Erin, "Navigation of mobile robots in the presence of obstacles". *Advances in Engineering software*, vol. 41, no. 10-11, pp. 1179–1186, 2010.
- [7] M. Hayajneh, M. Melega, L. Marconi, "Design of autonomous smartphone based quadrotor and implementation of navigation and guidance systems". *Mechatronics*, vol. 49, pp. 119–133, 2018.
- [8] M. Hayajneh, A. Badawi, "Automatic uav wireless charging over solar vehicle to enable frequent flight missions". 3rd international conference on automation, control and robots, 2019, pp. 44–49.
- [9] M. Al-Fetyani, M. Hayajneh, A. Alsharkawi, "Design of an executable anfis-based control system to improve the attitude and altitude performances of a quadcopter drone". *International Journal of Automation and Computing*, vol. 18, no. 1, pp. 124–140, 2021.
- [10] R. H. Abiyev, B. Erin, A. Denker, "Navigation of mobile robot using type-2 fuzzy system". in *International Conference on Intelligent Computing*. Springer, 2017, pp. 15–26.
- [11] A. Meléndez, O. Castillo, F. Valdez, J. Soria, M. Garcia, "Optimal design of the fuzzy navigation system for a mobile robot using evolutionary algorithms". *International Journal of Advanced Robotic Systems*, vol. 10, no. 2, p. 139, 2013.
- [12] S. BaniHani, M. Hayajneh, A. Al-Jarrah, S. Mutawe, "New control approaches for trajectory tracking and motion planning of unmanned tracked robot". *Advances in Electrical and Electronic Engineering*, vol. 19, no. 1, pp. 42–56, 2021.
- [13] J. Sebestyénová, P. Kordel, "Simulation of self-organizing multi-robotic system used for area coverage and surround of found targets". *WSEAS Transactions on Information Science and Applications*, vol. 11, pp. 130–138, 2014.
- [14] J. H. Liang, C. H. Lee, "Efficient collision-free pathplanning of multiple mobile robots system using efficient artificial bee colony algorithm". *Advances in Engineering Software*, vol. 79, pp. 47–56, 2015.
- [15] D.H. Lee, "Resource-based task allocation for multi-robot systems". *Robotics and Autonomous Systems*, vol. 103, pp. 151–161, 2018.
- [16] M. Saska, V. Vonásek, T. Krajník, L. Přeučil, "Coordination and navigation of heterogeneous MAV–UGV formations localized by a 'hawk-eye'-like approach under a model predictive control scheme". *The International Journal of Robotics Research*, vol. 33, no. 10, pp. 1393–1412, 2014.
- [17] P. K. Penumarthi, A. Q. Li, J. Banfi, N. Basilico, F. Amigoni, J. O'Kane, I. Rekleitis, S. Nelakuditi, "Multirobot exploration for building communication maps with prior from communication models". in *Multi-Robot and Multi-Agent Systems (MRS)*, 2017 International Symposium on. IEEE, 2017, pp. 90–96.
- [18] G. Loianno, V. Spurny, J. Thomas, T. Baca, D. Thakur, D. Hert, R. Penicka, T. Krajník, A. Zhou, A. Cho, M. Saska, "Localization, grasping, and transportation of magnetic objects by a team of mavs in challenging desert like environments". *IEEE Robotics and Automation Letters*, vol. 3, no. 3, pp. 1576–1583, 2018.
- [19] J.-E. Gomez-Balderas, G. Flores, L. G. Carrillo, R. Lozano, "Tracking a ground moving target with a quadrotor using switching control". *Journal of Intelligent & Robotic Systems*, vol. 70, no. 1-4, pp. 65–78, 2013.
- [20] S. Mutawe, M. Hayajneh, S. BaniHani, "Robust Path Following Controllers for Quadrotor and Ground Robot". 2021 International Conference on Electrical, Communication, and Computer Engineering (ICECCE), vol. 12 pp. 1-6, 2021.
- [21] M. Peasgood, C. M. Clark, J. McPhee, "A complete and scalable strategy for coordinating multiple robots within roadmaps". *IEEE Transactions on Robotics*, vol. 24, no. 2, pp. 283–292, 2008.
- [22] L. E. Parker, "Path planning and motion coordination in multiple mobile robot teams". *Encyclopedia of complexity and system science*, pp. 5783–5800, 2009.
- [23] B. Li, H. Liu, D. Xiao, G. Yu, Y. Zhang, "Centralized and optimal motion planning for large-scale agv systems: A generic approach". *Advances in Engineering Software*, vol. 106, pp. 33–46, 2017.
- [24] Y. Chen, L. Li, "Collision-free trajectory planning for dual-robot systems using B-splines". *International Journal of Advanced Robotic Systems*, vol. 14, no. 4, 2017.
- [25] G. Sanchez, J.-C. Latombe, "Using a PRM planner to compare centralized and decoupled planning for multi-robot systems". 2002 IEEE International Conference on Robotics and Automation, vol. 2, pp. 2112–2119, 2002.
- [26] J. López, D. Pérez, E. Zalama, "A framework for building mobile single and multi-robot applications". *Robotics and Autonomous Systems*, vol. 59, no. (3-4), pp. 151-162, 2011.
- [27] J. Verma, R. Virender, "Multi-Robot Coordination Analysis, Taxonomy, Challenges and Future Scope". *Journal of Intelligent & Robotic Systems* vol. 102, no.1, pp.1-36, 2021.
- [28] Y. Hirata, K. Kosuge, H. Asama, H. Kaetsu, K. Kawabata, "Decentralized control of mobile robots in coordination". 1999 IEEE International Conference on Control Applications, Vol. 2, pp. 1129-1134, 1999.
- [29] B. Gerkey, J. Mataric, "Are (explicit) multi-robot coordination and multi-agent coordination really so different?". *spring symposium on bridging the multi-agent and multi-robotic research gap*, pp. 1-3, 2004.
- [30] G. Korsah, A. Stentz, M. Dias, "A comprehensive taxonomy for multi-robot task allocation". *The International Journal of Robotics Research*, vol. 32, no.12, pp. 1495–1512, 2013.
- [31] T. Standley "Finding optimal solutions to cooperative pathfinding problems". *Twenty-Fourth AAAI Conference on Artificial Intelligence*, vol. 24, no. 1, pp. 173–178, 2010.
- [32] T. Standley, R. Korf, "Complete algorithms for cooperative pathfinding problems". *IJCAI International Joint Conference on Artificial Intelligence*, pp. 668–673, 2011.
- [33] G. Wagner, H. Choset, "Subdimensional expansion for multirobot path planning". *Artificial Intelligence*, vol. 219, pp. 1–24 2015.
- [34] N. Dung, A. Shimada, "Humanoid climbing robot modeling in matlab-simechanics". *IECON 2013-39th Annual Conference of the IEEE*, pp. 4162–4167, 2013.
- [35] M. Silva, R. Barbosa, T. Castro, "Multi-legged walking robot modelling in MATLAB/Simmechanics TM and its simulation". *Eighth EUROSIM Congress on Modelling and Simulation*. pp. 226–231, 2013.
- [36] R. Ismail, M. Ariyanto, W. Caesarendra, A. Nurmianto, "Development of robotic hand integrated with simmechanics 3D animation," *International Seminar on Intelligent Technology and Its Applications (ISITIA)*, pp. 629–634, 2016.
- [37] M. D. Murphy, "A modular virtual laboratory for quadrotor control simulation". *IFAC-PapersOnLine*, vol. 49, no. 6, pp. 93–98, 2016.
- [38] W. Li, T. Zhang, K. Kühnlenz, "A vision-guided autonomous quadrotor in an air-ground multi-robot system". 2011 IEEE International Conference on Robotics and Automation, pp. 2980–2985, 2011.
- [39] S. Minaeian, J. Liu, Y.-J. Son, "Vision-based target detection and localization via a team of cooperative UAV and UGVs".

- IEEE Transactions on Systems, Man, and Cybernetics: Systems, vol. 46, no. 7, pp. 1005–1016, 2016.
- [40] Y. Bi, H. Duan, “Implementation of autonomous visual tracking and landing for a low-cost quadrotor”. *Optik - International Journal for Light and Electron Optics*, vol. 124, no. 18, pp. 3296–3300, 2013.
- [41] K. Wenzel, A. Masselli, A. Zell, “Automatic take off, tracking and landing of a miniature UAV on a moving carrier vehicle”. *Journal of Intelligent Robotic Systems*, vol. 61, no. 1, pp. 221–238, 2011.
- [42] J. Higgins, N. Bezzo, “Negotiating visibility for safe autonomous navigation in occluding and uncertain environments”. *IEEE Robotics and Automation Letters*, vol. 6, no. 3, pp. 4409–4416, 2021.
- [43] E. Yel, N. Bezzo, “Gp-based runtime planning, learning, and recovery for safe UAV operations under unforeseen disturbances”. *2020 IEEE/RSJ International Conference on Intelligent Robots and Systems (IROS)*, 2020, pp. 2173–2180.
- [44] C. Hui, C. Yousheng, L. Xiaokun, W. Shing, “Autonomous takeoff, tracking and landing of a UAV on a moving UGV using onboard monocular vision”. *32nd Chinese Control Conference*, pp. 5895–5901, 2013.
- [45] J. Ni, M. Tang, Y. Chen, W. Cao, “An improved cooperative control method for hybrid unmanned aerial-ground system in multitasks”. *International Journal of Aerospace Engineering*, vol. 2020, pp. 1–14, 2020.
- [46] MF Lee, SF. Su, JW. Yeah, HM. Huang, J. Chen, “Autonomous landing system for aerial mobile robot cooperation”. *7th International Conference on Soft Computing and Intelligent Systems (SCIS) and 15th International Symposium on Advanced Intelligent Systems (ISIS)*, pp. 1306–1311, 2014.
- [47] EH. Harik, F. Guerin, F. Guinand, JF. Brethé, H. Pelvillain, JY. Paréde, “Fuzzy logic controller for predictive vision-based target tracking with an unmanned aerial vehicle”. *Advanced Robotics*, vol. 31, no. 7, pp. 368–381, 2017.
- [48] A. Sawarkar, V. Chaudhari, R. Chavan, V. Zope, A. Budale, F. Kazi, “HMD vision-based teleoperating UGV and UAV for hostile environment using deep learning”. *CoRR*, vol. abs/1609.04147, 2016.
- [49] D. Stolfi, M. Brust, G. Danoy, P. Bouvry, “Uav-ugvumv multi-swarms for cooperative surveillance”. *Frontiers in Robotics and AI*, vol. 8, p. 5, 2021.
- [50] Yiping Li, “Design of Path Tracking Control System for UAV Based on Adaptive Preview Method”. *Jordan Journal of Mechanical and Industrial Engineering*, vol.14, no.1, pp. 101 – 108, 2020.
- [51] W. Dixon, D.Dawson, E. Zergeroglu, A. Behal. *Nonlinear control of wheeled mobile robots*, 2001.
- [52] LC. Lai, CC. Yang, CJ. Wu, “Time-optimal control of a hovering quad-rotor helicopter”. *Journal of Intelligent and Robotic Systems*, vol. 45, no. 2, pp. 115–135, 2006.
- [53] P. Mukherjee and S. Waslander, “Direct adaptive feedback linearization for quadrotor control,” in *AIAA Guidance, Navigation, and Control Conference*, 2012, p. 4917.
- [54] M. Santos, V. Lopez, and F. Morata, “Intelligent fuzzy controller of a quadrotor”. *International Conference on Intelligent Systems and Knowledge Engineering (ISKE)*, pp. 141–146, 2010.
- [55] T. Lee, F. Leung, P. Tam, “Position control for wheeled mobile robots using a fuzzy logic controller”. *Industrial Electronics Society, IECON’99 Proceedings. The 25th Annual Conference of the*, vol. 2, pp. 525–528, 1999.

Control of Wake Behind an Unconfined Wedge Structure by Magnetohydrodynamics

Shailendra Rana^{a*}, Hari B. Dura, Rajendra Shrestha

Department of Mechanical and Aerospace Engineering, Pulchowk Campus, Institute of Engineering, Tribhuvan University, Kathmandu 00977, Nepal

Received July 7 2020

Accepted August 14 2021

Abstract

The laminar, viscous and incompressible flow of an electrically conducting fluid across an unconfined wedge structure in the presence of a transverse magnetic field has been studied. Two-dimensional numerical simulations have been performed for Reynolds number (Re) = 1-150 and Hartmann number (Ha) = 0-10 for a fixed blockage ratio (β) = $d/W = 1/30$. The magnetic induction method in magnetohydrodynamics module built in ANSYS FLUENT solver has been employed to compute the flow fields. Results show that the vortex shedding can be completely eliminated if the applied magnetic field is strong enough. In the steady flow regime, it has been found that the recirculation length reduces with the increase in Ha . A minimal reduction in the drag coefficient is observed with the increase in Ha as long as unsteady flow is maintained ($Ha < 7.3$). However, the drag coefficient has a tendency to significantly increase with the increase in Ha for steady flow. Similarly, the lift amplitude decreases with the increase in Ha indicating a diminishing effect on the strength of vortices. A critical Hartmann number (Ha_{cr}) of 7.3 has been found for $Re = 100$ at which complete suppression of vortex shedding is observed.

© 2021 Jordan Journal of Mechanical and Industrial Engineering. All rights reserved

Keywords: Magnetohydrodynamics, active vortex suppression, Strouhal number, magnetic Reynolds number, Hartmann number;

1. Introduction

Studies on bluff bodies have been extensively carried out because of their complex flow dynamics and relevance to practical engineering problems [1-4]. Examples of the engineering applications include heat exchangers, pipelines, offshore marine structures, high-rise buildings etc. Commonly used bluff bodies for numerical and experimental studies are circular, square or rectangular cylinders. These bodies, irrespective of their geometry, present many similarities in terms of wake structure at different Reynolds numbers. One important characteristic regarding the flow around these bodies is the unsteady periodic vortex shedding phenomena occurring at a particular Reynolds number. Under such flow conditions, these bluff bodies experience unsteady forces which may cause fatigue damage due to flow-induced vibrations. The unsteady forces acting on these bodies can be reduced by controlling the vortex shedding phenomena through several flow control techniques. Examples of such flow control techniques are electrical methods, use of thermal effects, geometrical modifications such as grooves, rotary oscillations, magnetohydrodynamics, etc. A comprehensive review of several active and passive control methods employed for the control of flow-induced vibrations was given by Rashidi et al. [5].

Among several flow control techniques, the concept of magnetohydrodynamics (MHD) has been exploited by many industries to control and manipulate the flow of electrically conducting fluids, such as liquid metals, electrolytes, etc. The concept is that the motion of an

electrically conducting fluid under the influence of an external magnetic field induces electric currents, which interacts with the magnetic field to produce Lorentz force [6]. This force has a dampening effect on the flow structure.

Vortex dynamics has been the subject of great interest to researchers for many years. Oyewola et al. [7] numerically investigated the effects of spacing ratios ($S/D = 1.1, 1.1, 1.8, 2.0, 2.2, 2.4, 3.0, 4.0$ and 5) on the forced convection flow of air at $Re = 23500$ over a pair of circular cylinders in tandem arrangement. They found that the increase in spacing ratios augments the local Nusselt number on the four portions of the cylinders. Bouakkaz et al. [8] studied the two-dimensional unsteady flow and heat transfer of water-based Cu nanofluid over a square cylinder considering nanoparticle volume fractions and angle of inclination in the range of 0-5% and 0-450 respectively. They concluded that the local Nusselt number increases with the rise in nanoparticle volume fraction for a fixed inclination angle. In the past, several works regarding the control of vortex shedding past bluff bodies using different techniques have been done. Hafsia and Nouri [9] investigated the effects of grooves and permeable plates on vortex shedding over a single circular cylinder at $Re = 20$ and 100. They found that the vortex shedding is considerably suppressed under the influence of two grooves and two permeable plates. Besides this, researchers have also shown keen interest in studying vortex dynamics using MHD. Singha et al. [10] investigated the laminar viscous flow of a conducting fluid past a square cylinder under the influence of transverse magnetic field at Reynolds numbers from 50 to 250. It was found that the size of the recirculation region behind the cylinder diminishes with the increment in

* Corresponding author e-mail: ranashailendra74@gmail.com

the magnetic field for a steady flow. Within the unsteady flow regime, a minimal increment in the Strouhal number was observed and the reduction in the amplitude of lift coefficient was observed implying that the strength of shed vortices has diminished. It was also concluded that the complete elimination of vortex shedding is achievable and steady flow could be attained if the applied magnetic field is strong enough. Singha and Sinhamahapatra [11] investigated the effect of transverse magnetic field on vortex shedding past a circular cylinder placed in a channel at $Re = 50-250$. The size of the recirculation zone formed behind the cylinder reduces with the increase in the strength of magnetic field. Also, a critical Hartmann number at $Re = 250$ was found to be 5.5. Farjallah et al. [12] studied the heat transfer and vortex shedding past a bounded square obstacle for $Re = 80-250$ and $Ha = 0-4$ at a fixed blockage ratio (β) = 1/4. Their results showed that the magnitude of drag and lift coefficients decrease on the application of magnetic field. They also found that at $Re = 200$, the periodic vortex shedding phenomena transitions to steady flow for $Ha = 4$. Chatterjee et al. [13] investigated the flow of a conducting fluid past circular and square cylinders in an unconfined medium for low $Re = 10-40$ and $Ha = 0-10$ at a blockage ratio (β) = 1/20 to control the steady separated flow using finite volume method. Their findings showed that the recirculation length and the separation angle decrease with the increase in Ha . Drag coefficient was found to increase with the increase in the magnitude of magnetic field. Chatterjee and Chatterjee [14] numerically analyzed the forced convection heat transfer past a circular cylinder for $Re = 10-80$ and $Ha = 0-10$ at a fixed blockage ratio (β) = 1/4 using ANSYS FLUENT. They considered three different working fluids having Prandtl number, $Pr = 0.02$ (liquid metal), 0.71 (air) and 7 (water) to analyze the heat transfer phenomena under the presence of transverse or aligned magnetic field. Their study concluded that the recirculation region gets suppressed at a faster rate for transverse magnetic field in comparison to aligned magnetic field. A significant increment in the drag coefficient for lower Re was observed and found to be more pronounced for transverse magnetic field in comparison with the aligned magnetic field. The Nusselt number was found to increase with Reynolds number and also with Hartmann numbers for a transverse magnetic field. Esfahani [15] employed finite volume method to study the effects of streamwise magnetic field on vortex shedding and wake structure behind a solid circular obstacle placed in a rectangular channel at $Re = 1-200$ and Stuart number (N) = 0-10. Their study concluded that at $N = 4$, the flow stabilizes as evidenced by the transition from unsteady flow pattern with vortex shedding to the steady state with symmetric recirculation bubbles. They also observed that the drag coefficient decreases for $N < 0.22$ whereas it increased rapidly for higher values of N (i.e. $N=5$). Rashidi et al. [16] performed a numerical investigation regarding the control of wake structure past a square cylinder confined in a rectangular channel under the streamwise magnetic field for $Re = 1-250$ and $N = 0-10$ using finite volume method. Their results showed that the Strouhal number decreases linearly with the increase in N . Also, the flow pattern changes from time-dependent with vortex shedding to the steady state with the increase in N . Recently, Hussam et al. [17] numerically investigated the effects of axial magnetic field on the fluid flow and heat

transfer of Galinstan (GaInSn) eutectic alloy past a confined triangular cylinder at $Re = 100-3000$ and $Ha = 100-2400$ for a blockage ratio (β) = 1/4. They found triangular cylinder to be superior promoter geometry in terms of heat transfer augmentation compared to the square or circular cylinders. From the review of above literature, it is evident that magnetohydrodynamics is an efficient technique to control the flow past bluff bodies. It can also be concluded that the shape of an obstacle has a significant influence on the flow dynamics. Like circular and square-shaped bodies, triangular cylinders also exhibit the periodic vortex shedding phenomena. Moreover, the presence of highly sharpened corners in triangular cylinders in comparison to circular or square cylinders contributes to more intense hydrodynamic instabilities. Such intense instabilities, therefore, require stronger magnetic fields for flow suppression [13].

Previous research works mentioned in the paper indicate that limited research works have been done regarding the control of flow around triangular cylinder using magnetic field. To the best of authors' knowledge, there are no reported works done regarding the control of vortex shedding and wake structure past triangular cylinders using magnetohydrodynamics in an unconfined medium at low Reynolds numbers. The low Reynolds numbers considered in this study i.e. $Re = 1-150$ are evident in microfluidic applications and in liquid metal flows in nuclear reactors and semi-conductors. Also, the turbulence created by triangular cylinders is essential to heat transfer enhancement. Moreover, this work will further supplement to the existing knowledge regarding magnetohydrodynamic flows over bluff bodies. Hence, this paper investigates the effects of magnetic field on vortex shedding and wake structure behind the triangular cylinder (wedge) in an unconfined medium at low Reynolds and Hartmann numbers.

2. Problem Description and Mathematical Modelling

2.1. Geometrical configuration

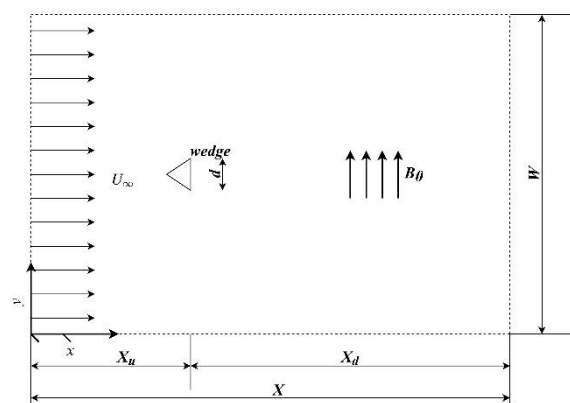


Figure 1. Schematic diagram of the computational model

The geometrical configuration for the current research is shown in Figure 1. Two-dimensional laminar incompressible viscous flow of an electrically conducting fluid having constant electrical conductivity (σ), kinematic viscosity (η) and density (ρ) across a wedge structure of side length (d) is considered. The wedge is an equilateral triangular cylinder placed in an unconfined medium.

However, to create a finite computational domain, the blockage ratio, $\beta = d/W = 1/30$ is set as per the domain independency test conducted by [2]. To simulate the unconfined flow, a free-slip boundary condition is assigned on the upper and lower walls of the computational domain. The fluid flow with free stream velocity (U_∞) in the presence of an external magnetic field (B_0) in a transverse direction is considered. All the solids walls are insulated. Table 1 gives the value of the normalized dimensions of the physical domain used in this study.

Table 1. Geometrical details

S.N.	Geometrical parameters	Dimensions
1	Upstream length (X_u/d)	12
2	Downstream length (X_d/d)	20
3	Total axial length (X)	32
4	Domain height (W/d)	30

2.2. Governing equations

Two-dimensional laminar unsteady flow of an incompressible conducting fluid with constant properties in the presence of a transverse magnetic field is considered. Under such assumptions, the dimensionless governing equations of conservation of mass and momentum can be expressed as follows [13]:

Conservation of mass:

$$\nabla \cdot V = 0 \tag{1}$$

Conservation of momentum:

$$\frac{\partial v}{\partial t} + (V \cdot \nabla)V = -\nabla P + \frac{1}{Re} \nabla^2 U + \frac{Ha^2}{Re} (J \times B) \tag{2}$$

Here, the term $J \times B$ represents the Lorentz force acting in the computational domain.

The derivation of the dimensional form of the magnetic induction equation is as follows:

Maxwell's equations:

$$\nabla \cdot B = 0 \tag{3}$$

$$\nabla \times E = -\frac{\partial B}{\partial t} \tag{4}$$

$$\nabla \cdot D = q \tag{5}$$

$$\nabla \times H = J + \frac{\partial D}{\partial t} \tag{6}$$

The induction fields H and D can be expressed as follows:

$$H = \frac{1}{\mu_0} B \tag{7}$$

$$D = \epsilon E \tag{8}$$

where ϵ is the electric permittivity and E is the electric field.

According to Ohm's law, the current density can be defined as:

$$J = \sigma E \tag{9}$$

If the fluid is moving with velocity field u in the presence of magnetic field B, the current density becomes,

$$J = \sigma(E + u \times B) \tag{10}$$

Using Eq. 4,

$$\frac{\partial B}{\partial t} = -\nabla \times E \tag{11}$$

From Eq. 10,

$$E = \frac{1}{\sigma} - u \times B \tag{12}$$

Applying curl both sides in Eq. (12), we get,

$$\nabla \times E = \nabla \times \left(\frac{1}{\sigma} - u \times B \right) \tag{13}$$

Combining Eqs. (11) and (13),

$$\frac{\partial B}{\partial t} = -\nabla \times \left(\frac{1}{\sigma} - u \times B \right) \tag{14}$$

$$\frac{\partial B}{\partial t} = -\nabla \times \left(\frac{1}{\sigma} \right) + \nabla \times (u \times B) \tag{15}$$

Neglecting the displacement current in Eq. 6, we obtain,

$$\nabla \times H = J \tag{16}$$

Inserting Eq. 7 into Eq. 16,

$$\frac{\nabla \times B}{\mu_0} = J \tag{17}$$

After substitution of Eq. 17 into Eq. 15, we obtain,

$$\frac{\partial B}{\partial t} = -\nabla \times \left(\frac{1}{\mu_0 \sigma} (\nabla \times B) \right) + \nabla \times (u \times B) \tag{18}$$

Eq. 18 can be rewritten as,

$$\frac{\partial B}{\partial t} = -\frac{1}{\mu_0 \sigma} \nabla \times (\nabla \times B) + \nabla \times (u \times B) \tag{19}$$

After a few mathematical operations, Eq. 19 can be expressed as follows:

$$\frac{\partial B}{\partial t} = -\frac{1}{\mu_0 \sigma} (\nabla(\nabla \cdot B) - B(\nabla \cdot \nabla)) + u(\nabla \cdot B) - B(\nabla \cdot u) \tag{20}$$

Using Eq. 3, we get,

$$\frac{\partial B}{\partial t} = \frac{1}{\mu_0 \sigma} \nabla^2 B + u(\nabla \cdot B) - B(\nabla \cdot u) \tag{21}$$

Finally, rearranging Eq. 21, we obtain,

$$\frac{\partial B}{\partial t} + B(\nabla \cdot u) = \frac{1}{\mu_0 \sigma} \nabla^2 B + u(\nabla \cdot B) \tag{22}$$

Eq. 22 represents the dimensional form of the magnetic induction equation derived from Ohm's law and Maxwell's equations.

The present calculations show that the magnetic Reynolds number, $Re_m = \mu_0 \sigma U_\infty d$, is in the order of 10^{-4} . Since $Re_m \ll 1$, the magnitude of induced magnetic field b is negligible in comparison to the total magnetic field B [18]. The Reynolds and Hartmann numbers have been defined on the basis of side length of the wedge as:

$$Re = \frac{U_\infty d}{\eta} \tag{23}$$

$$Ha = B_0 d \sqrt{\frac{\sigma}{\eta \rho}} \tag{24}$$

2.3. Grid structure and numerical details

Structured non-uniform grids have been generated using ICEM CFD software. The grid structure is shown in Figure 2 (a). The grid refinement around the vicinity of wedge is shown in Figure 2 (b). The grid used in this study consists of 114147 cells having 200 grid points on each side of the wedge. For grid resolution study, three progressively refined grids have been generated namely: G1, G2 and G3 each are having 114147 cells with size of the first grid point from the triangular body of $0.004d$, $0.0015d$ and $0.001d$ units respectively.

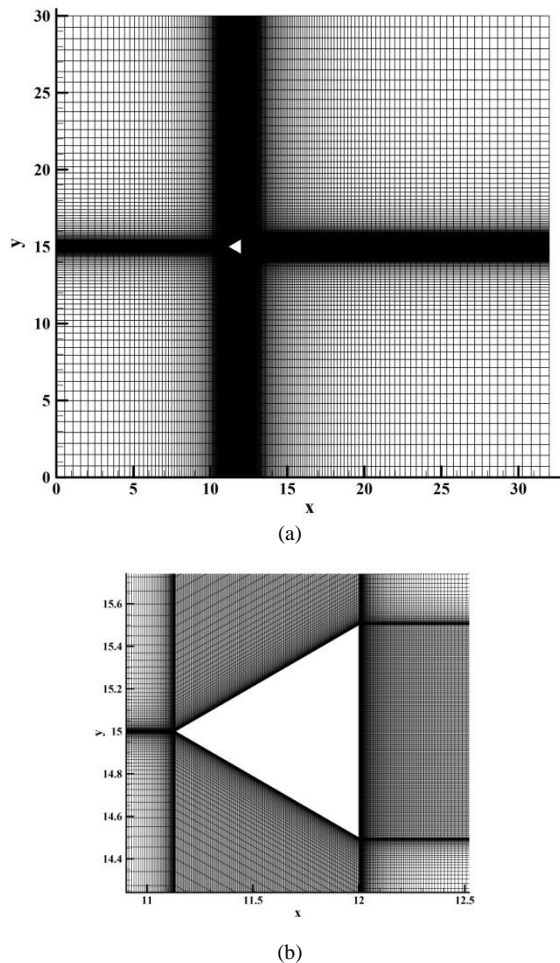


Figure 2. Grid structure: (a) Full view, (b) Zoomed view

In the present work, ANSYS FLUENT code based on finite volume method has been employed to carry out all numerical simulations. The magnetic induction method in MHD module built in ANSYS FLUENT has been used to simulate MHD flows. The SIMPLE (Semi-implicit Method for Pressure Linked Equations) algorithm is used for coupling between continuity and momentum equations. The second-order implicit scheme has been utilized for temporal discretization. For spatial discretization, the second-order upwind scheme has been used for convective terms while the central difference scheme has been employed for diffusive terms. A convergence criterion of 10^{-6} has been set.

The boundary conditions associated with the physical problem shown in Figure 1 are explained as follows:

1. *At the inlet plane:* A uniform fluid flow in free-stream condition is considered, that is, $u = 1$, $v = 0$. *Velocity inlet* condition has been assigned at the inlet boundary.
2. *On the top and bottom walls:* Since the present study considers an unconfined flow across the wedge, a *free slip* condition has been applied on the top and bottom boundaries of the flow domain.

3. *On the surface of wedge:* *No-slip* condition has been applied on the solid surface of the wedge, that is, $u = 0$, $v = 0$.
4. *At the exit plane:* *Pressure outlet* condition has been applied at the exit boundary.

2.4. Grid resolution study

For grid resolution study, simulations have been performed at $Re = 150$ with a time step size, $\Delta t = 0.01$ s using the three progressively refined grids namely: G1, G2 and G3. The results of grid resolution study are shown in Table 2. Table 2 shows the variation in the values of the drag coefficient (C_d) and the Strouhal number (St) for the aforementioned grids. It is observed that the percentage differences in the values of the mean drag coefficient and the Strouhal number between G1 and G3 grids are found to be 0.27% and 5.21% respectively. Similarly, for G2 and G3 grids, the percentage difference in the value of the mean drag coefficient has been found to be 0.05%, but no further changes in the Strouhal number has been observed. Hence, G2 grid with $\lambda = 114147$ cells and $\Delta = 0.0015d$ has been selected for the rest of the simulations.

Table 2. Grid resolution study at $Re = 150$

Grid	λ	Δ	C_d	St
G1	114147	$0.004d$	1.9188	0.211
G2	114147	$0.0015d$	1.9231	0.2
G3	114147	$0.001d$	1.9240	0.2

3. Results and Discussion

3.1. Non-MHD flows ($Ha = 0$)

3.1.1. Validation

A comparative analysis of the present numerical results of the drag coefficient and the Strouhal number against the published results of [1] and [2] has been done at $Re = 10-150$. An excellent agreement between the present results and the published literature of time-averaged drag coefficient at $Re = 50, 100$ and 150 has been obtained as shown in Figure 3. It is seen that the average difference between the present results and the published literature of time-averaged drag coefficient at $Re = 50, 100$ and 150 is 1.23%. Figure 4 shows the comparison of the present results of Strouhal number at $Re = 50, 100$ and 150 against the published literature. An excellent agreement between the present results and the published results of Strouhal number has been obtained. It is seen that the average difference between the present results and the published data of the Strouhal number is 2.32%.

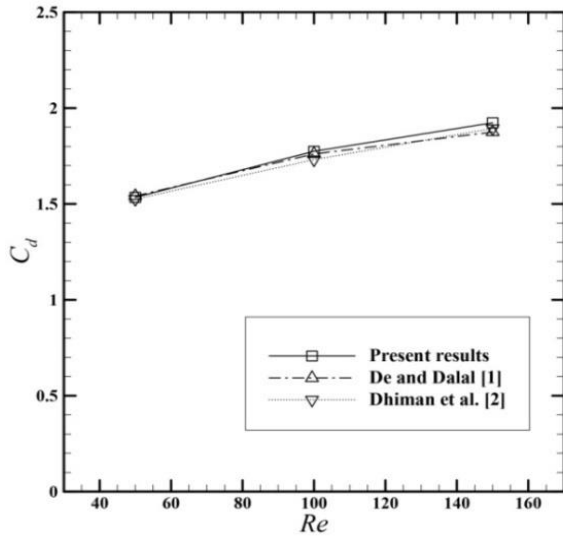


Figure 3. Validation of time-averaged C_d at $Re = 150$ ($Ha = 0$)

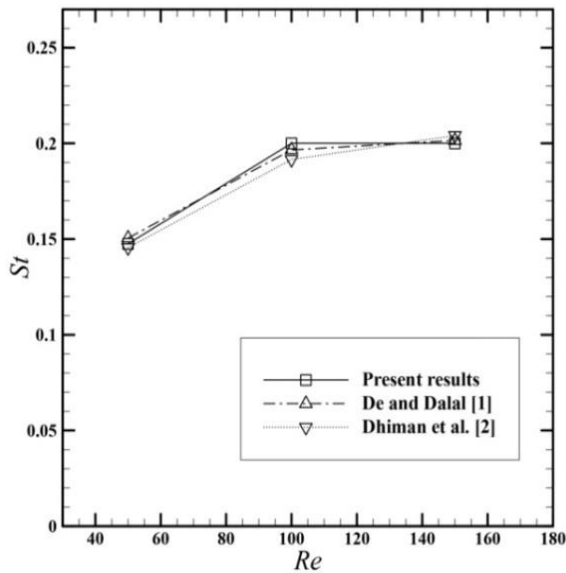


Figure 4. Validation of St at $Re = 150$ ($Ha = 0$)

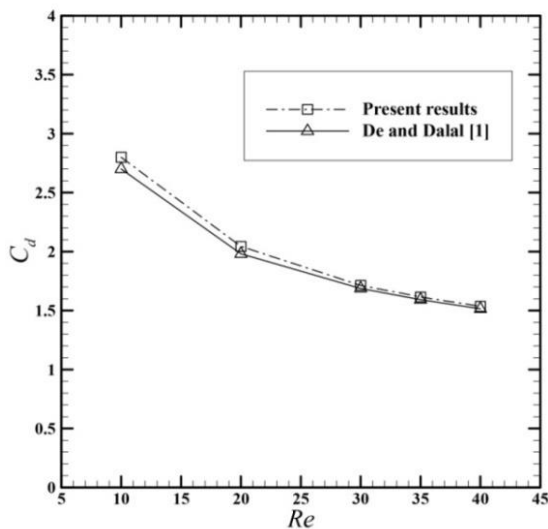


Figure 5. Validation of C_d at $Re = 10-40$ ($Ha = 0$)

Also, the drag coefficient for $Re = 10 - 40$ has been computed and compared with the data reported by the literature. An excellent agreement has been obtained between the present results and the published results of drag coefficient as shown in Figure 5. It is observed that the average difference between the present results and that of published literature of drag coefficient is 2.24%. Hence, non-MHD tests validate the present numerical solutions.

3.1.2. Flow structures

The flow around the wedge in the absence of magnetic field has been studied. The streamlines and vorticity contours for $Re = 1, 10, 30$ and 100 around the wedge in the absence of magnetic field are depicted in Figures 6 and 7. At low Reynolds number i.e. $Re = 1$, the fluid particles attaches to the surface of the wedge due to dominant viscous forces compared to the inertial forces and a creeping motion of the fluid with no flow separation is observed as shown in Figure 6 (a). For $Re = 10$ and 30 , the flow separates due to adverse pressure gradient, forming a closed steady recirculation zone behind the wedge consisting of symmetric twin vortices, also known as 'recirculation bubbles' as shown in Figures 6 (a). At $Re = 100$, the vortex shedding phenomenon begins to take place and vortices shed from the upper and the lower regions of the wedge as shown in Figure 7 (b).

3.2. MHD flows

3.2.1. Flow structures

The influence of magnetic field on the flow around the wedge at $Re = 30$ and 100 and $Ha = 0 - 10$ has been investigated. The magnetic field applied in a transverse direction produces a resistive force known as Lorentz force in the upstream direction which can alter the wake structure. Figure 8 shows the streamlines at $Re = 30$ in the presence of magnetic field. At $Ha = 0$ (i.e. without magnetic field), the flow at $Re = 30$ can be considered as purely hydrodynamic, characterized by the presence of closed steady symmetric recirculating bubbles formed behind the wedge as shown in Figure 8 (a). It is observed that the size of the recirculation bubbles decreases with the increase in Hartmann number as depicted in Figures 8 (a-c). As the Hartmann number is further increased, the recirculation bubbles disappear and a creeping flow structure with no flow separation is observed as shown in Figure 8 (d). Figures 9 and 10 show the streamlines and vorticity contours at $Re = 100$ under different strengths of magnetic field ($Ha = 0 - 10$). At $Ha = 0$, the flow is unsteady with the presence of alternate shedding of vortices from the upper and the lower regions of the wedge. At $Ha < 7.3$, the flow remains in the unsteady state evidenced by the presence of alternate shedding of vortices as shown in Figures 9 (a-c) and Figures 10 (a-c). However, at $Ha = 7.3$, the shedding of vortices is completely eliminated and the flow transitions to steady state forming a wake consisting of closed symmetric recirculation bubbles as shown in Figure 9 (d). As the Hartmann number is further increased, the size of the recirculation bubbles decreases due to dampening effect caused by the Lorentz force as shown in Figures 9 (d-e).

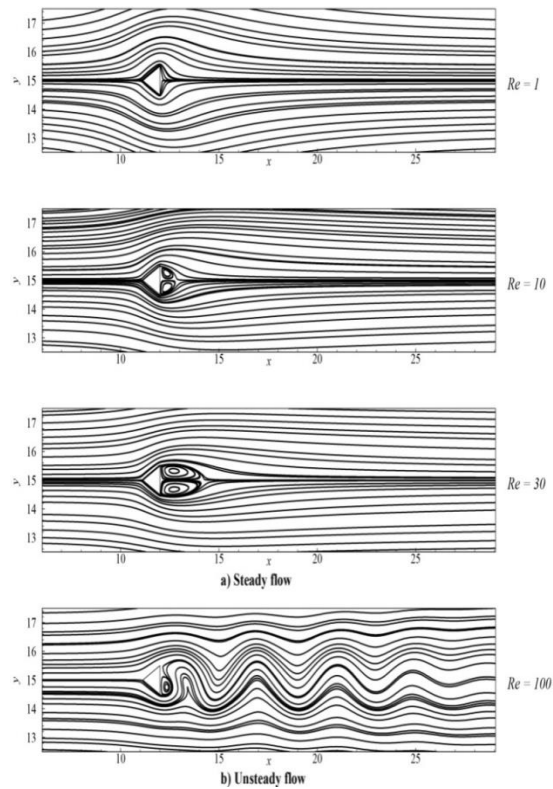


Figure 6. Streamlines: (a) Steady flow ($Re = 1, 10, 30$), (b) Unsteady flow ($Re = 100, t = 220$ s)

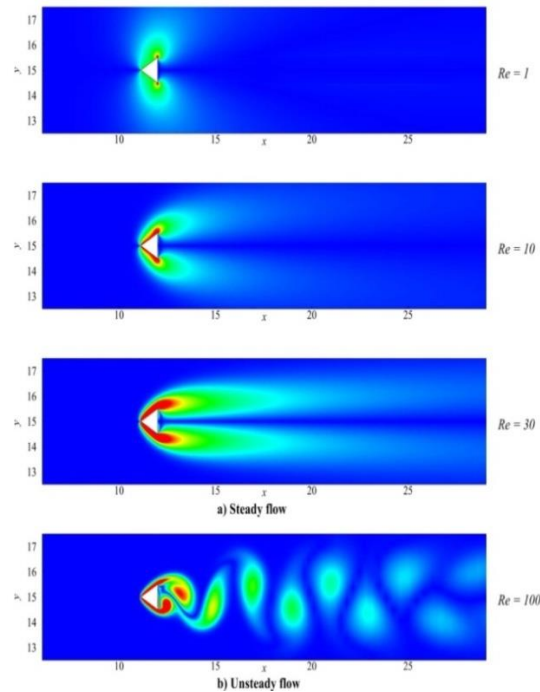


Figure 7. Vorticity contours: (a) Steady flow ($Re = 1, 10, 30$), (b) Unsteady flow ($Re = 100, t = 220$ s)

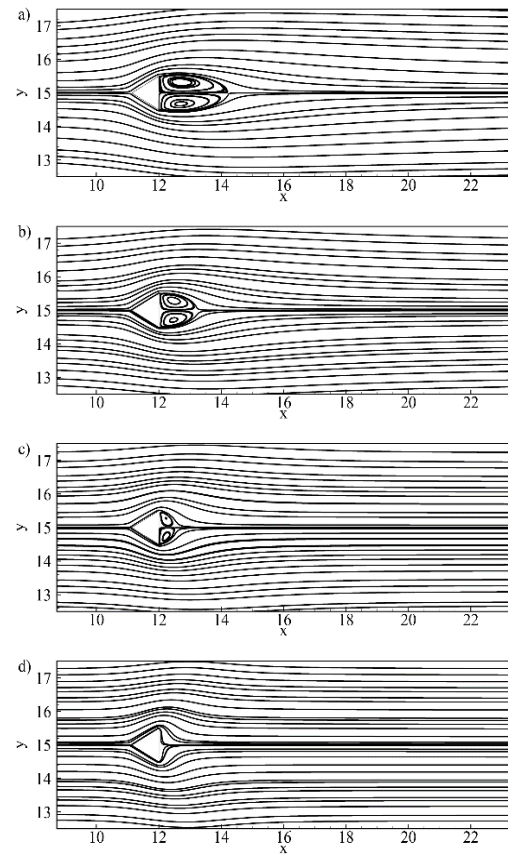


Figure 8. Streamlines for $Re = 30$: (a) $Ha = 0$, (b) $Ha = 2$, (c) $Ha = 5$, (d) $Ha = 10$

3.2.2. Influence on drag and lift coefficients

Figures 11 (a–e) show the temporal variation of the drag coefficient at $Re = 100$ for various Hartmann numbers. The drag coefficient is found to decrease up to certain Hartmann numbers as long as the flow remains in unsteady flow regime as shown in Figures 11 (a-c).

Such drop in drag coefficient may be attributed to the decrease in forces due to shear stress with the increase in Hartmann number within the unsteady flow regime. However, once the flow assumes the steady state at $Ha = 7.3$, the drag coefficient has a tendency to increase with a further increase in Hartmann number (i.e. $Ha = 10$). The possible explanation is that with further increase in Hartmann number, the velocity field is significantly suppressed, causing the boundary layer thickness to increase and hence the drag. The temporal variation of the lift coefficient for $Re = 100$ at different Hartmann numbers is shown in Figures 12 (a-e). As the Hartmann number is increased, the amplitude of lift coefficient is decreased, implying the reduction in strength of shed vortices as shown in Figures 12 (a-c). With further increase in Hartmann number, the lift coefficient is zero indicating that the flow has attained steady state as shown in Figures 12 (d-e).

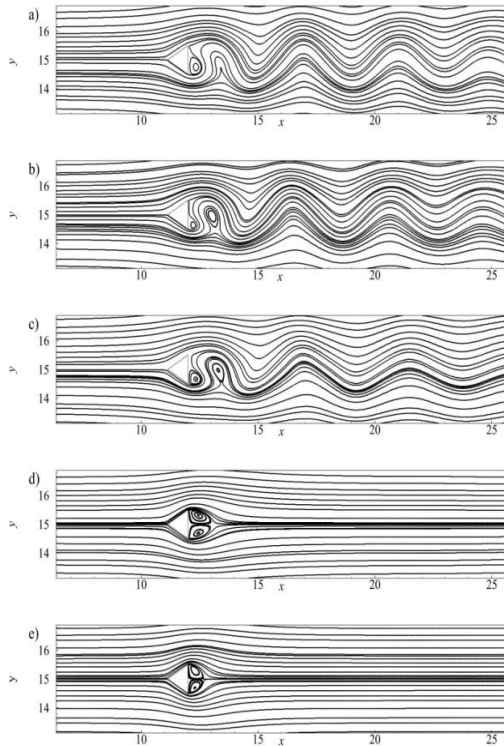


Figure 9. Instantaneous streamlines at $Re = 100$: (a) $Ha = 0$, $t = 220$ s, (b) $Ha = 2$, $t = 203$ s (c) $Ha = 5$, $t = 217$ s (d) $Ha = 7.3$, (e) $Ha = 10$

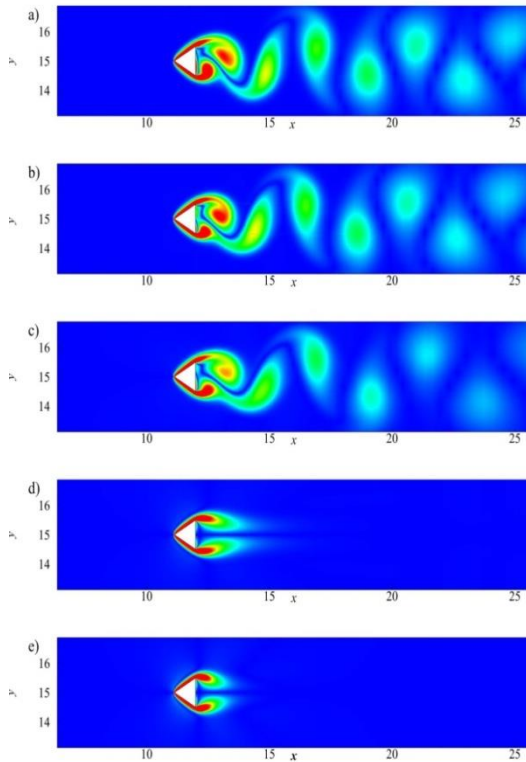


Figure 10. Instantaneous vorticity contours at $Re = 100$: (a) $Ha = 0$, $t = 220$ s, (b) $Ha = 2$, $t = 203$ s (c) $Ha = 5$, $t = 217$ s (d) $Ha = 7.3$, (e) $Ha = 10$

3.2.3. Critical Hartmann number

Critical Hartmann number refers to the minimum value of magnetic field at which the vortex shedding is completely

suppressed and a steady and symmetric flow is established. Such value is dependent on several factors such as shape of obstacle, blockage ratio, Reynolds number, etc. The present result of the critical Hartmann number for the wedge has been compared with the published data of circular and square cylinders.

Table 3. Published results of critical Hartmann number for different bluff bodies

Re	Square cylinder (Singha et al. [7])	Circular cylinder (Singha et al. [8])	Square cylinder (Farjallah et al. [9])
100	-	-	1.272
150	2.0-2.5	2.0-2.5	-
200	3.5-4.0	4.0-4.5	-
250	4.5-5.0	5.0-5.5	-

The values of critical Hartmann number at $Re = 100 - 250$ for confined square and circular cylinders with their blockage ratios (β) = 1/4 is provided in Table 3. It can be observed that with the rise in Reynolds number, the critical Hartmann number increases for both square and circular cylinders at a fixed blockage ratio. This can be explained by the fact that the inertial forces increase with the increment in Reynolds number, requiring higher strengths of magnetic field. In the present work, the flow over the wedge in an unconfined condition is considered. Under such condition, at $Re = 100$, the value of the critical Hartmann number has been found to be 7.3. A comparison of the present results of the critical Hartmann number has been made against the published results of Farjallah et al. [9]. In his work, he developed a theoretical correlation, $Ha_{cr} = 0.0239Re - 1.118$ for a confined square cylinder which characterizes the relationship between critical

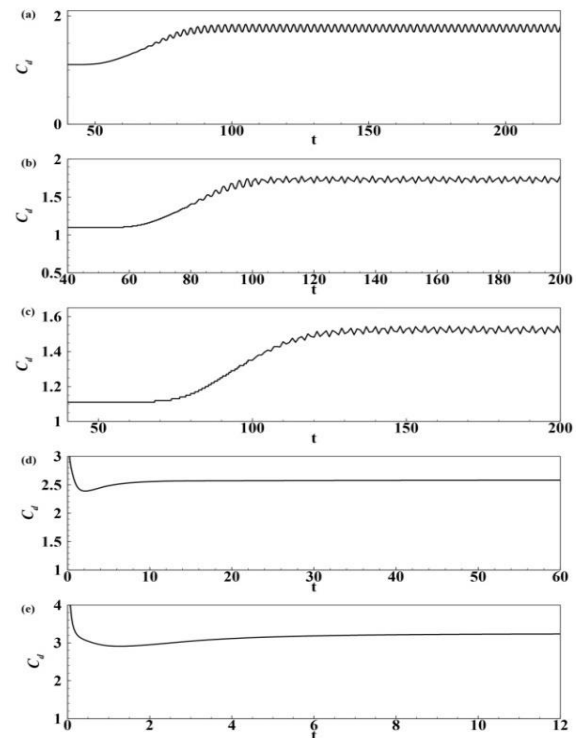


Figure 11. Temporal variation of drag coefficient at $Re = 100$: (a) $Ha = 0$, (b) $Ha = 2.0$, (c) $Ha = 5.0$, (d) $Ha = 7.3$, (e) $Ha = 10$

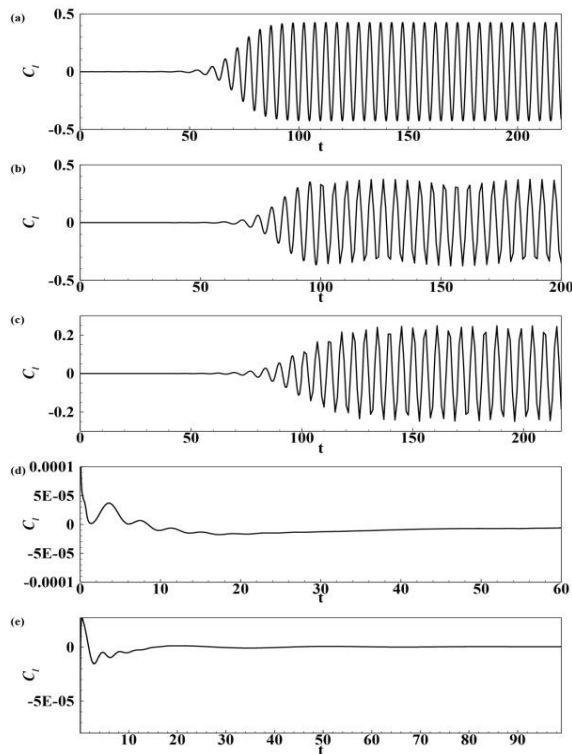


Figure 12. Temporal variation of lift coefficient at $Re = 100$: (a) $Ha = 0$, (b) $Ha = 2.0$, (c) $Ha = 5.0$, (d) $Ha = 7.3$, (e) $Ha = 10$

Hartmann number and Reynolds number. In comparison to the value of $Ha_{cr} = 1.272$, it can be observed that the value of Ha_{cr} for the wedge is much larger. This may be attributed to the fact that the wedge consists of sharply defined corners, leading to intense flow instabilities and thus, requires stronger magnetic field [13]. In addition, it is noteworthy that at high blockage ratios, the wall boundary layer has a stabilizing effect on the flow in such a way that it can inhibit vortex shedding around bluff bodies [19]. But in our case, the presence of walls at a larger distance has no influence on regular formation of vortex shedding past the wedge and thus, contributes to more magnetic field requirements.

4. Conclusions

In this paper, a laminar incompressible viscous flow of an electrically conducting fluid past a wedge in an unconfined medium in the presence of transverse magnetic field has been studied. The magnetic induction method in MHD module built in ANSYS FLUENT has been considered to carry out all MHD simulations. The conclusions drawn from this study are enumerated below:

1. If the magnetic field is strong enough, the complete elimination of vortex shedding is achievable.
2. A critical Hartmann number, $Ha_{cr} = 7.3$ has been found at $Re = 100$, at which complete elimination of vortex shedding is observed.
3. In the steady flow regime, the length of the recirculation zone reduces with the increment in Ha .
4. A minimal reduction in the drag coefficient has been observed for unsteady flow regime (i.e. $Ha < 7.3$). However, once the flow attains steady state at $Ha = 7.3$,

it starts to significantly increase with a further increase in Ha (i.e. $Ha = 10$).

5. The reduction in lift amplitude is observed with the increment in Ha , indicating a diminishing effect in the strength of shed vortices.

5. Acknowledgements

All the computer simulations were carried out in the Computer-Aided Engineering Laboratory, Department of Mechanical and Aerospace Engineering, Pulchowk Campus. The authors extend their heartfelt gratitude to the department for their continuous support by providing access to computational facilities.

Nomenclature

b	induced magnetic field	T
B	non-dimensional total magnetic field	
B	total magnetic field	T
B_0	external magnetic field	T
C_d	drag coefficient	
C_l	lift coefficient	
E	electric field	Vm^{-1}
H	magnetic field strength	Am^{-1}
D	electric displacement field	Cm^{-2}
q	charge density	Cm^{-3}
Ha	Hartmann number	
Ha_{cr}	critical Hartmann number	
Pr	Prandtl number	
J	current density	Am^{-2}
J	non-dimensional current density	
N	Stuart number	
Re	Reynolds number	
Re_m	magnetic Reynolds number	
St	Strouhal number	
τ	non-dimensional time	
t	dimensional time	s
u	dimensional velocity field	ms^{-1}
U_∞	freestream velocity	ms^{-1}
u	non-dimensional x-velocity	
V	non-dimensional velocity field	
v	non-dimensional y-velocity	
W	height of the domain	m
X	total length of the domain	m
X_u	upstream length of the domain	m
X_d	downstream length of the domain	m
D	diameter of cylinder	m
S	spacing between centres of cylinder	m
q	charge density	
x	stream-wise co-ordinate	m
y	transverse co-ordinate	m
Δt	time-step size	s

Greek symbols

β	blockage ratio	
Δ	first cell height	m
λ	total number of cells	
μ_0	magnetic permeability	Hm^{-1}
η	kinematic viscosity	m^2s^{-1}
ρ	density	kgm^{-3}
σ	electrical conductivity	Sm^{-1}

References

- [1] A.K. De, A. Dalal, "Numerical simulation of unconfined flow past a triangular cylinder". *International Journal for Numerical Methods in Fluids*, Vol. 52, No. 7, 2006, 801-821.
- [2] A. Dhiman, R. Shyam, "Unsteady heat transfer from an equilateral triangular cylinder in the unconfined flow regime". *ISRN Mechanical Engineering*, Vol. 2011, Feb., 2011, 1-13.
- [3] B.N. Rajani, A. Kandasamy, S. Majumdar, "Numerical simulation of laminar flow past a circular cylinder". *Applied Mathematical Modelling*, Vol. 33, No. 3, 2009, 1228-1247.
- [4] P. Catalano, M. Wang, G. Iaccarino, P. Moin, "Numerical simulation of the flow around a circular cylinder at high Reynolds numbers". *International Journal of Heat and Fluid Flow*, Vol. 24, No. 4, 2009, 463-469.
- [5] S. Rashidi, M. Hayatdavoodi, J.A. Esfahani, "Vortex shedding suppression and wake control: A review". *Ocean Engineering*, Vol. 126, Aug., 2016, 57-80.
- [6] Davidson PA. *An Introduction to Magnetohydrodynamics*. 1st ed. Cambridge, United Kingdom: Cambridge University Press; 2001.
- [7] O.M. Oyewola, O.S. Ismail, K. Abu, "Numerical simulation of forced convection flows over a pair of circular cylinders in tandem arrangement". *Jordan Journal of Mechanical and Industrial Engineering*, Vol. 13, No. 4, 2019, 221-230.
- [8] R. Bouakkaz, Y. Khelili, F. Salhi, "Unconfined laminar nanofluid flow and heat transfer around a square cylinder with an angle of incidence". *Jordan Journal of Mechanical and Industrial Engineering*, Vol. 13, No. 3, 2019, 191-196.
- [9] Z. Hafsia, S. Nouri, "The effect of grooves and permeable plates on the control of vortex shedding behind a single circular cylinder". *Journal of Advanced Research in Fluid Mechanics and Thermal Sciences*, Vol. 66, No. 2, 2020, 32-48.
- [10] S. Singha, K.P. Sinhamahapatra, S.K. Mukherjee, "Control of vortex shedding from a bluff body using imposed magnetic field". *Journal of Fluids Engineering*, Vol. 129, No. 5, 2007, 517-523.
- [11] S. Singha, K.P. Sinhamahapatra, "Control of vortex shedding from a circular cylinder using imposed transverse magnetic field". *International Journal of Numerical Methods for Heat and Fluid Flow*, Vol. 21, No. 1, 2011, 32-45.
- [12] H. Farjallah, H. Abbassi, S. Turki, "Vortex shedding of electrically conducting fluid flow behind square cylinder under magnetic field". *Engineering Applications of Computational Fluid Mechanics*, Vol. 5, No. 3, 2011, 349-356.
- [13] D. Chatterjee, K. Chatterjee, B. Mondal, "Control of flow separation around bluff obstacles by transverse magnetic field". *Journal of Fluids Engineering*, Vol. 134, No. 9, 2012, 1-11.
- [14] D. Chatterjee, K. Chatterjee, "Wall-bounded flow and heat transfer around a circular cylinder at low Reynolds and Hartmann numbers". *Heat Transfer-Asian Research*, Vol. 42, No. 2, 2013, 133-150.
- [15] J.A. Esfahani, "Control of wake and vortex shedding behind solid circular obstacle by magnetohydrodynamics". *Journal of Thermal Engineering*, Vol. 1, No. 7, 2015, 593-597.
- [16] S. Rashidi, M. Bovand, J.A. Esfahani, H.F. Oztop, R. Masoodi, "Control of wake structure behind a square cylinder by magnetohydrodynamics". *Journal of Fluids Engineering*, Vol. 137, No. 6, 2015, 1-8.
- [17] W.K. Hussam, A.H.A. Hamid, Z.Y. Ng, G.J. Sheard, "Effect of vortex promoter shape on heat transfer in MHD duct flow with axial magnetic field". *International Journal of Thermal Sciences*, Vol. 134, Dec., 2018, 453-464.
- [18] Shercliff JA. *A Textbook of Magnetohydrodynamics*. New York: Pergamon Press; 1965.
- [19] D.A. Perumal, G.V.S. Kumar, A.K. Dass, "Numerical simulation of viscous flow over a square cylinder using lattice Boltzmann method". *ISRN Mathematical Physics*, Vol. 2012, 1-16.

Numerical Study of Fluid Dynamics and Heat Transfer Characteristics for the Flow Past a Heated Square Cylinder

Rashid Ali^{*,a}, Anshumaan Singh^b

^aAssociate Professor, Dept. of Mechanical Engg., Zakir Husain College of Engg. & Tech., Aligarh Muslim University, Aligarh Pin 202002, INDIA,

^bResearch Scholar, Dept. of Mechanical Engg., Zakir Husain College of Engg. & Tech., Aligarh Muslim University, Aligarh Pin 202002, INDIA

Received November 5 2020

Accepted September 17 2021

Abstract

Effects of inertia and buoyancy forces are numerically investigated on fluid dynamics and heat transfer characteristics for the flow past a heated square cylinder in an unconfined flow regime. Non-dimensional number in the study chosen are $Re = 1 - 45$, $Ri = 0 - 1.50$, $\alpha = 0^\circ - 90^\circ$. The orientation of the cylinder and the Prandtl number are kept fixed as $\phi = 0^\circ$ and $Pr = 100$. Numerical experiments in generalized body-fitted coordinates subject to Boussinesq approximation were conducted in the form of solution of continuity, momentum and energy equations. The momentum and energy equations are discretized using finite difference method. The equations are solved by using SMAC type implicit pressure correction scheme. The flow is noticed steady for $1 \leq Re \leq 30$ and $0 \leq Ri \leq 0.50$ at $\alpha = 0^\circ$, $1 \leq Re \leq 20$ and $0 \leq Ri \leq 0.50$ at $\alpha = 45^\circ$, $1 \leq Re \leq 10$ and $1.0 \leq Ri \leq 1.50$ at $\alpha = 90^\circ$. Onset of vortex-shedding is observed initially at $Re = 30$, $\alpha = 45^\circ$, $0 \leq Ri \leq 0.50$, the flow becomes unsteady and periodic flow. At small magnitudes of Reynolds number, the wake on downstream side of cylinder is found thin, and it becomes wider at large magnitudes of Reynolds number. It is noticed that the width of the wake reduces in size with increasing Richardson number. Maximum mean lift coefficient is found to occur at $Re = 20$, $Ri = 1.5$ and $\alpha = 90^\circ$, and maximum mean drag coefficient is noted at $Re = 1$ for the chosen range of Richardson number and free-stream orientations. For the whole range of Reynolds and Richardson numbers, the front face(s) of the cylinder had more crowding of isotherms in comparison with other faces of the cylinder. The front face(s) of the cylinder have high rate of heat transfer as compared to other cylinder faces. Heat transfer rate from the cylinder is enhanced either with increase in Richardson number or Reynolds number.

© 2021 Jordan Journal of Mechanical and Industrial Engineering. All rights reserved

Keywords: Mixed convection, streamline and isotherms patterns, contours of vorticity, Nusselt number, rate of heat transfer.;

1. Introduction

The geometry of the cylindrical cross-section chosen in the present study is shown in Fig. 1, which affects the flow dynamics, wake properties and heat transfer characteristics significantly. In the past few decades, the fluid flow past bluff bodies of various cross-sections have been extensively examined, especially the cylindrical objects. Active and passive control methods are basically employed to control the vortex-shedding from bluff bodies. For a cylindrical object of square cross-section, the free-stream orientation is an important parameter, which affects the dynamics of flow considerably. In the present study, the mixed convective flow is considered as it is closer to real engineering applications such as tall buildings, chimneys, bridges, vortex generators etc. Electronic components, heat exchangers, extended surfaces, cooling towers are also important from the point of view of heat transfer. The present problem is closer to the engineering problems such as cooling of immersed assembly of core and windings in the oil in case of large electric transformers. Shell and tube oil cooler that is used for cooling of hydraulic power packs and hydraulic equipment like hydraulic systems on excavators and earthmoving equipment. Cooling of various electric and hybrid power train components in electric

vehicles etc. In the present study, the effects of $Re = 1, 5, 10, 20, 30, 40, 45$ and $Ri = 0, 0.25, 0.50, 1.0, 1.25, 1.50$ on fluid dynamics and characteristics of heat transfer are analyzed at a fixed Prandtl number $Pr = 100$ and cylinder orientation $\phi = 0^\circ$ with the range of orientations of the free-stream $0^\circ \leq \alpha \leq 90^\circ$. The CPU time required for computations in this study is 9072 hours.

The two-dimensional flow dynamics across an elevated square cylinder is considered in mixed convection by accounting Oberbeck-Boussinesq model. Variation of fluid properties in Oberbeck-Boussinesq model such as viscosity, specific heat, thermal diffusivity with temperature are ignored completely. The five dimensionless parameters that described the flow dynamics are as follows: the bluff-body orientation with respect to the x-axis = ϕ , Free-stream orientation with respect to gravity = α , Prandtl number (Pr)

$$= \frac{\nu_o}{\kappa_o}, \text{ Richardson number (Ri)} = \frac{g\beta(T_s - T_\infty)d}{U_\infty^2} \text{ and}$$

$$\text{Reynolds number (Re)} = \frac{U_\infty d}{\nu_o}. \text{ Where } \nu_o = \text{kinematic}$$

viscosity, κ_o = thermal diffusivity at a certain reference temperature (T_∞), T_s = uniform surface temperature of the bluff-body, T_∞ = fluid temperature of the free-stream, d =

* Corresponding author e-mail: rashidali1@zhcet.ac.in.

characteristic length scale of the body, β = co-efficient of volume expansion and g = gravitational intensity of the fluid.

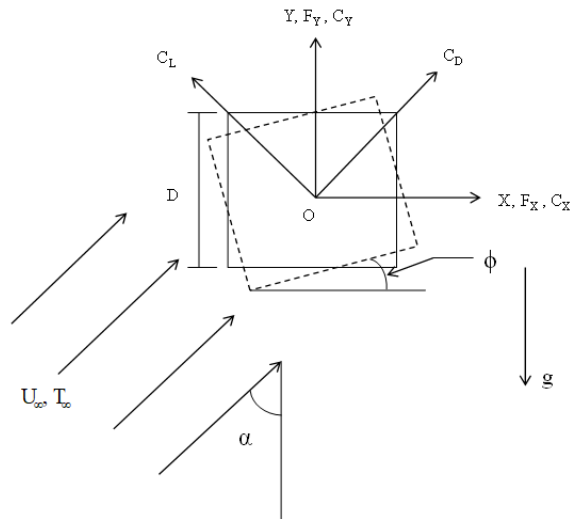


Figure 1. Geometry of the proposed problem with and without cylinder orientation (ϕ).

Sohankar et al. [1] investigated numerically 2-D, incompressible, unsteady air flow across a square cylinder for the conditions $45 \leq Re \leq 200$, $0 \leq \phi \leq 45^\circ$, $\alpha = 90^\circ$, $2.5\% \leq BR \leq 5\%$ (BR = blockage ratio). They compared the boundary conditions and showed that the Neumann boundary condition was less effective than the convective Sommerfield boundary condition in reducing the CPU time and upstream influence from the outlet of the computational domain. Sharma and Eswaran [2] studied numerically for parameters $Re = 100$, $-1 \leq Ri \leq 1$, $\alpha = 0^\circ$, $\phi = 0^\circ$, and $Pr = 0.7$, the heat transfer characteristics of two-dimensional flow across a cylinder of square cross section, the temperature of the cylinder is maintained constant. In energy equation, the viscous dissipation term is ignored completely and considered the effects of opposing and aiding buoyancy. They found that the shedding of vortices are completely suppressed at a critical Richardson number, $Ri = 0.15$. Sharma and Eswaran [3] numerically investigated the two-dimensional upward flow ($\alpha = 0^\circ$) by taking into account the opposing and aiding buoyancy, heat transfer characteristics across a cooled or heated square cylinder and the channel-confinement effect of different BR ($BR = 10\%$, 30% , and 50%) for $-1 \leq Ri \leq 1$, $Pr = 0.7$, $Re = 100$, $\alpha = 0^\circ$ and $\phi = 0^\circ$. They noticed that the least heating required for vortex-shedding suppression decreases with increasing blockage ratio up to a certain value of BR ($BR = 30\%$), and increases thereafter. Chatterjee and Mondal [4] investigated numerically the buoyancy (aiding/opposing) effects on the 2-D upward flow and heat transfer across a cooled or heated cylinder of square cross-section within the Boussinesq approximation at $BR = 2\%$, $50 \leq Re \leq 150$, $-1 \leq Ri \leq 1$, $Pr = 0.7$ and $\alpha = 0^\circ$. They observed that with increased heating there is an increment in Strouhal number and instantly falls to zero at some Richardson number (critical). They also noticed that with the increase in blockage ratio, the critical Richardson number was decreased.

Dhiman et al. [5] considered the upward, steady, confined flow in the vertical channel and investigate the characteristics of heat transfer for the flow around a square cylinder within the Boussinesq approximation, under aiding buoyancy at $1 \leq Re \leq 40$, $0 \leq Ri \leq 1$, $Pr = 0.7$ and $25\% \leq BR \leq 50\%$. They reported that the onset of flow separation

occurs at $2 \leq Re \leq 3$, $25\% \leq BR \leq 30\%$ and at $3 \leq Re \leq 4$, $BR = 50\%$, irrespective of the value of Richardson number. Also, with increase in Re and Ri , the surface mean Nusselt number was increased. Yang and Wu [6], numerically studied the effects of opposing/aiding buoyancy and side ratio on 2-D flow and characteristics of heat transfer past a rectangular cylinder (cooled/heated) by adopting the Boussinesq approximation at $0.5 \leq SR \leq 2$ (SR = side ratio), $\alpha = 0^\circ$, $-1 \leq Ri \leq 1$, $Pr = 0.7$ and $Re = 100$. They noticed the Karman vortex-street for the flow conditions. They also noticed the complete suppression of vortex-shedding at $Ri = 0.15$ and $SR = 1$. Moulai et al. [7] numerically investigated the mixed convective flow past a heated square cylinder under aiding buoyancy effect and heat transfer in air ($Pr = 0.71$), in a confined channel for the parameters $20 \leq Re \leq 45$ and $1.61 \times 10^3 \leq Gr \leq 6.33 \times 10^3$ at a fixed blockage ratio of 0.1. In their study, the strong dependency of wake region is observed on Grashof and Reynolds numbers. On decreasing the Grashof number and increasing the Reynolds number the wake region of square cylinder increase in their size. Enhancement of heat transfer from the front face of square cylinder is seen with increase in Reynolds number, and enhancement of heat transfer from the side faces of square cylinder is seen with increasing the Grashof number.

Rashid and Hasan [8] investigated numerically the phenomenon of vortex shedding and its suppression at $Re = 100$, $Pr = 0.71$, Ri and angles chosen in the study are 0 to 1.6 and $0^\circ \leq \alpha \leq 90^\circ$. Rashid and Hasan [9] studied the influence of free-stream orientation and buoyancy on the flow structure and aerodynamic characteristics around a square cylinder for $Re = 100$, $Pr = 0.71$, $0^\circ \leq \alpha \leq 90^\circ$ and $1.2 \leq Ri \leq 1.6$. Rashid and Hasan [10] investigated numerically the effect of free-stream orientations and buoyancy together on flow structure and heat transfer in two-dimensional mixed convective flow past a square cylinder. The numerical experiments have been conducted at a fixed Reynolds number (Re) of 100 and Prandtl number (Pr) of 0.71. The Richardson number (Ri) ranges from 1.2 to 1.6, while free-stream orientation chosen in the range from 0° to 90° . Haider and Rashid [11] investigated numerically the effect of Prandtl number on the flow past a square cylinder in mixed convective flow regime at $0^\circ \leq \alpha \leq 90^\circ$, $0 \leq Ri \leq 1.6$, $Pr = 0.7$ and 7 , $Re = 100$ and $\phi = 0^\circ$. Anshumaan and Rashid [12] studied numerically the effect of buoyancy and inertia forces on the flow and heat transfer characteristics for the conditions $1 \leq Re \leq 10$, $0 \leq Ri \leq 0.75$, $Pr = 100$, $\alpha = 90^\circ$ and $\phi = 0^\circ$. Rashid and Hasan [13] numerical investigated the transformations / bifurcations from steady to unsteady or unsteady to steady flow states in 2-D mixed convection across a square cylinder (heated) in laminar flow regime. The parameters chosen in their study were $0^\circ \leq \alpha \leq 90^\circ$ and $0 \leq Ri \leq 1.6$ and $Pr = 0.71$. The magnitudes of Reynolds and Richardson numbers were varied to obtain the neutral curves in Ri - α plane.

Yuan et al. [14] investigate numerically the flow patterns and vortex-shedding around a square cylinder using a control circular bar on upstream and downstream. The Lattice Boltzmann method (LBM) was used to investigate the flow over a square cylinder. $Re = 100$ for square cylinder, 30 and 50 for different circular bars were chosen (based on the width of the square cylinder (D) and diameter of circular bar (d)). The L/D and G/D ratios chosen were 1-5 (where L and G are the center-to-center distances between the bar and cylinder). They found that the maximum percentage reduction in drag coefficient was 59.86% by upstream control bar, and the maximum percentage reduction in rms lift coefficient was 73.69% by downstream

control bar. Yuan et al. [15] numerically investigate the patterns of flow across a square cylinder with a circular bar upstream and a splitter plate downstream by Lattice Boltzmann method (LBM). The parameters chosen in their study were $Re = 100$ (based on side length of square cylinder (D)), $D_s/D = 1-5$, $G/D = 0-7$ and $L/D = 1-6$ (where D_s , G and L are the center-to center distance, surface-to-surface distance and the splitter plate length). They found that the maximum percentage reduction in mean drag coefficient was 68.76% at $(d_s, g, l) = (2.5, 0, 3)$ which was in pattern VI. The vortex-shedding from the square cylinder and the circular bar was completely suppressed in pattern VI. They also observed that the small distance between the square cylinder and the splitter plate plays a more vital role in suppression of vortex-shedding as compared with large distance and length. Rafik et al. [16] used the finite-volume method to investigate the laminar 2-D unsteady flow of nanofluids and heat transfer characteristics past a square cylinder inclined with respect to the main flow. The Reynolds number, nanoparticle volume fraction and inclination angle are chosen 100, 0-5% and $0^\circ-45^\circ$, respectively. Enhancement of heat transfer is reported in their study with nanoparticles addition. It is also reported that by increasing the nanoparticles concentration for a specific inclination angle the local Nusselt number increases.

The survey of the earlier studies suggested that none of the previous studies have been carried out to investigate the effects of buoyancy and free-stream orientations on fluid dynamics and heat transfer characteristics for the flow past a heated square cylinder for the ranges of parameters, Reynolds number, $1 \leq Re \leq 45$, Richardson number, $0 \leq Ri \leq 1.50$, Prandtl number, $Pr = 100$, cylinder orientation, $\phi = 0^\circ$ and orientation of free-stream, $\alpha = 0^\circ, 45^\circ$ and 90° . The focus of the present study is to elucidate the role of Reynolds and Richardson numbers, and free-stream orientations on time histories of lift and drag coefficients, streamline patterns, contours of vorticity, isotherm patterns, mean (time mean) lift and drag coefficients (C_L and C_D), time mean coefficient of moment (C_M), surface pressure and surface vorticity. In addition, the local Nusselt number (Nu_L) and mean (time mean) Nusselt number (Nu) are investigated in detail. The novelty of the present work is the solution of complex problem of bluff-body numerically with the consideration of range of Richardson number, Reynolds number and orientation of free-stream. In the knowledge of the author no study of flow past bluff-body is found till date with these range of parameters, specifically the free-stream orientations range.

2. . MATHEMATICAL FORMULATION

In the current study, the fluid flow is considered as unsteady, 2D, incompressible, laminar and viscous across an elevated square cylinder. The buoyancy impacts are considered by the Oberbeck-Boussinesq model approximation (Tritton[17]). The equations involving continuity, momentum and energy have been written in the following form;

Continuity Equation

$$\nabla \cdot \vec{V} = 0 \quad (1)$$

Momentum Equation

$$\frac{D\vec{V}}{Dt} = -\frac{1}{\rho_\infty} \nabla P + \nu_\infty \nabla^2 \vec{V} - \vec{g}\beta(T - T_\infty) \quad (2)$$

Energy Equation

$$\frac{\partial T}{\partial t} + \vec{V} \cdot \nabla T = \kappa_\infty \nabla^2 T \quad (3)$$

In the above equations (1)-(3), T , P and \vec{V} are the temperature, pressure and the vector of local fluid speed. The density, thermal diffusivity as well as the kinematic viscosity at free-stream reference temperature (T_∞) are ρ_∞ , κ_∞ and ν_∞ , respectively. Figure 1 shows the proposed problem geometry considered in the present study. In figure 1, forces/span are F_x in x direction and F_y in x and y direction, C_L and C_D are the lifting and dragging coefficients, respectively with reference to orientation of free-stream. U_∞ is the free-stream velocity, ϕ is the cylinder orientation, d is the edge of square cylinder and g is the gravitational intensity.

The initial condition in the flow region are selected to be the free-stream variables written as,

$$P = P_\infty, \quad T = T_\infty, \quad \vec{V} = U_\infty (\sin \alpha \hat{i} + \cos \alpha \hat{j}) \quad (4)$$

The unit vectors in the x and y directions are \hat{i} and \hat{j} in the above relation.

Condition of no-penetration & no-slip are used as boundary conditions for the component of velocity on the square cylinder surface, the square cylinder surface is maintained at higher constant temperature T_s

$$\vec{V} = 0, \quad T = T_s \quad (5)$$

Normal momentum condition at the cylinder surface is used for pressure. At large distances from the cylinder, the uninterrupted free-stream conditions are used.

Mathematical equations of mass, momentum and energy are transformed into dimensionless form, with the time scales; velocity and length chosen are,

i) Time scale $\equiv 'd / U_\infty'$ = residence time spend by fluid particles in the neighborhood of the cylinder.

Non-dimensional time and velocities are written as,

$$\tau = tU_\infty/d, \quad u = U/U_\infty \quad \text{and} \quad v = V/U_\infty \quad (6)$$

ii) Velocity scale $\equiv 'U_\infty'$ = magnitude of the velocity of free-stream.

iii) Length scale $\equiv 'd'$ = side of square cylinder.

Fluid temperature change scale is $(T_s - T_\infty)$ & change in pressure scale is $\rho_\infty U_\infty^2$, and the non-dimensional pressure and temperature are written as,

$$\bar{p} = \frac{P - P_\infty}{\rho_\infty U_\infty^2}, \quad \theta = \frac{T - T_\infty}{T_s - T_\infty} \quad (7)$$

Mass, momentum and energy equations in dimensionless form with Oberbeck-Boussinesq approximation in Cartesian coordinates, modified into generalized body-fitted coordinates (Thompson et al. [18]) are written as,

Continuity:

$$\left(\xi_x \frac{\partial}{\partial \xi} + \eta_x \frac{\partial}{\partial \eta} \right) u + \left(\xi_y \frac{\partial}{\partial \xi} + \eta_y \frac{\partial}{\partial \eta} \right) v = 0, \quad (8)$$

x – Momentum:

$$\frac{\partial u}{\partial \tau} + U^\xi \frac{\partial u}{\partial \xi} + U^\eta \frac{\partial u}{\partial \eta} = - \left(\xi_x \frac{\partial \bar{p}}{\partial \xi} + \eta_x \frac{\partial \bar{p}}{\partial \eta} \right) + \frac{1}{\text{Re}} \tilde{\nabla}^2 u, \quad (9)$$

y – Momentum:

$$\frac{\partial v}{\partial \tau} + U^\xi \frac{\partial v}{\partial \xi} + U^\eta \frac{\partial v}{\partial \eta} = +\text{Ri}\theta - \left(\xi_y \frac{\partial \bar{p}}{\partial \xi} + \eta_y \frac{\partial \bar{p}}{\partial \eta} \right) + \frac{1}{\text{Re}} \tilde{\nabla}^2 v, \quad (10)$$

Energy Equation:

$$\frac{\partial \theta}{\partial \tau} + U^\xi \frac{\partial \theta}{\partial \xi} + U^\eta \frac{\partial \theta}{\partial \eta} = \frac{1}{(\text{Re} \cdot \text{Pr})} \tilde{\nabla}^2 \theta. \quad (11)$$

The corresponding non-dimensional Cartesian velocity components in the above equations are u and v . Dimensionless components of velocity are referred to as

U^ξ and U^η in ξ and η directions. The body-fitted velocity coordinate components are connected to the Cartesian components as,

$$U^\xi = \xi_x u + \xi_y v, \quad (12)$$

$$U^\eta = \eta_x u + \eta_y v. \quad (13)$$

$\tilde{\nabla}^2$ is the transformed Laplacian operator written as,

$$\tilde{\nabla}^2 \equiv \tilde{A} \frac{\partial^2}{\partial \xi^2} + 2\tilde{B} \frac{\partial^2}{\partial \xi \partial \eta} + \tilde{C} \frac{\partial^2}{\partial \eta^2} + \tilde{P} \frac{\partial}{\partial \xi} + \tilde{Q} \frac{\partial}{\partial \eta} \quad (14)$$

Coefficients \tilde{A} , \tilde{B} , \tilde{C} , \tilde{P} , and \tilde{Q} are,

$$\tilde{A} = \xi_x^2 + \xi_y^2, \tilde{B} = \xi_x \eta_x + \xi_y \eta_y, \tilde{C} = \eta_x^2 + \eta_y^2 \quad (15)$$

and,

$$\nabla^2 \xi = \tilde{P}, \quad \nabla^2 \eta = \tilde{Q}. \quad (16)$$

the Laplacian ∇^2 in the Cartesian coordinates are written as,

$$\nabla^2 \equiv \frac{\partial^2}{\partial x^2} + \frac{\partial^2}{\partial y^2}. \quad (17)$$

2.1. Boundary conditions

Condition of no-penetration and no-slip is used for components of velocity at the rigid surface of a square cylinder. $\theta = 1.0$ is used for temperature on the cylinder surface. The normal momentum equation is employed for pressure on the rigid cylinder surface,

$$\frac{\partial \bar{p}}{\partial \eta} = \frac{\partial \bar{p}}{\partial x} \frac{\partial x}{\partial \eta} + \frac{\partial \bar{p}}{\partial y} \frac{\partial y}{\partial \eta} \quad (18)$$

where, $\frac{\partial \bar{p}}{\partial x}$ and $\frac{\partial \bar{p}}{\partial y}$ on the surface of cylinder are

found from the momentum equations of x and y .

The artificial boundary is split into two portions to enforce the boundary conditions. One portion is the inflow and the other portion is the outflow. This is accomplished by controlling the local normal velocity variable direction. For a typical outer surface normal pointing towards the inside of the flow domain $\bar{U} \cdot \hat{n} > 0$ implies inflow and $\bar{U} \cdot \hat{n} < 0$ implies outflow. The boundary conditions on both the portions are written as

The inflow Portion

Uninterrupted free-stream conditions for speed and temperature are enforced at the inflow part, written as,

$$\theta = 0, \quad \bar{p} = 0, \quad \bar{U} = \text{Sin}\alpha \hat{i} + \text{Cos}\alpha \hat{j}. \quad (19)$$

Pressure is update by implementing the normal momentum equation.

The outflow Portion

Hasan et al. [19] proposes a numerical boundary condition for velocities at the outflow portion, this is executed in the present study. They utilizes vorticity considerations and mass conservation for incompressible flows to extrapolate the radial decay laws for the deviation / perturbation in circumferential and radial velocities created due to the presence of a body in an otherwise uniform undisturbed stream. They reported that by using their outflow velocity condition for domains comparatively smaller sizes, the precise computations would be carried out easily. The presence of the body causes deviations to the circumferential and radial velocity components are shown to obey radial decay laws with a leading order term written as (Hasan et al. [19]),

$$\left. \begin{aligned} v_r - v_{r\infty} &\propto S_1 / r^2 \\ v_\theta - v_{\theta\infty} &\propto \begin{cases} S_2 / r^2 & \text{if } \Gamma = 0 \\ S_2 / r & \text{if } \Gamma \neq 0 \end{cases} \end{aligned} \right\} \quad (20a)$$

The local circumferential and radial free-stream components are represented as $v_{\theta\infty}$ and $v_{r\infty}$, respectively, these components are obtained from the Cartesian free-stream velocity components. The circulation on the artificial boundary in the above equation is represented by the symbol ' Γ ', which can be estimated from the existing velocity field. The constants S_1 and S_2 are obtained by interpolating the values of the deviations in the circumferential and radial velocity components at an interior point (i). Thus, the circumferential and the radial velocity components on the artificial boundary at a point (B) would be determined using equations (20a) as,

$$\left. \begin{aligned} (v_r)_B &\propto (v_r - v_{r\infty})_i \left\{ r_i^2 / r_B^2 \right\} + (v_{r\infty})_B, \\ (v_\theta)_B &\propto \begin{cases} (v_\theta - v_{\theta\infty})_i \left\{ r_i^2 / r_B^2 \right\} + (v_{\theta\infty})_B & \text{if } \Gamma = 0 \\ (v_\theta - v_{\theta\infty})_i \left\{ r_i / r_B \right\} + (v_{\theta\infty})_B & \text{if } \Gamma \neq 0 \end{cases} \end{aligned} \right\} \quad (20b)$$

These components can then be utilized for obtaining the Cartesian components u , v . A derivative of second order for temperature in η direction is used, written as,

$$\frac{\partial^2 \theta}{\partial \eta^2} = K_2 \quad (20c)$$

At an interior point, K_2 is the magnitude of 2nd order derivative and uses the 2nd order backward difference scheme.

The boundary condition (traction free) of [20] and [21] is used for pressure, written as,

$$\bar{p} = \frac{1}{\text{Re}} \frac{\partial U^n}{\partial n}. \quad (21)$$

In the above equation the local normal is represented by n and the local normal velocity is U^n .

2.2. Grid structure

In the current research, a mesh that is uniform in ξ and η directions is taken into account in the mapped computational ξ - η plane. The spacing of mesh ($\Delta\xi$ and $\Delta\eta$) is assigned in terms of fixing the number of mesh points in the required (ξ and η) directions. The body-fitted coordinates $\xi(x, y)$ and $\eta(x, y)$ are chosen for the mapping of grid points in the physical plane to satisfy the Laplacian equations in the physical domain ($\tilde{P} = \tilde{Q} = 0$) written as,

$$\nabla^2 \xi = 0, \quad \nabla^2 \eta = 0. \tag{22}$$

Mapped/inverted equations in the computational ξ - η domain are given as,

$$D \frac{\partial^2 x}{\partial \xi^2} - 2E \frac{\partial^2 x}{\partial \xi \partial \eta} + F \frac{\partial^2 x}{\partial \eta^2} = 0, \tag{23}$$

$$D \frac{\partial^2 y}{\partial \xi^2} - 2E \frac{\partial^2 y}{\partial \xi \partial \eta} + F \frac{\partial^2 y}{\partial \eta^2} = 0. \tag{24}$$

In Eqs. (23)-(24) D, E, F are,

$$D = \left(\frac{\partial x}{\partial \eta} \right)^2 + \left(\frac{\partial y}{\partial \eta} \right)^2, \tag{25}$$

$$E = \left(\frac{\partial x}{\partial \xi} \right) \left(\frac{\partial x}{\partial \eta} \right) + \left(\frac{\partial y}{\partial \xi} \right) \left(\frac{\partial y}{\partial \eta} \right) \text{ and}$$

$$F = \left(\frac{\partial x}{\partial \xi} \right)^2 + \left(\frac{\partial y}{\partial \xi} \right)^2.$$

Discretization of Eqs. (23) - (24) on uniform grid ($\Delta\xi, \Delta\eta$) is done in computational plane in order to achieve grid in physical plane. An identical number of grid points are placed initially on the cylinder surface and finally on the artificial boundary, which corresponds to the number of mesh points in the computational plane in ξ direction. For elliptic Eqs. (23) - (24), the said boundary points function as Dirichlet boundary condition. The discrete solution of Eqs. (23)-(24) need a quasi-linear approach, as the equations are not linear to the undefined grid point coordinates (x, y). In the quasi-linearized method the D, E and F coefficients are discretized using the previous iterates, and the derivatives $\frac{\partial^2 x}{\partial \xi^2}, \frac{\partial^2 x}{\partial \xi \partial \eta}, \frac{\partial^2 x}{\partial \eta^2}, \frac{\partial^2 y}{\partial \xi^2}, \frac{\partial^2 y}{\partial \xi \partial \eta}$ and $\frac{\partial^2 y}{\partial \eta^2}$ are discretized using current/new iterates with finite difference schemes of second order (central). The corresponding linear algebraic set of equations were solved using Gauss-Seidel method to extract the new iterates from existing previous values. One Gauss-Seidel sweep is used per iteration for the two discretized equations (23)-(24). In previous study of Rashid and Hasan [13], the comprehensive analysis of grid structure is discussed.

The methodology constituting the generation of an O-type structured grid, numerical scheme utilized in present study, boundary conditions at cylinder's solid surface and on the artificial boundary (outflow/inflow portions) are elaborated in detail in the previous studies of Rashid and Hasan [13] Hasan and Rashid [22]. For pressure correction,

scheme identical to SMAC scheme is utilized which is elaborated in the study of Hasan and Sanghi [23] & Hasan et al. [19]. The discretization of governing equations of mass and momentum is done by employing spatial discretization of finite difference type on a non-staggered body-fitted grid. In the interior, a fourth-order central scheme is employed for diffusion terms, while for the convection terms a hybrid scheme of third-order upwind scheme (Kunio Kuwahara [24]) and fourth-order central is employed. For near boundary points (artificial and solid), second-order central schemes are employed for both convection and diffusion terms. For pressure interpolation, the concept of Rhie and Chow [25] is utilized.

2.3. Dimensionless output parameters

From application perspective, the influence of flow across a body is described in terms of the gross quantities, such as the moments or forces the fluid exerts on the object, and the overall rate of heat transfer between the fluid and the body. All such global parameters are described below in a dimensionless manner for the two-dimensional problem that is considered in the present study,

1. $C_L = C_y \sin \alpha - C_x \cos \alpha$, (Lift coefficient),
2. $C_D = C_x \sin \alpha + C_y \cos \alpha$, (Drag coefficient),
3. $C_M = 2M / \rho_o U_\infty^2 d^2$, (Moment coefficient),
4. $Nu = Q / [4k_o (T_s - T_\infty)]$, (Nusselt number),
5. $St = f d / U_\infty$. (Strouhal number).

C_y, C_x in the above equations are coefficients of forces in y and x directions given as,

$$C_x = \frac{2F_x}{\rho_o U_\infty^2 d} \text{ and } C_y = \frac{2F_y}{\rho_o U_\infty^2 d}. \tag{26}$$

F_x and F_y are the forces per unit cylinder span in x and y directions, respectively (Fig. 1). M is the overall moment the fluid exerted on the cylinder per unit span. Q is the maximum rate of heat transfer per unit cylinder span, and k_o is the fluid's thermal conductivity. The vortex-shedding frequency is expressed by 'f'.

The force coefficients in dimensionless form are,

$$C_x = 2 \int_0^1 \bar{J} \bar{p} \bar{\eta}_x d\xi + \frac{2}{Re} \int_0^1 \bar{J} \bar{\Omega} \bar{\eta}_y d\xi, \tag{27}$$

$$C_y = 2 \int_0^1 \bar{J} \bar{p} \bar{\eta}_y d\xi - \frac{2}{Re} \int_0^1 \bar{J} \bar{\Omega} \bar{\eta}_x d\xi, \tag{28}$$

$$C_M = 2 \int_0^1 \bar{J} \bar{p} (\bar{x} \bar{\eta}_y - \bar{y} \bar{\eta}_x) d\xi - \frac{2}{Re} \int_0^1 \bar{J} \bar{\Omega} (\bar{x} \bar{\eta}_x + \bar{y} \bar{\eta}_y) d\xi. \tag{29}$$

The Fourier's law of heat conduction is utilized to find out the heat transfer rate from the cylinder written as,

$$q = -\int k \frac{\partial T}{\partial n} b dl. \quad (30)$$

Heat transfer rate / unit width 'b' is calculated as,

$$\frac{q}{b} = -\int k \frac{\partial T}{\partial n} dl. \quad (31)$$

Nusselt number is represented as,

$$Nu = \frac{q/b}{4k_o (T_s - T_\infty)}. \quad (32)$$

Nusselt number in dimensionless form is written as,

$$Nu = \frac{1}{4} \int \bar{J} \frac{\partial \theta}{\partial \eta} (\bar{\eta}_x^2 + \bar{\eta}_y^2) d\xi. \quad (33)$$

2.4. Location of artificial boundary, grid size and time step selection

For finding out a suitable artificial boundary position, such that the numerical boundary conditions imposed on it does not affect considerably the dynamics of flow adjacent to the square cylinder. This is done by truncating the original grid with artificial boundary from the middle of the cylinder at a dimensionless distance of 120. The original grid of 241 x 325 mesh points is then truncate from the middle of the cylinder at dimensionless lengths of 100, 80, 60, 40 and 20 to give six numerical grids of equal grid cell size. For every truncated grid and at $\phi = 0^\circ$, $Pr = 0.71$, $Re = 100$, $Ri = 0$ and $\alpha = 0^\circ$, the Strouhal number, mean drag and lift coefficients are obtained from the numerical experiments. It is observed that change in the values of the lift coefficient are marginal for a dimensionless distance beyond 20 and change in the magnitudes of coefficient of drag and St beyond a dimensionless distance of 40 are quite small, and the length beyond 40 appears to be ideal for computations. The artificial boundary is positioned at a dimensionless distance of 40 from the middle of the cylinder for all subsequent reported computations. For the forced flow regime, the effects of grid size is analyzed by setting the far boundary at a distance of 40 from the middle of the square cylinder for $Re = 45$, $Pr = 100$, $\alpha = 90^\circ$, $\phi = 0^\circ$ and using a time step of 0.001 dimensionless units. Numerical experiments were conducted on 3 grids of 161 x 179 (G1), 241 x 258 (G2) & 321 x 338 (G3) mesh points for the close boundary spacing of 0.0197, 0.0137 & 0.0104, respectively. The drag coefficient (mean), Strouhal number & Nusselt number (mean) for a free-stream orientation of 90° are reported in Table 1 at various grid sizes. In moving from grid G1 to G2 the %age variation in the flow parameters including drag coefficient (mean), Strouhal number & Nusselt number (mean) is 0.275, 0.197 & 1.451, and in moving from grid G2 to G3 the %age variation is 0.701, 0.196 & 1.488, respectively. The outcome shows clearly that the %age variation in the flow parameter is very small (less than 1.5 percent) when moving from coarser to finer grid. Hence, the grid 241 x 258 (G2) is considered suitable for computations in order to conserve computational time.

Table 1. Grid size sensitivity for square cylinder at $Re = 45$, $Pr = 100$, $Ri = 0$ and $\alpha = 90^\circ$.

Grid	Near boundary spacing for the grid	Grid Size	\bar{C}_D	St	\bar{Nu}
G1	0.0197	161 x 179	1.5631	0.2030	17.6021
G2	0.0137	241 x 258	1.5588	0.2034	17.3503
G3	0.0104	321 x 338	1.5479	0.2038	17.0958

In order to determine the appropriate time step, the calculations were done in the forced & mixed convection regimes at the time steps of 0.0005 and 0.001 for $Re = 45$, $Pr = 100$, $\alpha = 90^\circ$ and $\phi = 0^\circ$. In Table 2 the drag coefficient (mean), Strouhal number & Nusselt number (mean), are compared for Richardson numbers 0 and 1.5 at different time steps. Moving from a time step of 0.0005 to 0.001 in the forced flow regime, the %age variation observed is 0.532, 0.098 & 0.811, respectively in the drag coefficient, Strouhal number & Nusselt number.

Table 2. Time step sensitivity for $\alpha = 90^\circ$, $\phi = 0^\circ$, $Re = 45$, $Pr = 100$ at $Ri = 0$ and 1.5.

Richardson number	Time step ($\Delta\tau$)	\bar{C}_D	St	\bar{Nu}
Ri = 0	0.0005	1.5671	0.2036	17.4911
	0.001	1.5588	0.2034	17.3503
Ri = 1.5	0.0005	1.6341	0.2587	17.6798
	0.001	1.6299	0.2583	17.7566

The %age variation in drag coefficient (mean), Strouhal number & Nusselt number (mean) in mixed convection at $Ri = 1.5$ is 0.257, 0.154 & 0.434, respectively. From the above discussion, it is suggested that minor span has no noticeable effect on the performance (<1 %). So a time step of 0.001 is selected for all the computations.

3. CODE VERIFICATION AND VALIDATION

Checking of numerical method, selection of numerical parameters, and the code used for numerical simulation is verified and validated by examining the present results with those reported in previous studies with in the forced and mixed convection. Numerical simulations were performed at $\alpha = 90^\circ$, $\phi = 0^\circ$, $Re = 5$, $Pr = 100$ and $0 \leq Ri \leq 0.50$. It is depicted in Table 3 that the present results of mean (time mean) drag coefficient (C_D) obtained from computations is in agreement with results reported in the earlier studies of Dhiman et al. [26], Paliwal et al. [27] and Dhiman et al. [28]. Computations have been carried out for the conditions, $Re = 5$, $Pr = 100$, $Ri = 0.0$ and $\alpha = 90^\circ$. It is seen from Table 4 that the present result of mean Nusselt number (Nu) is in agreement with the results of Dhiman et al. [28], Paliwal et al. [27] and [29] [30] [31].

Table 3. Mean drag coefficient (C_D) at $Re = 5$, $Pr = 100$, $Ri = 0.0$, 0.25 , 0.50 and $\alpha = 90^\circ$

	$Ri = 0.0$	$Ri = 0.25$	$Ri = 0.50$	
Dhiman et al. [26]	4.840			Numerical
Paliwal et al. [27]	4.814			Numerical
Dhiman et al. [28]		4.686	4.729	Numerical
Present Study	4.364	4.377	4.405	

Table 4. Mean Nusselt number (Nu) at $Re = 5$, $Pr = 100$, $Ri = 0.0$ and $\alpha = 90^\circ$

	Nu	
Dhiman et al. [28]	5.504	Numerical
Paliwal et al. [27]	5.723	Numerical
Present Study	5.370	

Table 5. Comparison of $\overline{C_{L,r.m.s}}$, $\overline{C_D}$, \overline{Nu} and St for square and circular cylinders at $Ri = 0$, $Re = 100$ and $Pr = 0.71$.

	Cylinder	$\overline{C_{L,r.m.s}}$	$\overline{C_D}$	\overline{Nu}	St
Experimental					
Okajima [32] $\alpha = 90^\circ$	Square	-	-	-	0.141-0.145
Luo et al. [33] $\alpha = 90^\circ$	Square	-	-	-	0.146
Collis and Williams [34] $\alpha = 90^\circ$	Circular	-	-	5.160	
Wang and Travnicsek [35] $\alpha = 90^\circ$	Circular	-	-	5.101	
Wang et al. [36] $\alpha = 90^\circ$	Circular	-	-	-	0.161
Numerical					
Sohankar et al. [1] $\alpha = 90^\circ$	Square	0.139	1.460	-	0.146
Saha et al. [37] $\alpha = 90^\circ$	Square	-	1.510	-	0.159
Sharma and Eswaran [2] $\alpha = 0^\circ$	Square	0.183	1.559	4.070	0.148
Ranjan et al. [38] $\alpha = 90^\circ$	Square	0.190	1.449	4.124	0.145
Yoon et al. [39] $\alpha = 90^\circ$	Square	0.179	1.428	-	-
Present ($\alpha = 0^\circ$)	Square	0.175	1.438	4.051	0.143
Present ($\alpha = 90^\circ$)	Circular	-	1.316	5.240	0.163

The discrepancies between present results and the previous results of Dhiman et al. [26], Paliwal et al. [27] and Dhiman et al. [28] reported in Table 3 and 4 are found due to the slight differences in the numerical procedures adopted and the level of accuracy of the discrete solutions chosen. In the previous studies of [26], [27] and [28] uses a confined flow field structure (channel flow with slip conditions) while in the current study the flow field is chosen to be unconfined. The boundary conditions chosen by [26], [27]

and [28] are different from the present study. In the studies of [26] and [28] finite volume method is utilized, and in the present study finite difference method is used. So it is difficult to get identical results with different numerical procedures, resulting in discrepancies in the results.

Table 5 compares the mean drag coefficient, rms lift coefficient, Strouhal number and mean Nusselt number, obtained in the current analysis with the data reported in earlier studies for circular and square cylinders at $\phi = 0^\circ$, $Ri = 0$, $Pr = 0.71$ and $Re = 100$. The data obtained from the current simulations are in close agreement with those obtained in the previous numerical and experimental studies. Present data of Strouhal number is in close relation with the data reported for both circular and square cylinders in earlier experimental studies.

4. RESULTS AND DISCUSSION

The current study is carried out for the range of parameters $1 \leq Re \leq 45$, $0 \leq Ri \leq 1.50$, $0^\circ \leq \alpha \leq 90^\circ$ at a fixed $\phi = 0^\circ$ and $Pr = 100$. Effects of Reynolds and Richardson numbers and orientation of the free-stream on patterns of streamline, vorticity contours, patterns of isotherm, non-dimensional time histories of drag and lift coefficients, mean (time mean) drag and lift coefficients (C_L and C_D), mean coefficient of moment (C_M), surface pressure and surface vorticity, local Nusselt number (Nu_L) and mean Nusselt number (Nu) have been carried out in detail.

4.1. Streamline Patterns, Contours of Vorticity and Isotherm Patterns

Patterns of streamline, vorticity contours and patterns of isotherm are depicted in Figs. 2-10 for $1 \leq Re \leq 45$, $0 \leq Ri \leq 1.50$, $0^\circ \leq \alpha \leq 90^\circ$, $\phi = 0^\circ$ and $Pr = 100$. It is seen from patterns of streamlines (Fig. 2-Fig. 4) and contours of vorticity (Figs. 5-7) that no vortices are formed at $Re = 1$ for the range of free-stream orientations and Richardson number chosen. The vortices are induced at higher magnitudes of Reynolds number, and further increases in their size with increase in Reynolds number. Similar trends are observed for the range of free-stream orientations chosen. With the increase in Richardson number the vortices are reduced in their size and the wake becomes thin as depicted in Figs. 2-7. Due to the fact that there is variation in density in the buoyancy term with increasing Richardson number, the incoming free-stream fluid near cylinder got accelerated with increase in Ri , accelerates the shear layer leading to less entrainment of fluid to the vortices from shear layers and hence the vortices are reduced in their size. Increase in Ri enforces thermal energy diffusion in the near wake of the cylinder which creates stabilizing buoyant forces with respect to the ambient fluid just outside the shear layer. The buoyancy induced current tends to stabilize the flow, thus thinning of wakes takes place. Figures. 2-7 depicted that, at a fixed Ri with increasing Re , the wakes became wider behind the cylinder because of high rate of momentum transfer to the fluid particles at higher Re . Also the entrainment of the fluid to the vortices increases with increasing Reynolds number.

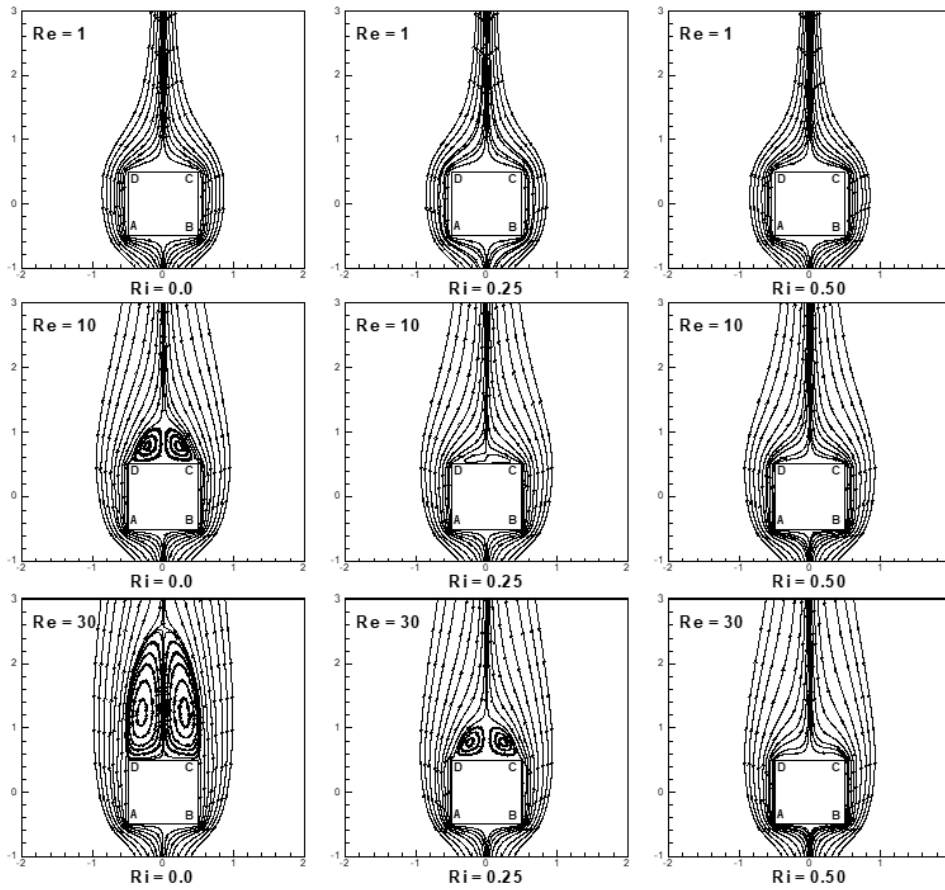


Figure 2. Streamline patterns for $1 \leq Re \leq 30$, $0 \leq Ri \leq 0.50$, $\alpha = 0^\circ$, at $Pr = 100$.

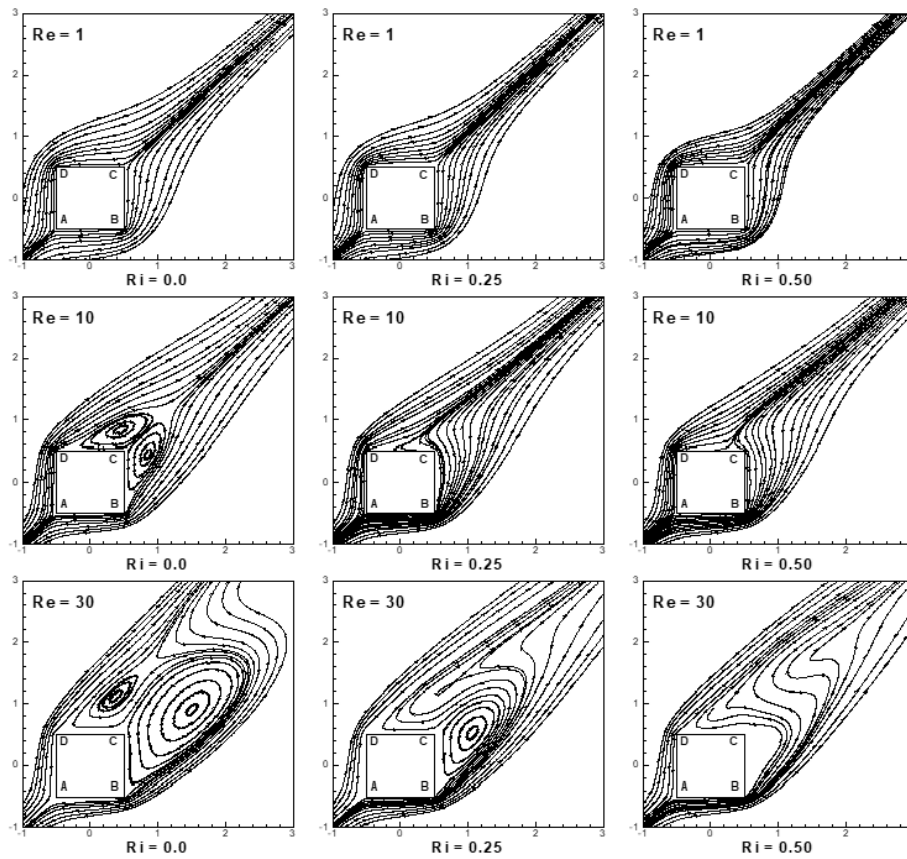


Figure 3. Streamline patterns for $1 \leq Re \leq 30$, $0 \leq Ri \leq 0.50$, $\alpha = 45^\circ$, at $Pr = 100$.

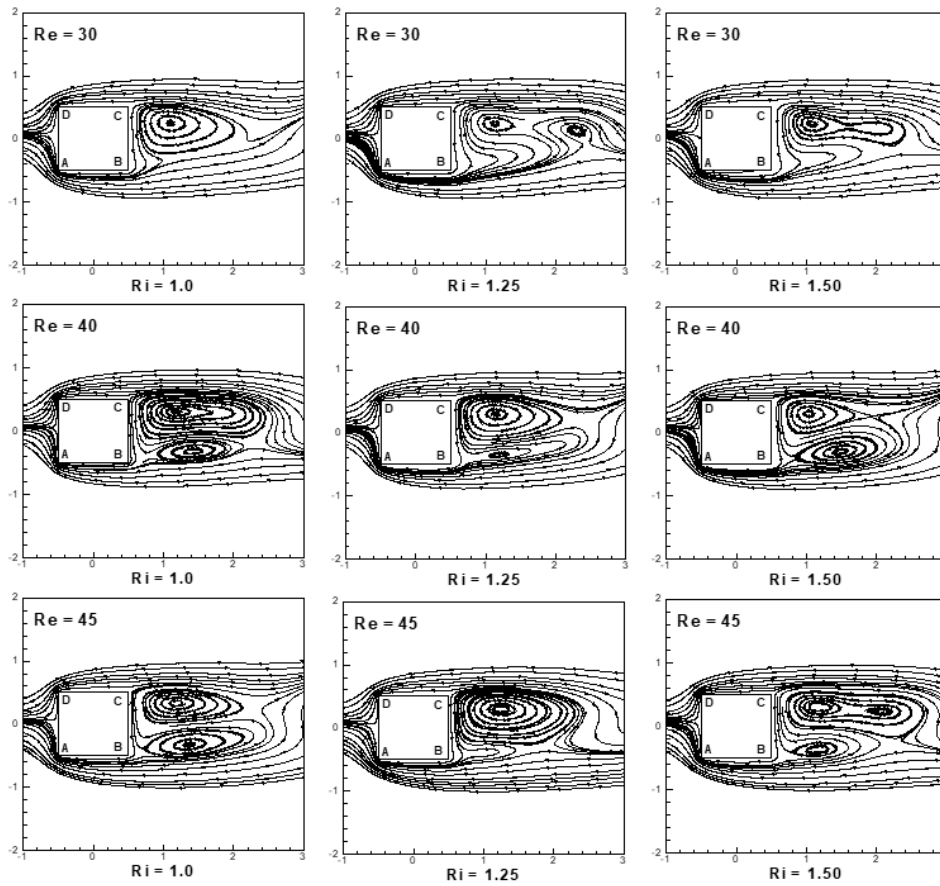


Figure 4. Streamline patterns for $30 \leq Re \leq 45$, $1.0 \leq Ri \leq 1.50$, $\alpha = 90^\circ$, at $Pr = 100$.

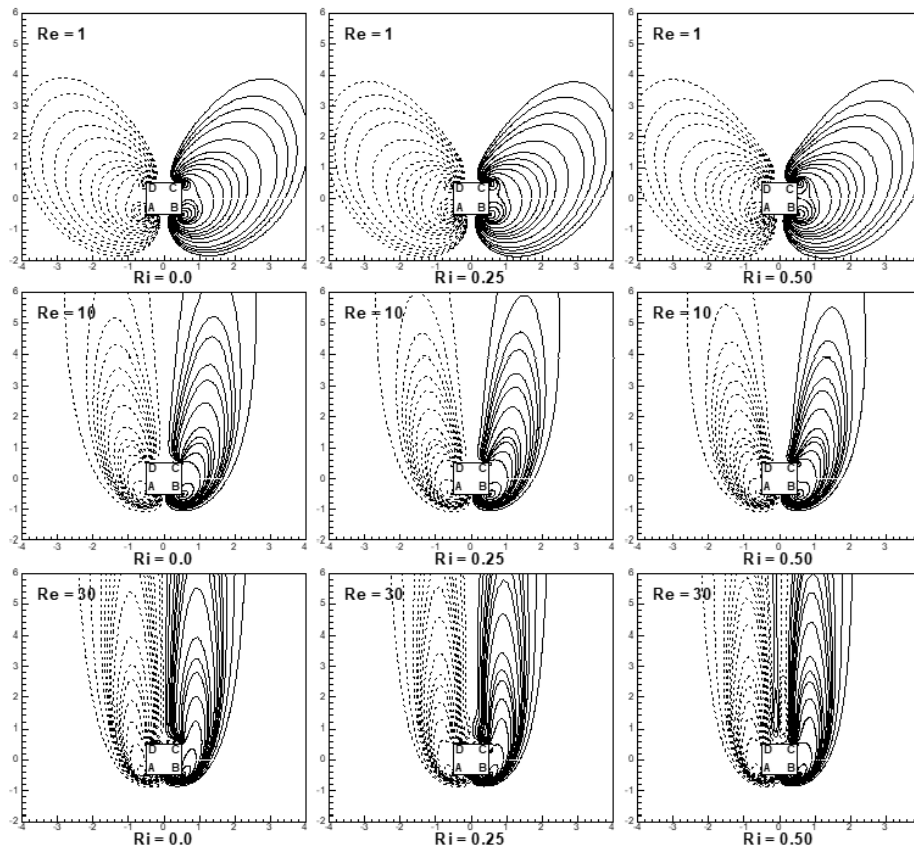


Figure 5. Contours of vorticity for the conditions ($Pr = 100$, $\alpha = 0^\circ$, $1 \leq Re \leq 30$, $0 \leq Ri \leq 0.50$).

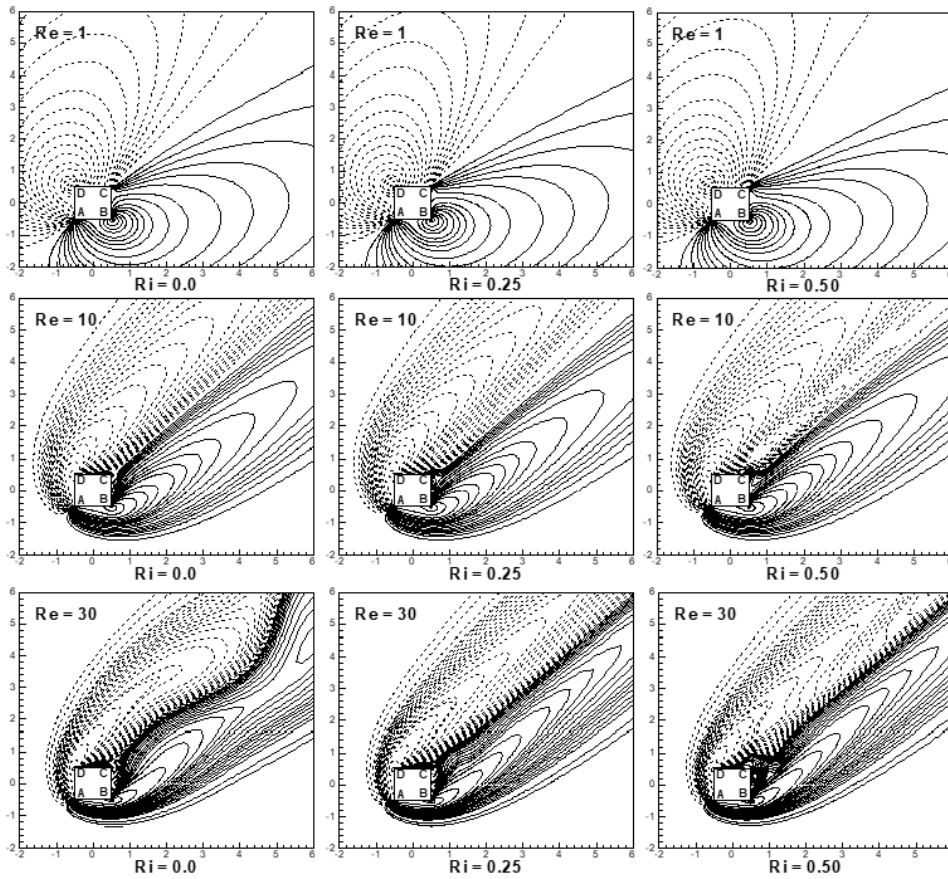


Figure 6. Contours of vorticity for the conditions ($Pr = 100$, $\alpha = 45^\circ$, $1 \leq Re \leq 30$, $0 \leq Ri \leq 0.50$).

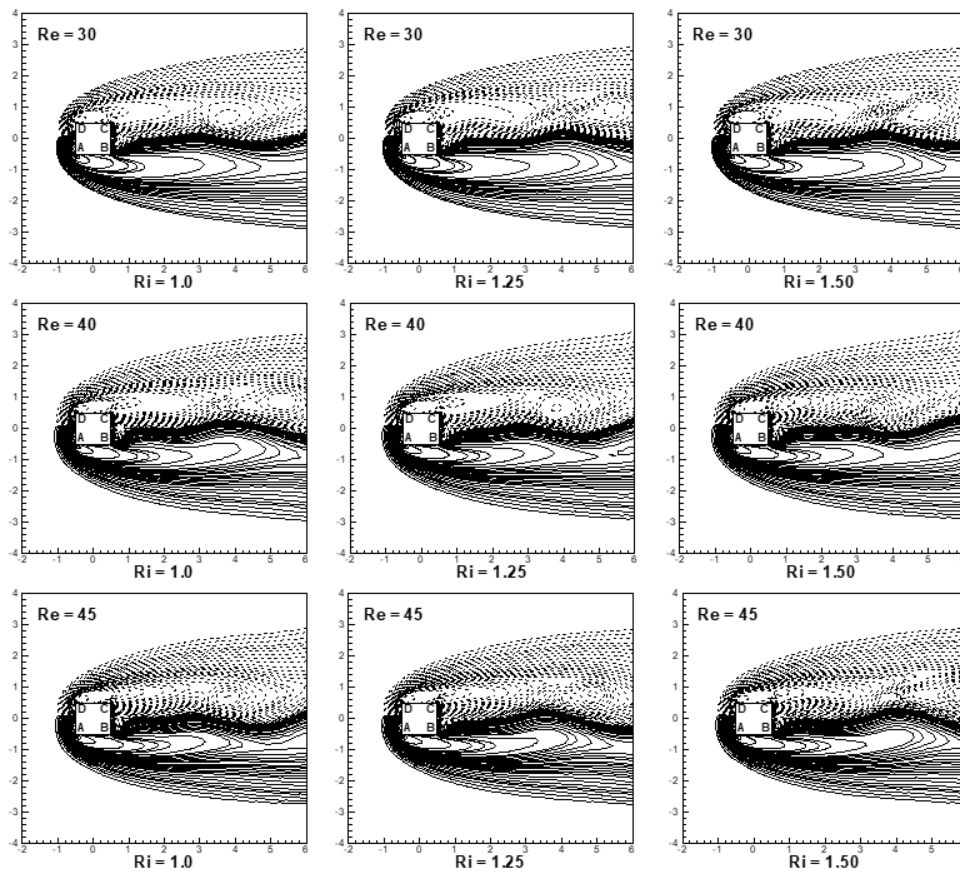


Figure 7. Contours of vorticity for the conditions ($Pr = 100$, $\alpha = 90^\circ$, $30 \leq Re \leq 45$, $1.0 \leq Ri \leq 1.50$).

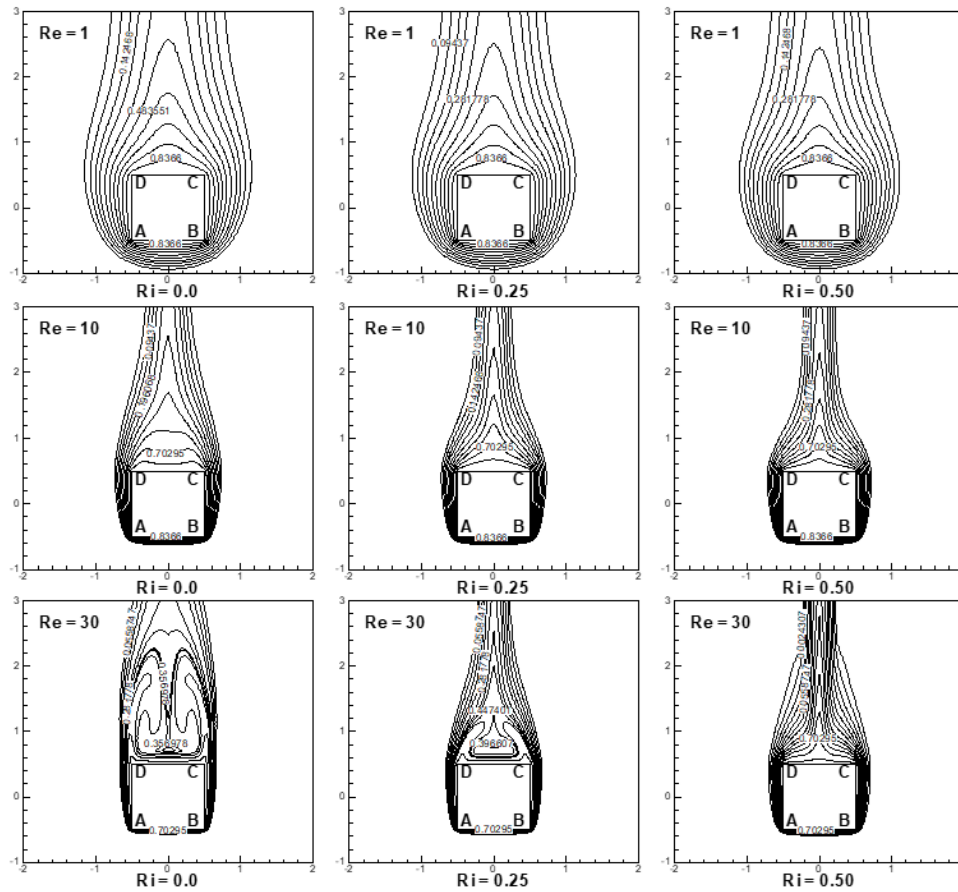


Figure 8. Isotherm patterns at $Pr = 100$, $\alpha = 0^\circ$, $Re = 1, 10, 30$ and $Ri = 0.0, 0.25, 0.50$.

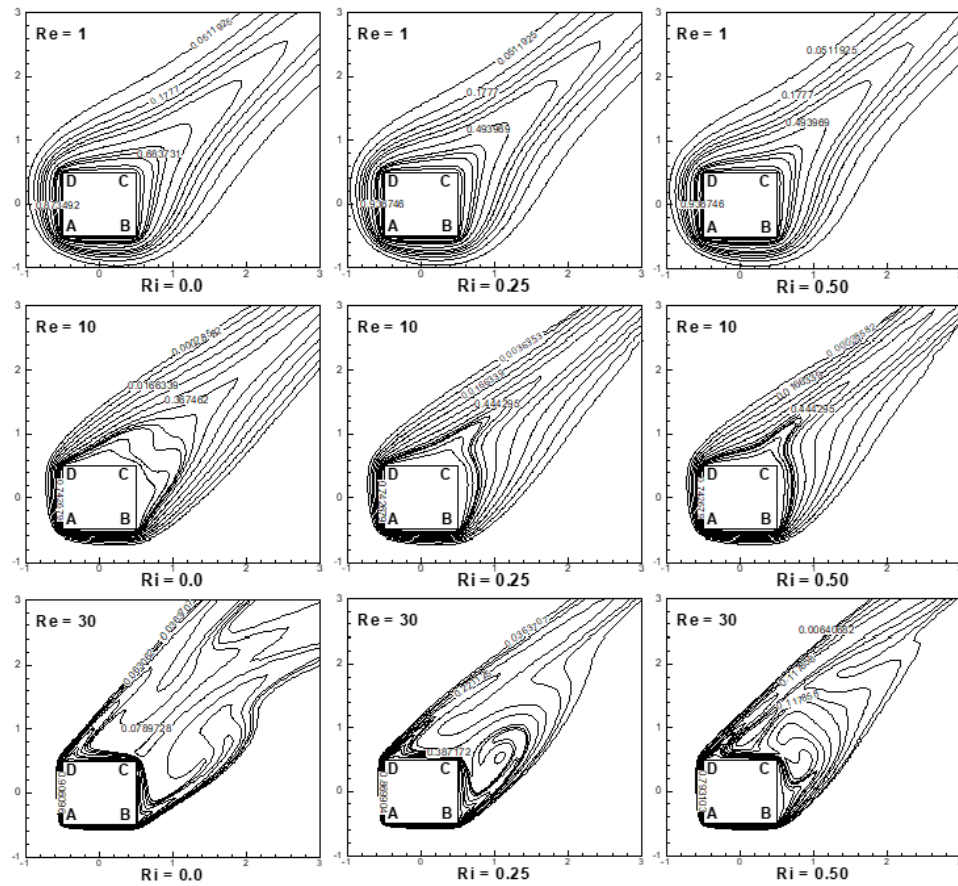


Figure 9. Isotherm patterns at $Pr = 100$, $\alpha = 45^\circ$, $Re = 1, 10, 30$ and $Ri = 0.0, 0.25, 0.50$.

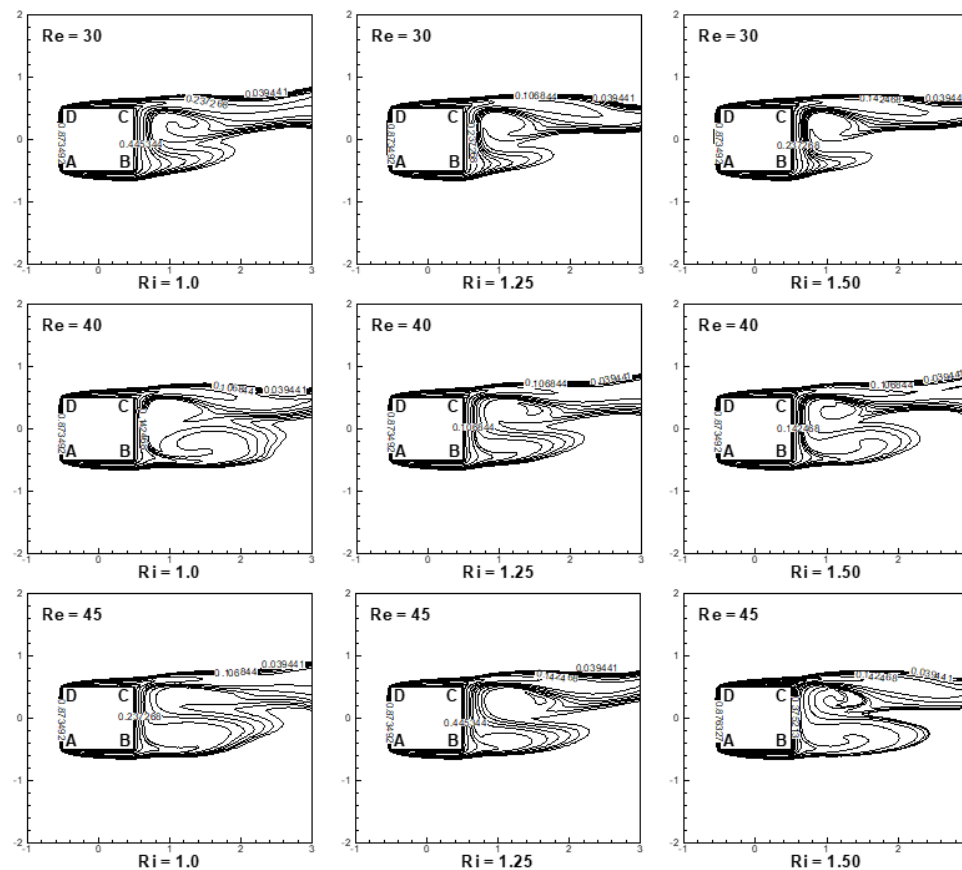


Figure 10. Isotherm patterns at $Pr = 100$, $\alpha = 90^\circ$, $Re = 30, 40, 45$ and $Ri = 1.0, 1.25, 1.50$.

The crowding of isotherms are observed more on leading face(s) of cylinder in comparison with other faces of cylinder as shown in Figs. 8-10 for condition ($0 \leq Ri \leq 1.50$, $1 \leq Re \leq 45, 0^\circ \leq \alpha \leq 90^\circ$, $\phi = 0^\circ$, $Pr = 100$). The trends are observed similar for the range of Richardson number chosen. Crowding of isotherms move near to the cylinder surface either with increase in Ri or Re as shown in Figs. 8-10. Similar trends have been observed for entire free-stream orientations range. More accumulation of isotherms on front face(s) of cylinder leading to higher rate of heat transfer from front face(s). The rate of heat transfer increases further either with increase in Richardson number or Reynolds number due to the fact that momentum of the fluid particles increases with the increase in Richardson or Reynolds numbers. More heated fluid particles replacement is observed from the colder fluid particles with increasing Richardson and Reynolds numbers leading to higher heat transfer rate from all the faces of square cylinder.

4.2. Surface Pressure and Surface Vorticity

Variation of surface pressure and surface vorticity at $Re = 1 - 45$, $Ri = 0 - 1.50$, $\alpha = 0^\circ - 90^\circ$, $Pr = 100$ and $\phi = 0^\circ$ is shown in Figs. 11-12. It is shown in Fig. 11 that the cylinder surface pressure is observed highest on the front face(s) (AB, AB and AD, AD at $\alpha = 0^\circ$, $\alpha = 45^\circ$ and $\alpha = 90^\circ$) of the cylinder that is placed in front of the free-stream. Surface

pressure is noticed minimum on the rear face(s) (CD, CD and BC, BC at $\alpha = 0^\circ$, $\alpha = 45^\circ$ and $\alpha = 90^\circ$) of the cylinder and intermittent for the side faces of the cylinder. Similar trends are seen for the range of free-stream orientations chose. It is shown in figure that with increase in the magnitudes of Reynolds number the pressure on the front face(s) decreases to a minimum due to an increase in the momentum of fluid particles with an increase in the magnitudes of Reynolds number. Pressure increases on the rear face(s) as the Reynolds number increase. The trend for the whole range of free-stream orientations is observed similar. An increment in the magnitude of Richardson number, leading to an increases in pressure gradient in the stream wise direction across the square cylinder for the selected range of Reynolds number chosen. Similar trends have been observed for the chosen range of the orientations of free-stream. The pressure at the vertices (A, B, C and D) of the cylinder is found to be maximum for the chosen parametric range, and it decreases due to acceleration (inertia/buoyancy induced) of the fluid particles around the cylinder vertices.

It is seen from Fig. 12 at $1 \leq Re \leq 45$, $0 \leq Ri \leq 1.50$, $0^\circ \leq \alpha \leq 90^\circ$, $\phi = 0^\circ$ and $Pr = 100$ that the vorticity along the surface is observed large on leading face(s) of cylinder for entire range α . Surface vorticity changes its sign across the stagnation point that lies on leading face(s) of cylinder as shown in Fig. 12.

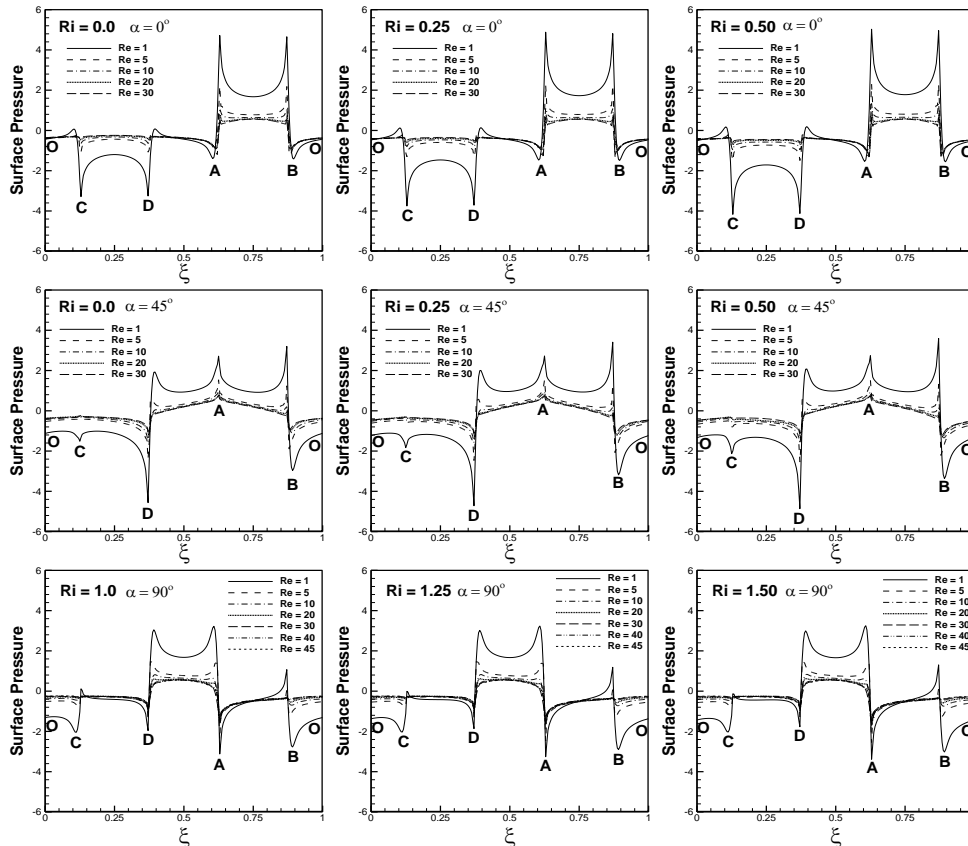


Figure 11. Variation of cylinder surface pressure $1 \leq Re \leq 45$, $0 \leq Ri \leq 1.50$, $\alpha = 0^\circ, 45^\circ, 90^\circ$.

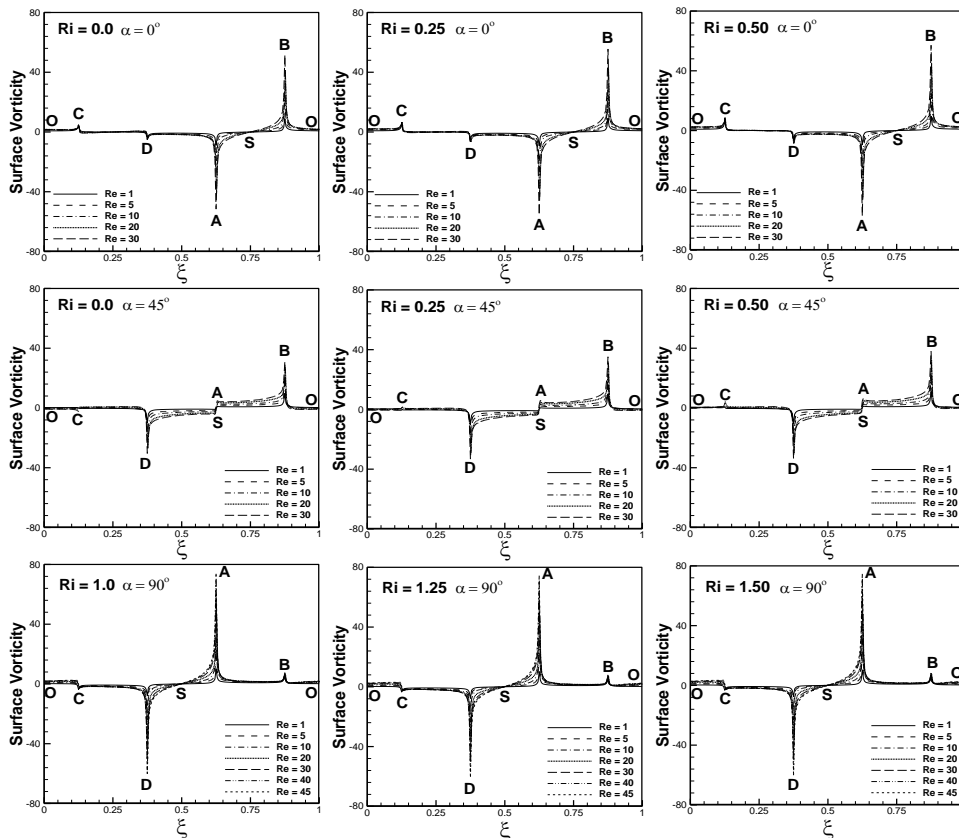


Figure 12. Surface vorticity variation for square cylinder at $1 \leq Re \leq 45$, $\alpha = 0^\circ, 45^\circ, 90^\circ$, $0 \leq Ri \leq 1.50$.

Magnitude of surface vorticity increases with increasing Reynolds number for the chosen range of orientations of the free-stream. Magnitude of surface vorticity also increases with increasing Ri , increase in Ri resulting in momentum gain of the shear layers which further increases the velocity of fluid particles and hence high surface vorticity. The vorticity is found to be maximum at the vertices adjacent to the front face(s) of the cylinder in comparison with other vortices. The reason is the large fluid particle velocities around the front face(s) vertices. This happens for the entire range of α .

4.3. Time Histories of Lift and Drag Coefficients

Figure 13 and figure 14 shows the variation of coefficients of lift and drag (C_L and C_D) with respect to non-dimensional time at $1 \leq Re \leq 45$, $0 \leq Ri \leq 1.50$, $0^\circ \leq \alpha \leq 90^\circ$, $\phi = 0^\circ$ and $Pr = 100$. It is depicted in time histories of lift & drag coefficients in figure 13 and figure 14 that the flow is found to be steady over the chosen range of free-stream orientations, Reynolds and Richardson numbers, except at $Re = 30$, $\alpha = 45^\circ$ and $20 \leq Re \leq 45$, $\alpha = 90^\circ$. At a Reynolds number $Re = 30$, $0 \leq Ri \leq 0.50$ and $\alpha = 45^\circ$ the onset of vortex-shedding is observed and the flow becomes unsteady and periodic flow. Figure 13 shows that the high amplitudes of lift coefficient for $\alpha = 45^\circ$ are observed due to the shedding of big size vortices on the downstream side of the cylinder wake. It can be seen from Fig. 13 that for $\alpha = 0^\circ$, the lift coefficient (negative) is found to be maximum at $Re = 1$ and decreases with increase in Reynolds number. Similar trends have been observed for the entire range of Richardson number. At $\alpha = 45^\circ$ and 90° , positive lift coefficient is found to occur at $Re = 1$ and changes to negative lift coefficient at higher magnitudes of Reynolds number. The lift coefficient (negative) is found to be maximum for $Re = 30$ at $\alpha = 45^\circ$ and $Re = 20$ at $\alpha = 90^\circ$. The trend remains same for the entire range of Richardson number.

Figure 14 indicates that the drag coefficient decreases substantially over the whole range of Richardson number with an increase in the magnitudes of Reynolds number. The pattern for the whole range of free-stream orientations is observed same. Magnitudes of drag coefficient increase substantially with an increase in magnitudes of Richardson number at $Re = 1$, and observed least for other selected Reynolds number. The effects of Ri is dominating at small magnitudes of Re and least at large magnitudes of Re as depicted in Fig. 14.

4.4. Mean Lift Coefficient, Mean Drag Coefficient and Mean Coefficient of Moment

Mean (time mean) lift coefficient (C_L) variation with Ri is shown in Fig. 15 for $1 \leq Re \leq 45$, $0 \leq Ri \leq 1.50$, $\alpha = 0^\circ$,

45° & 90° , $Pr = 100$ and $\phi = 0^\circ$. It is shown in figure that the mean lift coefficient either negative or positive increases with increasing Richardson number. Similar trends are observed for the entire free-stream orientations range. With reference to Fig. 1 negative lift coefficient means C_L is in downward direction and towards right. It is depicted in Fig. 15 that the magnitude of mean coefficient of lift is observed maximum at $Re = 20$, $Ri = 1.5$ and $\alpha = 90^\circ$. For the chosen range of Re , mean lift coefficient variation is observed minimum (of the order of 10^{-3} i.e. nearly zero) with increasing Ri at $\alpha = 0^\circ$. For the entire Reynolds number range the mean lift coefficient variation with Richardson number is found to be large at $\alpha = 45^\circ$ and 90° . At $\alpha = 0^\circ$ and with an increase in Reynolds number for a fixed Richardson number, the mean lift coefficient is shifted towards zero. At $\alpha = 45^\circ$ and 90° , the mean lifting coefficient for a given Richardson number is changed from +ve to -ve with an increasing Reynolds number other than $Ri = 0$ and $\alpha = 90^\circ$. The pressure gradient across the cylinder in transverse direction increases with increasing Re , resulting in high mean lift coefficient. Effect of Re on mean coefficient of lift is dominating as depicted in Fig. 15. Significant effects of Richardson number on mean lift coefficient is observed.

Figure 16 depicts the mean drag coefficient (C_D) variation with Ri at $1 \leq Re \leq 45$, $0 \leq Ri \leq 1.50$, $\alpha = 0^\circ, 45^\circ$ & 90° , $Pr = 100$ and $\phi = 0^\circ$. Figure 16 shows that the mean drag coefficient at a fixed magnitude of Richardson number decreases with an increase in the Reynolds number for the whole free-stream orientations range. For the chosen range of Richardson number, the mean coefficient of drag is always observed to be highest at $Re = 1$. The trend for the chosen range of free-stream orientations is observed similar. The pressure gradient across the cylinder in stream wise direction is found more at lower magnitudes of Reynolds number leading to large mean drag coefficient. Effects of Reynolds number are dominating and effects of Richardson number are slight on mean drag coefficient as depicted in Fig. 16.

Mean moment coefficient variation with Ri is shown in Fig. 17 for $1 \leq Re \leq 45$, $0 \leq Ri \leq 1.50$, $0^\circ \leq \alpha \leq 90^\circ$, $Pr = 100$ and $\phi = 0^\circ$. It is seen from figure that mean moment coefficient (C_M) variation with Ri and Reynolds number is slight (nearly zero, of the order of 10^{-3}) for $\alpha = 0^\circ$. For the chosen Re range, mean moment coefficient increases with increase in Ri at $\alpha = 45^\circ$ and 90° . For the range of Ri chosen, the mean moment coefficient decreases with increase in Re except for $Ri = 0$, $\alpha = 45^\circ$ and 90° as depicted in Fig. 17. At $Ri = 0$ the mean moment coefficient is found nearly zero for the entire range of Reynolds number. Mean moment coefficient for selected range of Richardson number is always observed highest at $Re = 1$. Same trend is observed for the chosen range of orientations of the free-stream.

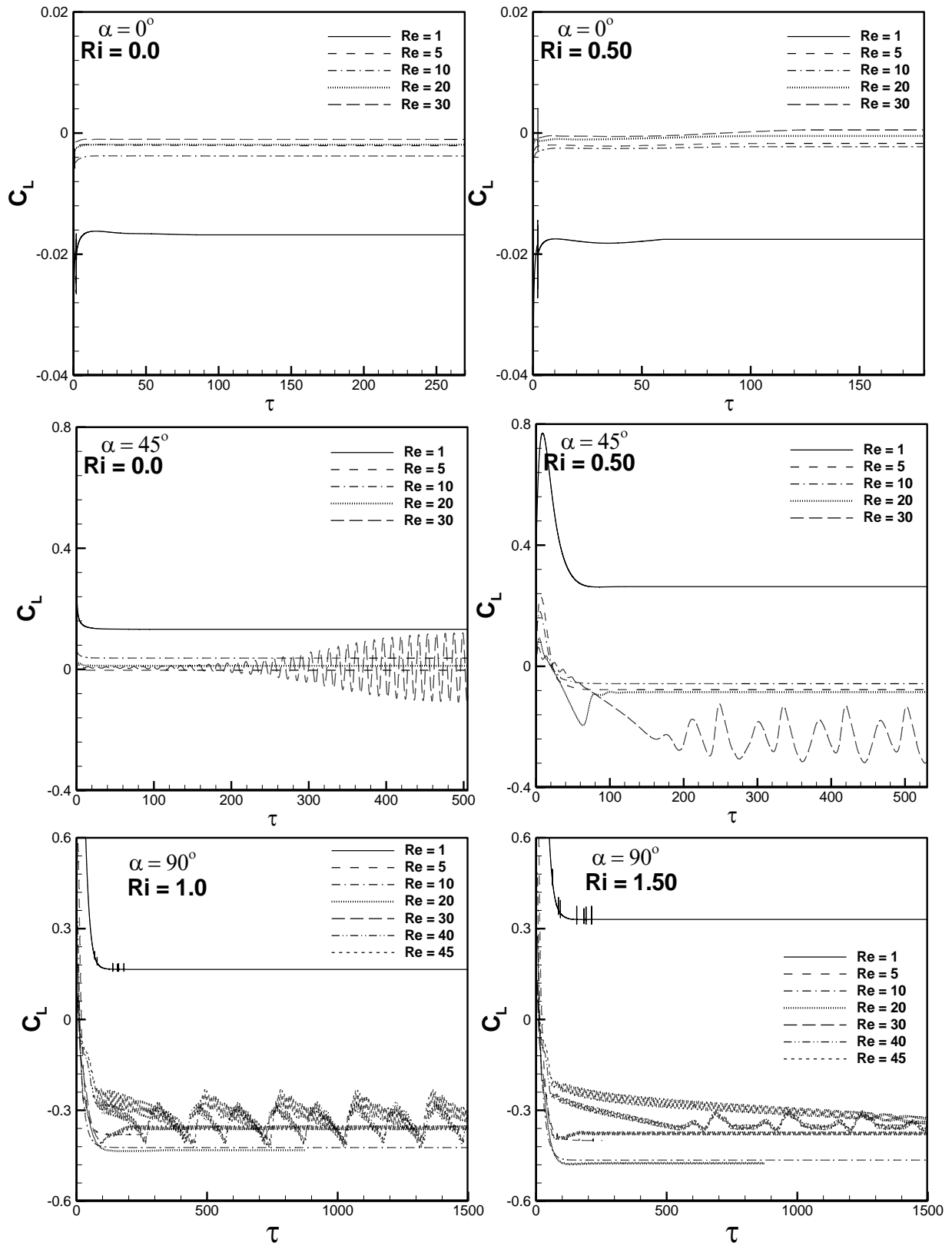


Figure 13. Variation of C_L with τ for $1 \leq Re \leq 45$, $0 \leq Ri \leq 1.50$, $\alpha = 0^\circ, 45^\circ \& 90^\circ$ at $Pr = 100$, $\phi = 0^\circ$.

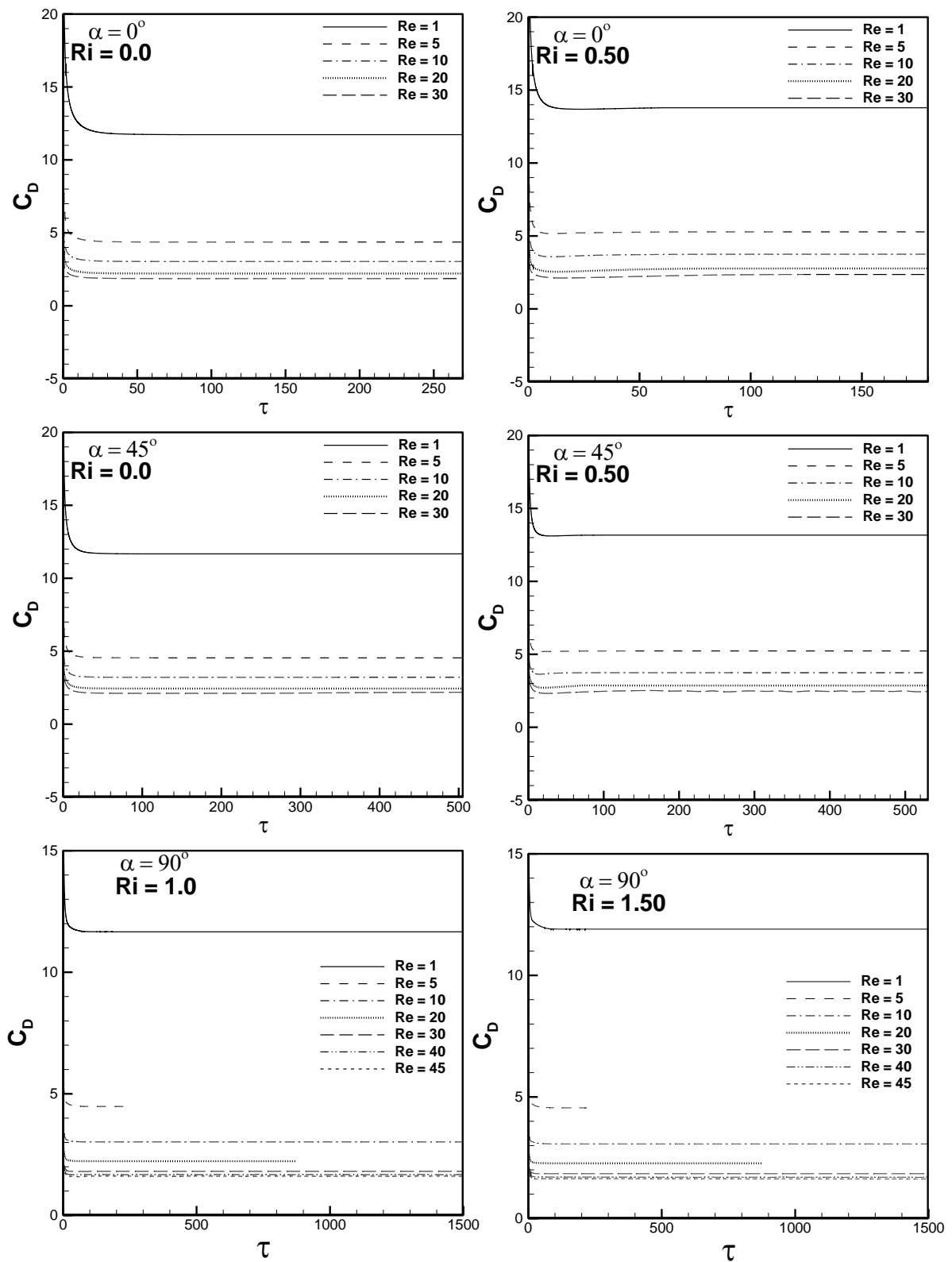


Figure 14. Variation of C_D with τ for $1 \leq Re \leq 45$, $0 \leq Ri \leq 1.50$, $\alpha = 0^\circ, 45^\circ \& 90^\circ$ at $Pr = 100$, $\phi = 0^\circ$.

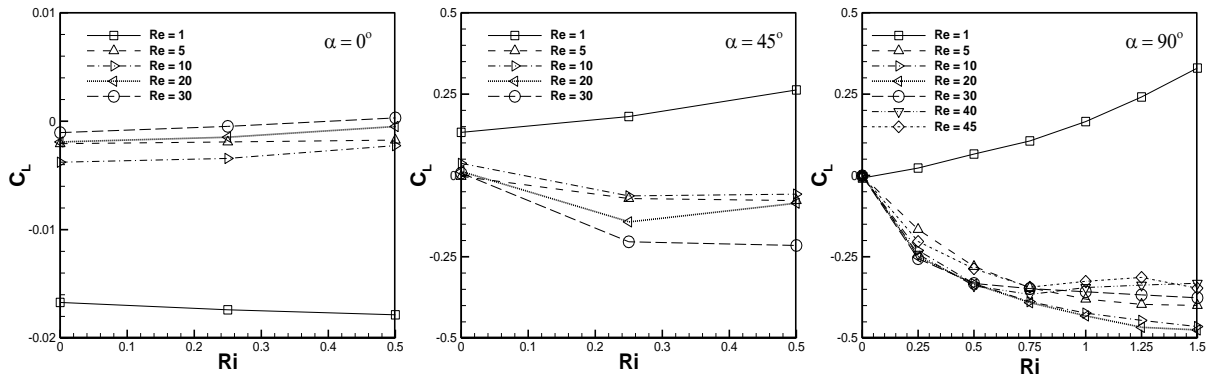


Figure 15. Variation of mean C_L with Richardson number for $1 \leq Re \leq 45$, $\alpha = 0^\circ, 45^\circ \& 90^\circ$ at $Pr = 100$.

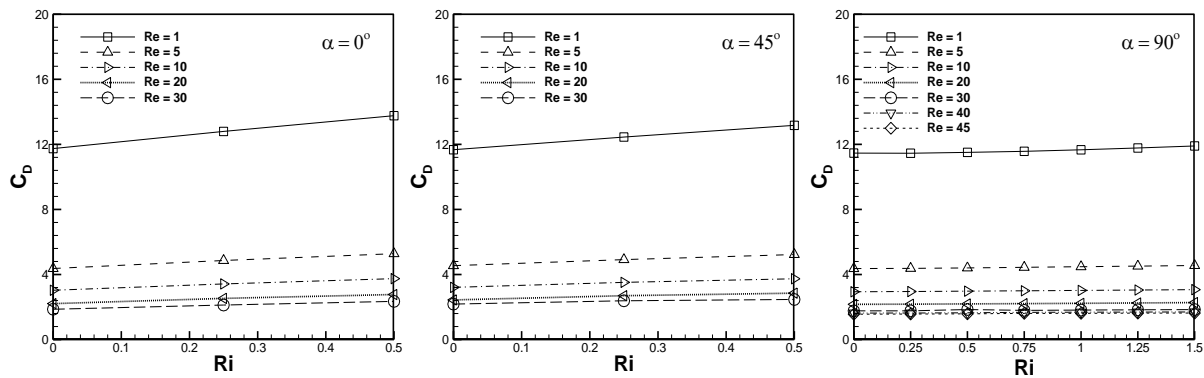


Figure 16. Variation of Mean C_D with Ri at $1 \leq Re \leq 45$, $0 \leq Ri \leq 1.50$, $\alpha = 0^\circ, 45^\circ, 90^\circ$ at $Pr = 100$.

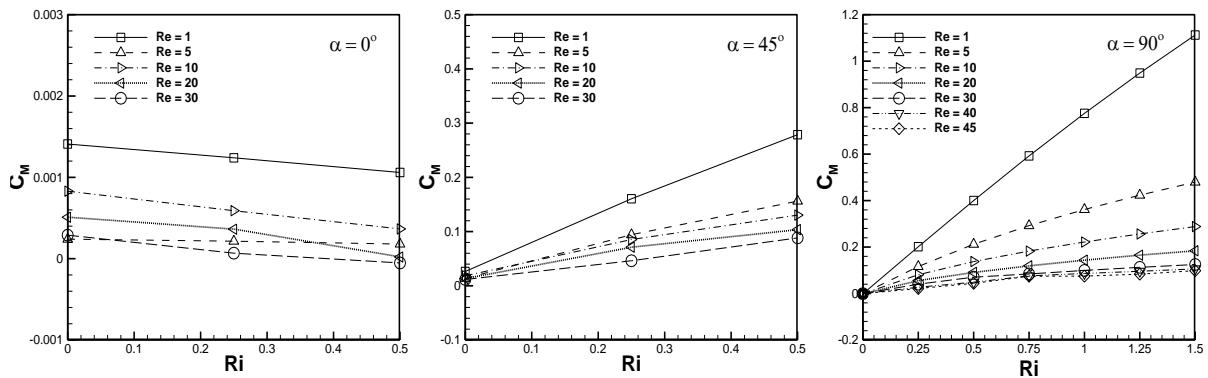


Figure 17. Variation of Mean moment Coefficient (C_M) with Ri for $1 \leq Re \leq 45$, $0 \leq Ri \leq 1.50$, $\alpha = 0^\circ, 45^\circ, 90^\circ$ at $Pr = 100$.

4.5. Surface Nusselt Number (Nu_L) and Mean Nusselt Number (Nu)

Figure 18 shows the local Nusselt number (Nu_L) variation around the square cylinder surface at $1 \leq Re \leq 45$, $0 \leq Ri \leq 1.50$, $0^\circ \leq \alpha \leq 90^\circ$, $\phi = 0^\circ$ and $Pr = 100$. It is seen from Fig. 18 that the local Nusselt number is observed maximum from the leading side(s) of the cylinder, low from the trailing side(s) of the cylinder and intermittent from the remaining side(s) of the square cylinder for the chosen range of orientations of the free-stream. With the rise in the magnitudes of Reynolds number and Richardson number, heat transfer from all sides of the cylinder increases. As can be seen from the figure 18 that the influence of Reynolds number on heat transfer is dominating.

The heat transfer rate from the square cylinder vertices is found to be maximum as shown in Figure 18. Increase in the magnitudes of Reynolds or Richardson numbers increases the fluid particles momentum, replaces the heated fluid particles at a faster rate from the faces and vertices of the cylinder with the relatively colder particles of the fluid, improves the heat transfer rate from the cylinder.

Time mean (mean) Nusselt number (Nu) variation with Ri is depicted in figure 19 for the conditions ($Re = 1 - 45$, $Ri = 0 - 1.50$, $\alpha = 0^\circ - 90^\circ$, $Pr = 100$, $\phi = 0^\circ$). It is depicted in Fig. 19 that the variation in mean Nusselt number with Richardson number is minimum for the whole range of Re . The trend for the selected range of free-stream orientations is observed the same. At a fixed magnitude of the Ri , the Nusselt number significantly increases with an increase in

the magnitudes of Re for the range of free-stream orientations chosen. The rise in the magnitudes of Reynolds number increases the velocity of fluid particles, resulting in quick displacement of warmer fluid particles in the vicinity

of square cylinder from the cooler fluid particles of the approaching free-stream. The rate of heat transfer from the cylinder increases with the increase in Reynolds number and Richardson number.

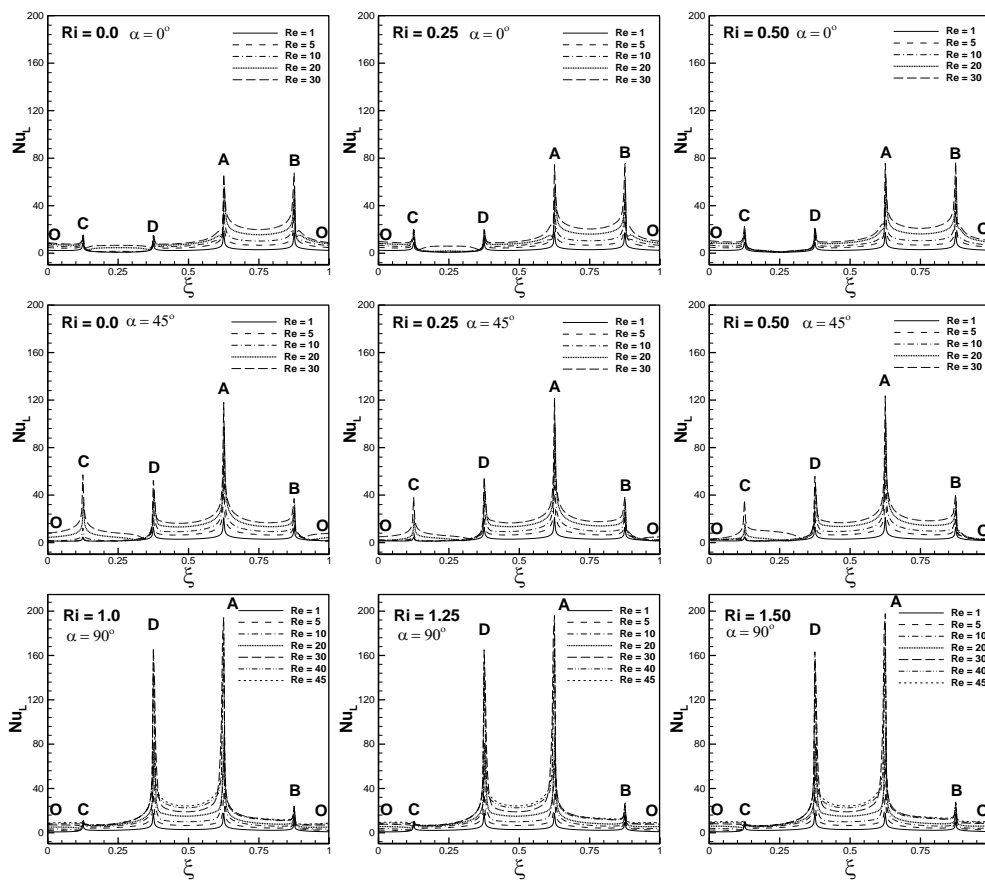


Figure 18. Local Nusselt number variation for $1 \leq Re \leq 45$, $0 \leq Ri \leq 1.50$ and $\alpha = 0^\circ, 45^\circ, 90^\circ$.

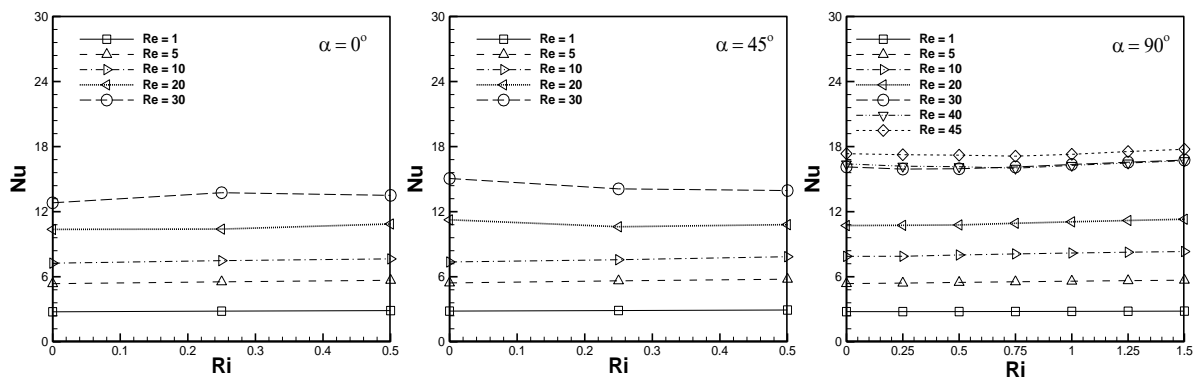


Figure 19. Variation of mean Nu with Ri for $1 \leq Re \leq 45$, $0 \leq Ri \leq 1.50$, $\alpha = 0^\circ, 45^\circ, 90^\circ$ at $Pr = 100$, $\phi = 0^\circ$.

5. CONCLUSIONS

In the current study the effects of Richardson number and Reynolds number with free-stream orientations on fluid dynamics and heat transfer characteristics are examined in detail for $1 \leq Re \leq 45$, $0 \leq Ri \leq 1.50$, $0^\circ \leq \alpha \leq 90^\circ$ and $Pr = 100$ at a fixed cylinder orientation $\phi = 0^\circ$. The following conclusions have been made;

1. The flow is found to be steady for $1 \leq Re \leq 30$, $0 \leq Ri \leq 0.50$ at $\alpha = 0^\circ$, $1 \leq Re \leq 20$, $0 \leq Ri \leq 0.50$ at $\alpha = 45^\circ$, and $1 \leq Re \leq 10$, $1.0 \leq Ri \leq 1.50$ at $\alpha = 90^\circ$, respectively. Vortex-shedding initiation or onset is observed at $Re = 30$, $0 \leq Ri \leq 0.50$ and $\alpha = 45^\circ$, the flow becomes unsteady and periodic flow. No vortex is observed at $Re = 1$, the vortices are induced at higher magnitudes of Reynolds number. The vortices are increased in size with increasing Reynolds number, and reduces in size with the increase in Richardson number.
2. Surface pressure and surface vorticity are found to be maximum on leading face(s) of cylinder that faces the upcoming stream of the fluid. Surface pressure is observed to be minimum on the trailing face(s) and intermittent on the side faces of the cylinder. It is identified that the surface vorticity changes its sign (+ve or -ve) across the stagnation point that is generated on the cylinder leading face(s). The surface pressure and surface vorticity is seen maximum at corners of square cylinder.
3. It is found that mean coefficient of lift (C_L) increases with increasing Ri for the selected range of free-stream orientations. Variation of mean lift coefficient is of the order of 10^{-3} that is nearly zero with increasing Richardson number for $\alpha = 0^\circ$. For the chosen range of Re, variation of mean coefficient of lift with Ri is found large at $\alpha = 45^\circ$ and 90° . Magnitude of mean drag coefficient (C_D) reduces significantly for the whole range of free-stream orientations with an increase in Reynolds number. The mean drag coefficient for the range of Richardson number is always observed highest at $Re = 1$. Moment coefficient (time mean) variation with Ri and Re is slight (nearly zero, of the order of 10^{-3}) at $\alpha = 0^\circ$. Magnitude of moment coefficient rises as the magnitude of Ri is increased at $\alpha = 45^\circ$ and 90° for the chosen Reynolds number range. The mean moment coefficient for the range of Richardson number selected is always observed highest at $Re = 1$.
4. The crowding of isotherms are observed maximum on the leading face(s) of the cylinder in comparison with other faces of cylinder. Crowding of isotherms on the leading face(s) of cylinder further increases with increasing Richardson number or Reynolds number, resulting in more heat transfer from the leading face(s) of the cylinder.
5. It is observed that the local heat transfer (Nu_L) increases with the increase in Reynolds number or Richardson number. Heat transfer from the vertices of cylinder is found maximum and increases further with increase in Reynolds/Richardson numbers owing to the rapid exchange of warm fluid particles with cooler fluid particles. Mean Nusselt number (Nu) at a fixed magnitude of Ri increases with increasing Re for the

selected range of orientations of the free-stream. It is observed that the rate of heat transfer increases either with increase in Richardson number or Reynolds number or both.

REFERENCES

- [1] Sohankar A., Norberg C. and Davidson L., "Low-Reynolds number flow around a cylinder at incidence: study of blockage, onset of vortex shedding and outlet boundary condition", *Int. J. Nume. Meth. Fluids* 26, pp. 39 – 56, 1998.
- [2] Sharma A. and Eswaran V., "Effect of aiding and opposing buoyancy on the heat and fluid flow across a square cylinder at $Re = 100$ ", *Nume. Heat Trans. Part A* 45, pp. 601 – 624, 2004.
- [3] Sharma A. and Eswaran V., "Effect of channel-confinement and aiding/opposing buoyancy on the two-dimensional laminar flow and heat transfer across a square cylinder. *Int. J. Heat and Mass Trans.* 48, pp. 5310 – 5322, 2005.
- [4] Chatterjee D. and Mondal B., "Effect of thermal buoyancy on the two-dimensional upward flow and heat transfer around a square cylinder", *HeatTrans. Engg.* 33 (12), pp. 1063 – 1074, 2012.
- [5] Dhiman A., Sharma N. and Kumar S., "Buoyancy-aided momentum and heat transfer in a vertical channel with a built-in square cylinder", *Int. J. Sust.Energy* 10.1080/14786451.2013.764878, pp. 1 – 22, 2013.
- [6] Yang G. and Wu J., "Effect of side ratio and aiding/opposing buoyancy on the aerodynamic and heat transfer characteristics around a rectangular cylinder at low Reynolds numbers", *Nume. Heat Trans. Part A* 64, pp. 1016 – 1037, 2013.
- [7] Moulai S., Korichi A. and Polidori G., "Aided mixed convection past a heated square cylinder", *Journal of Applied Fluid Mechanics*, Vol. 9, No. 1, pp. 303 – 310, 2016.
- [8] Rashid A. and Hasan N., "Vortex-shedding suppression in mixed convective flow past a heated square cylinder", *Int. J. Mech. Mecha. Engg.* 5, 6, pp. 953-961, 2011.
- [9] Rashid A. and Hasan N., "Influence of free-stream orientation and buoyancy on aerodynamic characteristics in mixed convective flow past a square cylinder", *Proc. 5th Int. Conf. Adv. Mech. Engg. (ICAME-2011)*, pp. 329-334, 2011.
- [10] Rashid A. and Hasan N., "Effect of free-stream orientation and buoyancy on heat transfer in mixed convective flow past a square cylinder", *World Academy of Science, Engg. Tech.* 79 pp. 471-478, 2011.
- [11] Haider S. A. and Rashid A., "Mixed convective flow past a square cylinder with variable Prandtl number", *Nat. Conf. Mech. Engg. Ideas, Innovations and Initiatives (NCMEI3-2016)*, pp. 339-344, 2016.
- [12] Anshumaan S. and Rashid A., "Effect of Buoyancy and Inertia Forces on the Flow Past a Heated Square Cylinder in Cross Flow Configuration", *Adv. Sci. Engg. Med.*, 10, 3, pp. 505-512, 2018.
- [13] Rashid A. and Hasan N., "Steady and Unsteady Flow Regimes in Two-Dimensional Mixed Convective Flow of Air past a Heated Square Cylinder" *Int. J. Mech. Sci.* Vol. 175, 105533, 2020.
- [14] Yuan Ma., Mohebbi R., Rashidi M. M. and Yang Z., "Numerical simulation of flow over a square cylinder with upstream and downstream circular bar using lattice Boltzmann method" *Int. J. Mod. Phys. C*, 29, 4, 1850030, 2018.
- [15] Yuan Ma., Rashidi M. M. and Yang Z., "Numerical simulation of flow past a square cylinder with a circular bar upstream and a splitter plate downstream", *J. Hydro.*, 31(5), 949-964, 2019.
- [16] Rafik B., Yacine K. and Faouzi S., "Unconfined laminar nanofluid flow and heat transfer around a square cylinder

- with an angle of incidence”, *Jordan Journal of Mechanical and Industrial Engineering*, 13, 191-196, 2019.
- [17] Tritton D. J., “*Physical fluid dynamics*”, ELBS Edi. Chap. 13, pp. 127 – 130, 1979.
- [18] Thompson J. F., Warsi Z. U. A. and Mastin C. W., “*Numerical grid generation foundations and applications*”. North Holland, 1985.
- [19] Hasan N., Anwar S. F. and Sanghi S., “On the outflow boundary condition for external incompressible flows: A new approach”, *J. Compu. phys.* 206, pp. 661 – 683, 2005.
- [20] Cheng L. and Armfield S., “A simplified marker and cell method for unsteady flows on non-staggered grids”. *Int. J. Nume. Meth. Fluids* 21 (1), 15 – 34, 1995.
- [21] Gresho P. M., “Incompressible fluid dynamics: some fundamental formulation issue”. *Annu. Rev. Fluid Mech.* 23, 413 – 454, 1991.
- [22] Hasan N. and Rashid A., “Vortex-shedding suppression in two-dimensional mixed convective flows past circular and square cylinders”, *Phys. Fluids* 25 (053603), pp. 1 – 27, 2013.
- [23] Hasan N. and Sanghi S., “The dynamics of two-dimensional buoyancy driven convection in a horizontal rotating cylinder”, *J. Heat Trans.* 126, pp. 963 – 984, 2004.
- [24] Kuwahara K., “Unsteady flow simulation and its visualization”, 30th AIAA *Fluid Dyna. Conf.* AIAA, 99 – 3405, 1999.
- [25] Rhie C. M. and Chow W. L., “Numerical study of the turbulent flow past an airfoil with trailing edge separation”, *AIAA J.* 21 (11), pp. 1525 – 1532, 1983.
- [26] Dhiman A. K., Chhabra R. P., Sharma A. and Eswaran V., “Effects of Reynolds and Prandtl numbers on heat transfer across a square cylinder in the steady flow regime”, *Nume. Heat Trans. Part A* 49, pp. 717 – 731, 2006.
- [27] Paliwal B., Sharma A., Chhabra R. P. and Eswaran V., “Power law fluid flow past a square cylinder: Momentum and heat transfer characteristics”, *Chem. Eng. Sci.* 58, pp. 5315 – 5329, 2003.
- [28] Dhiman A. K., Anjaiah N., Chhabra R. P. and Eswaran V., “Mixed convection from a heated square cylinder to Newtonian and Power-law fluids”, *J. Fluids Eng.* 129 (4), pp. 506 – 573, 2006.
- [29] Rashid A., “A numerical investigation of two-dimensional mixed convective flow past a square cylinder”, *Doctoral thesis*, <http://ir.amu.ac.in/id/eprint/9861>, 2016.
- [30] Rashid A., “A numerical investigation of two-dimensional mixed convective flow past a square cylinder”, *Doctoral thesis*, <https://shodhganga.inflibnet.ac.in/handle/10603/117546>, 2016.
- [31] Rashid A., Shahrukh V. Mubashshir A. A. and Anwar S. F., “Numerical investigation of fluid flow past a square cylinder in mixed convective flow regime”, IOP Conference Materials Science and Engineering, doi:10.1088/1757-899X/691/1/012038, 2019.
- [32] Okajima A., “Strouhal numbers of rectangular cylinders”. *J. Fluid Mech.* 123, 379-398, 1998.
- [33] Luo S. C., Chew Y. T. and Ng Y. T., “Characteristics of square cylinder wake transition flows”. *Phys. Fluids* 15 (9), 2549 – 2559, 2003.
- [34] Collis D. C. and Williams M. J., “Two-dimensional convection from heated wires at low Reynolds numbers”. *J. Fluid Mech.* 06:357-84, 1959.
- [35] Wang A.-B. and Travnicek Z., “On the linear heat transfer correlation of a heated circular cylinder in laminar cross flow using a new representative temperature concept”. *Int. J. Heat and Mass Transfer* 44:4635, 2001.
- [36] Wang A.-B., Travnicek Z. and Chia K.-C., “On the relationship of effective Reynolds number and Strouhal number for the laminar vortex shedding of a heated circular cylinder”. *Phys. Fluids* 12, 6 1401, 2001.
- [37] Saha A. K., Muralidhar K. and Biswas G., “Transition and chaos in two-dimensional flow past a square cylinder”. *J. Engg. Mech.* 125, 523 – 532, 2000.
- [38] Ranjan R., Dalal A. and Biswas G., “A numerical study of fluid flow and heat transfer around a square cylinder at incidence using unstructured grids”. *Nume. Heat Trans. Part A* 54, 890 – 913, 2008.
- [39] Yoon D.-H., Yang K.-S. and Choi C.-B., “Flow past a square cylinder with an angle of incidence”. *Phys. Fluids* 22 (043603), 1 – 12, 2010.

Investigation on the Performance of Order Release Methods in a Flow Shop with Bottlenecks

Aruna Prabhu^a, Raghunandana K^{b*}, Yogesh Pai P^c

^{a,b} Manipal Institute of Technology, Manipal.

^c Manipal Institute of Management, Manipal.

Manipal Academy of Higher Education, Manipal. 576104, Karnataka, India

Received September 29 2020

Accepted August 31 2021

Abstract

The workload control (WLC) is a popular concept in manufacturing planning and control, which plays a significant role in enhancing the efficiency of manufacturing firms that have uncertainty in meeting customer orders. Owing to changes in several set of factors, such as processing time variations, fluctuation in orders, and rise in quality issues etc., would disrupt production schedules and adversely affect the shop performance. Improvements are certainly possible by integrating WLC policies in distinct stages of production that in turn help to keep a steady workflow and balanced shop floor activities. In this study, we have considered the production of a part of a windmill that poses difficulties in production due to changes in processing times. A production shop simulation model was developed by considering real-time data. The model is simulated to analyze the performance under different order release methods at process time changes. In addition, we consider the influence of downtime and capacity cushion at bottleneck station. The objective of this research is to investigate the influence of the processing time variation, downtime, and capacity cushion on the performance of the shop floor and to evaluate the best release method suitable in different situations.

© 2021 Jordan Journal of Mechanical and Industrial Engineering. All rights reserved

Keywords: Workload control, Order release methods, Work in process, Simulation;

1. Introduction

Recently in the domain of production and operations, management workload control (WLC) has gained popularity in job-shop production systems for the multiple benefits of effectively controlling manufacturing [1]. In job shop production systems, the level of uncertainty is extremely high, as it accommodates the varieties of goods that are produced in different volumes. In addition to this, processing time variations, set up time changes, different job sequences, changes in resources etc., are the factors that could affect the production system and make the scheduling work complicated. All these aspects give rise to complexities and uncertainties in taking up new orders and running currently accepted orders [2]. Hence, the impact of such factors on system performance needs to be thoroughly investigated. The likelihood of impact of uncertainty on the system's performance would be predicted and needs to be incorporated into the production planning and scheduling phase. Therefore, a new decision-making model is crucial, that could be designed through WLC concepts to overcome the uncertain production situations.

WLC aligns planning the operations by coordinating and directing shop floor-related activities by integrating complexity issues. WLC makes the manufacturing processes clearer in understanding the manufacturing situation and evades any flaws in decision-making. Design and development of WLC delivers goods at the right time

along with more efficient operations by keeping a steady flow of work, controlled inventory of semi-finished goods and resource use at the best level. WLC is also recognized as input/output control, as it sets the release dates, chooses the processing sequence with effective use and effective monitoring of work progress [3]. Though there is an adequate amount of past research on WLC by Fredendall et al. [4]; Betterton and Silver [5]; Golmohammadi [6]; and Thüerer et al. [7-8], an important environmental factor such as processing time variations that could affect shop performance has not been considered. Thus, in this research, we develop a realistic model of flow shop with processing time variation and analyses performance under different order release methods.

2. Literature Review

The WLC has three major phases that includes job entry, job release and job processing. Job entry shows the orders accepted, but yet to be released on the shop floor for production. The release phase decides the date when each job is to be released on the shop floor. Once released it will remain on the shop floor until all the processes have been completed. The progress of the jobs is governed by the priority dispatch rules in the form of queues. The past literature suggests that researchers have developed a variety of policies that helps to integrate all the three phases to achieve the greatest performance. The main principle of WLC is to control queues and the key decision pertains to

* Corresponding author e-mail: raghu.bhat@manipal.edu.

order release [2-3]. In shops the variations in processing time results in bottleneck and based on the release method adopted leads to shifting of the bottleneck [8]. Goldratt used the concept of the theory of constraints (TOC) for scheduling jobs and developed a popular bottleneck-oriented release policy that is referred to as Drum-Buffer-Rope (DBR) [9]. Implementation of the theory of constraint (TOC) led to improved delivery time, profit, and lead time reduction. Combining TOC and WLC with a change of their order acceptance/buffer management system resulted in substantial improvements in reducing the delivery time [10]. Goldratt argued that the optimum performance would be achieved by keeping an extra capacity than the actual requirements. Although, this additional capacity results in desired imbalance they would be utilized during high production requirements. However, industries without any additional capacity face capacity problems during order fluctuations. This extra capability is referred to as a protective capacity and helps absorb fluctuating workloads and stabilize the system. This DBR method incorporates protective capability and schedules the bottleneck machines by limiting the buffer size in front of the bottleneck machines [4]. Chakravorty [11] integrated dispatch rules with the order methods like DBR, immediate release and modified infinite loading (MIL) in a job shop environment and demonstrated that coupling DBR with the shortest processing time (SPT) yielded better performance than coupling DBR with first-come-first-serve (FCFS) dispatch rule. Besides, DBR performs better than other control policies such as constant work in process (CONWIP) and clockwork (CW) in the case of a single bottleneck machine. Other release methods such as pull from both bottleneck machines (PFBB) performed better than CONWIP, CW, pull from first bottleneck machine (PFB1) and pull from second bottleneck machine (PFB2) for multiple bottlenecks [12]. Furthermore, Enns and Costa [13] found that the bottleneck-oriented release performed effectively in a job shop with high routing variability and aggregate load release outperformed bottleneck-oriented release in a unidirectional flow shop. Additionally, Kim et al. [14] proposed two release methods output flow control (OFC), bottleneck flow control (BFC) and compared with dynamic flow control (DFC) under uncertain production environment. OFC and BFC outperformed DFC in an unbalanced line with work centre breakdown, bottleneck shift and time variability. Golmohammadi [6] debated that the effectiveness of DBR scheduling method in a complex job shop is determined by identifying the most influencing input parameters of scheduling such as batch size, inter-arrival time between the batches and raw material release time etc., and by fine-tuning current rules in setting these parameters. Changes in workload limits are necessary when

a bottleneck shift occurs and there is a performance impact due to physical location, routing position. The effect of bottleneck position in convergent and divergent type flow shops needs to be studied as it forms a complex environment. Past research shows that the bottleneck position and workload limit are strongly associated variables, and it is important to explore dynamic solutions for linking these factors [7]. In a shop with bottlenecks, the schedule at the bottleneck determines shop performance precisely than the workload balancing and hence, release method must be chosen based on bottleneck severity. When there is a mix of jobs, routing varies and affects performance with or without bottleneck results in multiple bottlenecks and bottleneck shifting. The performance difference between WLC and DBR must be analyzed with multiple bottleneck shifting [15]. In general, with a line producing multiple products, each product will have a different constraint station. In such a condition, the influence of setups, a product mix on the location of constraints and their movements need to be investigated. Moreover, studying the relationship between the length of a production line and statistical variations of dependent events are also important [16]. The impact of direction and distance of bottleneck shift on the performance of a job shop must be investigated under the broad environmental settings such as machine failures, scrap rates and process time variability [14]. Research work conducted by Gilland [12]; Thürer et al.[7] demonstrate that DBR is superior to CONWIP, however, exploration is needed to identify the situations and contingent factors, that makes DBR dependent, when compared with CONWIP [8]. Therefore, our research sets up to bridge some of the above-found research gaps by considering an unbalanced line with two bottleneck stations. We perform relevant bottleneck-oriented order release methods in a multi-bottleneck line under a different environmental setting.

3. Conceptual Model

In the present research, we followed an approach proposed by Fernandes et al. [17], which involves developing a model of a production system based on process observation and analyzing the model. We consider a production shop, which manufactures a part of a windmill and production follows stage-by-stage processes in a fixed-line. In this flow shop production system, the arrival of jobs is assumed to be in a random fashion and hence, the inter-arrival times of jobs are considered to follow an exponential pattern [8]. The model is conceptualized through understanding processes and by closely observing the processes that are shown in figure 1.

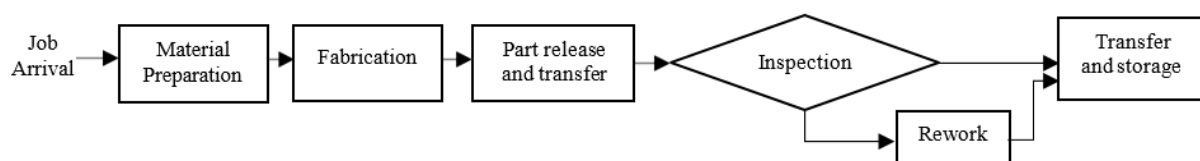


Figure 1. Conceptual model

The production of the part follows a fixed sequence, starts with material preparation, fabrication, release and transfer, an inspection of quality, rework, and finally transfer

and storage. In the material preparation stage, raw materials required for the fabrication of parts are prepared by cutting in required dimensions and kept ready for further processing.

Parts are fabricated in the second stage through the required processes. Once the fabricated parts are ready to release, then the parts are transferred to the inspection bay for quality check. If the defects are observed in the product, the parts are undertaken to repair in the rework area. Finally, the reworked parts are released and deposited in the storage area. In this system, production activities begin with the job release, and flow of jobs takes place serially through the different stages from one end to the other end. If one of the stages is blocked due to any reason, the whole line undergoes disruption and leads to various problems.

In this flow shop, material preparation, part release and transfer, inspection, and storage are the non-bottleneck stations. However, disruptions are quite common in two stages such as fabrication and rework. Fabrication stage contains moulds, the glass layers are laid up, matrix is infused and allowed to cure. Uncertainties in the stage are due to the following reasons: i) the process is labour oriented; ii) infusion is allowed only when the shop temperature is within the limit. Fabrication is time-consuming along with these uncertainties cause a bottleneck. The processing time variations in the rework stage are due to technical issues or observation of defects. It is difficult to predict the processing times due to the criticality of defects in the parts produced. The type, size, location, and severity of the defects are different for each product. Hence, the rework time would vary for each product and is probabilistic in nature. In addition, station breakdowns are the issue that affects the production schedule. These aspects cause bottlenecks and our research makes an effort to understand the benefits of workload control theory in eliminating the detrimental effects of bottlenecks. In supply chain, re-processing is a main stage and it is important to decide whether it is push or pull driven [18]. This research intends to evaluate the impact of change in defect severity on the performance of workload control strategies and determine a suitable strategy for an unbalanced flow shop. Thus, our research intends to examine the following questions that are based on the literature review and real-time issues as observed in the flow shop:

- What are the right release methods to be adopted when there is a variation in the processing time?
- How does the downtime and capacity cushion at bottleneck influence the flow shop performance?

As conducting this experiment is impossible in the real time at the real production shop, we developed a simulation model and analyze the dynamic performance.

4. Simulation Model

Overview of the simulated shop and job characteristics are outlined in section 4.1. Based on the past literature and shop characteristics, we considered bottleneck-oriented order release methods such as CONWIP, immediate release, pull from bottleneck-I, pull from bottleneck-II and pull from both bottlenecks as outlined in section 4.2, priority dispatching rule is described in section 4.3, and experimental design is described in section 4.4.

4.1. Overview of the simulated shop and job characteristics

A simulation model is implemented on Arena V15 software [19-20]. The simulation model is a representation of a pure flow shop with six workstations of dissimilar capacity. Each workstation is unique in terms of capacity and process. The process characteristics are computed through the observation of real-time production and re-entrants are not considered. Inter-arrival time follows an exponential distribution with a mean of 5.09 time units. Operating processing time of non-bottleneck stations follows a 2-Erlang distribution with a mean of 1.06 time units and a maximum of 1.63 time units. It was identified that there are two processes as bottleneck stations based on the process time requirements. In bottleneck station-II, the severity of defects is categorized into three levels based on the frequency of defects and rework time observed in the process. Operating processing time of bottleneck stations follows a 2-Erlang distribution with a mean of 2.4 time units and a maximum of 3.8 time units. Station downtime is measured based on the combination of mean time to repair and mean time between failures. The station downtime is set at three levels i.e., 10%, 15% and 20%. Capacity cushion is considered only at the first bottleneck station at three levels i.e., 0%, 2%, 4%. These shop and job characteristics modeled in the simulation study are summarized in Table 1.

Table 1: Summary of simulated shop and job characteristics

Shop Characteristics	
Shop Type	Pure flow shop; Fixed sequence
Characteristics	Real
Routing Variability	Unidirectional
Re-entrants	No
Number of workstations	6
Workstation capacity	Unequal
Job Characteristics	
Operation processing time (non-bottleneck station)	2-Erlang distribution; (min=0.45; mean = 1.06; max = 1.63) time units
Operation processing time (bottleneck stations)	2-Erlang distribution; (min=1; mean = 2.4; max = 3.8) time units
Inter-arrival times	Exponential distribution; mean=5.09 time units
Downtime levels	10%, 15%, 20%
Capacity cushion	0%, 2%, 4%

4.2. Order release methods (ORR)

Our research focus on the flow shop with bottleneck stations and past literature suggests the execution of bottleneck-oriented release methods. Hence, we considered relevant order release methods such as CONWIP, Immediate release, pull from bottleneck-I, pull from bottleneck-II, and pull from both bottlenecks.

4.3. CONWIP

In this release policy, the work in process in the entire production shop is kept constant. Every new release of the job to the production system is based on the completion of previously released job and work in process is kept under a specified limit.

4.4. Immediate Release (IMMD)

In the immediate release method, the jobs are released immediately to the shop floor without any prior conditions. This conservation policy follows first come first serve basis. The jobs are being released on the shop floor are immediately taken up for processing without applying any rules.

4.5. Pull from Bottleneck-1 (PFB1)

In this release policy, the quantity of jobs is held constant at the first bottleneck station. A new job is released only when the job finishes the first bottleneck station.

4.6. Pull from Bottleneck-2 (PFB2)

In this release method, the quantity of jobs is fixed before the second bottleneck station, and a new job is released only after the processing of the second bottleneck machine.

4.7. Pull from both Bottlenecks (PFBB)

In this release method, setting a maximum number of jobs before both the first and second bottleneck stations. A new job is released when work in process before each bottleneck is under the set limit.

4.8. Shop floor dispatching rules

Once the jobs are released to the shop floor, operations are performed in a particular sequence that depends on the type of dispatching rule used. Priority dispatching helps to monitor the progress of jobs waiting in the form of queues in front of machines on the shop floor. If an order release method is effective in keeping the length of queues in a desirable limit then dispatch rules become unproductive and, in such cases, use of conservative rule like first-come-first-serve (FCFS) would be beneficial [3]. In this research, we have considered a flow shop that processes only one type of product adopting a FCFS basis.

4.9. Experimental Design

We have conducted three distinct set of experiments for three variables such as processing time variation, station downtime, and capacity cushion. In each experiment, a full 5x3 factorial experimental design was used. Five release methods have been applied at three levels of each variable, which results in 15 experiments. In each combination strategy, five replications are used with initial 1000 hours

discarded (warm-up period) to reach steady-state conditions. Each experiment is run for 10000 hours. We consider one factor at a time for experimentation.

5. Simulation Results and analysis

We discuss the shop performance under three levels of process time variation, station downtime, and capacity cushion. In addition, we conduct an analysis of variance (ANOVA) for critical variable process time variation. The results are described in the subsequent sections.

5.1. Process time variation

We statistically analyzed the simulation results by conducting ANOVA to investigate the comparative effect of experimental factors. The ANOVA results help to understand the relationship between various release methods under each level of processing time variation (PTV). In this test, PTV is taken as the blocking factor for different processing time levels, are considered as the different systems. The main effects and interaction effects of PTV and ORR are captured and presented in the ANOVA Table 2.

The dependent variables in the study are production time, work in process inventory, fabrication waiting time, rework waiting time, and resource utilization. The independent variables are the PTV and ORR. At 5% significance level, the main effects of PTV, ORR and interaction effects of (PTV*ORR) are discussed. When the main effects are considered, with respect to p-values less than 0.05, first factor, PTV has significant influence on all the performance factors except fabrication time and resource-I utilization. Second factor, ORR has significant influence on fabrication waiting time and rework waiting time.

When the interaction effects of (PTV*ORR) are considered, the factors with p-values less than 0.05, i.e., p-value=0.028 for fabrication waiting time and p-value=0.00 for rework waiting time, shows the significant influence on the performance. This identifies that the relationship between order release methods and waiting times depends on process time variation. Hence, it is critical to identify the bottleneck stations to improve the performance of the shop. When the main effects are considered, process time variation has considerable influence on production time, work in process inventory, rework-waiting time and resource-II utilization and the results are insignificant with fabrication waiting time and resource-I utilization. Second factor, ORR significantly influence only fabrication waiting time and rework waiting time. Some significant facts have been observed from the results and graphs. Performance is measured based on the production time, work in process level, waiting time at two operations and resource utilization. The experimental results are plotted to understand the performance of various ORR. The performance is shown in the graphs, (Figure 2 to Figure 5) with the X-axis representing PTV from low to high.

Table 2. ANOVA Results

Performance Measure	Sources of variance	Degrees of freedom	Sum of squares	Mean squares	F-ratio	p-value
ProductionTime	Process time variation (PTV)	2	137633	68816.7	223.54	0.00
	Order release rules (ORR)	4	278	69.6	0.23	0.923
	PTV*ORR	8	1114	139.3	0.45	0.884
	Error	60	18471	307.9		
Work InProcess	Process time variation (PTV)	2	839.11	419.555	29.45	0.00
	Order release rules (ORR)	4	30.49	7.622	0.53	0.711
	PTV*ORR	8	95.63	11.953	0.84	0.572
	Error	60	854.8	14.247		
Fabrication Waiting time	Process time variation (PTV)	2	109885	54942	1.24	0.296
	Order release rules (ORR)	4	18739725	4684931	106.03	0.00
	PTV*ORR	8	834796	104349	2.36	0.028
	Error	60	2651107	44185		
Rework waiting time	Process time variation (PTV)	2	5591171	2795586	39.33	0.00
	Order release rules (ORR)	4	6798285	1699571	23.91	0.00
	PTV*ORR	8	3449631	431204	6.07	0.00
	Error	60	4265105	71085		
Resource-I Utilization	Process time variation (PTV)	2	0.000889	0.000445	0.46	0.634
	Order release rules (ORR)	4	0.002957	0.000739	0.76	0.554
	PTV*ORR	8	0.006621	0.000828	0.85	0.56
	Error	60	0.058156	0.000969		
Resource-II Utilization	Process time variation (PTV)	2	0.421736	0.210868	237.99	0.00
	Order release rules (ORR)	4	0.002332	0.000583	0.66	0.624
	PTV*ORR	8	0.005999	0.00075	0.85	0.566
	Error	60	0.053162	0.000886		

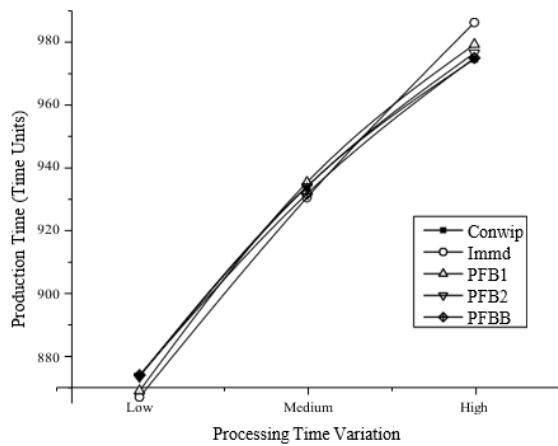


Figure 2. Production time (Time Units)

It is observed that the performances of individual order release rules are vary with the defect criticalities. Hence, a single order release method may not be suitable at a different level of settings.

Figure 2 demonstrates that when production time is considered with immediate-release, it shows better results in lower and medium levels of bottleneck severity, but shows poor results at a high level of bottleneck severity. CONWIP does not perform well at a lower level of bottlenecks, performs moderately at a medium level, and works out to be

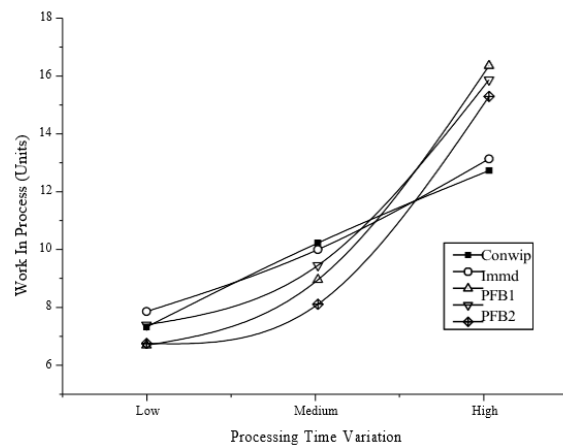


Figure 3. Work in process (Units)

better at high levels of bottleneck severity. PFB1 and PFB2 perform moderately at all levels of bottleneck severity. PFB3 shows better results only at high levels of bottleneck severity.

The Work in process inventory results is shown in figure 3. When work in process inventory is concerned, CONWIP followed by immediate release yields better results at high levels of PTV. PFB3 performed better in low and medium levels of PTV. PFB1 and PFB2 were not suitable in any levels of PTV due to its poor results.

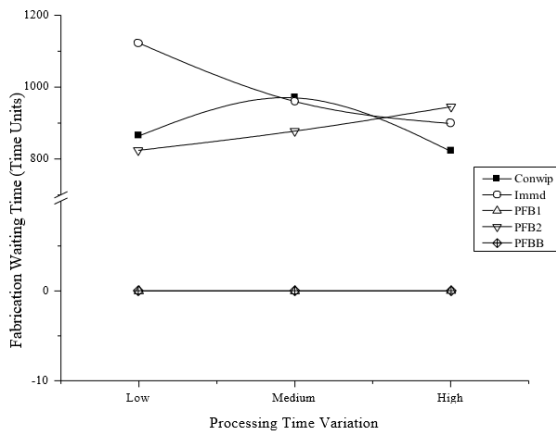


Figure 4. Fabrication waiting time (TimeUnits)

The fabrication-waiting time is shown in Figure 4. PFB1 and PFB3 yielded better results irrespective of levels of PTV as these release methods have closer control over the bottleneck station-1. When we compare the other three ORRs such as CONWIP, IMMD, and PFB2, PFB2 works better at lower and medium levels of PTV, CONWIP performs better only in the high level of PTV. IMMD works satisfactorily at higher levels of PTV and showed poor results at low and medium levels of PTV.

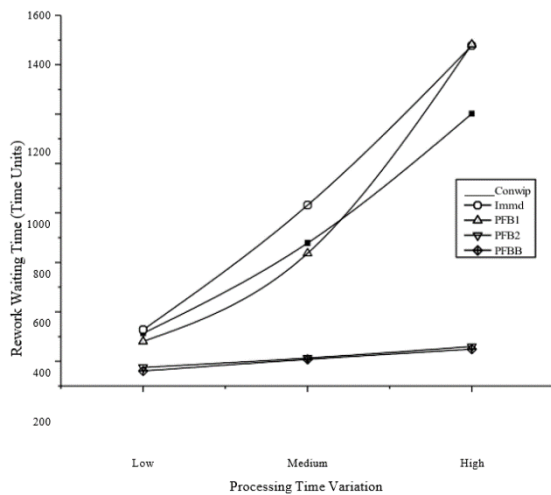


Figure 5. Rework waiting time (Time Units)

Figure 5 shows the results for rework waiting time, PFB1 and PFB3 are highly effective in reducing the waiting times at both bottleneck stations at all levels of severity. When CONWIP, immediate release and PFB1 are concerned, at a low level the results are same, but as the severity increases, CONWIP works better than other release policies. PFB1 shows better results at low and medium levels of severity but its performances diminish at the higher level of severity. PFB1 limits only the bottleneck station-I and parts passed the first bottleneck will wait at the second bottleneck, which results in work in process, hence performance declines.

Figure 6 shows the resource utilization of the first bottleneck station during PTV. Resource-I is utilized approximately from 83 to 85 per cent of the times irrespective of the level of PTV. This indicates the utilization of resource-I is uninterrupted due to the

changes in processing time. The variance observed in the bottleneck station-I is quite less compared to the bottleneck station-II.

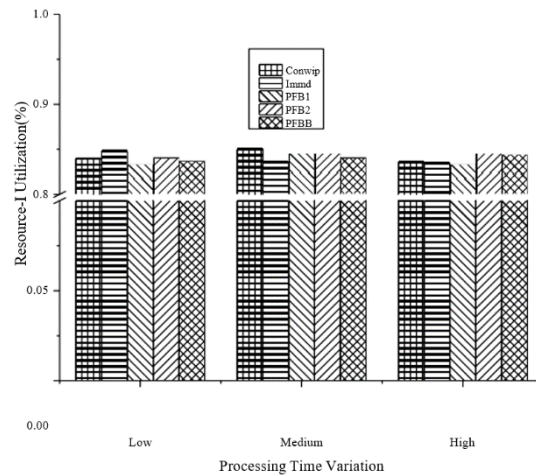


Figure 6. Resource-I Utilization (Percent)

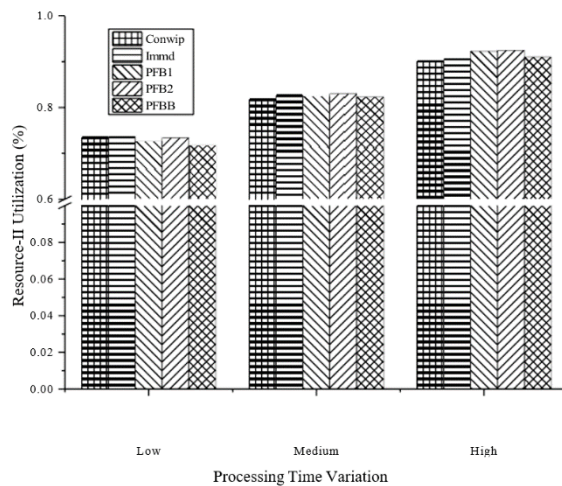


Figure 7. Resource-II Utilization (Percent)

From the graph, it is clear that utilization of resource-II increases from 71 to 92 per cent with the increases in process time variability. As the rework increases the resource requirements also increase which in turn improves the utilization. An extra 8 per cent of capacity cushion still is available to accommodate any variation in orders. Resource utilization of bottleneck station-II is shown in figure 7.

5.2. Downtime levels

The influence of different levels of downtime on performance of flow shop was also investigated. Consideration of downtime levels is based on factors that give rise to downtime such as unexpected machine breakdowns, tool failures and supply chain failures. We investigate the influence of three levels of down time on the work-in-process inventory and throughput under different release methods. The performance in terms of work in process and throughput of is shown in the graphs, (Figure 8 to Figure 9) with the X-axis representing downtime level from 10% to 20%.

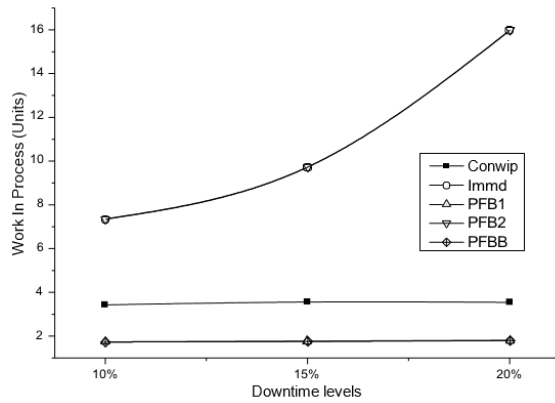


Figure 8. Work in process at downtime levels (Units)

The fluctuations in work-in-process under different down time level is shown in Figure 8. PFB1 and PFB3 generated better results regardless of levels of downtime. CONWIP performed moderately but performance is same at all levels. IMMD and PFB2 are not influenced by the downtime level.

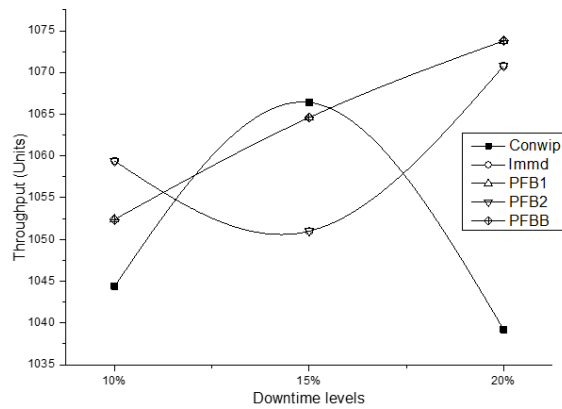


Figure 9. Throughput at downtime levels (Units)

Figure 9. Shows the throughput at various levels of downtime. We observed that release methods IMMD and PFB2 are suitable at lower downtime, CONWIP is best when downtime is moderate and PFB1 and PFB3 which works better when downtime level is high.

5.3. Capacity cushion at bottleneck-I

Literature shows that provision of protective capacity at non-constraints will improve the shop performance [18]. We consider the capacity cushion at constraint station in terms of improving skill level. We assume that skill level improvement will bring down the bottleneck process time. We examine the shop performance like work-in-process and throughput at different levels of capacity cushion. The performance in terms of work in process and throughput of is shown in the graphs, (Figure 10 to Figure 11) with the X-axis representing downtime level from 0% to 4%.

Capacity cushion versus work in process graph is shown in Figure 10. The work-in-process slightly decreases if capacity cushion is introduced but there is no significant improvement. PFB3, PFB1 and CONWIP were not much influenced by the variation of capacity. However, influence was observed in PFB2 and IMMD release methods.

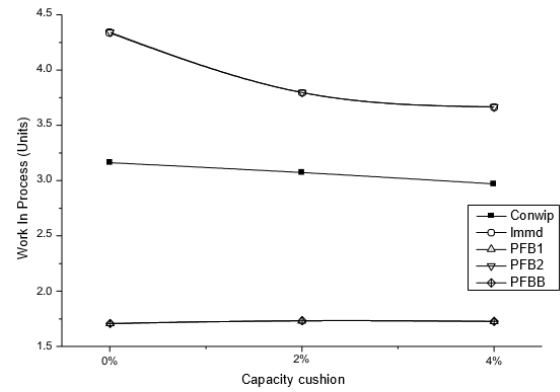


Figure 10. Work in process under capacity cushion (Units)

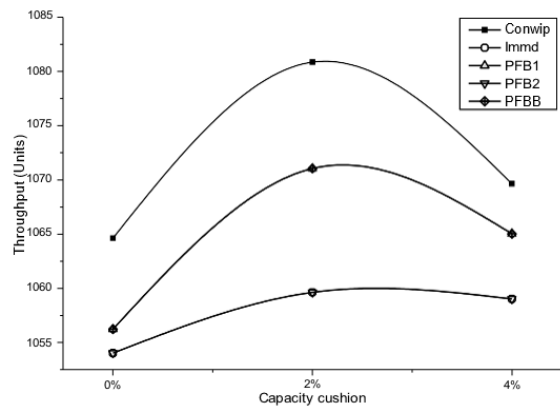


Figure 11. Throughput under capacity cushion (Units)

In Figure 11, we see that throughput improves at 2% improvement of skill level but decreases at 4% improvement. The trend of graph looks same with respect to all release methods. Further improvement of skill level may have adverse effect on the performance. Based on the throughput outcome CONWIP outperformed over other release methods.

5.4. Discussion of results

Gilland [12] argues that in case of dual bottlenecks PFB3 dominates other policies like COWIP, PFB1 and PFB2. In this case it may be certainly true but when process time variability is introduced in a shop with dual bottlenecks CONWIP outperforms other release methods. Gilland [12] demonstrates that if the limit for work in process is set maximum at second bottleneck machine PFB3 works exactly like PFB1. We observe similar behavior in our model and it is due to the shift in control point from second bottleneck to first bottleneck. Betterton and Cox [9] argued that release method can be chosen as to help overcome variability. Additionally, releasing jobs by assessing bottleneck capacity and stop release during unexpected downtimes as it might cause bottlenecks. We use similar approach in our model and observe that performance is not much influenced by the downtime level. It might be due to availability of buffer level in front of bottleneck machine which absorb fluctuations during long run. Research studies [21-22] focused on the influence of protective capacity towards reducing the bottleneck shifts. Research outcomes state that protective capacity at non-constraint stations helps to overcome bottleneck shifting and improve flow time.

Fredendall et al. [4] found that the bottleneck and the protective capacity important parameter to judge the shop performance. Thüerer et al. [7] describes that protective capacity can be changed either by redistributing capacity or by manipulating the flow shop work. Weredistribute work in flow shop by placing capacity cushion at bottleneck station in terms of improvement in skill level. We found that improvements are certainly possible with optimum level of capacity cushion.

6. Conclusion

This research has investigated the performance of a flow shop with different release methods under distinct levels of uncertainty. Simulation model of a production system was developed which has six workstations with two bottleneck stations. The performance of the production is measured in terms of production time, work in process inventory, throughput, resource utilization and waiting time at bottleneck machines. Simulation results show that CONWIP is best ORR in terms of all performance measures, at higher process time variability. However, when the performance is measured based on waiting time and work in process level, PFB1 performed better at the medium level of process time variability and PFBB is best at lower levels of process time variability. The improvement in resource utilization is observed, as there is an increase in the process time variation. The ANOVA results showed that PTV has a significant effect on performance. However, the main effects of ORR and the interaction effects of ORR*PTV are statistically significant only with respect to fabrication waiting time and rework waiting time. It is insignificant on other factors, which may be due to two following reasons: i) the process that considered has machines with less process time difference between the machines. ii) The bottleneck release methods exercised in this study are similar type. When downtime is introduced at bottleneck station, PFBB and PFB1 outperformed. CONWIP worked well when a capacity cushion placed at bottleneck station, results show that any further addition of capacity may lead to loss of performance. The release methods applied in the study used work in process as control criteria, i.e., the work in process level is varied in each release methods. Hence, the release methods are not significant for the considered scenario. However, as other studies this study too have limitation, we have not considered the aspect of due date which could be incorporated into future research and analyzed. Literatures suggest that six sigma practices would help to improve quality of product and reduce production time by concentrating on process parameters [23]. Further studies are also possible that focus on reducing quality problems by incorporating six sigma methodologies.

Acknowledgments

Author declares that there is no conflict of interest.

REFERENCES

[1] Thüerer, M., Stevenson, M., and Land, M.J., "On the integration of input and output control: Workload Control

- order release". *International Journal of Production Economics*, Vol. 174, 2016, 43–53.
- [2] Sabuncuoğlu, I., and Karapinar, H.Y., "A Load-based and Due-date-oriented Approach to Order Review/Release in Job Shops". *Decision Sciences*, Vol. 31 (2), 2000, 413–447.
- [3] Land, M.J., and Gaalman, G.J.C., "The Performance of Workload Control Concepts in Job Shops: Improving the Release Method". *International Journal of Production Economics*, Vol. 56–57, 1998, 347–364.
- [4] Fredendall, L.D., Ojha, D., and Patterson, J.W., "Concerning the theory of workload control." *European Journal of Operational Research*, Vol. 201, 2010, 99–111.
- [5] Betterton, C.E. and Silver, S.J., "Detecting bottlenecks in serial production lines – a focus on interdeparture time variance". *International Journal of Production Research*, Vol. 50 (15), 2012, 4158–4174.
- [6] Golmohammadi, D., "A study of scheduling under the theory of constraints". *International Journal of Production Economics*, Vol. 165, 2015, 38–50.
- [7] Thüerer, M., Qu, T., Stevenson, M., Li, C.D., and Huang, and G.Q., "Deconstructing bottleneck shiftiness: the impact of bottleneck position on order release control in pure flow shops". *Production Planning and Control*, Vol. 28 (15), 2017, 1223–1235.
- [8] Thüerer, M., and Stevenson, M., "Bottleneck-oriented order release with shifting bottlenecks: An assessment by simulation", *International Journal of Production Economics*, Vol. 197, 2018, 275–282.
- [9] Betterton, C.E., and Cox III, J.F., "Espoused drum-buffer-rope flow control in serial lines: A comparative study of simulation models". *International Journal of Production Economics*, Vol. 117, 2009, 66–79.
- [10] Eboş, J., Korte, G. J., and Land, M.J., "Improving a practical DBR buffering approach using Workload Control". *International Journal of Production Research*, Vol. 41 (4), 2003, 699–712.
- [11] Chakravorty, S.S., "An evaluation of the DBR control mechanism in a job shop environment". *OMEGA*, Vol. 29, 2001, 335–342.
- [12] Gilland, W.G., "A simulation study comparing performance of CONWIP and bottleneck-based release rules". *Production Planning Control*, Vol. 13 (2), 2000, 211–219.
- [13] Enns, S.T., and Prongue Costa, M., "The Effectiveness of Input Control Based on Aggregate versus Bottleneck Work Loads". *Production Planning and Control*, Vol. 13 (7), 2002, 614–624.
- [14] Kim, S., Davis, R.K., and Cox III, J.F., "An investigation of output flow control, bottleneck flow control and dynamic flow control mechanisms in various simple lines scenarios. *Production Planning and Control: The Management of Operations*", Vol. 14 (1), 2003, 15–32.
- [15] Thüerer, M., Stevenson, M., Silva, C., and Qu, T., "Drum-Buffer-Rope and workload control in high variety flow and job shops with bottlenecks: an assessment by simulation". *International Journal of Production Economics*, Vol. 188, 2017, 116–127.
- [16] Betterton, C.E., and Cox III, J.F. "Espoused drum-buffer-rope flow control in serial lines: A comparative study of simulation models". *International Journal of Production Economics*, 117, 2009, 66–79.
- [17] Fernandes, N.O., Silva, C., and Carmo-Silva, S., "Order release in the hybrid MTO–FTO production". *International Journal of Production Economics*, Vol. 170, 2015, 513–520.
- [18] Jayanth, A, Gupta, P and Garg, S.K., "Perspectives in Reverse Supply Chain Management(R-SCM): A State-of-the-Art Literature Review". *Jordan Journal of Mechanical and Industrial Engineering*, 2012, 87–102.

- [19] Renna, P. "Dynamic Control Card in a Production System Controlled by CONWIP Approach". Jordan Journal of Mechanical and Industrial Engineering, 2010. 425 – 432.
- [20] Kelton, W.D., Sadowski, R.P., and Swets, N.B. "Simulation with ARENA". McGrawHill Education. 2017.
- [21] Craighead, C.W., Patterson, J.W., and Fredendall, L.D. "Protective capacity positioning: Impact on manufacturing cell performance". European Journal of Operational Research, 134, 425-438.
- [22] Kadipasaoglu, S.N., Xiang, W., Hurley, S.F., and Khumawala, B.M. "A study on the effect of the extent and location of protective capacity in flow systems". International Journal of Production Economics, 63, 2000, 217-228.
- [23] Mandahawi, N., Fouad, R. H., Obeidat, S. "An Application of Customized Lean Six Sigma to Enhance Productivity at a Paper Manufacturing Company". Jordan Journal of Mechanical and Industrial Engineering, 2012, 103 – 109.

The Effects of Sulfur Content on the Mechanical Properties of Nitrile Butadiene Rubber with Different Aging Conditions

Nabeel Alshabatat^{a*}, Ahmad Abouel-Kasem^b

^aMechanical Engineering Department, Tafila Technical University, Tafila 66110, Jordan

^bMechanical Engineering Department, King Abdulaziz University, Rabigh 21911, Saudi Arabia

Received November 28 2020

Accepted August 15 2021

Abstract

This paper aims to investigate the effects of sulfur addition on enhancing the mechanical properties of Nitrile Butadiene Rubber (NBR) composites. The composites were prepared with the assistance of internal mixer and two-roll mill, and then the specimens were vulcanized by electrically heated press. The NBR composites were prepared with different sulfur contents (2, 3, 4, 5, and 7 phr). The tensile strength, hardness, compression set, tear strength, and swelling ratio were investigated. The experimental results showed that the addition of sulfur to NBR composites improved their mechanical properties. The unaged NBR composite containing 7 phr of sulfur gives the best 20% modulus (650% improvement), and shore A hardness (27.4% improvement). However, the unaged NBR composites containing 4 phr of sulfur gives the minimum compression set (i.e., 3.2%). Also, adding small amount of sulfur (less than 4 phr) increases the tear strength. The unaged NBR composite containing 2 phr of sulfur gives the best tear strength (106% improvement). The swelling ratio decreases significantly with adding sulfur contents. The unaged NBR composites containing more than or equal to 3 phr of sulfur give 0% swelling. Also, the effects of different aging conditions were investigated. The results showed that NBR composites which were aged in ozone and air degraded more seriously than those aged in oil.

© 2021 Jordan Journal of Mechanical and Industrial Engineering. All rights reserved

Keywords: Nitrile Butadiene Rubber; sulfur content; rubber aging; mechanical properties;

1. Introduction

Rubbers are extensively used in industrial components (vibration isolators, automotive belts, fuel hoses, oil seals, gaskets, etc.) [1], and can also be used in civil engineering applications to improve seismic performance [2]. Fillers and additives are used to control the mechanical properties of rubber, to reduce the cost of rubber products, and to improve rubber processing [1]. Different types of fillers and additives have been considered in rubber production, such as carbon black, silica [2], titanium dioxide [3], carbon fiber [4], carbon nanotubes [5], kaolin [6], nano kaolin [7], hybrid fillers [1], etc. The choice of fillers and additives is closely related to the kind of required properties. In recent years, several researchers have studied the effects of fillers and additives on the mechanical properties of Nitrile Butadiene Rubber (NBR). Carbon black (CB) is commonly used to enhance the mechanical properties of NBR. Mostafa et al. [8, 9] found that increasing CB content, improves the tensile and compressive strength, hardness, compression set ratio, and wear resistance of NBR, on the other hand, increasing CB content can reduce the ductility and swelling ratio. Salkhord and Ghari [10] found that using hybrid filler, which consists of organoclay and nano-calcium carbonate, showed reinforcement of NBR. This filler improved significantly the tensile strength and decreased the swelling coefficient. The effect of using silica and nanoclay as a

hybrid filler in NBR was investigated by Salehi et al. [11]. The results showed that this hybrid composite has higher strength and ductility compared to silica or nanoclay filled NBR. Düşünceli et al. [12] investigated the effect of polyurethane (PU) and carnuba wax (CW) on the mechanical properties of NBR coating gloves. They found that adding CW to NBR coating gloves increased slightly the breakage force, and decreased slightly the elongation at breakage, and increased the abrasion resistance. On the other hand, adding PU to NBR decreased the breakage force, and increased elongation at breakage, and decreased the abrasion resistance. Sadeghalvaad et al. [13] studied the effect of adding multiwall carbon nanotubes (MWCNT) and carbon nanofibers (CNF) to reinforce NBR. The results showed that increasing the contents of MWCNT or CNF increased the hardness, and decreased the elongation at break and compression set ratio. However, 5 phr of MWCNT or CNF gave the highest strength of the prepared NBR composites. The effects of waste materials on the mechanical properties of NBR were also studied. Setyarini et al. [14] considered the influence of the addition of waste materials on hardness and tensile strength of NBR. In particular, they investigated the effect of adding rice husk, recycled rubber, and charcoal. They found that the addition of these waste materials led to increase the hardness of NBR. On the other hand, various effects were observed on the tensile strength. For example, rice husk and charcoal led to reduce the tensile strength while the recycled rubber filler

* Corresponding author e-mail: nabeel@ttu.edu.jo.

led to increase the tensile strength slightly. Taib et al. [15] used nanocrystalline cellulose (CNC) as a reinforcement agent in NBR. They found that 5 phr of CNC was very efficient to improve the overall mechanical performance.

Sulfur is a vulcanizing agent which is widely used for chemically crosslinking of unsaturated elastomers. The use of sulfur alone leads to a slow reaction, so the optimal effect of sulfur vulcanization systems is attained in the existence of activators and accelerators [16]. The chemistry of vulcanization is complex and the resulting crosslinks may be monosulfidic (C-S-C), disulfidic (C-S₂-C), and polysulfidic (C-S_x-C, x = 3-6). The amounts of these bonds depend on the vulcanization system, the cure time, and the temperature. Increasing the ratio between sulfur and accelerators decreases the monosulfidic and increases the polysulfidic [17]. In general, increasing the ratio between sulfur content and accelerator in rubber increases the crosslink density [18]. The structure and density of the crosslinks have a significant influence on rubber composite properties [19]. Several researches have been performed to study the effects of sulfur addition on the mechanical properties of rubber composites. For example, González et al. [17] investigated the effect of using two vulcanization systems (i.e., conventional and efficient) on the physical properties of unfilled natural rubber (NR). High sulfur contents and low accelerator contents are called conventional cure systems, while, low sulfur contents with high accelerator contents are known as efficient cure systems. They found that the tensile and tear strengths are higher for conventional cure systems. Tamási and Kollár [19] investigated the effect of different content of sulfur curing system on the hardness of NR. It was found that the hardness of NR composites increased significantly with increasing sulfur content. El-Nemr [20] investigated the effect of different curing systems on the mechanical properties of NBR composites. The results showed that the crosslink density increased with increasing the contents of sulfur, dicumyl peroxide, dicumyl peroxide/coagent, and radiation/coagent. The NBR composites contained varied contents of sulfur (1, 1.5, and 2 phr) and a fixed content of CB (30 phr). With increasing sulfur content in NBR composites, the hardness, modulus of elasticity, and modulus at a given elongation increased, but swelling ratio decreased.

Most of the rubbers used in industry are frequently subjected to environmental conditions such as elevated temperature, ozone, oil, etc. If the rubbers are subjected to these conditions, their properties will degrade during the time (thermal aging). The main processes during thermal aging are (1) aging due to volatilization and loss of fillers and additives [21], and (2) thermal oxidative aging reactions including crosslink formation, crosslink breakage, main-chain scission, etc. [22]. The crosslinking and chain scission reactions change the network structure. These changes affect significantly the mechanical properties [23]. The effect of aging of NBR on its mechanical properties has been studied for many years. For example, Mostafa et al. [24] studied the effect of CB content on the thermal aging resistance of NBR composites under different aging temperature. They found that thermal aging in oven increased the hardness, decreased the tensile and compressive strengths. However, increasing CB content decreased the aging resistance. Zhao et al. [25] investigated

the effect of aging period and temperature on NBR composites using recovery from bending (RFB) test and hardness test. The obtained results showed that increasing the aging temperature and time decreased the RFB% and increased the hardness. The results showed that the aging process passed through three stages; before 60 h, between 60 h and 1700 h, and after 1700 h. In the first stage, NBR lost some additives such as paraffin and antioxidants. In the second stage, further loss in additives occurs and the cross linking plays a dominant role. In the third stage, the cross-linking density is very high and severe oxidation happens and causes chain scissions.

Although extensive researches were carried out to study the effect of fillers and additives on the mechanical properties of Rubbers, the studies on the effects of sulfur addition on mechanical properties of NBR composites are quite limited. To the best of authors' knowledge no article studies the effects of thermal aging resistance of NBR composites with variable sulfur contents. Therefore, the aim of the present study is to investigate the effects of adding sulfur with different amounts (2-7 phr) on the mechanical properties of NBR composites, filled with 50 phr of carbon black, and to determine the effects of thermal aging in oil, in air, and in ozone on the mechanical properties of the prepared composites. The mechanical properties are analyzed in the context of tensile properties, hardness, compression set, tear strength, and swelling ratio.

2. Experimental part

2.1. Materials

The constituent components for preparation of NBR composites include NBR-7150 (28% acrylonitrile, Moony viscosity (ML1+4) of about 51 at 100°C, and specific gravity of 0.98), zinc Oxide (ZnO), stearic acid, carbon black N330, aromatic oil, tetramethyl thiuram disulfide (TMTD), benzothiazole disulfide (MBTS), and sulfur. All the materials used in this study were supplied by the Higher Institute of Rubber, Yanbu, Kingdom of Saudi Arabia. The CB was used as a filler, ZnO and stearic acid were used to activate the curing process, TMTD and MBTS were used to accelerate the cure and control cure rate, sulfur was used as a curing agent, and the aromatic oil was used to help in mixing, calendaring, and molding. The specimens investigated in this study were composed of NBR composites with different contents of sulfur according to the recipes shown in Table 1. The code letter S represents sulfur and the subscript represents the amount of sulfur in part per hundred part of NBR (phr).

The mixing of the ingredients was carried out in two steps. In the first step, the NBR, CB, ZnO, stearic acid, and aromatic oil were mixed in the internal mixer. In the second step, the TMTD, MBTS, and sulfur were added to the blend and mixed on a two-roll rubber mill at 75°C. The optimal vulcanization parameters were determined using Moving Die Rheometer (MDR). The vulcanization was carried out using electrically heated press at 140°C for 20 min. Thereafter, the resulted vulcanized NBR sheets were maintained at ambient conditions for 24 hour, then test specimens, were cut from the sheets.

Table 1. Formulated composition of NBR composites.

Ingredient	Quantities (phr)					
	S ₀	S ₂	S ₃	S ₄	S ₅	S ₇
NBR-7150 (Low)	100	100	100	100	100	100
ZnO	5	5	5	5	5	5
Stearic acid	2	2	2	2	2	2
Aromatic oil	10	10	10	10	10	10
Carbon black (330)	50	50	50	50	50	50
MBTS	2	2	2	2	2	2
TMTD	0.15	0.15	0.15	0.15	0.15	0.15
Sulfur	0	2	3	4	5	7

2.2. Aging methods

One objective of this paper is to study the effect of sulfur content on the ability of NBR to withstand the effect of aging under different aging conditions to identify the behavior under degradation environment which rubber usually subjected. Three different aging scenarios were considered (i.e., aging in oil, aging in ozone, and aging in air). Thermal aging of NBR composites was carried out in a temperature-controlled air-circulating oven at 100 °C for 24 hours. Specimens were either hung in the air (air aging) or immersed in oil tubes open to air (oil aging). Then, the specimens were taken out of the oven, cleaned by tissues, and cooled to room temperature. The aging in ozone was carried out in an ozone climate chamber with an ozone concentration of 200 ppm for 24 hours.

2.3. Testing methods

The tensile characteristics of NBR composites were acquired using a 10 kN capacity tensile tester (AT 10, Alpha Technologies, OH, USA) based on ASTM D-412 standards [26]. The specimens were cut from NBR composites molded sheets into dumbbell shape using sharp and free of nicks cutting die (gauge length of 33 ± 0.25 mm, width of 6 ± 0.25 mm, and thickness of 2 ± 0.04 mm). The test cross head speed was 500 mm/min. The tensile tests were recorded as the average of three repeated tests for each NBR composite.

The hardness tests were applied according to ASTM D2240 standard [27]. The hardness was measured by using Shore A durometer (RX-DD-4, Electromatic, NY, USA) with an accuracy of 0.1 Shore A. On each specimen, the hardness was measured at five different locations, from which the average Shore A hardness was determined.

Compression set is a measure of the ability of rubber to retain their elastic properties after prolonged compression at constant strain. Compression set tests were applied based on ASTM D-395 standard [28]. The specimens have cylindrical shape with diameter of 29.0 ± 0.5 mm and thickness of 12.5 ± 0.5 mm. The molding assembly shown in Fig. 1 is used for the tests. It consists of two plates and four bolts to compress the NBR specimens, and two spacers to allow enough clearance for bulging of the NBR specimens. The specimens were compressed to 25% of the initial thickness and the whole assembly was placed in an oven at 100°C for 24 hour. Then, the specimens were allowed to cool (i.e., allow the specimens to rest on a poor

thermally conducting surface such as wood), and then the final thicknesses of the specimens were measured. The compression set percentage was used to measure the permanent deformation and can be given by

$$Comp.set \% = \frac{t_o - t_f}{t_o - t_s} \times 100\% , \quad (1)$$

where t_o and t_f are the original and final thicknesses of the specimen, respectively, and t_s is the spacer thickness. The compression set tests were recorded as the average of five repeated tests for each NBR composite.

The specimens of the tear strength were cut into 90 degree angle-shaped specimens and the tests were applied according to ASTM D624 standards [29] using a 10 kN capacity tensile tester (AT 10, Alpha Technologies, OH, USA) with cross-head speed of 8.5 mm/s. The testing machine applies a tension force on the specimen until the tear take place some way perpendicular to stress direction. Tear strength is given by F_{max}/t ; where F_{max} is the maximum force required to rip a rubber sample, and t is the average thickness. The tear tests were recorded as the average of three repeated tests for each NBR composite.

Swelling tests were applied based on ASTM D-471 standards [30]. The dimensions of test specimens are 25 mm x 15 mm x 2 mm. Initially, the weights of the dry specimens were measured. Then the specimens were immersed in oil (i.e., Castrol Engine Oil 20w-50) in a heating device at 100° C and for 24 hours. After that, the specimens were removed from the test tubes, the oil was cleaned from specimens' surfaces, and the specimens were immediately weighed. The swelling ratio ($Q\%$) was used to describe the swelling behavior of NBR composites and defined as

$$Q\% = \frac{W_A - W_o}{W_o} \times 100\% , \quad (2)$$

where W_o and W_A are the weights of the specimens before and after swelling, respectively. The oil swelling tests were recorded as the average of five repeated tests for each NBR composite.

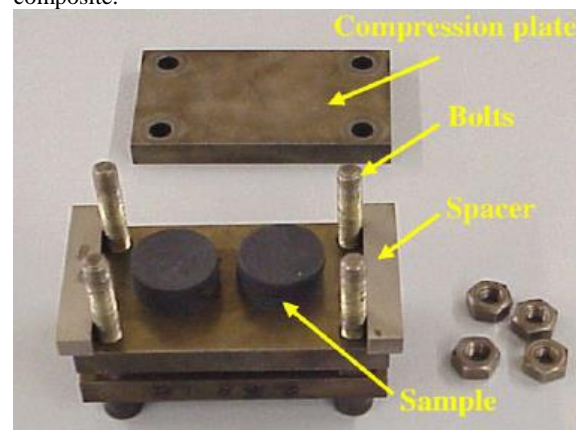


Figure 1. Compression set assembly

3. Results and Discussion

To determine the effect of sulfur addition on the mechanical properties of NBR composites, specimens with different sulfur contents were prepared according to recipes in Table 1. The results of tensile test are represented in Figs.

2 and 3. Figure 2 shows the variation of stress at 20% strain (20% modulus) with sulfur content for different aging scenarios, and Fig. 3 shows the variation of strain at 1.5 MPa-stress. It is clear from Fig. 2 that the NBR composites with sulfur have high strength compared with NBR composites without sulfur. For example, the 20% modulus of the unaged NBR composites with 7 phr sulfur was 4.92 MPa in comparison with 0.65 MPa for unaged NBR composites without sulfur. This might be attributed to the crosslinking density which, in general, increases with increasing sulfur content in rubber [18] (i.e., with increasing sulfur content, the number of sulphidic bonds increases and thus the crosslinking density increases also). The increase of the crosslinking density leads to the reduction of rubber chains mobility. As a consequence, lower strain is observed with adding sulfur (see Fig. 3). For example, the strain, at 1.5 MPa-stress, of unaged NBR composites with 7 phr sulfur was 0.054 in comparison with 1.487 for unaged NBR composites without sulfur.

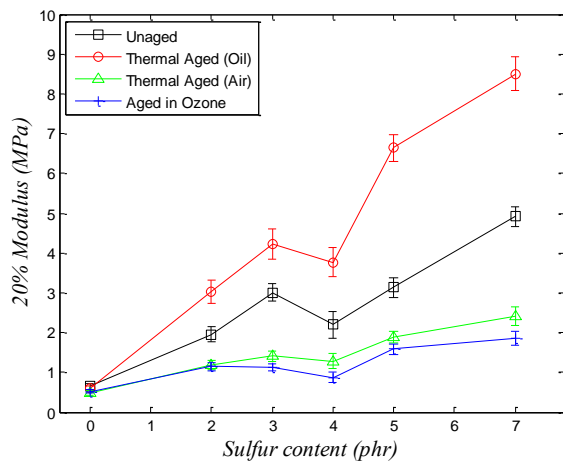


Figure 2. The variation of tensile stress of NBR composite with different sulfur contents and aging scenarios at 20% strain (20% modulus).

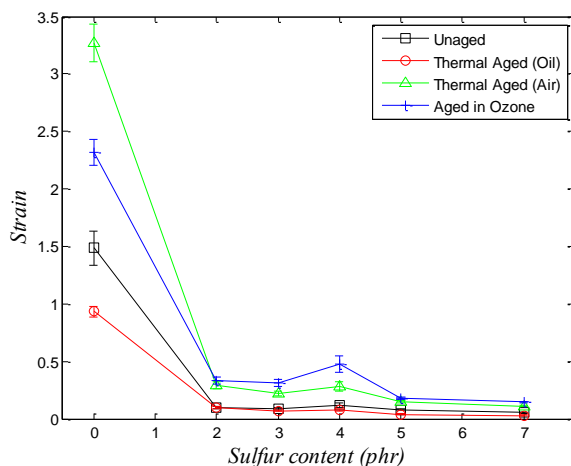


Figure 3. The variation of strain of NBR composites with different sulfur contents and aging scenarios at 1.5 MPa-stress.

During aging, NBR composites lost some additives and fillers [21], and some oxidation reactions occurred such as crosslinking and chain scission [22]. In general, the loss of additives and fillers has a negative effect on the strength of NBR composites. On the other hand, increasing the crosslinks increases the strength to some limit. After that,

the higher crosslinking density results in the reduction of the strength (i.e., over crosslinking takes place) [23]. As shown in Fig. 2, thermal aging in air reduced the strength of NBR composites and this might be attributed to the dominant effect of the loss of additives and fillers. However, thermal aging in oil enhanced the strength of NBR composites, and this might be explained as the oil itself adhered to the surface of NBR specimens and formed a protective layer which slowed down the migration and volatilization of the additives and fillers from NBR composites. Also, the oil itself oxidized which lowered the oxygen concentration around the rubber specimens [31]. Thus, the effect of crosslinking is dominant in this case. It is worth to note that, in this study, the accelerating aging processes were carried out for duration of 24 h only. For longer thermal aging period, the crosslinking density becomes very high and severe oxidation happens and causes more chain scissions [25].

The hardness results of the prepared NBR composites are presented in Fig. 4. The results were dependent on the content of sulfur and type of aging. For all NBR composites, the hardness increased by increasing sulfur content, and this results might be attributed to the fact that increasing sulfur content increases the crosslinking density which makes the NBR composites harder. Results with similar trend, for unaged NBR composites, were obtained by El-Nemr [20]. For unaged NBR composites, the highest hardness was 79 ShA for the unaged NBR composites with 7 phr sulfur which is greater than the hardness of the unaged NBR composites without sulfur by 27.4%. As shown in Fig. 4, aging NBR composites in air and ozone increased the hardness due to the crosslinks formation and the oxidizing layer at the surface of specimens [24]. However, aging in oil decreased the hardness because the oil penetrated into the rubber caused softening for the surface of specimens.

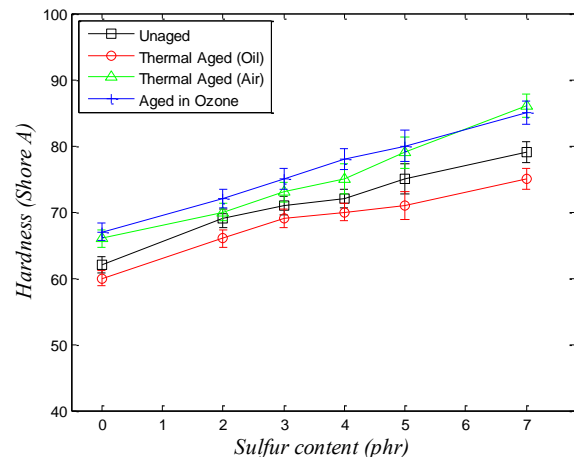


Figure 4. The variation of shore hardness of NBR composites with different sulfur contents and aging scenarios.

The results of the compression set tests are presented in Fig. 5. The figure shows the variations of the compression set percentage of NBR with sulfur contents and type of aging. As shown, the compression set of NBR decreased rapidly by adding sulfur. The results can be interpreted by the increase in the crosslinking density in NBR composites. Therefore, the mobility of the rubber chains decreased. For example, the compression set percentage for unaged NBR composites with 4 phr sulfur content was 3.2% in comparison with 58.3% for unaged NBR composites

without sulfur. Aging processes decreases significantly the ability of NBR composites to elastic recovery after removing the load. By aging, the crosslinking increased and the network structure became tighter, and thus the compression set increased [32]. The compression set of NBR composites aged in air and ozone is greater than that of NBR composites aged in oil, indicating the more severe degradation. Results with similar trend, for unaged hydrogenated NBR seals, were obtained by Lou et al. [33]. For thermally aged specimens, with increasing sulfur content, the compression set decreased noticeably followed by an increase. The increase of compression set percentage, at high sulfur content, might be attributed to the formation of polysulfidic bonds between rubber molecules. These polysulfidic bonds are more susceptible to cleavage during thermal aging than mono- and disulfidic bonds [17]

The tear strength of NBR rubber composites with different sulfur contents is shown in Fig.6. Tear strength increased with increasing sulfur contents up to 2 phr of sulfur, and then the tear strength decreased with increasing the sulfur contents. For unaged specimens, the maximum tear strength was 35 kN/m, which is 106 % greater than the tear strength of NBR without sulfur. By increasing sulfur content, the crosslinking density increased. Reasonable increasing of crosslinking density improved the tear strength considerably. High crosslinking density (i.e., over-crosslinking) caused unbalanced distribution of crosslinking points and caused stress concentration during loading process, which finally resulted in a reduction of tear strength of rubber composites [17].

In addition to mechanical properties, the capability of NBR composites to swell oil was investigated. Oil swelling has negative effects on rubber. Oil may extract chemicals from rubber or it may chemically react with it which can lead to deterioration of the mechanical properties with time. The results of swelling tests, for unaged specimens, are shown in Fig.7. It can be seen that the swelling ratio of NBR composites decreased significantly with adding sulfur due to the increase of crosslinking density. These crosslinks restrict extensibility of the rubber chains induced by swelling and make it more difficult for oil to diffuse into the gaps between rubber molecules and decrease the swelling percentage. The swelling ratio for NBR composites, with sulfur contents equal or greater than 3 phr, was almost 0%.

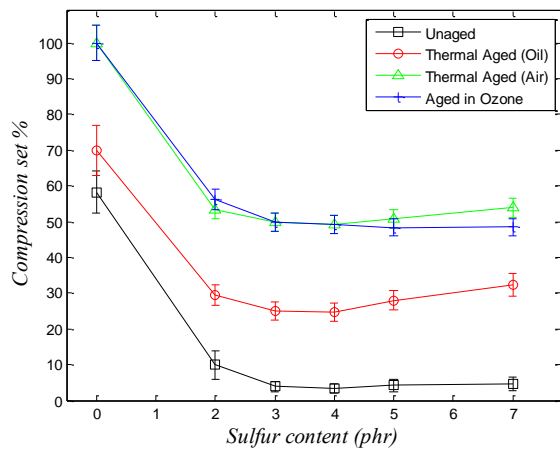


Figure 5. The variation of compression set ratio of NBR composites with different sulfur contents and aging scenarios.

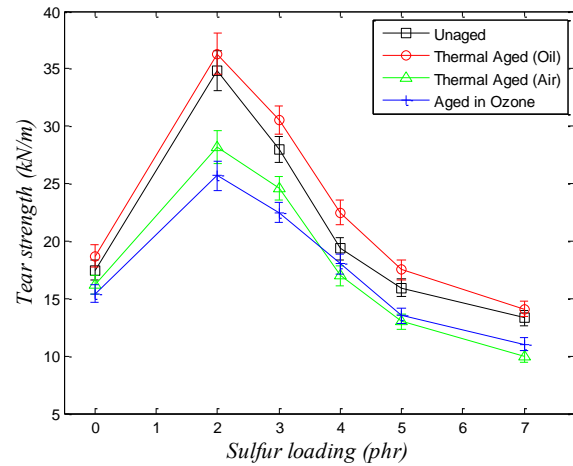


Figure 6. The variation of tear strength of NBR composite with different sulfur contents and aging scenarios.

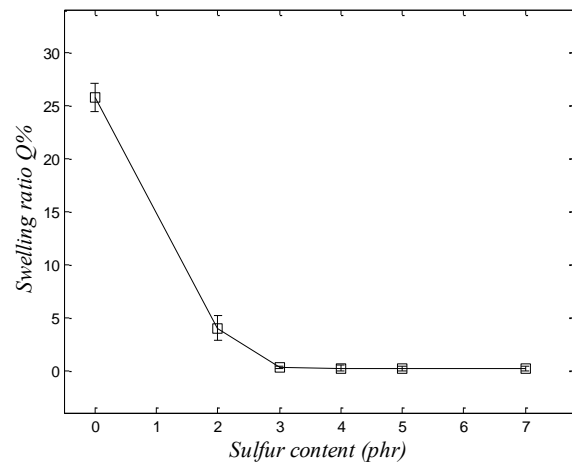


Figure 7. The variation of swelling ratio of NBR composite with different sulfur contents

4. Conclusion

The current work investigates the influence of sulfur contents and aging conditions on the mechanical properties of NBR composites. Tensile, hardness, compression set, tear strength, and swelling properties were examined. Also, accelerating aging of NBR composites in oil, air, and ozone for 24 h was investigated. The following conclusions can be made:

1. Sulfur addition affects significantly the tension properties of NBR composites. In general, the 20% modulus increases and strain at 1.5 MPa-stress decreases with increasing sulfur content. The average 20% modulus of unaged specimens, with 7 phr of sulfur, is 4.92 MPa while that of unaged specimens, without sulfur, is 0.65 MPa. Thermal aging of NBR composites in oil increases the 20% modulus while aging them in air or ozone decreases the 20% modulus.
2. Sulfur addition increases the shore A hardness of NBR composites. The average shore A hardness of unaged specimens, with 7 phr of sulfur, is greater than that of unaged specimens, without sulfur, by 27.4%. The aging of NBR composites in air or ozone increases shore A hardness. On the other hand, the aging of NBR composites in oil decreases shore A hardness.

3. Increasing sulfur content in NBR composites decreases compression set considerably. For unaged NBR composites, using 4 phr of sulfur, decreases the compression set percentage to 3.2%, while the compression set percentage for specimens without sulfur is 58.3%. Thus, NBR composites with sulfur content are very good candidate to use in gaskets, seals, and vibration isolation blocks. Aging of NBR composites in air or ozone increases the compression set and reaches a value of 100% for specimens without sulfur.
4. Tear strength of NBR composites increases by increasing sulfur content and reaches a maximum value at 2 phr of sulfur content. Then, increasing sulfur content decreases the tear strength. For unaged specimens, with 2 phr of sulfur content, the maximum tear strength was 35 kN/m, which is 106 % greater than the tear strength of unaged specimens without sulfur.
5. Adding sulfur to NBR composites decreases significantly the swelling ratio. The swelling ratio reaches 0% when the sulfur content greater than or equal to 3 phr.
6. NBR composites which are aged in ozone and air degrade more seriously than those aged in oil.

References

- [1] Z. Abdul Salim, A. Hassan, H. Ismail, "A review on hybrid fillers in rubber composites". *Polymer-Plastics Technology and Engineering*, Vol. 57, No. 6, 2018, 523-539.
- [2] J. Bai, Y. Zhang, S. Wu, "Review study of physical and mechanical characteristics on mixed soil with scrap tire rubber particles". *Jordan Journal of Mechanical and Industrial Engineering*, Vol. 14, No. 1, 2020, 71-79.
- [3] Z. Abdul Salim, A. Hassan, H. Ismail, "The effect of high purity rice husk silica synthesized using solvent-thermal extraction method on the properties of natural rubber compounds". *Bioresources*, Vol. 13, No. 3, 2018, 6936-6951.
- [4] J. Datta, P. Kosiorok, M. Wloch, "Effect of high loading of titanium dioxide particles on the morphology, mechanical and thermos-mechanical properties of natural rubber-based composites". *Iranian Polymer Journal*, Vol. 25, 2016, 1021-1035.
- [5] R. Soundararaj, K. Senthilvel, N. Rathinam, B. Prabu, "Experimental studies on mechanical properties of natural rubber carbon black-carbon nanotube composite". *Materials Today: Proceedings*, Vol. 38, 2021, 3077-3084.
- [6] N. Nasruddin, S. Agustini, M. Sholeh, "Utilization of kaolin as a filling material for rubber solid tire compounds for two-wheeled electric scooters". In *IOP Conference Series: Materials Science and Engineering*, Vol. 1143, No. 1, 2021, 1-6.
- [7] A. Al Robaidi, N. Anagreh, M.A. Addous, S. Massadeh, "Crystallization behavior of iPP/LLDPE blend filled with nano kaolin particles". *Jordan Journal of Mechanical and Industrial Engineering*, Vol. 7, No. 1, 2013, 35-39.
- [8] A. Mostafa, A. Abouel-Kasem, M. Bayoumi, M. El-Sebaie, "The influence of CB loading on thermal aging resistance of SBR and NBR rubber compounds under different aging temperature". *Materials & Design*, Vol. 30, No. 3, 2009, 791-795.
- [9] A. Mostafa, A. Abouel-Kasem, M. Bayoumi, M. El-Sebaie, "Insight into the effect of CB loading on tension, compression, hardness and abrasion properties of SBR and NBR filled compounds". *Materials & Design*, Vol. 30, No. 5, 2009, 1785-1791.
- [10] S. Salkhord, H. Sadeghi Ghari, "Synergistic reinforcement of NBR by hybrid filler system including organoclay and nano-CaCO₃". *Journal of Applied Polymer Science*, Vol. 132, No. 44, 2015, 42744 (1-14).
- [11] M.M. Salehi, T. Khalkhali, A.R. Dourbash, "Effect of Simultaneous Use of Silica and Nanoclay in Rubber Compounds Based on Nitrile Rubber". *Journal of Rubber Research*, Vol. 21, No. (3), 2018, 165-181.
- [12] N. Düşünceli, L. Akyüz, N. Şahin, H. Duru, "The effect of polyurethane and carnauba wax on the mechanical and physicochemical properties of acrylonitrile butadiene nitrile rubber coating working gloves". *Journal of Elastomers & Plastics*, Vol. 51, No. 1, 2019, 36-51.
- [13] M. Sadeghalvaad, E. Dabiri, S. Zahmatkesh, P. Afsharimoghadam, "Improved curing conditions and mechanical/chemical properties of nitrile butadiene rubber composites reinforced with carbon based nanofillers". *Journal of Nanostructures*, Vol. 9, No. 3, 2019, 453-467.
- [14] P. Setyarini, P. Purnomo, D. H. Sulistyarini, A. Asfia, "The effect of addition of waste materials on nitrile butadiene rubber to the mechanical properties of roller rubber". *Key Engineering Materials*, Vol. 851, 2020, 47-52.
- [15] M. Taib, W. Yehye, N. Julkapli, "Synthesis and characterization of nanocrystalline cellulose as reinforcement in nitrile butadiene rubber composites". *Cellulose Chemistry and Technology*, Vol. 54, No. 1, 2020, 11-25.
- [16] J. Kruželák, R. Sýkora, I. Hudec, "Sulphur and peroxide vulcanisation of rubber compounds — overview". *Chemical papers*, Vol. 70, No. 12, 2016, 1533-1555.
- [17] L. González, A. Rodríguez, J.L. Valentin, A. Marcos-Fernández, P. Posadas, 2005. "Conventional and efficient crosslinking of natural rubber: Effect of heterogeneities on the physical properties". *Kautschuk Gummi Kunststoff*, Vol. 58, 2005, 638-643.
- [18] A. Masa, S. Soontaranon, N. Hayeemasae, "Influence of sulfur/accelerator ratio on tensile properties and structural inhomogeneity of natural rubber". *Polymer*, Vol. 44 No. 4, 2020, 519-526.
- [19] K. Tamási, M.S. Kollár, "Effect of different sulfur content in Natural Rubber mixtures on their thermo-mechanical and surface properties". *International Journal of Engineering Research and Science*, Vol. 4, No. 2, 2018, 28-37.
- [20] K.F. El-Nemr, "Effect of different curing systems on the mechanical and physico-chemical properties of acrylonitrile butadiene rubber vulcanizates". *Materials & Design*, Vol. 32, No. 6, 2011, 3361-3369.
- [21] X. Liu, J. Zhao, Y. Liu, R. Yang, "Volatile components changes during thermal aging of nitrile rubber by flash evaporation of Py-GC/MS". *Journal of analytical and applied pyrolysis*, Vol. 113, 2015, 193-201.
- [22] J. Zhao, R. Yang, R., Iervolino, B. van der Vorst, S. Barbera, "The effect of thermo-oxidation on the continuous stress relaxation behavior of nitrile rubber". *Polymer Degradation and Stability*, Vol. 115, 2015, 32-37.
- [23] W. Lou, W., Zhang, H. Wang, T. Jin, X. Liu, "Influence of hydraulic oil on degradation behavior of nitrile rubber O-rings at elevated temperature". *Engineering Failure Analysis*, Vol. 92, 2018, 1-11.
- [24] A. Mostafa, A. Abouel-Kasem, M. Bayoumi, M. El-Sebaie, "The influence of CB loading on thermal aging resistance of SBR and NBR rubber compounds under different aging temperature". *Materials & Design*, Vol. 30, No. 3, 2009, 791-795.
- [25] J. Zhao, R. Yang, R., Iervolino, S. Barbera, "Changes of chemical structure and mechanical property levels during thermo-oxidative aging of NBR". *Rubber Chemistry and Technology*, Vol. 86, No. 4, 2013, 591-603.
- [26] ASTM D412-16: 2016- Standard Test Methods for Vulcanized Rubber and Thermoplastic Elastomers-Tension, ASTM International, West Conshohocken, PA.

- [27] ASTM D2240-15: 2015- Standard Test Method for Rubber Property— Durometer Hardness, ASTM International, West Conshohocken, PA.
- [28] ASTM D395-18: 2018- Standard Test Method for Rubber Property— Compression Set, ASTM International, West Conshohocken, PA.
- [29] ASTM D624-00: 2020- Standard Test Method for Tear Strength of Conventional Vulcanized Rubber and Thermoplastic Elastomers, ASTM International, West Conshohocken, PA.
- [30] ASTM D471-16a: 2016- Standard Test Method for Rubber Property— Effect of Liquids, ASTM International, West Conshohocken, PA.
- [31] X. Liu, J. Zhao, R. Yang, R. Iervolino, S. Barbera, “ Effect of lubricating oil on thermal aging of nitrile rubber”. *Polymer Degradation and Stability*, Vol. 150, 2018, 136-143.
- [32] R. Han, Y. W. X. Q. K. Niu, “Effects of crosslinking densities on mechanical properties of nitrile rubber composites in thermal oxidative aging environment”. *Applied Polymer*, 49076, 2020.
- [33] W. Lou, W., Zhang, T. Jin, X. Liu, W. Dai “Synergistic effects on multiple environmental factors on degradation of hydrogenated nitrile rubber seals”. *Polymers*, Vol. 10, 2018, 897.

A Hybrid Batch-Fabrication Decision for a Vendor–Buyer Integrated System with Multiple Deliveries, Rework, and Machine Failures

Yuan-Shyi Peter Chiu^a, Chia-Ming Lai^a, Tiffany Chiu^b, Chung-Li Chou^{c,*}

^a*Dept. of Industrial Engineering & Management, Chaoyang University of Technology, Taichung 413, Taiwan*

^b*Anisfield School of Business, Ramapo College of New Jersey, Mahwah, NJ 07430, USA*

^c*Dept. of Business Administration, Chaoyang University of Technology, Taiwan*

Received December 2 2020

Accepted September 8 2021

Abstract

Transnational firms operate in turbulent and competitive marketplaces. They continually find ways to optimize their internal supply chains to guarantee that firms achieve operating goals of high quality, quick response time, smooth fabrication schedules, and timely deliveries under the reality of limited capacity and unreliable machines/processes. This study considers a vendor–buyer integrated batch-fabrication problem with outsourcing, rework, machine failures, and multiple deliveries to facilitate better decision making and assist enterprises in increasing their competitive advantages. We assume that a portion of a batch is outsourced in order to reduce manufacturing uptime, and in-house production experiences undesirable situations, such as machine failures and nonconforming stock making. Corrective action on failures and repair tasks of the nonconforming are undertaken in each cycle as they occur. The finished stocks are then shipped under the multiple-deliveries plan. We build a model to explicitly depict the problem and determine the problem's cost function through formulations and derivations. The convexity of cost function and the optimal uptime are obtained via differential calculus and a proposed specific algorithm. Lastly, we offer a numerical example to show our proposed model makes diverse crucial system information, such as the individual and joint impact of outsourcing, rework, random failures, as well as the frequency of delivery on different features and the optimal uptime of the problem, easily accessible, to assist enterprises in strategic planning, management, and decision making in their practical intra-supply-chain environments.

© 2021 Jordan Journal of Mechanical and Industrial Engineering. All rights reserved

Keywords: Vendor-buyer integrated system, Hybrid batch fabrication, Machine failures, Rework, Multi-delivery;

1. Introduction

To facilitate better decision-making for transnational enterprises and assist them in increasing competitive advantages, we explore a vendor-buyer integrated batch-fabrication problem with outsourcing, rework, machine failures, and multiple deliveries. Many real-world production processes experience undesirable situations, such as machine failures and nonconforming stock making. Corrective actions on failures and repair tasks of the nonconforming are undertaken to avoid unwanted disruption/delay in production and poor/unacceptable product quality. Lee and Moinzadeh [1] considered a multi-echelon batch-ordering-based repairable system to analyze its operating characteristics. The authors evaluated the outstanding orders' distribution and subsequently backorders as two parameters in their proposed approximation scheme. Through tests of various scenarios of infinite and finite servers, they found that their proposed scheme could effectively determine the system stock levels that minimize the total inventory holding and backordering costs. The authors also compared certain outstanding

orders' distribution to that in the existing literature. Groenevelt et al. [2] explored the batch-production problem considering an unreliable manufacturing facility and safety stocks. They assumed the machine failure rate is constant, but failure repair time is random. To meet the desired service level, safety stocks are used. Different bounds for service levels were set to explore the influence of various system parameters on these ranges. The authors introduced a policy for production control to show how safety stock works under the renewal process type of a specific single-server queue. They also demonstrated how their results could be fitted in a wider resource allocation managerial decision making. Moini and Murthy [3] considered the batch-sizing problem of an unreliable fabrication system. The authors built a model to clearly characterize their unreliable system and different repair strategies to determine the cost-minimization batch sizes under these separate strategies. Sha et al. [4] studied a photolithography scheduling problem for wafer fabrication considering an on-line rework policy. The authors incorporating on-line rework into the dispatching rule with the aim of reducing production procedure and machine workload, as well as increasing the output rate. Goerler and Voß [5] investigated

* Corresponding author e-mail: echungc@cyut.edu.tw.

the impacts of nonconforming stock and rework process on the batch-size problem with limited capacity. The mixed-integer programming technique was presented to deal with the problem. Diverse numerical experiments were carried out to analyze the influences of variations in defective occurrences on computer times needed to generate the batch size solution. Extra studies [6-14] explored the influence of various characteristics of the unreliable machine and rework strategy on manufacturing systems and operations management.

In the production planning/scheduling stage, the outsourcing alternative can effectively achieve these goals to reduce the manufacturing uptime and/or release some workloads from the machine. Gaimon [15] examined the strategic trade-offs problem regarding subcontracting versus capacity expansion, specifically, for the service-sector environments featuring excessive seasonal demand or quick technological improvement, where demand exceeds current inventory/capacity. The author explored the critical influence of subcontracting on the company's competitive pricing strategy and found out that the optimal price policy can be determined by the higher of either unit subcontracting cost or unit in-house fabrication cost. Jolayemi and Olorunniwo [16] examined a deterministic multi-plant production-transportation problem with multiple warehouses and subcontracting options. A profit-maximization model was developed to help decide the optimal plans for the (1) batch sizes for each factory, (2) shipping quantities from each factory to each warehouse, (3) on-hand inventories for each warehouse, and (4) subcontracting quantities for each warehouse. The authors gave numerical examples to demonstrate how their model works and discussed the limitations of their proposed model. Arias-Aranda et al. [17] considered the benefits and operations flexibility from implementing an outsourcing strategy in service-oriented enterprises. The authors carried out their study by the structural analysis to reveal that outsourcing benefits significantly increase as the operations' flexibility rises, especially in the operational areas of the firms' markets, personnel, expansion, and information systems. Rosar [18] studied the relationship between strategic subcontracting and the optimal purchase policy. The author first presented an outsourcing option that relies on non-cost-savings subcontracting mechanisms and then extended to cost-savings relevant rationale, discussing the incentives of sellers who are involved in nested subcontracting policies. Additional works [19-23] explored the influence of diverse outsourcing characteristics on the manufacturing sectors and business management.

Furthermore, in real-world supply-chain environments, goods' transportation is often arranged via multiple shipments at specific time intervals. Banerjee and Burton [24] examined the influence of coordinated versus independent stock replenishing disciplines on a single-vendor multi-buyers problem. The authors performed numerous simulation experiments to show that for discrete-lots procurements in a single-vendor multi-buyers problem, the classical batch-size models cannot satisfactorily solve them. The authors recommended that the coordinated common replenishing cycle model is a better approach. Swenseth and Godfrey [25] incorporated the existing transportation cost functions (in the literature) into the stock replenishing decision making without giving in the

accuracy of the decision or increasing unnecessary complexity to its process. Toews et al. [26] examined the classical economic batch ordering/production quantity problems allowing partial backordering option, wherein the backlogging rate is a linear function of the time to delivery. Montarelo et al. [27] studied the four-echelon inventory management decision in the decentralized supply-chain environments using a Tabu searching metaheuristic. The authors assumed different service levels to cope with the market's stochastic demands. They proposed a global simulation approach to explore/optimize the four-echelon linear/nonlinear supply chains and revealed significant differences among echelons in critical inventory and cost parameters. Furthermore, the authors believed that their proposed approach could be generalized for border applications.

Recent studies explored the influence of various features of multiple deliveries on different fabrication-transportation and supply-chain systems. Focusing of these works, including on pricing and lot sizing in a two-echelon supply chain [28], optimization of a specific closed-loop green supply chain [29], price profit structuring for single-vendor and multi-buyer system [30], multiproduct multi-shipment system with expedited rate and rework [31], and stochastic supply chain featuring imperfect production and controllable defects [32]. Since few of the works mentioned above have examined the collective influence of machine failures, outsourcing, multiple deliveries, and rework on batch-fabrication decision making, this study aims to bridge the gap and explicitly build a decision support model to help today's transnational firms handle the challenge of vendor's unreliable fabrication process, meeting buyer's timely needs of quality multiproduct, and keeping the total operating expenses at a minimum.

2. The proposed hybrid batch fabrication vendor-buyer coordinated system

The description of the proposed vendor-buyer coordinated system with stochastic failure, rework, outsourcing, and multi-delivery is given below. Consider that a buyer's annual demand rate λ units of a particular product are to be met by a vendor using a hybrid batch fabrication plan. In order to shorten the cycle length, a π (where $0 < \pi < 1$) portion of the batch size Q is subcontracted to an outside provider, and the remaining portion is made in-house with an annual fabrication rate P_1 . Thus, a particular unit cost C_π and setup cost K_π are connected to the outsourcing plan, with $C_\pi = (1 + \beta_2)C$ and $K_\pi = (1 + \beta_1)K$, where β_2 and β_1 are the connecting parameters; and C and K denote the in-house unit and setup costs, respectively. We assume that the receipt time of outsourced items is scheduled before starting stock transportation time in each cycle. The outside provider promises the quality of outsourced products.

The fabrication machine is subject to a Poisson distributed failure, with the mean $= \beta$ per year. Thus, time to a machine failure t obeys the Exponential distribution (i.e., density function $f(t) = \beta e^{-\beta t}$). An abort/resume discipline is used when a failure occurs. Under this discipline, the failure repair work starts immediately. A fixed repair time t_r is assumed (in case that actual repair time is greater than t_r , a rental/spare machine will be put in use to

$$T'_\pi = t_{1\pi} + t_r + t'_{2\pi} + t'_{3\pi} \tag{1}$$

$$H_0 = (P_1 - d_1)t \tag{2}$$

$$t_{1\pi} = \frac{Q(1-\pi)}{P_1} \tag{3}$$

$$H_1 = (P_1 - d_1)t_{1\pi} \tag{4}$$

$$t'_{2\pi} = \frac{(1-\pi)Q(x)}{P_2} \tag{5}$$

$$H_2 = H_1 + P_2 t'_{2\pi} \tag{6}$$

$$t'_{3\pi} = T'_\pi - (t_{1\pi} + t_r + t'_{2\pi}) \tag{7}$$

$$T'_\pi = \frac{Q + \lambda t_r}{\lambda} \tag{8}$$

$$d_1 t_{1\pi} = x(P_1 t_{1\pi}) = (1-\pi)Q(x) \tag{9}$$

2.1.1. Stock status in $t'_{3\pi}$ of situation 1

At the beginning of product distribution time $t'_{3\pi}$, the outsourced and safety products are added to the finished lot to bring the shipping quantity up to H .

$$H = H_2 + \pi Q + \lambda t_r \tag{10}$$

The stock level during $t'_{3\pi}$ can be calculated by Eq. (11) [31].

$$\left(\frac{1}{n^2}\right) \left(\sum_{i=1}^{n-1} i\right) H t'_{3\pi} = \left(\frac{n-1}{2n}\right) H t'_{3\pi} \tag{11}$$

2.1.2. The buyer's stock holding status

The buyer's stock holding status in T'_π can be computed by Eq. (12) [31].

$$\frac{1}{2} \left[\frac{H t'_{3\pi}}{n} + (H - \lambda t'_{3\pi}) T'_\pi \right] \tag{12}$$

2.1.3. Total cost per cycle of situation 1

$TC(t_{1\pi})_1$, the total cost per cycle, consists of both the variable and setup costs for fabrication and outsourcing,

$$TC(t_{1\pi})_1 = C[(1-\pi)Q] + K + C_\pi(\pi Q) + K_\pi + C_1(\lambda t_r) + h_3(\lambda t_r)(t_{1\pi} + t_r + t'_{2\pi}) + M + C_R(1-\pi)Q(x) + nK_1 + C_T[Q + \lambda t_r] + \frac{h_2}{2} \left[\frac{H t'_{3\pi}}{n} + (H - \lambda t'_{3\pi}) T'_\pi \right] + h_1 \frac{P_2 t'_{2\pi}}{2} (t'_{2\pi}) + h \left[\frac{H_1 + d_1 t_{1\pi}}{2} (t_{1\pi}) + (H_0 t_r) + (d_1 t) t_r + \frac{H_1 + H_2}{2} (t'_{2\pi}) + \left(\frac{n-1}{2n}\right) H t'_{3\pi} \right] \tag{13}$$

$$E[TC(t_{1\pi})_1] = C(t_{1\pi} P_1) + K + C_\pi(\pi t_{1\pi} P_1 y_1) + K_\pi + C_1 \lambda g + h_3 \left[\lambda g t_{1\pi} + \lambda g^2 + \frac{\lambda g E[x] t_{1\pi} P_1}{P_2} \right] + M + C_R E[x] t_{1\pi} P_1 + nK_1 + C_T [t_{1\pi} P_1 y_1 + \lambda g] + h(P_1 t g) + \frac{t_{1\pi}^2 P_1^2 (h_2 - h)}{2n\lambda(1-\pi)} (y_1 - y_2) + \frac{E[x]^2 t_{1\pi}^2 P_1^2 (h_1 - h)}{2P_2} + h_2 \left[\frac{g t_{1\pi} P_1}{2} (y_1 + y_2) \right] + \frac{g t_{1\pi} P_1 (h_2 - h) (y_1 - y_2)}{2n} + \frac{h_2 t_{1\pi}^2 P_1^2 y_1}{2} \left(\frac{y_2}{\lambda}\right) + h \left[\frac{g t_{1\pi} P_1}{2} (y_1 - y_2) \right] + \frac{h t_{1\pi}^2 P_1^2 y_1}{2\lambda} \left[y_1 + \frac{\lambda(-\pi)}{P_1} + \frac{\lambda E[x](1-2\pi)}{P_2} \right] + h_2 \left(\frac{\lambda g^2}{2}\right) \tag{14}$$

safety products' relevant costs (refer to Fig. 2), repair cost for equipment failure, rework cost, both setup and variable distribution costs, and total holding costs (including buyer's stocks, reworked, finished, and nonconforming) during T'_π , as exposed in Eq. (13).

Substitute formulas (1) to (12) in Eq. (13), and apply the expected value to deal with the randomness of x , the following expected total system cost per cycle of situation one, $E[TC(t_{1\pi})_1]$ could be gained.

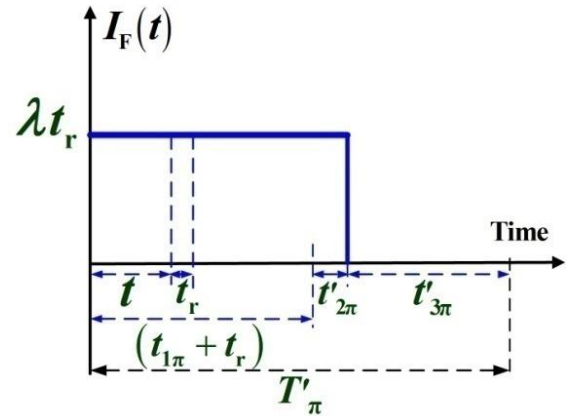


Figure 2. The safety stock level in situation 1 of the proposed system

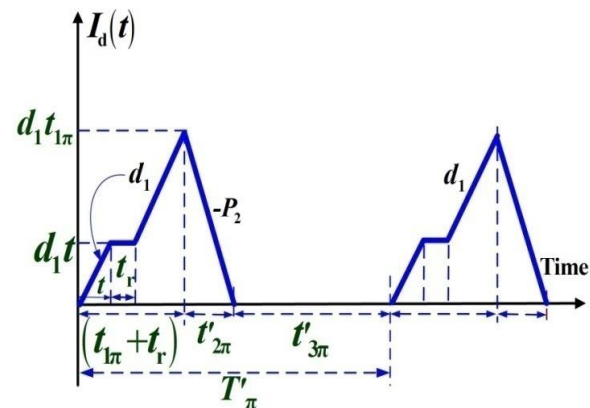


Figure 3. The nonconforming stock level in situation 1 of the proposed system

where

$$y_1 = \frac{1}{(1-\pi)}; y_2 = \lambda \left[\frac{1}{P_1} + \frac{E[x]}{P_2} \right].$$

The expected cycle length in situation one can be gained from Eq. (8) as follows:

$$E[T'_\pi] = \frac{Q + \lambda t_r}{\lambda} = \frac{t_{1\pi} P_1 y_1 + \lambda t_r}{\lambda} \quad (15)$$

2.2. Situation 2: No failure happening in $t_{1\pi}$

In situation two, we have time to failure occurrence $t \geq t_{1\pi}$. Because no failure is happening, the perfect stock level accumulates to H_1 when $t_{1\pi}$ ends, and it reaches H_2 when $t_{2\pi}$ completes. Meantime, the receipt of outsourced products further brings the finished stock level to H at the beginning of distribution time $t_{3\pi}$. Finally, the stock level declines to zero at the end of the fabrication cycle (see Figure 4).

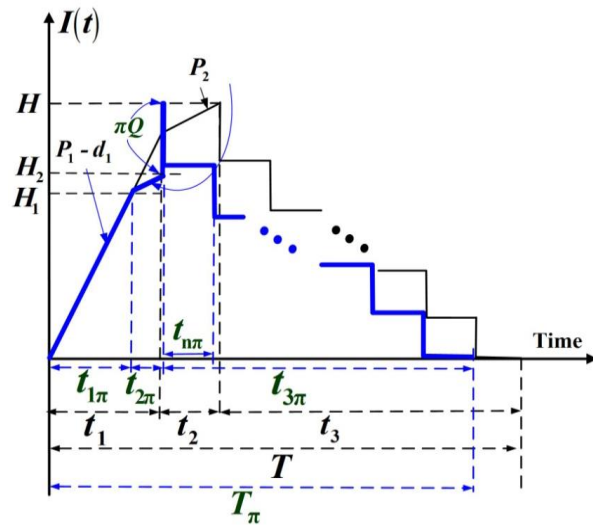


Figure 4. The level of perfect stock in the proposed hybrid batch fabrication vendor-buyer integrated system with multi-delivery and rework, but no failure happening (in blue) as compared to that of a system with rework and multi-delivery (in black)

The safety stock level in situation two remains unchanged throughout T_π . Likewise; the following formulas

$$TC(t_{1\pi})_2 = C[(1-\pi)Q] + K + C_\pi(\pi Q) + K_\pi + h_3(\lambda t_r)T_\pi + nK_1 + C_T Q + C_R(1-\pi)Q(x) + \frac{h_2}{2} \left[\frac{H t_{3\pi}}{n} + (H - \lambda t_{3\pi})T_\pi \right] + h_1 \frac{P_2 t_{2\pi}}{2} (t_{2\pi}) \quad (25)$$

$$+ h \left[\frac{H_1 + d_1 t_{1\pi}}{2} (t_{1\pi}) + \frac{H_1 + H_2}{2} (t_{2\pi}) + \left(\frac{n-1}{2n} \right) H t_{3\pi} \right]$$

$$E[TC(t_{1\pi})_2] = C(t_{1\pi} P_1) + K + C_\pi(\pi t_{1\pi} P_1 y_1) + K_\pi + h_3 g(t_{1\pi} P_1 y_1) + nK_1 + C_T(t_{1\pi} P_1 y_1) + C_R E[x] t_{1\pi} P_1 + \frac{E[x]^2 t_{1\pi}^2 P_1^2 (h_1 - h)}{2 P_2} + \frac{h_2 t_{1\pi}^2 P_1^2}{2(1-\pi)} \left(\frac{y_2}{\lambda} \right) + \frac{t_{1\pi}^2 P_1^2 (h_2 - h) y_1}{2n\lambda} (y_1 - y_2) + \frac{h t_{1\pi}^2 P_1^2 y_1}{2\lambda} \left[y_1 + \frac{\lambda(-\pi)}{P_1} + \frac{\lambda E[x](1-2\pi)}{P_2} \right] \quad (26)$$

where

$$y_1 = \frac{1}{(1-\pi)}; y_2 = \lambda \left[\frac{1}{P_1} + \frac{E[x]}{P_2} \right].$$

The expected cycle length in situation two can be gained as follows:

$$E[T_\pi] = \frac{Q}{\lambda} = \frac{t_{1\pi} P_1 y_1}{\lambda} \quad (27)$$

can be directly obtained from the description of the proposed model and by observation of Figure 4:

$$T_\pi = t_{1\pi} + t_{2\pi} + t_{3\pi} \quad (16)$$

$$H_1 = (P_1 - d_1) t_{1\pi} \quad (17)$$

$$H_2 = H_1 + P_2 t_{2\pi} \quad (18)$$

$$H = H_2 + \pi Q \quad (19)$$

$$t_{1\pi} = \frac{Q(1-\pi)}{P_1} \quad (20)$$

$$t_{2\pi} = \frac{(1-\pi)Q(x)}{P_2} \quad (21)$$

$$t_{3\pi} = T_\pi - (t_{1\pi} + t_{2\pi}) \quad (22)$$

Equation (9) remains valid in situation two. Total holding inventories in $t_{3\pi}$ and at the buyer's location (see Figs. 4 and 5) can be gained by applying Eqs. (23) and (24) [31].

$$\left(\frac{1}{n^2} \right) \left(\sum_{i=1}^{n-1} i \right) H(t_{3\pi}) = \left(\frac{n-1}{2n} \right) H(t_{3\pi}) \quad (23)$$

$$\frac{1}{2} \left[\frac{H(t_{3\pi})}{n} + (H - \lambda t_{3\pi})T_\pi \right] \quad (24)$$

2.2.1. Total cost per cycle of situation 2

$TC(t_{1\pi})_2$, the total cost per cycle, consists of both the variable and setup costs for fabrication and outsourcing, safety products' holding cost (see Figure 7), setup and variable distribution costs, rework cost, and total holding costs (including buyer's stocks, finished, nonconforming, and reworked items) during T_π , as exposed in Eq. (25).

Substitute equations (16) to (24) and (9) in Eq. (25), and use the expected value to deal with the randomness of x , the following expected total system cost per cycle for situation 2, $E[TC(t_{1\pi})_2]$ could be gained.

3. Solving the proposed system

As we assume that Poisson distributed failure rate β per year, so, the time to failure t follows the Exponential distribution, with $f(t) = \beta e^{-\beta t}$ and $F(t) = (1 - e^{-\beta t})$ (i.e., the density and cumulative density functions). We employ the renewal reward theorem to solve the $E[TCU(t_{1\pi})]$ as follows.

Substitute formulas (15) and (27) in formula (29), and then formulas (14), (26), and (29) in formula (28), along

with additional efforts in derivations, $E[TCU(t_{1\pi})]$ can be gained as follows (see Appendix A for details).

The first- and second-derivatives of $E[TCU(t_{1\pi})]$ are shown in equations (B-1) and (B-2) in Appendix B. Since the first term on the right-hand side (RHS) of Eq. (B-2) is positive, it follows that the $E[TCU(t_{1\pi})]$ is convex if the second term on the RHS of Eq. (B-2) is also positive. That means if $\tau(t_{1\pi}) > t_{1\pi} > 0$ holds (see Eq. (B-3) for details).

Once Eq. (B-3) is verified to be true, we can solve the optimal $t_{1\pi}^*$ by setting the first-derivative of $E[TCU(t_{1\pi})] = 0$ (refer to Eq. (B-1)). Since the first term on the RHS of Eq. (B-1) is positive, we have the following.

$$E[TCU(t_{1\pi})] = \frac{\left\{ \int_0^{t_{1\pi}} E[TC(t_{1\pi})_1] \cdot f(t) dt + \int_{t_{1\pi}}^{\infty} E[TC(t_{1\pi})_2] \cdot f(t) dt \right\}}{E[T_{\pi}]} \tag{28}$$

where

$$E[T_{\pi}] = \int_0^{t_{1\pi}} E[T'_{\pi}] \cdot f(t) dt + \int_{t_{1\pi}}^{\infty} E[T_{\pi}] \cdot f(t) dt \tag{29}$$

$$E[TCU(t_{1\pi})] = \left[\frac{\lambda}{y_1 + \frac{\lambda g [1 - e^{-\beta t_{1\pi}}]}{t_{1\pi} P_1}} \right] \left\{ \frac{u_0}{t_{1\pi}} + \frac{u_1}{t_{1\pi}} + u_2 + t_{1\pi} v_3 - h g e^{-\beta t_{1\pi}} + \frac{u_3 e^{-\beta t_{1\pi}}}{t_{1\pi}} \right. \tag{30}$$

$$\left. \left. \begin{aligned} &+ \left[(h g + v_0 + v_1 + v_2) P_1 (y_1 P_1 \beta e^{-\beta t_{1\pi}}) + v_3 P_1 (y_1 P_1 - \lambda g \beta e^{-\beta t_{1\pi}}) \right] t_{1\pi}^2 \\ &+ \left[u_3 P_1 (-y_1 P_1 \beta e^{-\beta t_{1\pi}}) + v_3 P_1 (2 \lambda g - 2 \lambda g e^{-\beta t_{1\pi}}) + (h g - u_2) P_1 \lambda g (\beta e^{-\beta t_{1\pi}}) \right] t_{1\pi} \\ &- (u_0 + u_1) P_1 (y_1 P_1 + \lambda g \beta e^{-\beta t_{1\pi}}) + u_3 P_1 (-\lambda g \beta e^{-\beta t_{1\pi}} - y_1 P_1 e^{-\beta t_{1\pi}}) \\ &- (h g + v_0 + v_1 + v_2) P_1 \lambda g (-e^{-2 \beta t_{1\pi}} + e^{-\beta t_{1\pi}}) - (u_2 + v_0 + v_1 + v_2) P_1 \lambda g (e^{-\beta t_{1\pi}} - 1) \end{aligned} \right\} = 0 \tag{31}$$

Let w_0 , w_1 , and w_2 stand for the following:

$$\begin{aligned} w_0 &= \left[(h g + v_0 + v_1 + v_2) P_1 (y_1 P_1 \beta e^{-\beta t_{1\pi}}) + v_3 P_1 (y_1 P_1 - \lambda g \beta e^{-\beta t_{1\pi}}) \right] \\ w_1 &= \left[u_3 P_1 (-y_1 P_1 \beta e^{-\beta t_{1\pi}}) + v_3 P_1 (2 \lambda g - 2 \lambda g e^{-\beta t_{1\pi}}) + (h g - u_2) P_1 \lambda g (\beta e^{-\beta t_{1\pi}}) \right] \\ w_2 &= -(u_0 + u_1) P_1 (y_1 P_1 + \lambda g \beta e^{-\beta t_{1\pi}}) + u_3 P_1 (-\lambda g \beta e^{-\beta t_{1\pi}} - y_1 P_1 e^{-\beta t_{1\pi}}) \\ &\quad - (h g + v_0 + v_1 + v_2) P_1 \lambda g (-e^{-2 \beta t_{1\pi}} + e^{-\beta t_{1\pi}}) - (u_2 + v_0 + v_1 + v_2) P_1 \lambda g (e^{-\beta t_{1\pi}} - 1) \end{aligned}$$

Then, Eq. (31) can be rearranged as follows:

$$w_0 (t_{1\pi})^2 + w_1 (t_{1\pi}) + w_2 = 0 \tag{32}$$

Finally, $t_{1\pi}^*$ can be gained by applying the following square roots solution:

$$t_{1\pi}^* = \frac{-w_1 \pm \sqrt{w_1^2 - 4 w_0 w_2}}{2 w_0} \tag{33}$$

Since $F(t_{1\pi}) = (1 - e^{-\beta t_{1\pi}})$ and its complement $e^{-\beta t_{1\pi}}$ are both over the interval $[0, 1]$, and Eq. (33) can be rearranged as follows:

$$e^{-\beta t_{1\pi}} = \frac{-v_3 t_{1\pi} P_1 (y_1 P_1 - 2 \lambda g) + (u_0 + u_1) P_1^2 y_1 - (u_2 + v_0 + v_1 + v_2) P_1 \lambda g}{\left\{ \begin{aligned} &(h g + v_0 + v_1 + v_2) P_1^2 y_1 \beta t_{1\pi}^2 + \left[-u_3 P_1^2 y_1 \beta - v_3 t_{1\pi} P_1 \lambda g \beta + (h g - u_2) P_1 \lambda g \beta \right] t_{1\pi} \\ &- \left[(u_2 + v_0 + v_1 + v_2) P_1 \lambda g \right] - \left[(h g + v_0 + v_1 + v_2) P_1 \lambda g (1 - e^{-\beta t_{1\pi}}) \right] - 2 v_3 t_{1\pi} P_1 \lambda g \\ &- \left[(u_0 + u_1) P_1 (\lambda g \beta) \right] + \left[u_3 P_1 (-\lambda g \beta - y_1 P_1) \right] \end{aligned} \right\}} \tag{34}$$

To solve $t_{1\pi}^*$, first, let $e^{-\beta t_{1\pi}} = 0$ and $e^{-\beta t_{1\pi}} = 1$, then calculate Eq. (33) to gain the bounds for $t_{1\pi}$ (i.e., $t_{1\pi U}$ and $t_{1\pi L}$). Next step, use the current $t_{1\pi U}$ and $t_{1\pi L}$ to calculate the update values of $e^{-\beta t_{1\pi U}}$ and $e^{-\beta t_{1\pi L}}$. Re-apply Eq. (33) with the current $e^{-\beta t_{1\pi U}}$ and $e^{-\beta t_{1\pi L}}$ to find a set of update bounds $t_{1\pi U}$ and $t_{1\pi L}$. If $(t_{1\pi U} = t_{1\pi L})$ is true, then $t_{1\pi}^*$ is found (i.e., $t_{1\pi U} = t_{1\pi L} = t_{1\pi}^*$), otherwise, repeat the aforementioned steps, until $t_{1\pi U} = t_{1\pi L}$.

4. Numerical example

This section offers a numerical illustration of the proposed hybrid batch fabrication problem in a vendor-buyer integrated environment featuring multi-delivery, rework, and machine failure. The parameters' values are assumed as follows (see Table 1):

Table 1. The assumed parameters' values in this illustration

K_π	C_π	λ	β	β_2	K_1	P_2	C_R	C	C_1	K	h_2
60	2.8	4000	1	0.4	90	5000	1.0	2.0	2.0	200	1.6
x	π	P_1	M	β_1	C_T	g	h_1	n	h_3	h	
20%	0.4	10000	2500	-0.70	0.01	0.018	0.4	3	0.4	0.4	

We first verify the convexity of $E[TCU(t_{1\pi})]$ by using the aforementioned values of parameters (i.e., make sure that $\tau(t_{1\pi}) > t_{1\pi} > 0$ (see Eq. (B-3)).

Because $e^{-\beta t_{1\pi}}$ falls within the range of [0, 1], we first set $e^{-\beta t_{1\pi}} = 0$ and $e^{-\beta t_{1\pi}} = 1$, and apply Eq. (33) to find $t_{1\pi U} = 0.2780$ and $t_{1\pi L} = 0.0886$. Then, use the present values of $t_{1\pi U}$ and $t_{1\pi L}$ to calculate $e^{-\beta t_{1\pi U}}$ and $e^{-\beta t_{1\pi L}}$. Lastly, apply Eq. (B-3) with the obtained values of $e^{-\beta t_{1\pi L}}$, $e^{-\beta t_{1\pi U}}$, $t_{1\pi L}$, and $t_{1\pi U}$ to confirm that $\tau(t_{1\pi U}) = 0.5205 > t_{1\pi U} = 0.2780 > 0$ and $\tau(t_{1\pi L}) = 0.3073 > t_{1\pi L} = 0.0886 > 0$, respectively. Hence, we confirm the convexity of $E[TCU(t_{1\pi})]$ for $\beta = 1.0$, thus, the optimal $t_{1\pi}^*$ exists. Furthermore, a wider range of β values have been used for the convexity test to show the boarder applicability of our proposed system, for details please refer to Table 2.

Table 2: Convexity test on $E[TCU(t_{1\pi})]$ with a wider range of β values

β	$\tau(t_{1\pi U})$	$t_{1\pi U}$	$\tau(t_{1\pi L})$	$t_{1\pi L}$
10	0.7323	0.2750	0.0465	0.0215
8	0.5757	0.2751	0.0571	0.0261
6	0.4749	0.2752	0.0740	0.0334
4	0.4201	0.2755	0.1053	0.0456
3	0.4126	0.2758	0.1336	0.0553
2	0.4290	0.2763	0.1834	0.0690
1	0.5205	0.2780	0.3073	0.0886
0.5	0.7162	0.2813	0.5175	0.1013
0.01	6.0021	0.5099	5.5977	0.1160

Now, to find $t_{1\pi}^*$, again we first set $e^{-\beta t_{1\pi}} = 0$ and $e^{-\beta t_{1\pi}} = 1$, then apply Eq. (33) to gain the initial bounds for $t_{1\pi}$ (i.e., $t_{1\pi U} = 0.2780$ and $t_{1\pi L} = 0.0886$). Next, we use the current $t_{1\pi U}$ and $t_{1\pi L}$ to compute and update the values of $e^{-\beta t_{1\pi U}}$ and $e^{-\beta t_{1\pi L}}$. Then, we apply Eq. (33) repeatedly using the current $e^{-\beta t_{1\pi U}}$ and $e^{-\beta t_{1\pi L}}$ to obtain a set of update bounds $t_{1\pi U}$ and $t_{1\pi L}$. If $(t_{1\pi U} = t_{1\pi L})$ is true, then $t_{1\pi}^*$ is found (i.e., $t_{1\pi U} = t_{1\pi L} = t_{1\pi}^*$), otherwise, repeat the aforementioned steps, until $t_{1\pi U} = t_{1\pi L}$. Iterative results for finding $t_{1\pi}^*$ are exhibited in Table 3. Hence, the optimal uptime for this example $t_{1\pi}^* = 0.1181$ and $E[TCU(t_{1\pi}^*)] = \$12,295.06$.

4.1. Effect of main system feature on the problem

The effect of uptime $t_{1\pi}$ on expected total system costs $E[TCU(t_{1\pi})]$ is illustrated in Figure 5. It shows the initial bounds for $t_{1\pi}$ and the result of the final solution along with the convexity of $E[TCU(t_{1\pi})]$.

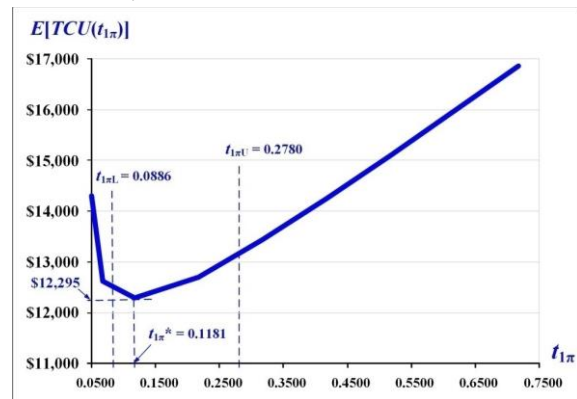


Figure 5. The effect of uptime $t_{1\pi}$ on expected total system costs $E[TCU(t_{1\pi})]$

Table 3: Iterative results for finding $t_{1\pi}^*$

Step #	$t_{1\pi U}$	$e^{-\beta t_{1\pi U}}$	$t_{1\pi L}$	$e^{-\beta t_{1\pi L}}$	$t_{1\pi U} - t_{1\pi L}$	$E[TCU(t_{1\pi U})]$	$E[TCU(t_{1\pi L})]$
-	-	0	-	1	-	-	-
1	0.2780	0.7573	0.0886	0.9152	0.1894	\$13,130.30	\$12,384.26
2	0.1480	0.8625	0.1115	0.8945	0.0365	\$12,349.70	\$12,298.62
3	0.1244	0.8830	0.1167	0.8899	0.0077	\$12,297.94	\$12,295.23
4	0.1195	0.8874	0.1178	0.8889	0.0017	\$12,295.20	\$12,295.07
5	0.1184	0.8883	0.1181	0.8886	0.0003	\$12,295.07	\$12,295.06
6	0.1182	0.8885	0.1181	0.8886	0.0001	\$12,295.06	\$12,295.06
7	0.1181	0.8886	0.1181	0.8886	0.0000	\$12,295.06	\$12,295.06

The influence of changes in rework-relevant ratio C_R/C on $E[TCU(t_{1\pi}^*)]$ is depicted in Figure 6. It indicates that as C_R/C increases, $E[TCU(t_{1\pi}^*)]$ rises accordingly; and it confirms that $E[TCU(t_{1\pi}^*)] = \$12,295$ when $C_R/C = 0.5$ (as assumed in our example).

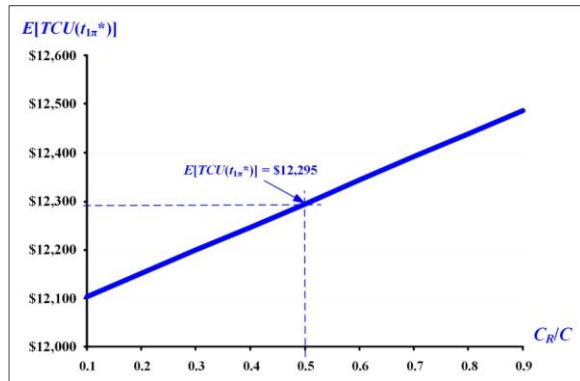


Figure 6. The influence of changes in rework relevant ratio C_R/C on $E[TCU(t_{1\pi}^*)]$

The influence of variations in the number of deliveries per cycle n on relevant costs is illustrated in Figure 7. It specifies that as n increases, the shipping cost rises drastically due to more frequent deliveries, and in-house stock holding goes up accordingly for the slow stock movement from the vendor to the buyer. When $n = 1$, it shows a significantly higher holding cost at the buyer end.

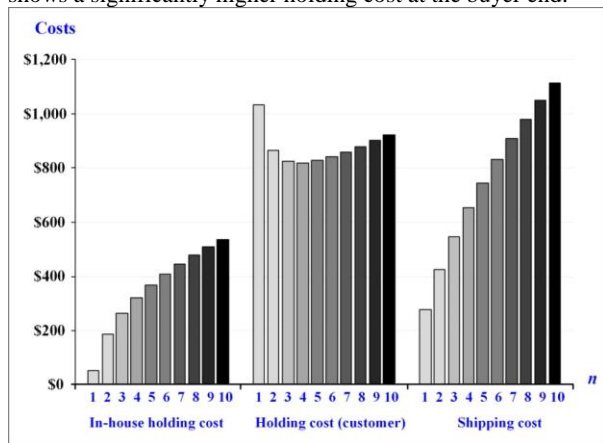


Figure 7. The impact of variations in the number of shipments per cycle n on relevant costs

The influence of the number of deliveries n on $E[TCU(t_{1\pi}^*)]$ is displayed in Figure 8. It reconfirms at $n = 3$, the solution of our example $t_{1\pi}^* = 0.1181$ and $E[TCU(t_{1\pi}^*)] = \$12,295$. Also, Figure 8 exposes that when $n = 2$, we have the minimal $E[TCU(t_{1\pi}^*)]$, and $E[TCU(t_{1\pi}^*)]$ surges significantly, as n rises.

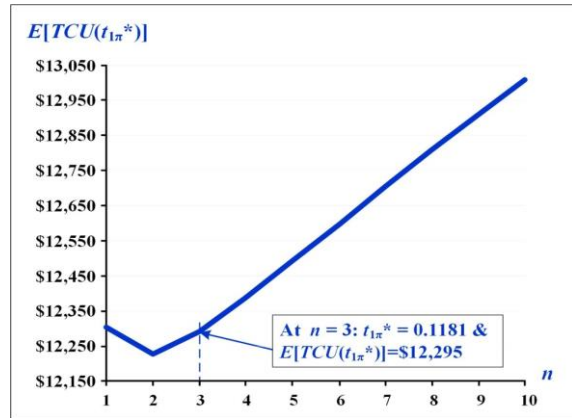


Figure 8. The influence on $E[TCU(t_{1\pi}^*)]$ concerning n

Figure 9 exhibits the breakup of $E[TCU(t_{1\pi}^*)]$. It shows that the setup and variable outsourcing costs add up to 37.2%. Total in-house fabrication relevant costs sum up to 51.3% (main contributors include variable cost 38.8% and breakdown-relevant cost 5.1%). The share of supply-chain integration-related costs is 11.5% (in which buyer holding cost contributes 6.7%).

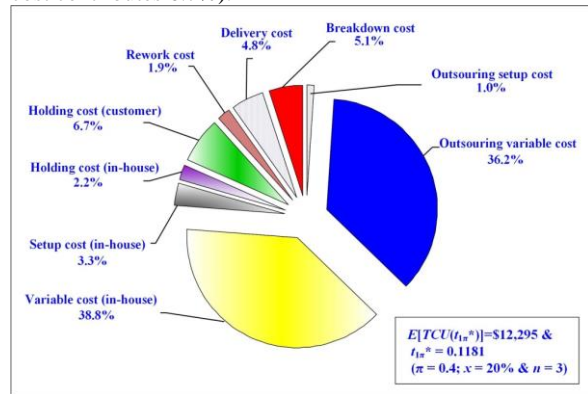


Figure 9. The breakup of $E[TCU(t_{1\pi}^*)]$

The influences of variations in π factor on utilization are shown in Figure 10. It indicates that when $\pi = 0.4$ (as assumed in our example), utilization decreases from 47.68% to 28.68%, and in general, utilization declines significantly as π increases.

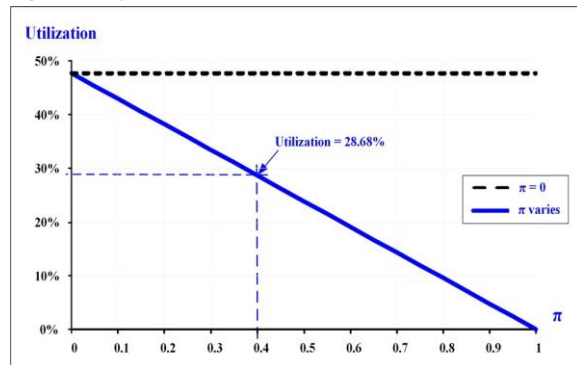


Figure 10. The effect of variations in outsourcing portion π on utilization

Further analysis reveals that the critical π value is 0.71, which can facilitate the “make-or-buy” decision making (see Figure 11). That is, once $\pi \geq 0.71$, the partial outsourcing policy will no longer be beneficial; the better decision is to use outside providers solely for meeting the product demand.

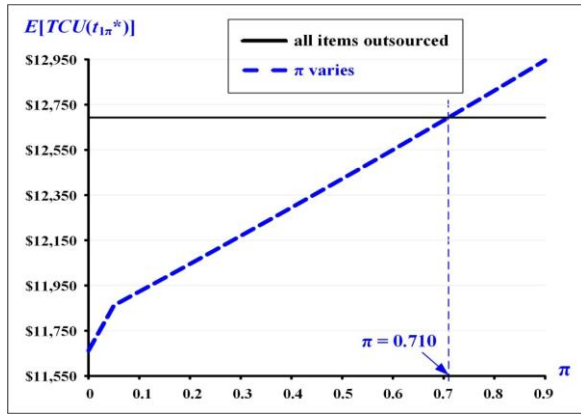


Figure 11. The critical π value for make-or-buy decision making

The influence of differences in mean-time-to-failure $1/\beta$ on $E[TCU(t_{1\pi}^*)]$ is exhibited in Figure 12. It confirms our optimal cost $E[TCU(t_{1\pi}^*)] = \$12,295$, and it also shows that $E[TCU(t_{1\pi}^*)]$ declines significantly as $1/\beta$ increases (especially, when $1/\beta$ rises beyond 0.13). Furthermore, it specifies that as $1/\beta$ goes up to extremely large (for example, $1/\beta \geq 100$), $E[TCU(t_{1\pi}^*)] = \$11,730$, which is the same as the solution obtained from a problem without any failure occurrence.

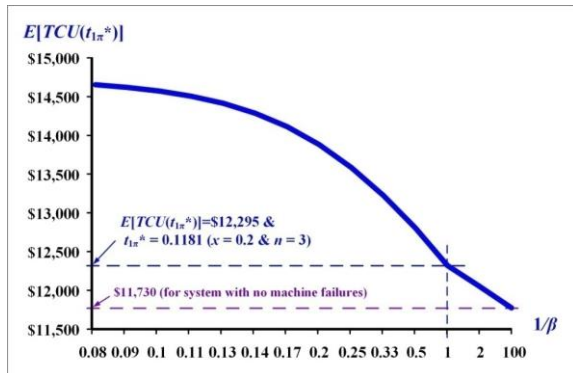


Figure 12. The influence of differences in $1/\beta$ on $E[TCU(t_{1\pi}^*)]$

The effect of changes in the number of deliveries per cycle n on the optimal decision variable $t_{1\pi}^*$ is demonstrated in Figure 13. When $n = 3$, it confirms our result $t_{1\pi}^* = 0.1811$ (years); and as n increases, uptime $t_{1\pi}^*$ rises significantly.

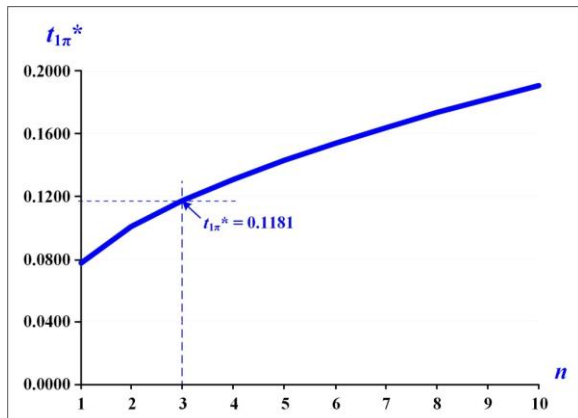


Figure 13. The influence of changes in n on the delivery and stock-holding costs

4.2. Combined effects of the main system feature on the problem

Figure 14 exhibits analytical results of the combined effects of changes in rework relevant ratio C_R/C and outsourcing factor π on $E[TCU(t_{1\pi}^*)]$. It reveals that when π is small, as C_R/C increases, $E[TCU(t_{1\pi}^*)]$ rises considerably; and as π increases, it seems to be irrelevant to C_R/C ratios, $E[TCU(t_{1\pi}^*)]$ upsurges drastically.

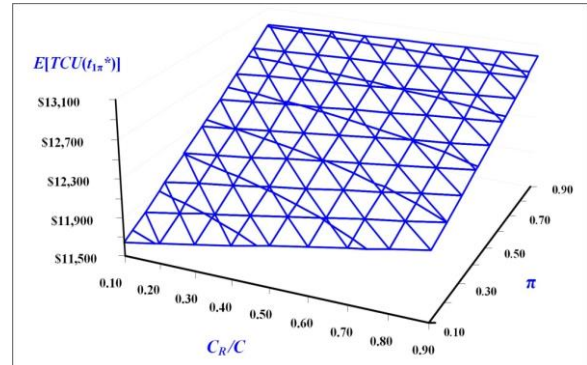


Figure 14. Combined effects of changes in C_R/C and π on $E[TCU(t_{1\pi}^*)]$

The joint influences of variations in random nonconforming rate x and extra proportion β_2 of unit cost on the optimal uptime $t_{1\pi}^*$ are illustrated in Figure 15. It reveals that x has more influence on $t_{1\pi}^*$ than β_2 ; for $t_{1\pi}^*$ decreases significantly, as x increases; and it is slightly changed, as β_2 increases.

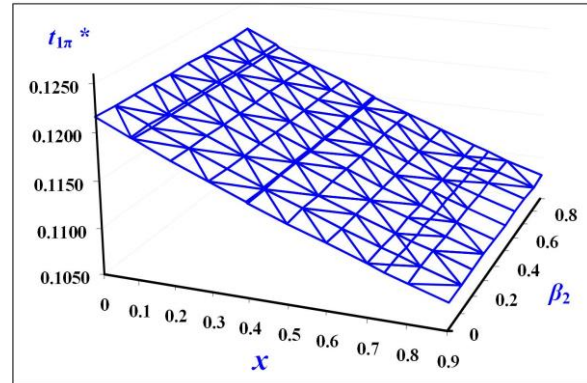


Figure 15. Joint influences of variations in x and β_2 on $t_{1\pi}^*$

4.3. Discussion and limitation

As this study assumed, the cases of only one or no machine failures take place in production uptime. The probabilities of various Poisson-distribution failure rates are exhibited in Table C-1 (see Appendix C). It indicates that the proposed model is appropriate for a good-condition machine (or with an average annual failure rate ≤ 1). There is over 99.35% probability that the number of machine failures ≤ 1 (refer to Table C-1). Further, for a fair-condition machine (or with an average annual failure rate ≤ 3), our model is appropriate as there is over 94.11% chance of one or no failures occurring (see Table C-1). Our model's suitability falls below 94.11% as a machine having a mean failure rate higher than three per year. In such a case, the production planner needs to consider building a different model to explore the best fabrication policy for a system with such particular production equipment.

5. Conclusions

This study builds a mathematical model representing a vendor-buyer integrated system featuring machine failures, outsourcing, multiple deliveries, and rework. Through formulations and derivations, we determine the problem's cost function. The convexity of cost function and the optimal uptime are gained via differential calculus and a proposed specific algorithm. Lastly, we offer a numerical example to show our proposed model makes diverse crucial system information; such as the individual and joint impact of outsourcing, rework, random failures, as well as frequency of delivery on different features and the optimal uptime of the problem (see Figures 6 to 15), easily accessible, to assist enterprises in strategic planning, management, and decision making in their practical intra-supply-chain environments.

Managerial insights: upon completion of the proposed study, the production planners could apply this particular

decision-support model to their hybrid batch fabrication vendor-buyer integrated systems to expose the following systems' characteristics: (1) the optimal fabrication runtime policy; (2) the total system expenses, relevant cost contributors, and machine utilization of their systems; (3) the individual/collective influence of their system's features on the optimal policy and other essential system performances. For future research, the incorporation of stochastic demand into the same context of the proposed model is an interesting direction.

Acknowledgment

The authors thank the Ministry of Science and Technology of Taiwan for supporting this research (Grant#: MOST 107-2221-E-324-015).

Appendix – A

Derivations of Eq. (30) are provided as follows:

First, the integration outcomes of the numerator and denominator of Eq. (28) are given in Eqs. (A-1) and (A-2), respectively.

$$\begin{aligned} & \left\{ \int_0^{t_{1\pi}} E[TC(t_{1\pi})_1] \cdot f(t) dt + \int_{t_{1\pi}}^{\infty} E[TC(t_{1\pi})_2] \cdot f(t) dt \right\} \\ &= K_{\pi} + K + nK_1 + t_{1\pi}\delta_1 + t_{1\pi}^2\delta_2 + M(1 - e^{-\beta t_{1\pi}}) + C_T\lambda g(1 - e^{-\beta t_{1\pi}}) + C_1\lambda g(1 - e^{-\beta t_{1\pi}}) \\ &+ h(P_1g) \left(-t_{1\pi}e^{-\beta t_{1\pi}} - \frac{1}{\beta}e^{-\beta t_{1\pi}} + \frac{1}{\beta} \right) + h_3\lambda g^2(1 - e^{-\beta t_{1\pi}}) + \frac{1}{2}h_2\lambda g^2(1 - e^{-\beta t_{1\pi}}) \\ &+ \frac{g}{2n}(h_2 - h)(t_{1\pi}P_1)(y_1 - y_2)(1 - e^{-\beta t_{1\pi}}) + \frac{hg}{2}(t_{1\pi}P_1)(y_1 - y_2)(1 - e^{-\beta t_{1\pi}}) \\ &+ \frac{g}{2}[h_2 + 2h_3](t_{1\pi}P_1)(y_1 + y_2)(1 - e^{-\beta t_{1\pi}}) \end{aligned} \tag{A-1}$$

$$E[T_{\pi}] = \frac{t_{1\pi}P_1y_1}{\lambda} + g[1 - e^{-\beta t_{1\pi}}] \tag{A-2}$$

where

$$\delta_1 = C_{\pi}\pi P_1y_1 + CP_1 + C_Ty_1P_1 + C_R E[x]P_1 \tag{A-3}$$

$$\begin{aligned} \delta_2 = & \frac{E[x]^2 P_1^2 (h_1 - h)}{2P_2} + \frac{P_1^2 (h_2 - h) y_1}{2n\lambda} (y_1 - y_2) + \frac{h_2 P_1^2 y_1}{2} \left(\frac{y_2}{\lambda} \right) \\ & + \frac{h P_1^2 y_1}{2\lambda} \left[y_1 + \frac{\lambda(-\pi)}{P_1} + \frac{\lambda E[x](1 - 2\pi)}{P_2} \right] \end{aligned} \tag{A-4}$$

With further derivation, one obtains $E[TCU(t_{1\pi})]$ as follows:

$$E[TCU(t_{1\pi})] = \left[\frac{\lambda}{y_1 + \frac{\lambda g [1 - e^{-\beta t_{1\pi}}]}{t_{1\pi} P_1}} \right] \left\{ \begin{aligned} & \frac{u_0}{t_{1\pi}} + \frac{u_1}{t_{1\pi}} + u_2 + t_{1\pi}v_3 - hge^{-\beta t_{1\pi}} + \frac{u_3 e^{-\beta t_{1\pi}}}{t_{1\pi}} \\ & + (v_0 + v_1 + v_2) - (v_0 + v_1 + v_2)e^{-\beta t_{1\pi}} \end{aligned} \right\} \tag{30}$$

where

$$u_0 = \frac{K_{\pi}}{P_1} + \frac{K}{P_1} + \frac{nK_1}{P_1}$$

$$u_1 = \left[\frac{M}{P_1} + \frac{C_T\lambda g}{P_1} + \frac{C_1\lambda g}{P_1} + \frac{h_3\lambda g^2}{P_1} + \frac{1}{2} \frac{h_2\lambda g^2}{P_1} + \frac{hg}{\beta} \right]$$

$$u_2 = [C_{\pi}\pi y_1 + C + C_Ty_1 + C_R E[x]]$$

$$u_3 = \left[\frac{M}{P_1} - \frac{C_T\lambda g}{P_1} - \frac{C_1\lambda g}{P_1} - \frac{h_3\lambda g^2}{P_1} - \frac{1}{2} \frac{h_2\lambda g^2}{P_1} - \frac{hg}{\beta} \right]$$

$$v_0 = \frac{hg}{2}(y_1 - y_2)$$

$$v_1 = \frac{g}{2n}(h_2 - h)(y_1 - y_2)$$

$$v_2 = \frac{g}{2}(h_2 + 2h_3)(y_1 + y_2)$$

$$v_3 = \left[\frac{E[x]^2 P_1 (h_1 - h)}{2P_2} + \frac{P_1 (h_2 - h) y_1}{2n\lambda} (y_1 - y_2) + \left[\frac{h_2 P_1 y_2}{2\lambda (1 - \pi)} \right] + \frac{h P_1 y_1}{2\lambda} \left[y_1 + \frac{\lambda(-\pi)}{P_1} + \frac{E[x]\lambda}{P_2} [1 - 2\pi] \right] \right]$$

Appendix – B

The first- and second-derivatives of $E[TCU(t_{1\pi})]$ are shown in equations (B-1) and (B-2) below:

$$\frac{dE[TCU(t_{1\pi})]}{d(t_{1\pi})} = \frac{\lambda}{\left[y_1 t_{1\pi} P_1 + \lambda g (1 - e^{-\beta t_{1\pi}}) \right]^2} \left\{ \begin{aligned} &-(u_0 + u_1) P_1 (y_1 P_1 + \lambda g \beta e^{-\beta t_{1\pi}}) \\ &+ u_3 P_1 (-y_1 t_{1\pi} P_1 \beta e^{-\beta t_{1\pi}} - \lambda g \beta e^{-\beta t_{1\pi}} - y_1 P_1 e^{-\beta t_{1\pi}}) \\ &+ v_3 t_{1\pi} P_1 (y_1 t_{1\pi} P_1 + 2\lambda g - 2\lambda g e^{-\beta t_{1\pi}} - t_{1\pi} \lambda g \beta e^{-\beta t_{1\pi}}) \\ &-(hg + v_0 + v_1 + v_2) P_1 \left(\begin{aligned} &-y_1 t_{1\pi}^2 P_1 \beta e^{-\beta t_{1\pi}} - \lambda g e^{-2\beta t_{1\pi}} \\ &-t_{1\pi} \lambda g \beta e^{-\beta t_{1\pi}} + \lambda g e^{-\beta t_{1\pi}} \end{aligned} \right) \\ &-(u_2 + v_0 + v_1 + v_2) P_1 \lambda g (t_{1\pi} \beta e^{-\beta t_{1\pi}} + e^{-\beta t_{1\pi}} - 1) \end{aligned} \right. \tag{B-1}$$

and

$$\frac{d^2 E[TCU(t_{1\pi})]}{d(t_{1\pi})^2} = \frac{\lambda}{\left(y_1 t_{1\pi} P_1 + \lambda g (1 - e^{-\beta t_{1\pi}}) \right)^3} \cdot \left\{ \begin{aligned} &(u_0 + u_1) P_1 (2y_1^2 P_1^2 + y_1 t_{1\pi} P_1 \lambda g \beta^2 e^{-\beta t_{1\pi}} + 4y_1 P_1 \lambda g \beta e^{-\beta t_{1\pi}} + \lambda^2 g^2 \beta^2 e^{-2\beta t_{1\pi}} + \lambda^2 g^2 \beta^2 e^{-\beta t_{1\pi}}) \\ &+ u_3 P_1 e^{-\beta t_{1\pi}} \left(\begin{aligned} &y_1^2 t_{1\pi}^2 P_1^2 \beta^2 + 2y_1^2 P_1^2 + 2y_1^2 t_{1\pi} P_1 \beta + 2y_1 t_{1\pi} P_1 \lambda g \beta^2 + 2y_1 P_1 \lambda g \beta \end{aligned} \right) \\ &+ v_3 P_1 \lambda g \left(\begin{aligned} &y_1 t_{1\pi}^3 P_1 \beta^2 e^{-\beta t_{1\pi}} + 2\lambda g e^{-2\beta t_{1\pi}} + t_{1\pi}^2 \lambda g \beta^2 e^{-2\beta t_{1\pi}} - 4\lambda g e^{-\beta t_{1\pi}} \end{aligned} \right) \\ &+ 4t_{1\pi} \lambda g \beta e^{-2\beta t_{1\pi}} + t_{1\pi}^2 \lambda g \beta^2 e^{-\beta t_{1\pi}} - 4t_{1\pi} \lambda g \beta e^{-\beta t_{1\pi}} + 2\lambda g \end{aligned} \right. \tag{B-2}$$

$$\left. \begin{aligned} &-(hg + v_0 + v_1 + v_2) P_1 e^{-2\beta t_{1\pi}} \left(\begin{aligned} &y_1^2 t_{1\pi}^3 P_1^2 \beta^2 e^{\beta t_{1\pi}} + 2y_1 t_{1\pi}^2 P_1 \lambda g \beta^2 e^{\beta t_{1\pi}} - 2y_1 t_{1\pi} P_1 \lambda g \beta e^{\beta t_{1\pi}} \\ &+ y_1 t_{1\pi}^2 P_1 \lambda g \beta^2 + 2\lambda^2 g^2 \beta + 4y_1 t_{1\pi} P_1 \lambda g \beta + t_{1\pi} \lambda^2 g^2 \beta^2 e^{\beta t_{1\pi}} \\ &+ 2y_1 P_1 \lambda g - 2y_1 P_1 \lambda g e^{\beta t_{1\pi}} - 2\lambda^2 g^2 \beta e^{\beta t_{1\pi}} + t_{1\pi} \lambda^2 g^2 \beta^2 \end{aligned} \right) \\ &+(u_2 + v_0 + v_1 + v_2) P_1 \lambda g \left(\begin{aligned} &t_{1\pi} \lambda g \beta^2 e^{-2\beta t_{1\pi}} + t_{1\pi} \lambda g \beta^2 e^{-\beta t_{1\pi}} + 2\lambda g \beta e^{-2\beta t_{1\pi}} - 2\lambda g \beta e^{-\beta t_{1\pi}} \\ &+ y_1 t_{1\pi}^2 P_1 \beta^2 e^{-\beta t_{1\pi}} + 2y_1 P_1 e^{-\beta t_{1\pi}} + 2y_1 t_{1\pi} P_1 \beta e^{-\beta t_{1\pi}} - 2y_1 P_1 \end{aligned} \right) \end{aligned} \right\}$$

Since the first term on the right-hand side (RHS) of Eq. (B-2) is positive, it follows that the $E[TCU(t_{1\pi})]$ is convex if the second term on the RHS of Eq. (B-2) is also positive. That means if the following $\tau(t_{1\pi}) > t_{1\pi} > 0$ holds.

$$\tau(t_{1\pi}) = \frac{\begin{aligned} &(u_0 + u_1) (2y_1^2 P_1^2 + 4y_1 P_1 \lambda g \beta e^{-\beta t_{1\pi}} + \lambda^2 g^2 \beta^2 e^{-2\beta t_{1\pi}} + \lambda^2 g^2 \beta^2 e^{-\beta t_{1\pi}}) \\ &+ u_3 e^{-\beta t_{1\pi}} \left(\begin{aligned} &2y_1^2 P_1^2 + 2y_1 P_1 \lambda g \beta + \lambda^2 g^2 \beta^2 \end{aligned} \right) + v_3 \lambda g (2\lambda g e^{-2\beta t_{1\pi}} - 4\lambda g e^{-\beta t_{1\pi}} + 2\lambda g) \\ &-(hg + v_0 + v_1 + v_2) e^{-2\beta t_{1\pi}} (2y_1 P_1 \lambda g - 2y_1 P_1 \lambda g e^{\beta t_{1\pi}} - 2\lambda^2 g^2 \beta e^{\beta t_{1\pi}} + 2\lambda^2 g^2 \beta) \\ &+(u_2 + v_0 + v_1 + v_2) \lambda g (2\lambda g \beta e^{-2\beta t_{1\pi}} - 2\lambda g \beta e^{-\beta t_{1\pi}} + 2y_1 P_1 e^{-\beta t_{1\pi}} - 2y_1 P_1) \end{aligned}}{\left(\begin{aligned} &(u_0 + u_1) (y_1 P_1 \lambda g \beta^2 e^{-\beta t_{1\pi}}) + u_3 e^{-\beta t_{1\pi}} y_1 (y_1 t_{1\pi} P_1^2 \beta^2 + 2y_1 P_1^2 \beta + 2P_1 \lambda g \beta^2 + P_1 \lambda g \beta^2 e^{-\beta t_{1\pi}}) \\ &+ v_3 \lambda g (y_1 t_{1\pi}^2 P_1 \beta^2 e^{-\beta t_{1\pi}} + t_{1\pi} \lambda g \beta^2 e^{-2\beta t_{1\pi}} + 4\lambda g \beta e^{-2\beta t_{1\pi}} + t_{1\pi} \lambda g \beta^2 e^{-\beta t_{1\pi}} - 4\lambda g \beta e^{-\beta t_{1\pi}}) \\ &-(hg + v_0 + v_1 + v_2) e^{-2\beta t_{1\pi}} \left[\begin{aligned} &y_1^2 t_{1\pi}^2 P_1^2 \beta^2 e^{\beta t_{1\pi}} + 4y_1 P_1 \lambda g \beta + y_1 t_{1\pi} P_1 \lambda g \beta^2 + \lambda^2 g^2 \beta^2 \\ &+ 2y_1 t_{1\pi} P_1 \lambda g \beta^2 e^{\beta t_{1\pi}} - 2y_1 P_1 \lambda g \beta e^{\beta t_{1\pi}} + \lambda^2 g^2 \beta^2 e^{\beta t_{1\pi}} \end{aligned} \right] \\ &+(u_2 + v_0 + v_1 + v_2) \lambda g (\lambda g \beta^2 e^{-2\beta t_{1\pi}} + \lambda g \beta^2 e^{-\beta t_{1\pi}} + y_1 t_{1\pi} P_1 \beta^2 e^{-\beta t_{1\pi}} + 2y_1 P_1 \beta e^{-\beta t_{1\pi}}) \end{aligned} \right)} > t_{1\pi} > 0 \tag{B-3}$$

Appendix C**Table C-1:** Probability of various Poisson-distribution failure rates

β	$t_{1\pi}^*$	$P(y=0)$	$P(y=1)$	$P(y \leq 1)$	$P(y > 1)$
6.0	0.1736	35.30%	36.76%	72.06%	27.94%
5.0	0.1560	45.84%	35.76%	81.60%	18.40%
4.0	0.1412	56.85%	32.11%	88.96%	11.04%
3.0	0.1300	67.71%	26.40%	94.11%	5.89%
2.0	0.1224	78.29%	19.16%	97.45%	2.55%
1.0	0.1181	88.86%	10.50%	99.35%	0.65%
0.01	0.1172	99.88%	0.12%	100.00%	0.00%

$$\frac{e^{-\beta t_{1\pi}^*} (\beta t_{1\pi}^*)^y}{y!} \quad (C-1)$$

References

- [1] H.L. Lee, K. Moinzadeh, "Two-parameter approximations for multi-echelon repairable inventory models with batch ordering policy". *IIE Transactions*, Vol. 19, No. 2, 1987, 140-149.
- [2] H. Groenevelt, L. Pintelon, A. Seidmann, "Production batching with machine breakdowns and safety stocks". *Operations Research*, Vol. 40, No. 5, 1992, 959-971.
- [3] A. Moini, D.N.P. Murthy, "Optimal lot sizing with unreliable production system". *Mathematical and Computer Modelling*, Vol. 31, No. 10-12, 2000, 245-250.
- [4] D.Y. Sha, S.Y. Hsu, Z.H. Che, C.H. Chen, "dispatching rule for photolithography scheduling with an on-line rework strategy". *Computers and Industrial Engineering*, Vol. 50, No. 3, 2006, 233-247.
- [5] A. Goerler, S. Voß, "Dynamic lot-sizing with rework of defective items and minimum lot-size constraints". *International Journal of Production Research*, Vol. 54, No. 8, 2016, 2284-2297.
- [6] S.W. Chiu, S-L. Wang, Y-S.P. Chiu, "Determining the optimal run time for EPQ model with scrap, rework, and stochastic breakdowns". *European Journal of Operational Research*, Vol. 180, No. 2, 2007, 664-676.
- [7] S.W. Chiu, "Robust planning in optimization for production system subject to random machine breakdown and failure in rework". *Computers & Operations Research*, Vol. 37, No. 5, 2010, 899-908.
- [8] X. Liu, J. Pei, L. Liu, H. Cheng, M. Zhou, P.M. Pardalos, *Optimization and Management in Manufacturing Engineering*, Springer Optimization and Its Applications, 2017.
- [9] Z. Zahedi, A. Salim, R. Yusriski, H. Haris, "Optimization of an integrated batch production and maintenance scheduling on flow shop with two machines". *International Journal of Industrial Engineering Computations*, Vol. 10, No. 2, 2019, 225-238.
- [10] S.W. Chiu, J-S. Kuo, Y-S.P. Chiu, H-H. Chang, "Production and distribution decisions for a multi-product system with component commonality, postponement strategy and quality assurance using a two-machine scheme". *Jordan Journal of Mechanical and Industrial Engineering*, Vol. 13, No. 2, 2019, 105-115.
- [11] M.I. Mustajib, U. Ciptomulyono, N. Kurniati, "Determining factors of quality uncertainty and its control analysis in remanufacturing system". *International Journal of Applied Science and Engineering*, Vol. 16, No. 1, 2019, 35-45.
- [12] M.F. Aly, I.H. Afefy, R.K. Abdel-Magied, E.K.A. Elhalim, "A comprehensive model of reliability, availability, and maintainability (RAM) for industrial systems evaluations". *Jordan Journal of Mechanical and Industrial Engineering*, Vol. 12, No. 1, 2019, 59-67.
- [13] S.W. Chiu, H-Y. Wu, P-C. Sung, "Optimal hybrid inventory replenishment runtime for a vendor-buyer coordinated system with breakdowns and rework/disposal of nonconforming items". *Journal of Applied Research and Technology*, Vol. 18, No. 4, 2020, 197-213.
- [14] T. Dohi, J. Zheng, H. Okamura, "A Note on the Time to Failure of a Two-Unit Parallel Redundant System with Deterioration on a Lattice". *International Journal of Mathematical, Engineering and Management Sciences*, Vol. 6, No. 1, 2021, 3-14.
- [15] C. Gaimon, "Subcontracting versus capacity expansion and the impact on pricing of services". *Naval Research Logistics*, Vol. 41, No. 7, 1994, 875-892.
- [16] J.K. Jolayemi, F.O. Olorunniwo, "A deterministic model for planning production quantities in a multi-plant, multi-warehouse environment with extensible capacities". *International Journal of Production Economics*, Vol. 87, No. 2, 2004, 99-113.
- [17] D. Arias-Aranda, O.F. Bustinza, V. Barrales-Molina, "Operations flexibility and outsourcing benefits: an empirical study in service firms". *The Service Industries Journal*, Vol. 31, No. 11, 2011, 1849-1870.
- [18] F. Rosar, "Strategic outsourcing and optimal procurement". *International Journal of Industrial Organization*, Vol. 50, 2017, 91-130.
- [19] Y-S. P. Chiu, C-J. Liu, M-H. Hwang, "Optimal batch size considering partial outsourcing plan and rework". *Jordan Journal of Mechanical and Industrial Engineering*, Vol. 11, No. 3, 2017, 195-200.
- [20] M. García-Vega, E. Huergo, "The role of international and domestic R&D outsourcing for firm innovation". *Journal of Economic Behavior and Organization*, Vol. 157, 2019, 775-792.
- [21] Y-S.P. Chiu, Z-Y. Zhao, S.W. Chiu, V. Chiu, "A vendor-buyer coordinated system featuring an unreliable machine, scrap, outsourcing, and multiple shipments". *International Journal of Industrial Engineering Computations*, Vol. 11, No. 3, 2020, 341-358.
- [22] S. Yadav, A.K. Agrawal, M.K. Vora, "A single manufacturer multiple buyers integrated production-inventory model with third-party logistics". *International Journal of Business Performance and Supply Chain Modelling*, Vol. 11, No. 2, 2020, 91-127.
- [23] Y-S.P. Chiu, J-H. Jhan, V. Chiu, S.W. Chiu, "Fabrication cycle time and shipment decision for a multiproduct intra-supply chain system with external source and scrap". *International Journal of Mathematical, Engineering and Management Sciences*, Vol. 5, No. 4, 2020, 614-630.
- [24] A. Banerjee, J.S. Burton, "Coordinated vs. independent inventory replenishment policies for a vendor and multiple buyers". *International Journal of Production Economics*, Vol. 35, 1994, 215-222.
- [25] R.S. Swenseth, R.M. Godfrey, "Incorporating transportation costs into inventory replenishment decisions". *International Journal of Production Economics*, Vol. 77, No. 2, 2002, 113-130.
- [26] C. Toews, D.W. Pentico, M.J. Drake, "The deterministic EOQ and EPQ with partial backordering at a rate that is linearly dependent on the time to delivery". *International Journal of Production Economics*, Vol. 131, No. 2, 2011, 643-649.
- [27] L.A. Montarelo, R. Glardon, N. Zufferey, "A global simulation-optimisation approach for inventory management in a decentralised supply chain". *Supply Chain Forum: An International Journal*, Vol. 18, No. 2, 2017, 112-119.
- [28] Y. Díaz-Mateus, B. Forero, H. López-Ospina, G. Zambrano-Rey, "Pricing and lot sizing optimization in a two-echelon supply chain with a constrained logit demand function". *International Journal of Industrial Engineering Computations*, Vol. 9, No. 2, 2018, 205-220.
- [29] M. Rahimi, H. Fazlollahtabar, "Optimization of a closed loop green supply chain using particle swarm and

- genetic algorithms". Jordan Journal of Mechanical and Industrial Engineering, Vol. 12, No. 2, 2018, 77-91.
- [30] A.K. Agrawal, S. Yadav, "Price and profit structuring for single manufacturer multi-buyer integrated inventory supply chain under price-sensitive demand condition". Computers & Industrial Engineering, Vol. 139, 2020, Art. No. 106208.
- [31] S.W. Chiu, C-S. Wu, C-T. Tseng, "Incorporating an expedited rate, rework, and a multi-shipment policy into a multi-item stock refilling system". Operations Research Perspectives, Vol. 6, 2019, Art. No. 100115, 1-12.
- [32] S. Sarkar, B.C. Giri, "Stochastic supply chain model with imperfect production and controllable defective rate". International Journal of Systems Science: Operations & Logistics, Vol. 7, No. 2, 2020, 133-146.



الجامعة الهاشمية



المملكة الأردنية الهاشمية

المجلة الأردنية
للمهندسة الميكانيكية والصناعية

JJMIE

مجلة علمية عالمية محكمة
تصدر بدعم من صندوق البحث العلمي

<http://jjmie.hu.edu.jo/>

ISSN 1995-6665

المجلة الأردنية للهندسة الميكانيكية والصناعية

المجلة الأردنية للهندسة الميكانيكية والصناعية: مجلة علمية عالمية محكمة تصدر عن الجامعة الهاشمية بالتعاون مع صندوق دعم البحث العلمي والابتكار - وزارة التعليم العالي والبحث العلمي في الأردن.

هيئة التحرير

رئيس التحرير

الأستاذ الدكتور محمد سامي الأشهب

مساعد رئيس التحرير

الدكتور احمد المقدادي

الدكتور مهند جريسات

الأعضاء

الأستاذ الدكتور طارق العزب

جامعة البلقاء التطبيقية

الأستاذ الدكتور محمد الوديان

جامعة العلوم والتكنولوجيا الاردنية

الأستاذ الدكتور جمال جابر

جامعة البلقاء التطبيقية

الأستاذ الدكتور محمد تيسير هياجنه

جامعة العلوم والتكنولوجيا الاردنية

الأستاذ الدكتور محمد الطاهات

الجامعة الاردنية

الأستاذ الدكتور علي جوارنه

الجامعة الهاشمية

فريق الدعم

المحرر اللغوي

الدكتور بكر محمد بني خير

تنفيذ وإخراج

م . علي أبو سليمة

ترسل البحوث إلى العنوان التالي

رئيس تحرير المجلة الأردنية للهندسة الميكانيكية والصناعية

الجامعة الهاشمية

كلية الهندسة

قسم الهندسة الميكانيكية

الزرقاء - الأردن

هاتف : 00962 5 3903333 فرعي 4147

Email: jjmie@hu.edu.jo

Website: www.jjmie.hu.edu.jo